

REPORT DOCUMENTATION PAGE

Form Approved
OMB No. 0704-0188

Public reporting burden for this collection of information is estimated to average 1 hour per response, including the time for reviewing instructions, searching existing data sources, gathering and maintaining the data needed, and completing and reviewing the collection of information. Send comments regarding this burden estimate or any other aspect of this collection of information, including suggestions for reducing this burden, to Washington Headquarters Services, Directorate for Information Operations and Reports, 1215 Jefferson Davis Highway, Suite 1204, Arlington, VA 22202-4302, and to the Office of Management and Budget, Paperwork Reduction Project (0704-0188), Washington, DC 20503.

1. AGENCY USE ONLY (Leave blank)			2. REPORT DATE 9 Jan 97	3. REPORT TYPE AND DATES COVERED
4. TITLE AND SUBTITLE High Energy Slit Aperture Spect and Simplified Invitro Methods For the Dosimetry of Positron Emitting Rodiotracers			5. FUNDING NUMBERS	
6. AUTHOR(S) Mark Christopher Wrobel				
7. PERFORMING ORGANIZATION NAME(S) AND ADDRESS(ES) University of Michigan			8. PERFORMING ORGANIZATION REPORT NUMBER 96-42D	
9. SPONSORING/MONITORING AGENCY NAME(S) AND ADDRESS(ES) DEPARTMENT OF THE AIR FORCE AFIT/CIA 2950 P STREET WPAFB OH 45433-7765			10. SPONSORING/MONITORING AGENCY REPORT NUMBER	
11. SUPPLEMENTARY NOTES				
12a. DISTRIBUTION AVAILABILITY STATEMENT Unlimited			12b. DISTRIBUTION CODE	
13. ABSTRACT (Maximum 200 words)				
DTIG QUALITY INSPECTED 2				
19970116 014				
				15. NUMBER OF PAGES 198
				16. PRICE CODE
17. SECURITY CLASSIFICATION OF REPORT	18. SECURITY CLASSIFICATION OF THIS PAGE	19. SECURITY CLASSIFICATION OF ABSTRACT	20. LIMITATION OF ABSTRACT	

DISCLAIMER NOTICE



THIS DOCUMENT IS BEST
QUALITY AVAILABLE. THE
COPY FURNISHED TO DTIC
CONTAINED A SIGNIFICANT
NUMBER OF PAGES WHICH DO
NOT REPRODUCE LEGIBLY.

ABSTRACT

HIGH ENERGY SLIT APERTURE SPECT AND SIMPLIFIED INVITRO METHODS FOR THE DOSIMETRY OF POSITRON EMITTING RADIOTRACERS

by

Mark Christopher Wrobel

Captain, USAF

1996

198 pages

PhD, Environmental Health Sciences

University of Michigan

Co-Chairs: James E. Martin, W. Leslie Rogers

The dosimetry of new positron emitting radiopharmaceuticals is initially estimated using animal tissue and organ biodistributions assessed invitro. Such methods are time and labor intensive and can have limited accuracy. This research investigated two alternative methods by which biodistribution can be obtained from the laboratory rat: invitro organ measurements using a reduced sacrifice technique, and invivo measurements using single photon emission computed tomography (SPECT).

As an alternative to a four time-point sacrifice method, a two time-point method was evaluated as a means to determine the organ cumulated activity of ^{11}C labeled radiopharmaceuticals. Residence times calculated using two time-points acquired during the first half-life of ^{11}C were either equivalent or larger than those resulting from using four sacrifice times. Correction factors were required for the urinary bladder and gallbladder when using this simplified technique due to delayed uptakes.

Invivo assessments were performed with SPRINT, a full ring detector SPECT system using a slit aperture to obtain a 3-to-1 object to image magnification ratio.

Acceptable resolution for 511 keV photons was achieved using a high energy parallel slice collimator and a novel technique to correct for penetration of the slit aperture by high energy photons. The resulting system resolution was approximately 4.5 mm axially and transaxially. System sensitivity was \sim 55 cpm/ μ Ci, a consequence of high resolution collimation and poor intrinsic detector efficiency .

Qualitative and quantitative high energy imaging was performed using two-dimensional and three-dimensional phantoms and live rats injected with [18 F]fluorodeoxyglucose. Phantoms displayed well resolved hot and cold objects, and animal images showed good contrast of the brain and heart regions. Hot phantom regions and animal organs were quantified with an accuracy of \pm 8% of the known activity, with a standard deviation of \pm 15%. Accurate determination of region activity required substantial activity concentrations (\sim 100 μ Ci/ml) and imaging times of one hour.

Analysis of animal biodistributions using a reduced sacrifice protocol provides results in good agreement with and generally conservative to results using all sacrifice intervals. Animal biodistributions assessed invivo with slit aperture SPECT can show good accuracy for organs with substantial uptakes, but the method is hindered by very poor system sensitivity.

**HIGH ENERGY SLIT APERTURE SPECT AND SIMPLIFIED
INVITRO METHODS FOR THE DOSIMETRY OF POSITRON
EMITTING RADIOTRACERS**

by

Mark Christopher Wrobel

A dissertation submitted in partial fulfillment
of the requirements for the degree of
Doctor of Philosophy
Environmental Health Sciences
in The University of Michigan
1996

Doctoral Committee:

Associate Professor James E. Martin, Co-Chair
Professor W. Leslie Rogers, Co-Chair
Assistant Professor James E. Carey
Assistant Professor David M. Hamby
Professor Michael R. Kilbourn

Dedicated to my wife Valerie, and my children, Shannon and Sean

ACKNOWLEDGMENTS

Foremost, my thanks to Professor Leslie Rogers who has tirelessly supported my research, and who has been both mentor and guide during the last three years. My thanks also to Professor James E. Martin, whose support has allowed timely completion of this effort. Further thanks to my thesis committee for their understanding and encouragement during this research. Additional thanks to Neil Clinthorne, Yong Zhang and Chor-yi Ng for their kind help and continuous guidance on the many technical issues of this work. Special thanks to Phil Sherman for his assistance with animal biodistribution measurements, Scott Wilderman for his assistance with Monte Carlo simulations, Scott Swanson for his support with MR imaging, Julia Hrycko for her assistance with PET imaging and Ted Webster for his assistance with collimator construction. Final thanks to the PET cyclotron staff, particularly Lou Tluczek and Steve Conner for their support in providing fluorine-18 and other positron emitters.

TABLE OF CONTENTS

DEDICATION.....	ii
ACKNOWLEDGMENTS	iii
LIST OF FIGURES	vii
LIST OF TABLES.....	xii
CHAPTER	
I. INTRODUCTION.....	1
Problem Statement and Research Objectives.....	1
Objectives	2
Background	2
Physical Concepts and the MIRD Formalism.....	4
MIRD Equations for the General Case	5
Outline of Dissertation.....	7
II. A PROPOSED REDUCED SACRIFICE TECHNIQUE FOR THE DOSIMETRY OF ^{11}C LABELED RADIOPHARMACEUTICALS.....	11
Theory	12
Urinary Bladder and Gallbladder	15
Methods.....	16
Urinary Bladder and Gallbladder	19
Results.....	20
Urinary Bladder and Gallbladder	25
Discussion	27
Conclusions.....	31
III. NON-INVASIVE ASSESSMENT OF ANIMAL BIODISTRIBUTIONS	36
Characteristics of SPRINT II: A Second Generation Single Photon Ring Tomograph.....	41

Design and Construction.....	41
IV. TWO DIMENSIONAL IMAGE RECONSTRUCTION FOR SPRINT	49
Filtered Backprojection Algorithms.....	49
The Central Section Theorem and Parallel-Beam Filtered Backprojection.....	51
Convolution Backprojection	55
Converging and Slit-Aperture Filtered Backprojection	56
Slit (Pinhole) Reconstruction Factors for SPRINT	62
The Filter in Filtered Backprojection.....	63
Statistical Reconstruction Algorithms	66
Maximum Likelihood Estimation and the Expectation Maximization (EM) Algorithm.....	67
Properties of the Poisson Distribution	68
The EM Algorithm in Emission Computed Tomography	69
The Space-Alternating Generalized EM Algorithm for Penalized Maximum-Likelihood Image Reconstruction	71
Generation of the SPRINT System Weights.....	73
V. DESIGN, CONSTRUCTION AND PERFORMANCE OF ONE-DIMENSIONAL LEAD FOIL PARALLEL PLATE AND FAN-BEAM COLLIMATORS FOR SPRINT	77
Design Criteria and Early Construction Methods	77
Collimator Materials	80
Collimator Construction Methods	81
Parallel Collimators	81
Fan-Beam Collimators	83
Performance Results	90
Intrinsic Collimator Uniformity	90
Intrinsic Resolution	92
System Sensitivity	94
Summary	96
VI. CORRECTING FOR APERTURE PENETRATION BY HIGH ENERGY GAMMA-RAYS	98
Background	98
Methods.....	100
Initial Attempts to Correct for Penetration	100
A Proposed Solution: Correction Through Blocking.....	102
Correcting for the Non-Ideal Block Response	104

Data Acquisition and Image Reconstruction.....	107
Results.....	109
Discussion.....	112
An Iterative Technique for Improving the Proposed Aperture Penetration Correction Method	116
Summary	118
VII. QUANTITATIVE HIGH ENERGY SPECT IMAGING USING SPRINT	121
SPRINT Calibration and Factors Addressed for Image	
Quantification	121
System Set-Up and Calibration.....	121
Event Position Estimation and Edge Effects at High Energy	122
Decay and Deadtime Correction	126
Flood Correction	130
Attenuation and Scatter Correction.....	131
Correction for Background Radiation.....	135
Summary	136
Quantitative Imaging of 2-D and 3-D Phantoms	138
SPECT Imaging Procedure	140
MRI Imaging Procedure.....	145
Results.....	147
Discussion	158
Quantitative Rat Organ Imaging	160
Methods.....	161
Results.....	165
Discussion	171
Acute FDG Uptake by the Harderian Gland	173
Comparison of Image Performance with Positron Emission Tomography	176
Methods.....	176
Results and Discussion	179
Summary	184
VIII. SUMMARY AND CONCLUSIONS.....	188
Recommended Future Work	191
Conclusions.....	196

LIST OF FIGURES

Figure

2.1. Two-Compartment Kinetics Model for Organ Radioactivity Determination	14
2.2. Simplified Model Proposed for ^{11}C Labeled Radiotracers.	15
2.3. Three-Compartment Kinetics Model for Urinary Bladder and Gallbladder Radioactivity Determination.	15
2.4. Biodistribution of $[^{11}\text{C}]$ Epinephrine in Rat Kidneys	22
3.1. A Generalized SPECT System Featuring a Parallel Hole Collimator	38
3.2. Picture and Exploded View of SPRINT-II Gantry, Slice Collimator and Slit Aperture.	40
3.3. Cross Sectional View of SPRINT-II Showing Key Features	43
3.4. Calculation of Theoretical In-Plane System Resolution	45
3.5. Determination of Geometric Axial Resolution	46
4.1. (A) Acquisition of Point Source Projection at First Detector Location. (B) Backprojected Distribution Of Source Into All Picture Elements Along Acquired Projection's Representative Angle.....	50
4.2. Illustration of the Central Section Theorem.....	51
4.3. Projection of a Two-Dimensional Function.....	52
4.4. Comparison of Field-of-Views and Ray Paths for Three Collimators.....	57
4.5. Comparison of Fan-Beam and Slit Aperture Showing Equidistant Rays.	57
4.6. (A) Fan Beam Geometry With Imaginary Detector Plane at D1'-D2', (B) Nomenclature for Fan Beam Derivation.....	59

4.7. Given Pixel (r,θ) , Define a New Variable U and S'	60
4.8. Obliquity Factors Effecting Measured Fluence Rates.....	63
4.9. Ramp Filter to Correct for $1/r$ Blur in Frequency Domain	64
4.10. Combined High-Pass Ramp Filtering with Low-Pass Hamming or Hanning Filters.....	65
4.11. Weight Generation for Image Voxels Observed by a Detector Element	75
5.1. Design Comparison of Collimator Performance from Monte Carlo Simulations .	78
5.2. Cross-Sectional Views of Low Energy Parallel and ^{131}I Converging Collimators	79
5.3. Stock Materials for Collimator Construction.....	85
5.4. Heated Press for Slice Bonding	85
5.5. Vacuum Chuck for Slice Milling.....	86
5.6. Mounted Rotary Cutters Shown with Completed Collimator Slice.....	86
5.7. Low Energy Collimator Stack in Progress.....	87
5.8. Completed Collimator Stack Under Compression, Prepared For Heating	87
5.9. Spindle Mounted Fly-Cutter Producing Radial Taper	88
5.10. Side Mounted Rotary Cutters Making Inner and Outer Radii Cuts	88
5.11. Slice Prepared for Radial Cut Using Side Mounted Template	89
5.12. Completed Collimators: High Energy, Converging and Low Energy from Left to Right, with Converging Collimator Mounted in SPRINT.	89
5.13. Uniformity of Collimators: Images are Shown for Each of the 11 Detectors Comprising the SPRINT Detector Ring.....	91
5.14. Low Energy Parallel Collimator Intrinsic Response Functions Measured at 0.5 mm Intervals Along Center of SPRINT Field-of-View	93
5.15. Medium Energy Converging Collimator Intrinsic Response Function Measured at 0.5 mm Intervals Along the Center of SPRINT Field-of-View	93
5.16. High Energy Parallel Collimator Intrinsic Response Functions Measured at 0.5 mm Intervals Along the Center of SPRINT Field-of-View	93

6.1. Demonstrated Aperture Penetration Measured for 511 keV Annihilation Radiation	99
6.2. Spatially Variant Penetration Tails Observed for Line Sources Moved Throughout the Field-of View	101
6.3. Projection Profiles for Open Slit and Blocked Slit Apertures	103
6.4. Comparison of Open and Blocked Slit Profiles for Various Location Across the Field of View	103
6.5. Net Line Source Projections Obtained from Difference Between Open and Blocked Slit Data	104
6.6. Ray-Tracing from Point Source Locations in Field of View Through DU Block and Aperture Edges	105
6.7. Demonstration of Spatially Variant Penetration and Penumbral Effects Observed with Actual Block (Dimensions are in/mm)	106
6.8. Effect of Imperfect Aperture Blocking. Figure A and Bottom Profile Indicate Effect of Directly Subtracting Measured Penetration from Open Slit Data.....	107
6.9. Slit Aperture Arrangement and Sampling Protocol for High Energy Imaging. Edges of Slit are Edged with DU.	108
6.10. Six Line Source Array Reconstructed Using FBP, Without and With Penetration Correction	110
6.11. Images of μ Jaszczak Phantom, Hot Lines from 4.0 mm to 1.5 mm	111
6.12. U of M, Without and With Penetration Correction.....	111
6.13. Comparative Point Source Profiles of Aperture Blocked with DU Bar and a Perfect Attenuator	113
6.14. Simulated Assessment of Penumbral Effects and Aperture Block Penetration.	114
6.15. Comparison of Monte Carlo Based Weight to Empirically Derived Blackman Window.....	115

6.16. Comparative Point Source Profiles of Aperture Blocked with Cylindrical DU Bar and a Perfect Attenuator	117
6.17. Comparison of the Net Penetration Through a DU Cylinder Compared to Forward Projected Point Sources Using SPRINT System Weights.....	118
7.1. Vertical Energy Deposition as a Function of Incident Energy.....	124
7.2. Horizontal Fractional Energy Deposition as a Function of Incident Energy..	125
7.3. Comparison of ^{99m}Tc and ^{18}F Flood Profiles	125
7.4. Difference Flood Image for ^{99m}Tc and ^{18}F	126
7.5. Observed Module Count Rate as a Function of Source Activity.....	127
7.6. Comparison Of Uniform Cylinder Imaged Without (A) and With (B) Deadtime Correction	129
7.7. Extrinsic Flood Images of ^{99m}Tc and ^{18}F	130
7.8. Comparison of Energy Spectra from Normalized Line Sources in Air and in Water Filled Phantom.....	133
7.9. Line Source Profiles, in Air and Attenuation Corrected Within Phantom.....	134
7.10. Energy Spectra of Background Radiation.....	136
7.11. Two-Dimensional Syringe Phantom, with Holder (Note Fiduciary Markers) and Lid (Note Injection Port).	139
7.12. Three-Dimensional Phantom Consisting of Two 3 ml Egg Shaped Objects....	140
7.13. MR and SPECT Images of Rod Source.....	148
7.14. MR and SPECT Images of 3-D Egg Phantom.	151
7.15. Serial Acquisitions of Center Slice of Egg Phantom Reconstructed with FBP and Butterworth Filtering (0.9 cm^{-1}).	153
7.16. Serial Acquisitions of Center Slice of Egg Phantom Reconstructed with SAGE and $\beta=2^{-25}$	153
7.17. Total Image Counts as a Function of Total Flux Emitted by the Phantom.....	154
7.18. Animal Prepared for MR and SPECT Imaging.....	162

7.19. Animal During MR Imaging: The Receiver Probe Supports the Rat	162
7.20. Animal (Tail) in SPRINT During SPECT Acquisition.....	164
7.21. MR and SPECT Images of Rat Head and Upper Chest.....	166
7.22. SPECT Images of Rat Cardiac Region, 6 mm Thick Slices Continued from ... Figure 7.21.....	167
7.23. Contrast Enhanced SPECT Images of Rat Brain (Top Row) and Cardiac Regions (Bottom Row).....	168
7.24. Assessment of Focal ^{18}FDG Uptake Medial, Inferior and Posterior to Rodent Eye.	174
7.25. Rat in Animal Holder During PET Imaging.	178
7.26. Image and Profiles for Uniform Cylinder Source and Line Sources Imaged by Positron Emission Tomography.....	180
7.27. Comparative MRI and FDG PET Images of a 275 gm SD Rat. .	183
8.1. Module Spectra of Simultaneously Acquired ^{131}I and ^{18}F Sources.....	195

LIST OF TABLES

Table

2.1. ^{11}C PET Radiotracers Evaluated	14
2.2. Important Source and Target Organs Considered for ^{11}C PET Radiotracers.....	19
2.3. Rat Residence Times for the Three Solid Organs Receiving the Largest Absorbed Dose	23
2.4. Estimated Human Absorbed Dose per Unit Administered Activity for the Three Solid Target Organs Receiving the Largest Dose	24
2.5. Rat Residence Times for the Urinary Bladder and Gallbladder.....	26
2.6. Absorbed Dose per Unit Administered Activity for the Gallbladder Wall and Urinary Bladder Wall.....	27
3.1. SPRINT-II Salient Characteristics	44
3.2. Anatomical Data for the Laboratory Rat.....	47
5.1. Uniformity of Collimators at Different Energies	92
5.2. Intrinsic Collimator Resolution.....	94
5.3. Sensitivity of Collimators as Measured With a Point Source Centered in the SPRINT-II Gantry	95
7.1. Simulation Results of Highly Collimated Photons Incident on a 5x5 cm NaI Slab Sampled at 0.5 mm Intervals with a Lower Energy Window of 460 keV.	123
7.2. Deadtimes for SPRINT Modules.	128
7.3. Effective Transmission and Interaction Probabilities for Annihilation Radiation in Various Tissue Thickness	132

7.4. Corrections Applied to SPRINT Projection Data and Incorporated into Image Reconstruction.	137
7.5. Acquisition Parameters for Rod (2-D) and Egg (3-D) SPRINT Imaging.	143
7.6. Parameters Used for MR Phantom Imaging on CSI 2T System.	146
7.7. Quantitative Analysis for 2-D Phantom, FBP and SAGE Reconstruction.	149
7.8. Bias Introduced by Uncompensated System Deadtime.	154
7.9. Quantitative Analysis for 3-D Egg Phantom, SAGE Reconstruction.	156
7.10. Bias and Standard Deviation Assessed for Hot Egg and Uniform Background of Three Dimensional Phantom.	157
7.11. Acquisition Parameters for Rat MR and SPRINT Imaging.	164
7.12. Measured Invitro Biodistributions and Estimated Organ Activity Concentrations for the Rat Heart and Brain.	169
7.13. Quantitative Image Analysis of Rat Heart, Brain and Lung.	170
7.14. Acquisition Parameters for Rat MR and PET Imaging.	177
7.15. Quantitative Results Obtained from PET Image Analysis.	182
8.1. Characteristics of LSO as a High Efficiency Scintillator.	191
8.2. Comparison of Pinhole Collimator Resolution and Sensitivities for ^{99m}Tc for Several Imaging Systems.	193

CHAPTER I

INTRODUCTION

Problem Statement and Research Objectives

Absorbed dose calculations are required to evaluate the risks posed by the use of new positron emission tomography (PET) radiotracers in medical studies. Human absorbed doses are initially estimated using animal tissue and organ biodistributions assessed invitro and invivo¹. The focus of this research is to investigate two methods by which biodistribution information can be obtained from the laboratory rat: invitro organ measurements using a reduced sacrifice technique and invivo organ measurement using single photon emission computed tomography (SPECT).

Determining the biodistribution of PET radiotracers using conventional tissue counting techniques is labor intensive and requires the sacrifice of numerous animals. Conventional methods require four or more temporal measurements out to 3 or 4 half-lives of ¹¹C, with four to six animals required per sampling interval. Animal sacrifice data for several ¹¹C labeled radiopharmaceuticals such as epinephrine, raclopride, and 2 α -tropanyl benzilate ([¹¹C]TRB) suggest that only one or two sacrifice intervals soon after injection could provide a preliminary assessment of organ cumulated activity that is in good agreement with conventional multiple time sacrifice methods.

Invivo assessment of radionuclide organ activities via single photon emission computed tomography (SPECT) is a desirable alternative to conventional sacrifice methods if it can be shown to accurately determine organ specific uptake and clearance. The advantage of such a method is the ability to trace the biodistribution pattern over time

within the same animal. Further, invivo assessment should prove more accurate than conventional methods for organs which have complex biodistributions such as the urinary bladder and gallbladder. This work proposed to determine the efficacy of assessing animal biodistributions of 511 keV emitting radiotracers using a newly developed SPECT system² as an alternative to conventional animal sacrifice methods.

Objectives

- 1) To evaluate for ¹¹C labeled radiopharmaceuticals whether a limited sacrifice method can be used as a simple but efficient estimator of human organ doses for short-lived PET agents.
- 2) To evaluate the potential and limitations of using a full-ring single photon emission computed tomography system to non-invasively determine the biokinetics of positron emitting labeled radiopharmaceuticals in the rat.

Background

In the development of new radiotracers, a single site in the body, such as the brain, and a given metabolic process, such as glucose metabolism, are of scientific or medical interest to the investigator. However, radiation doses are received from all tissues of the body following the systemic introduction of a radiotracer. Estimation of the absorbed dose delivered to particular organs and tissues for a radiotracer is needed to determine the effective dose to the patient, establish the optimal diagnostic regimen to minimize dose, establish limits on administered activity so that regulatory limits are not exceeded ³, and, as far as practical, to compare risks attributable to the radiation with the possible benefits of the investigation. In order to determine the dose received by a given tissue or organ, the complex relationship between the physical characteristics of the radionuclide used and the biological behavior of the ligand and its metabolites must be known.

In general, the dosimetry of a radiopharmaceutical requires the following types of information:

- (a) the activity administered
- (b) the physical half-life of the radionuclide,
- (c) the type, energy and frequency of particulate and electromagnetic emissions;
- (d) the identity and hence location, mass and shape of target organs,
- (e) the temporal and spatial distribution of activity in source regions,
- (f) the fraction of radiation energy emitted in the source region which is absorbed

in the target region.

The first three involve only physical data, and are generally well-known. The latter three however require biological information, are often difficult to establish and can show significant variation between species and from subject to subject. In particular, measuring the temporal biodistribution of a new radiotracer is the greatest challenge in assessing dosimetry since data for d) and f) are available for a variety of “standard human” geometries⁴. Since radiation dosimetry requires biodistribution information, investigators must use animals, particular the laboratory rat, to establish approximate yet conservative measures of the activity present in various tissues as a function of time post injection. Historically, animal data has included total body radioactivity measurements, the assay of specimens of blood and excreta, and the invitro analysis of whole organs following sacrifice. Within the last several years, pinhole collimated SPECT and high resolution PET have also been proposed as a means for invivo quantification of organ activity in small laboratory animals^{5,6,7,8,9,10,11,12}. A focus of this work will be to evaluate the limitations and benefits of pinhole imaging for high energy gamma-rays. From invivo or invitro serial measurements a “model” for the variation with time of activity in various organs can be constructed. This information then allows estimation of human dose using the Medical Internal Radiation Dosimetry formalism.

Physical Concepts and the MIRD Formalism

The Medical Internal Radiation Dosimetry (MIRD) schema has been broadly adopted for the assessment of internal dose resulting from the internal application of radioactivity in medicine¹. The MIRD method has been described fully by Loevinger and Berman¹³. The fundamental concept of this schema is that absorbed dose calculations are performed for pairs of regions, one of which is called the source region, and the other the target region. The activity in the source region emits radiation which imparts energy to the target region. Source and target regions can be equal, overlap, separate, or one region can entirely encompass another region. Certain quantities depend on interactions between a source and target region, and to distinguish between the two, the dependence is shown as $(r_k \leftarrow r_h)$, where r_k is the target and r_h is the source.

The *absorbed fraction* in a volume from a region is defined as the energy imparted to a target volume v from source region r divided by the energy emitted by the source region:

$$\phi(v \leftarrow r)$$

The absorbed fraction is defined only for target regions that are volumes. The *specific absorbed fraction*, Φ , is defined for a target volume v as the quotient of the absorbed fraction and the mass of v :

$$\Phi(v \leftarrow r) = \frac{\phi(v \leftarrow r)}{m_v}$$

In general, the specific absorbed fraction in any target region r_k from any source region r_h is defined as:

$$\Phi(r_k \leftarrow r_h) = \lim_{v \rightarrow r_k} \Phi(v \leftarrow r_h)$$

In the MIRD schema, the *model* is used to designate the assumptions used in the dose calculation. This typically will include two specific sub-models: an anatomic model which provides information on the spatial and structural assumption of the human,

and a kinetic model which includes assumptions relative to the biodistribution including uptake and clearance of an administered substance. The absorbed dose of interest is the energy imparted per unit mass to specified regions of the anatomic model. The regions of the anatomic model are assumed to be uniform and homogenous, unless macroscopic variations in density or structure are specifically included.

Characterization of a source region requires knowledge of the decay mechanisms of the radionuclide. The number of decays which a radionuclide undergoes in a given source region is designated *cumulated activity* and is normally expressed in microcurie-hour ($\mu\text{Ci}\cdot\text{hr}$), which equals 1.332×10^8 nuclear transformations. The unit of energy is the rad-gram (rad-g), which equals 6.242×10^7 MeV. In general, the mean energy emitted per unit cumulated activity for type *i* radiation is:

$$\Delta_i \left(\frac{\text{rad g}}{\mu\text{Ci} \cdot \text{hr}} \right) = 2.13 n_i E_i$$

where n_i is the number of particles of type *i* emitted per transformation and E_i is the energy of the particle in MeV.

MIRD Equations for the General Case

Consider a pair of source and target regions. Energy is emitted from source region r_h and some fraction of the energy is absorbed by a target region r_k . Let the total activity in r_h equal A_h , the mean energy emitted per nuclear transformation be Δ , and the specific absorbed fraction be $\Phi(r_k \leftarrow r_h)$. Then the rate of energy absorption per unit mass of the target region is the mean absorbed dose rate:

$$\overline{\dot{D}}(r_k \leftarrow r_h) = A_h \Delta \Phi(r_k \leftarrow r_h)$$

There is generally more than one type of radiation associated with a radionuclide, as is the case for positron emitters, and the above equation can be expanded to a more general form to account for each radiation emitted:

$$\bar{D}(r_k \leftarrow r_h) = A_h \sum_i \Delta_i \Phi_i(r_k \leftarrow r_h)$$

If this expression is integrated over some time interval of interest, the total absorbed dose to a given target is obtained. It is generally assumed that Φ_i is independent of time, so the equation for mean dose becomes:

$$\bar{D}(r_k \leftarrow r_h) = \tilde{A}_h(t_1, t_2) \sum_i \Delta_i \Phi_i(r_k \leftarrow r_h)$$

where $\tilde{A}_h(t_1, t_2)$ is the integral of $A_h(t)$ from t_1 to t_2 . For a given radionuclide and a given source target geometry, the quantities Δ_i and Φ_i can be uniquely determined, and a quantity S can be defined as:

$$S(r_k \leftarrow r_h) = \sum_i \Delta_i \Phi_i(r_k \leftarrow r_h)$$

The quantity S is designated the S -value and equals the mean absorbed dose per unit cumulated activity, with typical units of rad/ μ Ci-hr. In actual application, there can be many source regions irradiating a given target. The total mean absorbed dose to a target region r_k is:

$$\begin{aligned}\bar{D}(r_k) &= \sum_h \bar{D}(r_k \leftarrow r_h) \\ \bar{D}(r_k) &= \sum_h \tilde{A}_h S(r_k \leftarrow r_h)\end{aligned}$$

For application to models in medicine and biology, it is frequently assumed that the relative spatial distribution of activity within a given source region (i.e. a tissue or organ) is constant over time, while the total activity in a source region is expected to vary with time. Under these conditions, the quantities which relate the energy emitted by a given source to the energy absorbed by a given target are independent of time, and the S -value is a constant.

When the assumption is made that the source and target organs are in a large homogeneous absorbing material where edge effects can be ignored and activity is uniformly distributed in source regions, the criteria for the *uniform isotropic model* are obtained. Under such conditions, a reciprocal relationship exists between any pair of

source-target organs: the specific absorbed fraction Φ and the mean absorbed dose per unit cumulated activity S are independent of which region is designated the target or source.

The uniform isotropic model is used in this research. S -values are thus constant and have been extracted for reference man⁴ from the MIRD-III program¹⁴. Source regions will typically be either whole organs or whole organ contents for which activity content must be determined as a function of time.

Outline of Dissertation

This dissertation describes research on methods of assessing radiotracer biodistributions in the laboratory rat. Chapter II discusses the methods and findings associated with a reduced sacrifice technique for determining rat biodistributions and compares the results with conventional multiple time-point methods. In Chapter III, the concepts of SPECT are introduced and the salient characteristics and expected performance of SPRINT are described. Chapter IV examines conventional SPECT image reconstruction using direct and iterative methods. The conventional filtered back-projection for parallel and fan-beam geometries is presented, and statistical iterative reconstruction techniques are examined with focus on the space-alternating generalized expectation-maximization (SAGE) algorithm.

Chapter V focuses on the slice collimator requirements of SPRINT, with emphasis on high energy imaging. This chapter discusses those design, construction methods, and performance characteristics of parallel and fan-beam slice collimation that are necessary for achieving a desired axial resolution with SPRINT. In Chapter VI, the issues of quantitative SPECT imaging using SPRINT are introduced, with focus on new research conducted to correct for aperture penetration of high energy gamma rays. Chapter VII discusses other factors considered for conducting high energy imaging using

SPRINT and then presents qualitative and quantitative results of 511 keV imaging of 2-D and 3-D phantoms and live rats injected with [¹⁸F]fluorodeoxyglucose. Finally, Chapter VIII presents summary observations and identifies areas of future work.

References to Chapter I

¹ International Commission on Radiation Units and Measurements, Methods of Assessment of Absorbed Dose in Clinical use of Radionuclides, *ICRU Report 32*, Pergamon Press: New York; 1979.

² Rogers WL, Clinthorne NH, Shao L, Chiao P, Ding Y, Stamos, JA, Koral KF. SPRINT II: A second generation single photon ring tomograph. *IEEE Trans on Med Imaging* 1988;7(4):291-297.

³ Food and Drug Administration. Part 361--Prescription drugs for human use generally recognized as safe and effective and not misbranded: drugs used in research. *Fed Reg* 1990;21:200-205.

⁴ International Commission on Radiological Protection. Report of the task group on reference man, *ICRP Publication 23*, Pergamon Press, New York, 1975.

⁵ Olsson L, Ahlgren L. Tomographic scintigraphy using a pinhole collimator and a rotating gamma camera. *J Nucl Med* 1990;29:47-50.

⁶ Palmer J, Wollmer P. Pinhole emission computed tomography: method and experimental evaluation. *Phys Med Biol* 1990;35:339-350.

⁷ Moore FH, Ohtani H, Khaw BA, Strauss HW. High resolution pinhole sequence imaging of small laboratory animals. *J Nucl Med* 1991;32:987.

⁸ Li J, Jaszcak RJ, Greer KL, Coleman RE, A filtered backprojection algorithm for pinhole SPECT with a displaced center-of-rotation. *Phys Med Biol* 1994;39:165-176.

⁹ Jaszcak RJ, Li J, Wang, H, Zalutsky MR, Coleman RE. Pinhole collimation of ultra-high resolution small-field-of-view SPECT studies. *Phys Med Bio* 1994;39:425-437.

¹⁰ Weber DA, Ivanovic M, Franceschi D, Strand S-E, Erlandsson K, Franceschi M, Atkins HL, Coderre JA, Susskind H, Button T, Ljunggren K. Pinhole SPECT: An approach to invivo high resolution SPECT imaging in small laboratory animals. *J Nucl Med*; 1994 35:342-348.

¹¹ Magata Y Saji H Choi SR Tajima K Takagaki T Sasayama S Yonekura Y Kitano H, Watanabe M, Okada H, et al. Noninvasive measurement of cerebral blood flow and glucose metabolite rate in the rat with high-resolution animal positron emission tomography (PET): a novel in vivo approach for assessing drug action in the brains of small animals. *Biol Pharm Bull* 1995;18(5):753-6.

¹² Cutler PD, Cherry SR, Hoffman EJ, Digby WM, Phelps ME. Design features and performance of a PET system for animal research. *J Nucl Med* 1992;33(4):595-604.

¹³ Loevinger R and Berman M. *A revised scheme for calculating absorbed dose from biologically distributed radionuclides*. MIRD Pamphlet No. 1, revised. New York: Society of Nuclear Medicine; 1976.

¹⁴ Watson E, Stabin M and Bolch W. *MIRDose V3.0*. Oak Ridge Associated Universities, Oak Ridge, Tennessee, 1995.

CHAPTER II

A PROPOSED REDUCED SACRIFICE TECHNIQUE FOR THE DOSIMETRY OF ^{11}C LABELED RADIOPHARMACEUTICALS

Human absorbed dose from carbon-11 (^{11}C) labeled radiopharmaceuticals is initially estimated using animal tissue and organ biodistributions¹, typically in the rat. For a new ^{11}C labeled radiotracer, this determination will usually include measuring organ activities at four or five time points during the first three or four physical half-lives of ^{11}C , using four to six animals per time-point. Organ time-radioactivity profiles are obtained from the measured organ radioactivity, and cumulated activity, residence time, and organ absorbed dose per unit administered radioactivity are calculated.

Determination of animal radioactivity biodistributions for ^{11}C labeled radiotracers is not trivial. The short 20 minute half-life of ^{11}C requires a rapid sacrifice protocol and the use of a significant number of animals to provide high precision and accuracy in the determination. These issues have been recognized by Gatley², who has recommended eliminating animal measurements and basing dose estimates on human cardiac output models, and Schaumann³ who has recommended limiting sacrifice data for long lived ^{14}C -labeled agents. One of the objectives of this study was to evaluate the use of a simplified technique which employs only two sacrifice intervals to assess residence time. Animal biodistribution data were obtained for ten ^{11}C labeled radiopharmaceuticals, and dosimetry estimates were compared between using all sacrifice intervals and a simplified technique. Such an alteration yielded acceptable estimates of human dosimetry.

The accurate assessment of urinary bladder wall dose and gallbladder wall dose are often overlooked when evaluating new short-lived radiotracers. This is partly due to

the difficulty of measuring the residence time for these organs as well as the perception that because of delayed filling and the short physical half-life of ^{11}C , they will be of lesser dosimetric importance than organs which receive first-pass depositions from the blood pool. The urinary bladder contents and estimated gallbladder contents residence times in the rat for ten ^{11}C radiotracers were estimated using measured organ activities and a set of conservative assumptions based on ICRP-53 recommendations⁴. Results indicate that the bladder organs can be critical in determining the limiting dose of new ^{11}C labeled radiotracers for human patients.

Theory

Given a single bolus injection of radioactivity, A_o , into the blood pool, the radioactivity in organ or tissue S is modeled using the following expression:

$$\frac{A_s(t)}{A_o} = F_s \sum_{j=n+1}^{n+m} a_j \sum_{i=1}^n \left\{ a_i \frac{\lambda_j}{\lambda_j - \lambda_i} \left[\exp - (\lambda_i + \lambda_p)t - \exp - (\lambda_j + \lambda_p)t \right] \right\}$$

where F_s is the fractional distribution to organ or tissue S, a_i is the fraction of F_s eliminated with biological removal constant λ_i ; a_j is the fraction of F_s taken up with biological uptake constant λ_j ; n is the number of elimination components; m is the number of uptake components and λ_p is the physical decay constant⁵. This behavior is diagrammatically presented in figure 2.1. A bolus of activity A_o is injected into the transfer compartment, equivalent to the blood pool or systemic circulation in which instantaneous uniform mixing assumed. Pathways are then one-way determined by time-invariant transfer constants.

For absorbed dose calculations in nuclear medicine, and for very short half-life tracers in particular ($T_{1/2} \leq 20$ minutes), several simplifying assumptions to the above model may be applied. First, uptake is either based on a single component or instantaneous uptake is assumed⁴. Further, the effective removal of radioactivity from an organ is described by a single component, and for very short half-life radiotracers can be

taken to be equal to the physical decay constant⁴. With single uptake and excretion components, the above model becomes:

$$\frac{A_s(t)}{A_0} = F_s \times \frac{\lambda_j}{(\lambda_j - \lambda_i)} [\exp - (\lambda_i + \lambda_p)t - \exp - (\lambda_j + \lambda_p)t]$$

The rat organ time-radioactivity profiles for the ¹¹C-labeled compounds listed in table 2.1 demonstrate that the maximum organ radioactivity is found at the time of first sacrifice, which is either two or five minutes post injection. Radioactivity then decreases according to either a mono-exponential or bi-exponential curve with inflection consistently occurring after the second sacrifice interval, 10 to 15 minutes post injection. The trend in organ activity during the first 15 minutes post injection indicates either initial drug washout with an effective removal constant ($\lambda_i + \lambda_p$) being greater than λ_p , or delayed organ uptake with an effective removal constant less than λ_p but greater than 0. Sampling points after this period provide the “tail” of the biodistribution to four or five physical half-lives of the radiopharmaceutical. Exceptions to this finding are the urinary bladder and gastrointestinal track which have complex profiles because of delayed filling and emptying. Removal of radioactivity in the “tail” region was observed to be mono-exponential and either predominantly or solely due to physical decay.

These findings suggest that the above model may be revised to use two discrete time intervals. The first interval is characterized by single uptake and clearance components with physical decay and is identical to the original model. The second interval is characterized by a single clearance component weighted by physical decay, with $\lambda_k \leq \lambda_p$ (figure 2.2). A suitable model for first compartment source organs with a bolus injection of a ¹¹C radiotracer then becomes:

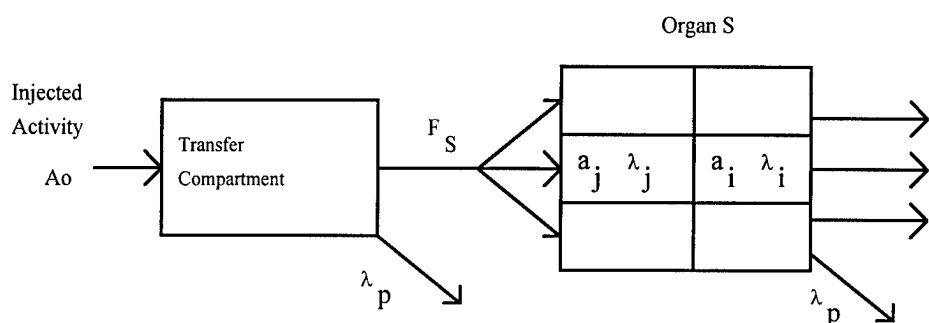
$$A_s(t) = A_o F_s \times \frac{\lambda_j}{(\lambda_j - \lambda_i)} [\exp - (\lambda_i + \lambda_p)t - \exp - (\lambda_j + \lambda_p)t] \quad t \leq 15 \text{ min}$$

$$A_s(t) = A_s(15) \exp - (\lambda_k + \lambda_p)t \quad t > 15 \text{ min}$$

Table 2.1. ^{11}C PET Radiotracers Evaluated

Name or Abbreviation	Chemical Name and Behavior
[^{11}C]EPI	[^{11}C]epinephrine (hydrophilic)
[^{11}C]mHED	[^{11}C]metahydroxyephedrine (hydrophilic)
[^{11}C]PHE	[^{11}C]phenylephrine (hydrophilic)
[^{11}C]MTBZ	[^{11}C]methoxytetraabenazine (lipophilic, amine (3°))
[^{11}C]NMPB	[^{11}C]N-methyl piperidyl benzilate, (lipophilic, amine (3°))
[^{11}C]TBZ	[^{11}C]tetrabenazine (lipophilic, amine (3°))
[^{11}C]TRB	[^{11}C](+)-2 α -tropanyl benzilate (lipophilic, amine (3°))
[^{11}C]FNZPAM	[^{11}C]flunitrazepam (lipophilic, amide)
[^{11}C]PK11195	[^{11}C]1-(2-chlorophenyl-N-methyl-N-(1-methylpropyl)-3-isoquinoline carboximide (lipophilic, amide)
[^{11}C]RAC	[^{11}C]raclopride (variable behavior)

If this model is valid, and assuming λ_k is small, two sacrifice intervals should then be sufficient to describe the biodistribution. This expected behavior allows us to present the hypothesis that differences will be small between biodistributions assessed from multiple sacrifice data and that from a simplified method using two sacrifice times, one very early post injection and the second after one physical half-life of ^{11}C .

**Figure 2.1. Two-Compartment Kinetics Model for Organ Radioactivity Determination.**

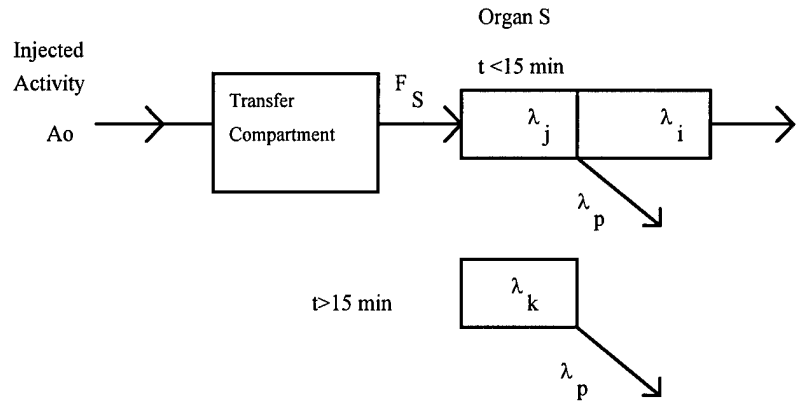


Figure 2.2. Simplified Model Proposed for ^{11}C Labeled Radiotracers.

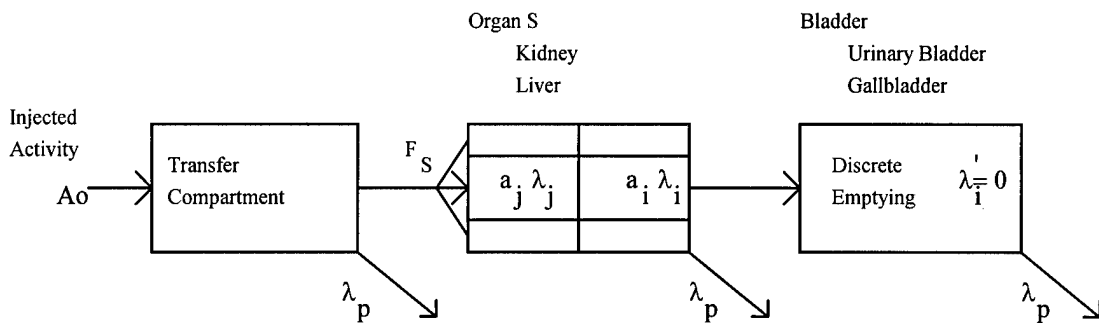


Figure 2.3. Three-Compartment Kinetics Model for Urinary Bladder and Gallbladder Radioactivity Determination.

Urinary Bladder and Gallbladder

Simplified models have been developed to predict radioactivity in the urinary bladder^{4 5 6} and gallbladder^{4 7 8 9 10} using two, three or more catenary compartments (figure 2.3). The model demonstrates a delayed uptake path to the bladder organ, which then empties in discrete time intervals. The ICRP model assumes a 3.5 hour voiding interval for the urinary bladder and 3 hours for the gallbladder. Since these times are long compared to the physical half-life of ^{11}C , biological removal is often ignored. However, such models generally over-simplify the physiological processes involved and the complex relationship between urine or bile flow rate, emptying periods, and the volume

present in the bladder which actually occurs ¹¹ ¹². A three compartment model implies that sampling be performed at a minimum of six time-points, assuming that measured time-radioactivity profiles can be simplified to only three transfer coefficients. In practice, four to five time-points have been used to estimate bladder residence times, with data reflecting significant variability between both animals at a given time point, as well as between compounds. Under such conditions, the simplifying assumptions made for solid first-pass organs are not valid for the bladder organs.

Methods

To evaluate whether a reduced sacrifice protocol is sufficient to estimate cumulated activity, the ten ¹¹C labeled radiotracers in table 2.1 were examined. Biodistributions were evaluated at four sacrifice times with four to five Sprague-Dawley rats (mixed sex) sacrificed per interval. Animals were injected IV (femoral vein) with up to 600 μ Ci of the subject radiotracer, prepared by the University of Michigan PET Facility. Subgroups were then sacrificed at of 2 to 5, 10 to 15, 30 to 45 and 60 to 90 minutes post injection and whole organs dissected out, weighed, and assessed for ¹¹C in a sodium iodide well counter. These intervals will be referred to as T1, T2, T3 and T4, respectively. Organ cumulated activities and residence times were calculated from this data, and a statistical analysis conducted to determine standard deviations and confidence intervals. The results provided a reference for comparison with the proposed simplified technique. The reduced sacrifice method used the above data, but only one or two sacrifice intervals were employed to characterize each radiotracer and organ. Cumulated activity and residence times assessed from the simplified method were compared using a Student's t-test and the percent difference from the conventional multiple point sacrifice method.

Five permutations of available data were tested. Three permutations used two sacrifice intervals: T1 and T2, T1 and T4, and T2 and T4, while the remaining two used a single sacrifice interval: either T1 or T2. Cumulated activities assessed from these simplified methods were compared using a t-test and the percent difference from the extensive multiple point sacrifice method.

The assessment of cumulated activity was determined using the method of Smith, Brownell and Ellett¹³ modified for direct integration to determine the cumulated activity between each available data point. This point-to-point integration method was deemed appropriate because of the limited tissue distribution data available. A limitation of this method is that it does not address the radioactivity profile for time before the first sacrifice interval, thus excluding a possibly important fraction of the total cumulated activity. The most conservative estimate of this profile is obtained by assuming an exponential curve extrapolated back from the first two available data points. This curve will be characterized by a y-intercept which gives a conservative value for the organ radioactivity at time equals zero, and an effective removal constant equal to the slope of the curve. In addition, the method excludes consideration of any natural trend in the time-radioactivity profile, such as being predominantly exponential. For the specific case of carbon-11 compounds where physical decay dominates the time-radioactivity profile, an exponential fit between sacrifice intervals is the most reasonable.

For the animal activities at each sacrifice interval, the sample average and sample standard deviation were calculated. These were then used in the following expression to determine the cumulated activity in the organ from the time of injection to infinity:

$$\begin{aligned}
\tilde{A}(0 \rightarrow \infty) = & \frac{A_0}{\lambda_{\text{eff}(T_1 \rightarrow T_2)}} \left[1 - \exp(-\lambda_{\text{eff}(T_1 \rightarrow T_2)} T_2) \right] \\
& + (A_2 - A_3) \left(\frac{(T_3 - T_2)}{\ln(A_2) - \ln(A_3)} \right) \\
& + (A_3 - A_4) \left(\frac{(T_4 - T_3)}{\ln(A_3) - \ln(A_4)} \right) \\
& + 1.44 \times T_p \times A_4
\end{aligned}$$

The first term on the right of this expression represents the cumulated activity from the time of injection to the second sacrifice interval. This assumes an instantaneous uptake in the organ of A_0 equal to the y-intercept of an exponential fit of the first two sacrifice intervals, and a slope of λ_{eff} . The next two terms assess the cumulated activity between the second and third and then the third and fourth sacrifice intervals based on an integration between these points, and again assuming an exponential fit. The last term represents the cumulated activity from the final sacrifice interval to infinity based on physical decay as the removal mechanism from the organ.

The above calculation requires determination of A_0 and λ_{eff} derived from the first two sacrifice activities and times, and are equal to:

$$\begin{aligned}
A_0 &= \exp \left(\frac{T_1 \times \ln(A_2) - T_2 \times \ln(A_1)}{T_1 - T_2} \right) \\
\lambda_{\text{eff}}(T_1 \rightarrow T_2) &= \left(\frac{\ln(A_2) - \ln(A_1)}{T_2 - T_1} \right)
\end{aligned}$$

For determination of the cumulated activity using a two or single sacrifice interval method, the expressions for cumulated activity reduce to:

$$\tilde{A}(0 \rightarrow \infty) = \frac{A_0}{\lambda_{\text{eff}(T_1 \rightarrow T_2)}} \left[1 - \exp(-\lambda_{\text{eff}(T_1 \rightarrow T_2)} T_2) \right] + 1.44 \times T_p \times A_2 \quad (2 \text{ points})$$

$$\tilde{A}(0 \rightarrow \infty) = 1.44 \times T_p \times [A_1 \exp(\lambda_p T_1)] \quad (1 \text{ point})$$

The source organs considered in this evaluation are listed in table 2.2. They were collected and measured as part of established protocols for determination of the biodistribution of a new radiotracer. Once the residence times in all source organs were

established, they were corrected using factors recommended by Roedler¹⁴ to account for the difference in organ to total body weight proportions between standard rat and standard man. Appropriate S-values (rad/uCi-hr) for all important source-target pairs were obtained from the MIRDose III program¹⁵, with the S-values for the rest of body assessed using the method of Coffey and Watson¹⁶. The dose to a given target organ was then determined from the conventional MIRD formalism^{17 18}. Absorbed dose for all target organs listed in table 2.2 were determined in this manner.

Table 2.2. Important Source and Target Organs Considered for ¹¹C PET Radiotracers

Source Organs (organs harvested as part of sacrifice protocols)				
Adrenals	Kidneys	Ovaries	Spleen	Rest of Body
Brain	Liver	Pancreas	Testes	
Heart	Lung	Small Intestine	Urinary Bladder Contents	
Target Organs (organs for which absorbed dose was calculated)				
Adrenals*	Kidneys	Pancreas	Testes	Red Marrow‡
Brain	Liver	Spleen	Ovaries	Bone Surfaces‡
Heart Wall	Lungs		Uterus†	Total Body
		Urinary Bladder Wall		Gallbladder Wall

*Target organs highlighted were critical organs for one or more of the radiopharmaceuticals considered.

† Uterine dose is assessed to approximate fetal dose, and assumes no transplacental transport of the radiotracer or its metabolites.

‡ Dose to bone surfaces and bone marrow are estimated using remainder of body residence time.

Urinary Bladder and Gallbladder

Dosimetry for the urinary bladder and gallbladder required special consideration.

Urinary bladder residence time was assessed in ligated male rats from the measured bladder contents. Female data was obtained from the radioactivity assessed as “missing”

in rat at the time of sacrifice. Missing radioactivity was that not accounted for in the measured organs and carcass, and was assumed to have been excreted by the animal during the waiting period between injection and sacrifice. The two measures were combined to calculate an effective cumulated activity, resulting in a conservative estimate of bladder residence time and subsequent absorbed dose per unit injected dose. For the purposes of this paper, a conservative estimate of a parameter indicates a value larger than the true value.

The determination of a dose to the small intestine wall or gallbladder wall per unit injected radioactivity is impossible to assess in the rat since the animal has no gallbladder and excretion from the liver is shunted directly to the small intestine. The ICRP indicates that for most very short-lived radiopharmaceuticals, gastrointestinal residence times can be ignored for dosimetric purposes⁴, since clearance from the human gallbladder is considered to occur in bolus amounts, with the first clearance time at three hours post injection which is long compared to the half-life of carbon-11. It is assumed the radioactivity directly shunted to the small intestine results in a small overall dose to the intestine because of delayed uptake and its large mass, and subsequently small S-value. A conservative determination of gallbladder wall dose was made using the ICRP-53 biliary excretion model which assumes that thirty percent of the biliary excretion would be deposited in the gallbladder⁴. Thus, thirty percent of the measured small intestine residence time was used as an estimate for the gallbladder residence time.

Results

The study included four to five animals per time point, with 13 animal organs evaluated at each time point for each of the ten radiotracers. The most prevalent biodistribution observed (65% of cases) was characterized by a rapid maximum uptake at T1, followed by rapid clearance to the second sacrifice interval. After this time, removal

was equal to or somewhat greater than that expected by physical decay. This biodistribution is demonstrated in figure 2.4, and was most characteristic of the hydrophilic compounds such as [¹¹C]epinephrine and [¹¹C]mHED. This behavior was also seen for [¹¹C]NMPB (lipophilic, amine), [¹¹C]FNZPAM (lipophilic, amide) and [¹¹C]raclopride, with the biodistribution exhibiting significant biological removal after the second sacrifice interval. Delayed organ uptakes were demonstrated for the liver and testes of all hydrophilic compounds and for most organ uptakes of [¹¹C]TBZ, [¹¹C]MTBZ and [¹¹C]TRB, accounting for 20% of the cases examined. The radioactivity measured in the carcass and remaining tissues typically followed a mono-exponential profile of pure physical decay, accounting for 15% of the cases.

Because biodistributions varied dramatically during the first 15 minutes post injection, the only acceptable reduced sacrifice permutation required use of the two sacrifice intervals measured within the first physical half-life of ¹¹C. This method had the advantage of preserving information during the period when biological uptake and clearance played a significant role determining the time-radioactivity profile. After the second time of sacrifice, physical decay was assumed to be the only removal mechanism. All other attempted permutations failed to adequately model the measured biodistribution resulting in considerable error in the estimated cumulated activity.

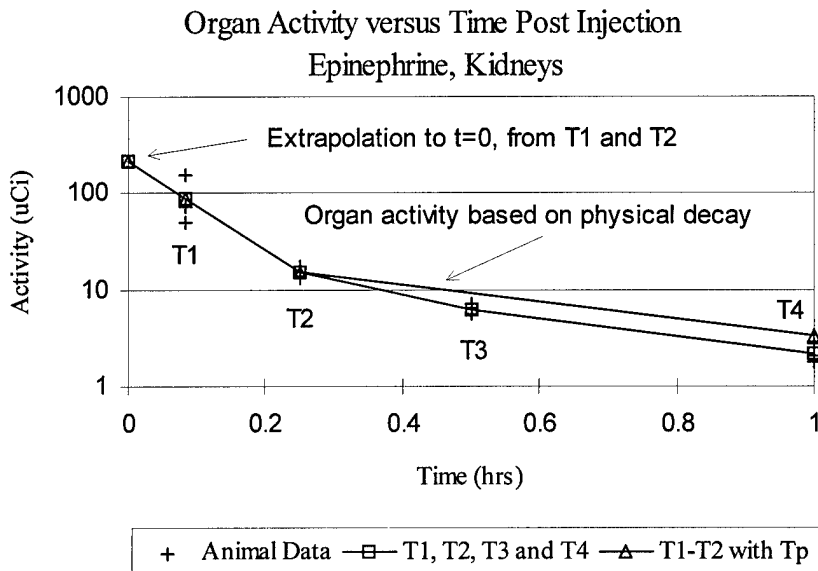


Figure 2.4. Biodistribution of $[^{11}\text{C}]$ Epinephrine in Rat Kidneys. Top Line Indicates Removal By Physical Decay Only After the Second Sacrifice Interval.

The residence times determined using all four sacrifice intervals and only the first two sacrifice intervals are compared in table 2.3 for the three solid organs receiving the highest absorbed dose. The residence time assessed from the simplified method varied from being 50% larger (conservative) to 15% smaller than that assessed using the all available time points. In the vast majority of cases, a conservative measure of residence time resulted as compared to using all data. For those cases where a positive percent difference was measured (i.e. the cumulated activity assessed from all data was greater than that assessed using the reduced method), the difference was small and typically there was no statistical difference between the values as indicated by a Student's t-test. In less than 10% of the cases was the measured residence time using the new method lower than the assessed using the conventional method, up to a maximum difference of 15%.

Table 2.3. Rat Residence Times for the Three Solid Organs Receiving the Largest Absorbed Dose

Drug	Source	All Data Assessed		%Diff†
		Organ	τ_h (s) $\pm \sigma$ τ_h (s) *	
EPI	Heart	32 \pm 2.7	37 \pm 5.0	-16%
	Kidney	88 \pm 40	95 \pm 36	-7.8%
	Liver	420 \pm 39	440 \pm 76	-4.8%
mHED	Heart	39 \pm 3.3	41 \pm 4.7	-4.8%
	Liver	370 \pm 37	360 \pm 49	0.35%
	Kidney	63 \pm 48	69 \pm 41	-11%
PHE	Ovaries	1.1 \pm 0.19	1.1 \pm 0.18	-3.2%
	Kidney	41 \pm 5.0	44 \pm 5.8	-7.8%
	Heart	10 \pm 0.74	12 \pm 1.7	-17%
MTBZ	Ovaries	3.1 \pm 0.53	2.9 \pm 0.90	6.2%
	Adrenals	3.5 \pm 0.63	3.4 \pm 1.1	1.0%
	Pancreas	32 \pm 3.2	37 \pm 6.6	-18%
NMPB	Ovaries	2.5 \pm 0.39	3.3 \pm 0.47	-29%
	Kidney	68 \pm 13	72 \pm 15	-6.6%
	Brain	74 \pm 6.2	77 \pm 7.4	-4.5%
TBZ	Adrenals	2.9 \pm 0.48	3.3 \pm 0.68	-16%
	Ovaries	2.1 \pm 0.26	2.1 \pm 0.15	-1.2%
	Pancreas	65 \pm 5.8	62 \pm 7.5	-16%
TRB	Lung	63 \pm 6.2	75 \pm 11	-17%
	Brain	80 \pm 6.1	93 \pm 12	-16%
	Heart	18 \pm 1.0	23 \pm 1.3	-24%
FNZPAM	Adrenals	1.5 \pm 0.54	2.4 \pm 0.91	-55%‡
	Liver	160 \pm 27	210 \pm 45	-28%
	Ovaries	0.34 \pm 0.09	0.39 \pm 0.08	-15%
PK11195	Adrenals	10 \pm 2.3	9.5 \pm 4.1	5.0%
	Heart	72 \pm 3.4	86 \pm 3.7	-18%
	Ovaries	5.8 \pm 1.8	6.7 \pm 1.7	-15%
RAC	Ovaries	2.1 \pm 0.47	2.3 \pm 0.65	-8.9%
	Kidney	55 \pm 8.2	67 \pm 9.6	-20%
	Liver	230 \pm 15	270 \pm 21	-20%

* The standard deviation of the measured residence time in seconds.

†The percent difference between the measured residence resulting from the two methods, where a negative percent difference indicates a conservative (higher) result using the simplified technique

‡ Anomalous difference based on small organ activities and difficulty in precise determination of adrenal organ activity.

Table 2.4. Estimated Human Absorbed Dose per Unit Administered Activity for the Three Solid Target Organs Receiving the Largest Dose

Drug	Target	All Data Assessed		Limited Data T1 & T2			%Diff†
		Organ	mGy/MBq $\pm\sigma^*$	rad/mCi $\pm\sigma^*$	mGy/MBq $\pm\sigma^*$	rad/mCi $\pm\sigma^*$	
EPI	Heart Wall		0.016 \pm 0.0012	(0.060 \pm 0.0043)	0.019 \pm 0.0024	(0.069 \pm 0.0087)	-15%
	Kidneys		0.012 \pm 0.0043	(0.045 \pm 0.016)	0.013 \pm 0.0045	(0.049 \pm 0.017)	-7.9%
	Liver		0.010 \pm 0.0009	(0.039 \pm 0.0034)	0.011 \pm 0.0017	(0.041 \pm 0.0065)	-5.2%
mHED	Heart Wall		0.019 \pm 0.0018	(0.073 \pm 0.0066)	0.021 \pm 0.0022	(0.076 \pm 0.0082)	-4.9%
	Liver		0.0092 \pm 0.0007	(0.034 \pm 0.0025)	0.0092 \pm 0.0011	(0.034 \pm 0.0042)	-0.19%
	Kidneys		0.0091 \pm 0.0047	(0.034 \pm 0.017)	0.010 \pm 0.0051	(0.037 \pm 0.019)	-9.8%
PHE	Ovaries		0.0073 \pm 0.0007	(0.027 \pm 0.0027)	0.0071 \pm 0.0008	(0.026 \pm 0.0028)	2.8%
	Kidneys		0.0063 \pm 0.0006	(0.023 \pm 0.0022)	0.0068 \pm 0.0007	(0.025 \pm 0.0027)	-7.5%
	Heart Wall		0.0060 \pm 0.0005	(0.022 \pm 0.0018)	0.0070 \pm 0.0008	(0.026 \pm 0.0031)	-16%
MTBZ	Ovaries		0.015 \pm 0.0023	(0.055 \pm 0.0084)	0.014 \pm 0.0038	(0.052 \pm 0.0141)	4.8%
	Adrenals		0.0145 \pm 0.0025	(0.054 \pm 0.0092)	0.015 \pm 0.0039	(0.054 \pm 0.0144)	-0.25%
	Pancreas		0.0089 \pm 0.0007	(0.033 \pm 0.0027)	0.010 \pm 0.0015	(0.038 \pm 0.0054)	-16%
NMPB	Ovaries		0.013 \pm 0.0017	(0.048 \pm 0.0063)	0.016 \pm 0.0020	(0.059 \pm 0.0074)	-22%
	Kidneys		0.0096 \pm 0.0017	(0.036 \pm 0.0063)	0.010 \pm 0.0019	(0.038 \pm 0.0071)	-6.6%
	Brain		0.0095 \pm 0.0008	(0.035 \pm 0.0029)	0.010 \pm 0.0009	(0.037 \pm 0.0034)	-4.9%
TBZ	Adrenals		0.012 \pm 0.0018	(0.045 \pm 0.0068)	0.014 \pm 0.0025	(0.051 \pm 0.0092)	-14%
	Ovaries		0.011 \pm 0.0010	(0.039 \pm 0.0036)	0.011 \pm 0.0007	(0.039 \pm 0.0024)	-0.06%
	Pancreas		0.0084 \pm 0.0009	(0.031 \pm 0.0033)	0.0095 \pm 0.0015	(0.035 \pm 0.0057)	-13%
TRB	Lung		0.012 \pm 0.0011	(0.043 \pm 0.0042)	0.014 \pm 0.0018	(0.050 \pm 0.0065)	-16%
	Brain		0.010 \pm 0.0007	(0.039 \pm 0.0027)	0.012 \pm 0.0016	(0.045 \pm 0.0058)	-15%
	Heart Wall		0.010 \pm 0.0006	(0.038 \pm 0.0022)	0.013 \pm 0.0006	(0.046 \pm 0.0024)	-21%
FNZPAM	Adrenals		0.0070 \pm 0.0019	(0.026 \pm 0.0071)	0.010 \pm 0.0033	(0.037 \pm 0.012)	-44%
	Liver		0.0045 \pm 0.0005	(0.017 \pm 0.0020)	0.0056 \pm 0.0010	(0.021 \pm 0.0038)	-23%
	Ovaries		0.0041 \pm 0.0004	(0.015 \pm 0.0016)	0.0044 \pm 0.0004	(0.016 \pm 0.0015)	-7.2%
PK11195	Adrenals		0.039 \pm 0.0079	(0.14 \pm 0.029)	0.037 \pm 0.015	(0.14 \pm 0.054)	4.2%
	Heart Wall		0.036 \pm 0.0015	(0.14 \pm 0.0055)	0.043 \pm 0.0018	(0.16 \pm 0.0065)	-17%
	Ovaries		0.027 \pm 0.0067	(0.10 \pm 0.025)	0.032 \pm 0.0073	(0.12 \pm 0.027)	-13%
RAC	Ovaries		0.011 \pm 0.0021	(0.040 \pm 0.0076)	0.012 \pm 0.0028	(0.043 \pm 0.010)	-7.5%
	Kidneys		0.0083 \pm 0.0010	(0.031 \pm 0.0036)	0.0097 \pm 0.0012	(0.036 \pm 0.0045)	-17%
	Liver		0.0063 \pm 0.0004	(0.023 \pm 0.0013)	0.0073 \pm 0.0005	(0.027 \pm 0.0018)	-15%

*The standard deviation of the measured organ dose per unit injected radioactivity in mGy/MBq (mrad/mCi).

†The percent difference between the calculated absorbed dose per unit injected dose resulting from the two sacrifice methods.

The comparison of absorbed dose per unit injected radioactivity for the three solid organs receiving the highest dose from each radiotracer is shown in table 2.4. Of the 13 organs for each of the ten radiotracers evaluated, the average percent difference between the reduced sacrifice technique and the extensive technique was 8%. The range of differences between the two methods was from 55% larger (conservative) to 19% smaller. In over half the cases, there was less than a 10% difference between the two methods, and in over 85% of the cases there was less than a 20% difference between the two methods. Overall the reduced sacrifice method lead to a conservative measure of absorbed dose per unit injected activity in 85% of the cases, excluding the gallbladder wall dose and the urinary bladder wall dose. In only 15% of the cases was a positive percent difference measured, and these differences were within the standard deviation of the calculated organ doses.

Urinary Bladder and Gallbladder

Residence times for urinary bladder contents and estimated gallbladder contents, and dosimetry for the gallbladder wall and urinary bladder wall are presented in tables 2.5 and 2.6, respectively. The standard deviation in urinary bladder residence times were on the order of 5% to 50%, and were reasonable considering the expected variability between male bladder contents and the radioactivity assessed as missing from the female rats. The standard deviation for the “gallbladder contents” ranged from 10% to 20%. The bladder data indicated a consistent negative bias between the multiple time-point and reduced sacrifice methods for many of the radiotracers, on the order of thirty to forty percent (i.e. the reduced sacrifice method provided a smaller measure of residence time than the current method). This is largely attributable to the delayed filling of these organs which is not assessed when using a reduced number of sampling points. Similar results are observed for the estimated gallbladder residence time and gallbladder wall dose. A

maximum negative bias of 20% was measured between the four time-point and two time-point methods, again indicative of the delayed uptake in the “gallbladder” from the liver-biliary pathway.

Table 2.5. Rat Residence Times for the Urinary Bladder and Gallbladder

Drug	Source	Organ	All Data Assessed	Limited Data T1 & T2	Bladder Content	
			τ_h (s) $\pm \sigma$ τ_h (s) *	τ_h (s) $\pm \sigma$ τ_h (s) *	%Diff†	Method‡
EPI	U. Bladder	240 \pm 79	250 \pm 20	-5.7%	1	
		Sm. Intest.	122 \pm 24	110 \pm 23	9.7%	
mHED	U. Bladder	260 \pm 23	160 \pm 51	39%	2	
		Sm. Intest.	n.a.	n.a.		
PHE	U. Bladder	450 \pm 27	300 \pm 26	33%	3	
		Sm. Intest.	82 \pm 18	73 \pm 7.5	11%	
MTBZ	U. Bladder	18 \pm 0.96	17 \pm 0.37	3.7%	2	
		Sm. Intest.	95 \pm 12	96 \pm 17	-1.3%	
NMPB	U. Bladder	390 \pm 37	270 \pm 73	32%	4	
		Sm. Intest.	320 \pm 29	267 \pm 46	15%	
TBZ	U. Bladder	110 \pm 25	71 \pm 32	36%	4	
		Sm. Intest.	66 \pm 5.8	62 \pm 7.2	5.1%	
TRB	U. Bladder	138 \pm 30	87 \pm 60	37%	4	
		Sm. Intest.	n.a.	n.a.		
FNZPAM	U. Bladder	360 \pm 58	400 \pm 71	-9.7%	3	
		Sm. Intest.	n.a.	n.a.		
PK11195	U. Bladder	330 \pm 100	350 \pm 178	-6.9%	1	
		Sm. Intest.	n.a.	n.a.		
RAC	U. Bladder	n.a.	n.a.			
		Sm. Intest.	160 \pm 29	130 \pm 50	20%	

* The standard deviation of the measured residence time in seconds.

† The percent difference between the measured residence resulting from the two methods.

‡ Method by which animal urinary bladder radioactivity was determined: 1) Males used measured bladder contents, females used unrecovered radioactivity, 2) Bladder radioactivity based on male bladder contents, essentially 100% recovery in females, 3) Urine not collected, bladder radioactivity estimated from missing radioactivity at time of sacrifice, females only, 4) Urine not collected, bladder radioactivity estimated from missing radioactivity at time of sacrifice, males and females

n.a. = not available

Table 2.6. Absorbed Dose per Unit Administered Activity for the Gallbladder Wall and Urinary Bladder Wall

Drug	Target	All Data Assessed		Limited Data T1 & T2			%Diff†
		Organ	mGy/MBq $\pm\sigma^*$	rad/mCi $\pm\sigma^*$	mGy/MBq $\pm\sigma^*$	rad/mCi $\pm\sigma^*$	
EPI	UB Wall		0.046 \pm 0.015	(0.17 \pm 0.055)	0.049 \pm 0.0037	(0.18 \pm 0.014)	-6.1%
	GB Wall		0.026 \pm 0.0046	(0.098 \pm 0.017)	0.024 \pm 0.0045	(0.090 \pm 0.017)	7.6%
mHED	UB Wall		0.050 \pm 0.0044	(0.19 \pm 0.016)	0.031 \pm 0.0096	(0.12 \pm 0.035)	38%
	GB Wall	n.a.		n.a.	n.a.	n.a.	
PHE	UB Wall		0.085 \pm 0.0050	(0.32 \pm 0.018)	0.058 \pm 0.0050	(0.22 \pm 0.018)	32%
	GB Wall		0.018 \pm 0.0035	(0.068 \pm 0.013)	0.017 \pm 0.0015	(0.062 \pm 0.0054	8.6%
MTBZ	UB Wall		0.006 \pm 0.0002	(0.021 \pm 0.0008)	0.006 \pm 0.0001	(0.021 \pm 0.0005	-0.82%
	GB Wall		0.021 \pm 0.0023	(0.079 \pm 0.0085)	0.022 \pm 0.0033	(0.081 \pm 0.012)	-2.3%
NMPB	UB Wall		0.074 \pm 0.0069	(0.28 \pm 0.026)	0.051 \pm 0.014	(0.19 \pm 0.051)	31%
	GB Wall		0.063 \pm 0.0056	(0.23 \pm 0.021)	0.054 \pm 0.0089	(0.20 \pm 0.033)	14%
TBZ	UB Wall		0.023 \pm 0.0047	(0.085 \pm 0.018)	0.016 \pm 0.0059	(0.058 \pm 0.022)	32%
	GB Wall		0.016 \pm 0.0011	(0.058 \pm 0.0042)	0.015 \pm 0.0015	(0.056 \pm 0.0054	3.7%
TRB	UB Wall		0.028 \pm 0.0056	(0.10 \pm 0.021)	0.019 \pm 0.011	(0.069 \pm 0.042)	34%
	GB Wall	n.a.		n.a.	n.a.	n.a.	
FNZPAM	UB Wall		0.070 \pm 0.011	(0.26 \pm 0.040)	0.076 \pm 0.013	(0.28 \pm 0.049)	-9.3%
	GB Wall	n.a.		n.a.	n.a.	n.a.	
PK11195	UB Wall		0.064 \pm 0.019	(0.24 \pm 0.069)	0.068 \pm 0.033	(0.25 \pm 0.12)	-6.1%
	GB Wall	n.a.		n.a.	n.a.	n.a.	
RAC	UB Wall	n.a.		n.a.	n.a.	n.a.	
	GB Wall		0.035 \pm 0.0055	(0.13 \pm 0.021)	0.028 \pm 0.0096	(0.10 \pm 0.036)	19%

*The standard deviation of the measured organ dose per unit injected radioactivity in mGy/MBq (mrad/mCi).

†The percent difference between the calculated absorbed dose per unit injected dose resulting from the two sacrifice methods.

n.a. = not available

Discussion

The biodistributions observed for ten carbon-11 labeled radiopharmaceuticals suggested that a time-dependent model could be used for solid organs that adequately described the variable initial uptake and clearance of the radiotracer followed by mono-

exponential clearance. Application of a reduced sacrifice technique based on this model made use of two sacrifice times at 2 or 5 minutes and 10 or 15 minutes post injection. Assessment of residence time and absorbed dose per unit injected dose from this technique provided results in good agreement with using extensive sacrifice methods. This proposed simplification in biodistribution assessment provides several advantages over that proposed by Gatley¹⁹, which determined a theoretical upper limits of dose based on cardiac output models. Use of only modeled biodistribution can be overly conservative and does not necessarily provide good agreement with the radiotracer's measured biodistribution. With the use of animal data, conservatism is maintained, and actual organ activities are relied upon for dose estimation.

The magnitude of a given organ dose was most dependent on the measured residence time for that organ and its self-irradiation S-value. This is a consequence of the dose from ¹¹C being principally due to energy deposition by the positron, with relatively little energy deposited by annihilation radiation²⁰. S-values for organ self-irradiation are subsequently three to five orders of magnitude higher than when a target organ is irradiated by a different source organ. This observation allows some flexibility in the protocols used to establish organ residence times for positron emitters since external source organs will contribute negligible dose to a given target. Organs which are dosimetrically unimportant can be assessed quickly using a reduced technique, and protocols tailored to focus on critical organs such as the gonads or bladder organs.

In general the liver, "remainder of body" and urinary bladder contents had the largest residence times regardless of compound and were typically one or two orders of magnitude higher than other organs assessed. However, because of the inverse relationship between organ mass and S-value, smaller body organs were often found to have the highest absorbed dose per unit injected radioactivity. Solid organs which consistently demonstrated the highest dose per unit injected radioactivity included the

liver, kidneys and heart for hydrophilic compounds, and the ovaries, adrenals, kidneys and lung for lipophilic compounds, dependent on the designed receptor site.

Two organs which demonstrated consistently large cumulated activities were the urinary bladder contents and “estimated” gallbladder contents, with high absorbed doses resulting for the urinary bladder wall and gallbladder wall, respectively. Comparing the absorbed dose data between the bladder organs and solid organs, it is apparent that the urinary bladder is frequently the critical organ limiting administered dose. The exceptions include [¹¹C]raclopride for which the gallbladder is limiting and [¹¹C]MTBZ where the ovaries are limiting. However, considerable difficulty was encountered in determining a time-radioactivity profile for these organs. For the case of the urinary bladder, only two or three male rats are currently used per time-point. Because the measured urine radioactivity can vary significantly between these animals due to physiological differences, a valid residence time was difficult to establish. The current method does not address any diluting volume of urine at the time of ligation, and the bladder may be so expanded from urine accumulation at the time of sacrifice that it may affect measured kidney radioactivity. Further, the ligation may fail or the animal can remove the ligation if not properly restrained causing a loss of data. Instead, urinary bladder residence time was conservatively assessed from a combination of the available male data and the radioactivity assessed as “missing” in female rats at the time of sacrifice. The conservatism introduced by using only missing data from the female is observed for [¹¹C]phenylephrine and [¹¹C]FNZPAM where no male data were acquired. The assessed bladder residence times for these two cases were considerably larger than any other radiotracer considered. Ideally, the use of customized metabolic cages for collection of excreted material is desired, but these can greatly complicate the measurement process. Excluding the use of metabolic cages, the current method provides results which show surprisingly small variance and lead to conservative estimates of human radiation dose. Similar observations are made in assessing the residence time of

the gallbladder contents where radioactivity was observed to vary markedly between radiopharmaceutical category (lipophilic verses hydrophilic) as well as between animals. The dose calculated for the gallbladder wall was found to be significant for most radiopharmaceuticals examined, second only to the dose to the urinary bladder wall. The additional complication of rat bladder dosimetry is its applicability to the human. The well known metabolic differences between rat and human contribute additional conservatism to the measured bladder wall doses²¹.

Because of the variability in bladder organ time-radioactivity profiles, the described reduced sacrifice technique requires particular consideration when applied to bladder organs where uptake is clearly delayed and organ concentration is not readily determined by a simple model. Observation of tables 2.5 and 2.6 indicates that correction of the measured urinary bladder residence time by 60% will result in good agreement between the two methods, with a range in bias from 0 to 50% (conservative). A similar correction of 25% can be applied to gallbladder residence times assessed with the two-point method to correct its negative bias, providing a range of differences from 0 to 22% (conservative). If necessary, refinement of the estimated urinary bladder dose can be performed using metabolic cages and application of the dynamic bladder model⁴. Unfortunately, the short half-life of ¹¹C prevents a similar method for invitro verification of the gallbladder wall dose. Recent works have discussed the application of high resolution PET imaging for small animal work^{22 23}. Invivo quantification of urinary bladder and gallbladder contents may someday prove to be a better method of measuring organ radioactivity non-invasively with improved time resolution and accuracy compared to sacrifice methods. Alternatively, bladder data are perhaps best determined “after the fact” from actual human subjects based on invivo quantification and invitro measurement of samples. Since the urinary bladder was commonly the limiting organ in terms of allowable injectable dose, collection of actual human data is important to validate the conservative and error prone animal data.

Recent recommendations of the ICRP²⁴ have supported the use of effective dose in the determination of risk versus benefit in biomedical research. The current tissue weighting factor for the gonads is four times that of the urinary bladder²⁵, placing greater significance in the gonadal dose in determining limiting patient dosage. Should present regulatory bodies adopt ICRP recommendations, increased emphasis will be placed in the accurate determination of both gonadal dose and bladder doses, since these organs were found to receive the maximum effective dose overall. Since both organs are assessed with limited precision in mixed sex animal studies, validation of these organ biodistributions in higher animals or during initial human trials will have increased importance.

Conclusions

Measurement of residence time can be performed conservatively and quickly using a reduced sacrifice method focusing on two intervals within one half-life post injection. The method essentially reduces the time and animal sacrifice requirements by half, while still maintaining necessary accuracy. The applicability of a reduced sacrifice method can be extended to other short or very short half-life radiopharmaceuticals, such as those labeled with 10 minute half-life ¹³N. Considering the inaccuracies in using rat data to characterize human biodistributions, the use of this reduced sacrifice method provides results which are quite acceptable.

The measured biodistributions of both hydrophilic and lipophilic compounds indicates that the urinary bladder wall and gallbladder wall can be dosimetrically important. A correction factor of 1.6 is required for urinary bladder residence times and 1.25 for estimated gallbladder residence time assessed using the reduced sacrifice technique due to the delayed filling of these organs. Using the regulatory limits of 3 rads to the gonads and lens of eye and 5 rads to other organs²⁶, the smallest injectable

radiopharmaceutical dosage was found to be 410 MBq (11 mCi) for [¹¹C]FNZPAM, where the bladder wall dose was limiting. All other radiotracers have considerably higher permissible activities. These doses should be sufficient for initial evaluation of a new radiotracer on current two-dimensional imaging systems. The advent of septaless three-dimensional imaging PET systems will provide significant improvements in sensitivity, by as much as a factor of six to ten^{27 28 29}. This will subsequently allow researchers to investigate the performance of new radiotracers with doses well below the conservative dose limits assessed from the reduced sacrifice method. Investigators should verify bladder time-radioactivity profiles in human subjects during initial imaging trials to refine the recognized conservative bladder measurements made in the rat.

References to Chapter II

¹International Commission on Radiation Units and Measurements. *Methods of Assessment of Absorbed Dose in Clinical use of Radionuclides*, ICRU Report 32, Pergamon Press: New York; 1979.

²Gatley JS. Estimation of upper limits on human radiation absorbed doses from carbon-11 labeled compounds. *J Nucl Med* 1993;34:2208-2215.

³Schaumann W, Neubert P. Animal experiments for estimating the radiation exposure of human subjects by radioactive drugs. *Pharmacology* 1988;37:333-340.

⁴International Commission on Radiological Protection. *Radiation Dose to Patients from Radiopharmaceuticals*. Oxford: Pergamon Press; ICRP Report 53, 1988.

⁵Coutier RJ, Smith SA, Watson EE, Snyder WS, Warner GG. Dose to the fetus from radionuclides in the bladder. *Health Physics* 1973;25:147-161.

⁶Syed IB. Dosimetry of indium-113m radiopharmaceuticals with special attention to the urinary bladder. *Radiopharmaceutical Dosimetry Symposium*. HEW Publication (FDA 76-8044), pp 306-369. Department of Health Education and Welfare, Bureau of Radiological Health, Rockville, Maryland; 1976.

⁷MIRD, Medical Internal Radiation Dose Committee. Estimate Report No. 7 Summary of current radiation dose estimates to humans from 123-I, 124-I, 125-I, 126-I, 130-I and 131-I as Sodium Rose Bengal. *J Nucl Med* 1975;16:1214-1217.

⁸Koutoulidis C, Chiotellis E, Lymberis C. Absorbed dose estimation of some ^{99m}Tc-hepatobiliary agents. *Eur J Nucl Med* 1979;4:441-444.

⁹Brown PH, Krishnamurthy GT, Bobby VR, Kingston E. Radiation-dose calculation for Tc-99m HIDA in health and disease. *J Nucl Med* 1981;22:177-183.

¹⁰Brown PH, Krishnamurthy GT, Bobby VR, Kingston E, Turner FE. Radiation dose calculation for five Tc-99m IDA hepatobiliary agents. *J Nucl Med* 1982;23:1025-1030.

¹¹Snyder WS Ford MR. Estimation of doses to the urinary bladder and to the gonads. *Radiopharmaceutical Dosimetry Symposium*, HEW Publication (FDA 76-8044) pp 313-349, Department of Health, Education and Welfare, Bureau of Radiological Health, Rockville, Maryland; 1976.

¹²Smith T, Veall R, Wootton R. Bladder wall dose from administered radiopharmaceuticals: The effect of variation in urine flow rate, voiding interval, and initial bladder content. *Radiat Prot Dosim* 1982;2:183-189.

¹³Wagner HN, Smith EM, Brownell GL, Ellett WH. *Principles of Nuclear Medicine, Chapter XII, Radiation Dosimetry*, pp 742-784, Saunders, Philadelphia, Pennsylvania; 1968.

¹⁴Roedler HD. Accuracy of internal dose calculations with special consideration of radiopharmaceuticals biokinetics. *Third International Radiopharmaceutical Dosimetry Symposium*, Oak Ridge National Laboratory, HHS-Publ (FDA) 81-8166; pp 1-20, 1980.

¹⁵Watson E, Stabin M, Bolch W. *MIRDOSE V3.0*. Oak Ridge Associated Universities, Oak Ridge, TN, 1995.

¹⁶Coffey JL, Watson E. Calculating dose from remaining body activity: A comparison of two methods. *Med Phys* 1979;6:307-308.

¹⁷Loevinger R, Berman M. *MIRD Pamphlet No. 1, revised, A revised scheme for calculating absorbed dose from biologically distributed radionuclides*. New York: Society of Nuclear Medicine; 1976.

¹⁸Berman M. *MIRD Pamphlet No. 12: Kinetics models for absorbed dose calculations*, New York: Society of Nuclear Medicine; 1977.

¹⁹Gatley JS. Estimation of upper limits on human radiation absorbed doses from carbon-11 labeled compounds. *J Nucl Med* 1993;34:2208-2215.

²⁰Christman DR. Tissue distributions of radiopharmaceuticals labeled with positron emitters and problems relating them to human studies. *Third International Radiopharmaceutical Dosimetry Symposium*, Oak Ridge National Laboratory, HHS-Publ (FDA) 81-8166; pp 250-258, 1980.

²¹McAfee JG, Subramanian G. Interpretation of interspecies differences in the biodistribution of radiative agents. *Third International Radiopharmaceutical Dosimetry Symposium*, Oak Ridge National Laboratory, HHS-Publ (FDA) 81-8166; pp 292-306, 1980.

²²Magata Y, Saji H, Choi SR, Tajima K, Takagaki T, Sasayama S, Yonekura Y, Kitano H, Watanabe M, Okada H, et al. Noninvasive measurement of cerebral blood flow and glucose metabolite rate in the rat with high-resolution animal positron emission tomography (PET): a novel in vivo approach for assessing drug action in the brains of small animals. *Biol Pharm Bull* 1995;18(5):753-6.

²³Cutler PD, Cherry SR, Hoffman EJ, Digby WM, Phelps ME. Design features and performance of a PET system for animal research. *J Nucl Med* 1992; 33(4):595-604.

²⁴International Commission on Radiological Protection. *Radiological protection in biomedical research*. ICRP Report 62, Oxford: Pergamon Press; 1993.

²⁵International Commission on Radiological Protection. *1990 Recommendation of the International Commission on Radiological Protection*. ICRP Report 60, Oxford: Pergamon Press; 1991.

²⁶Food and Drug Administration. Part 361--Prescription drugs for human use generally recognized as safe and effective and not misbranded: drugs used in research. *Fed Reg* 1990;21:200-205.

²⁷ Koeppe, B. Operational characteristics of Siemens EXACT scanner with modification for 3D septaless imaging. *Personal communication*. Feb 1996.

²⁸ Cherry SR, Dahlbom M, Hoffman EJ. 3D PET using a conventional multislice tomograph without septa. In: *J Comput Assist Tomogr* (1991)15(4):655-68.

²⁹ Lecomte R. Analytical study of performance in a 3D PET scanner. *Phys Med Biol* 1992, 37(3):623-34.

CHAPTER III

NON-INVASIVE ASSESSMENT OF ANIMAL BIODISTRIBUTIONS

Invivo assessment of the organ activity of a radiotracer is desirable because it can trace biodistribution within the same subject, relieving problems associated with inter-animal variability. The method could specifically facilitate the assessment of organs with complex biodistribution patterns such as the gallbladder and urinary bladder, as well as be useful for the dosimetry of tumors where a sequential history of tumor uptake and removal in the same animal is required. Historically, several methods have been used for invivo assessment of organ burdens including use of a single external detector (e.g. thyroid burden and bladder activity assessment), use of rectilinear scans, and Anger camera scintigraphy. Conjugate-view counting remains a common tool for invivo quantification. These conventional methods however suffer from interference by background radiation sources extraneous to the organ of interest, i.e. from other tissues overlying, underlying and adjacent to the organ being counted¹.

The development of emission computed tomography (ECT) 30 years ago² has provided a methodology for obtaining estimates of three dimensional activity distributions in a given tissue. Two methods of ECT are currently in use, single photon emission computed tomography (SPECT) and positron emission tomography (PET). In the prior case, nuclides emitting single gamma rays are measured via planar scintigraphy at multiple angles around the patient. A general SPECT system is shown in figure 3.1. In SPECT imaging, a patient is administered a gamma ray emitting radiopharmaceutical. The drug is designed to preferentially localize in a given tissue or to follow a certain physiologic process. Photons emitted by the radionuclide in the patient are detected by a

sodium iodide (NaI) gamma camera, where lead collimation and detector position electronics are used to localize the ray along which the gamma ray was emitted. The camera thus forms a scintigraph, or projection image of the pharmaceutical distribution in the patient. Collimation can be interchanged on the gamma camera to achieve optimal sensitivity and resolution for the energy of the gamma emitter and the target tissue under consideration. The camera is rotated about the patient in a series of steps, and a new planar image is collected at each location. The collected images are reconstructed through a process of Fourier analysis, convolution techniques, or iterative reconstruction techniques to arrive at a transaxial image (or slice view) of the patient. A three-dimensional image of the radioactive source distribution can be obtained by stacking and further manipulating the reconstructed slices. In PET, a positron emitting radiopharmaceutical is injected into the patient, and annihilation radiation is detected by a ring of inorganic scintillators (typically bismuth germinate, or BGO) which are connected to a complex coincidence circuit. Only annihilation photons arriving at transposed detectors within a specific time interval (< 10 nsec) are recorded and used for producing the reconstructed transaxial image. A critical difference between SPECT and PET is the use of conventional lead collimation to restrict the field of view in SPECT systems. In PET, collimation is primarily accomplished electronically through the coincidence counting circuit³. A significant advantage of PET over SPECT is that electronic collimation is at least an order of magnitude more sensitive than mechanical collimation, and sensitivity is not a function of spatial resolution.

If scatter and attenuation in the patient are temporarily ignored, the gamma ray emissions counted via SPECT or PET are proportional to the line integral of activity viewed by the camera. If resolution distance is small (i.e. high resolution) compared to the size of uniform objects being imaged, the reconstructed image will have a voxel count rate which is proportional to the concentration of activity in the organ or tissue. This *invivo* measurement method thus removes the effect of confounding overlying and

underlying activity common in planer imaging, and permits dynamic visualization of a given physiological process in the same patient.

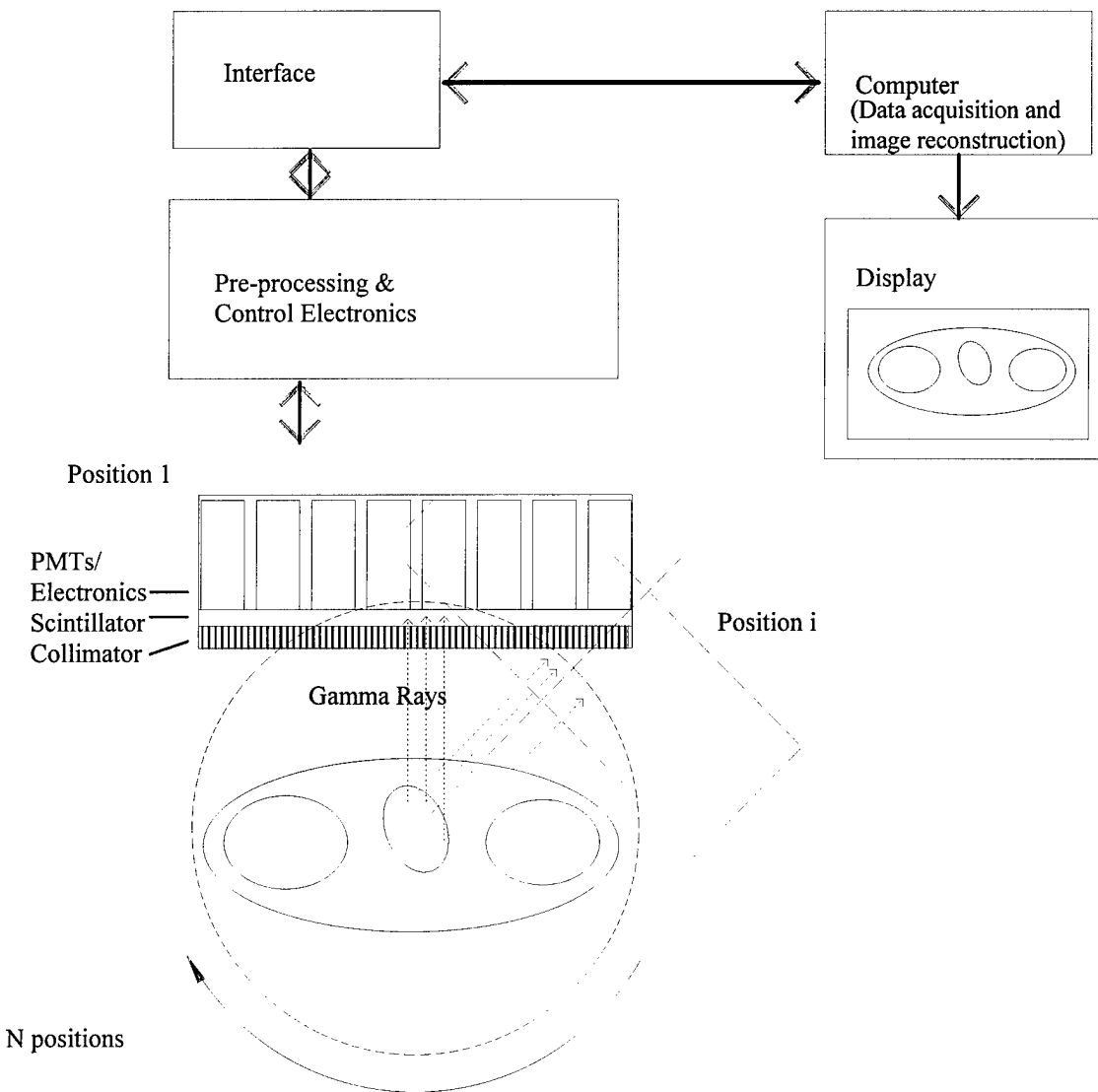


Figure 3.1. A Generalized SPECT System Featuring a Parallel Hole Collimator

Accurate quantification of radionuclide distribution by emission computed tomography is dependent on numerous factors, most notably system resolution and sensitivity. The system extrinsic resolution determines the minimum size object which can be quantified accurately and good system resolution is a requisite to maximize image contrast and organ definition. Poor system resolution causes bias in uptake estimates and

degrades image quality. In general, system resolution depends on 1) geometric and electronic resolution of the detector collimator-system, 2) the adequacy of the sampling geometry, and 3) the range of the positrons (approximately 360 mg/cm^2 for maximum energy ^{11}C positrons). This latter effect cannot be controlled and introduces a loss of at least one to two millimeters in resolution. The intrinsic detector resolution and the collimator resolution combine (approximately in quadrature) to define the limiting system resolution. However, there is an inverse relationship between sensitivity and resolution. Projection image data are inherently deficient in counts due to limits on injected activity, the specificity of the compound for the target tissue, the counting time and the limited system sensitivity. This can result in large statistical fluctuations in the imaged photons, which in turn results in noise in the reconstructed image. High sensitivity is desired to minimize image noise, but this is typically only accomplished by increasing the detector thickness for high energy photons or increasing collimator sensitivity each of which results in a commensurate reduction in resolution. Accurate quantification also requires attention to factors which impact measurement of true line integrals. These include effects of attenuation within the patient, errors due to accidental coincidence in PET, effects of scattered radiation in the object, environmental background and septal or aperture penetration of the measured gamma rays through the lead collimation⁴.

Current systems used clinically for PET and SPECT have neither sufficient sensitivity nor resolution to accurately quantify time dependent radionuclide distributions in small laboratory animals, such as the rat. Work by Rogers et al. at the University of Michigan has focused on development of a small animal SPECT system in order to accelerate and simplify the design and evaluation of new radiopharmaceuticals. This research will focus on characterizing the performance of this instrument for high energy imaging.

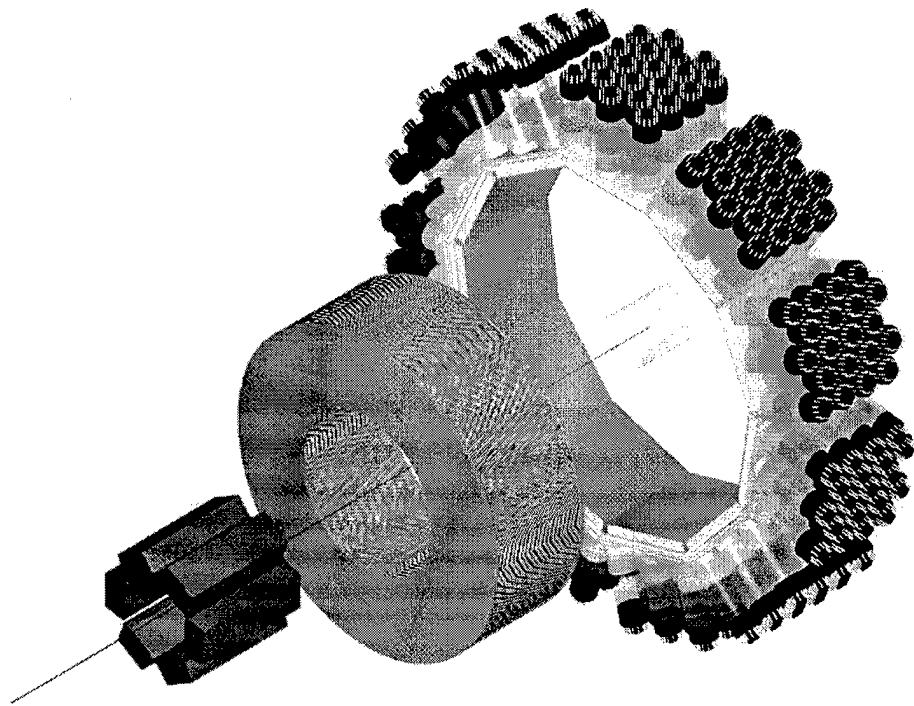
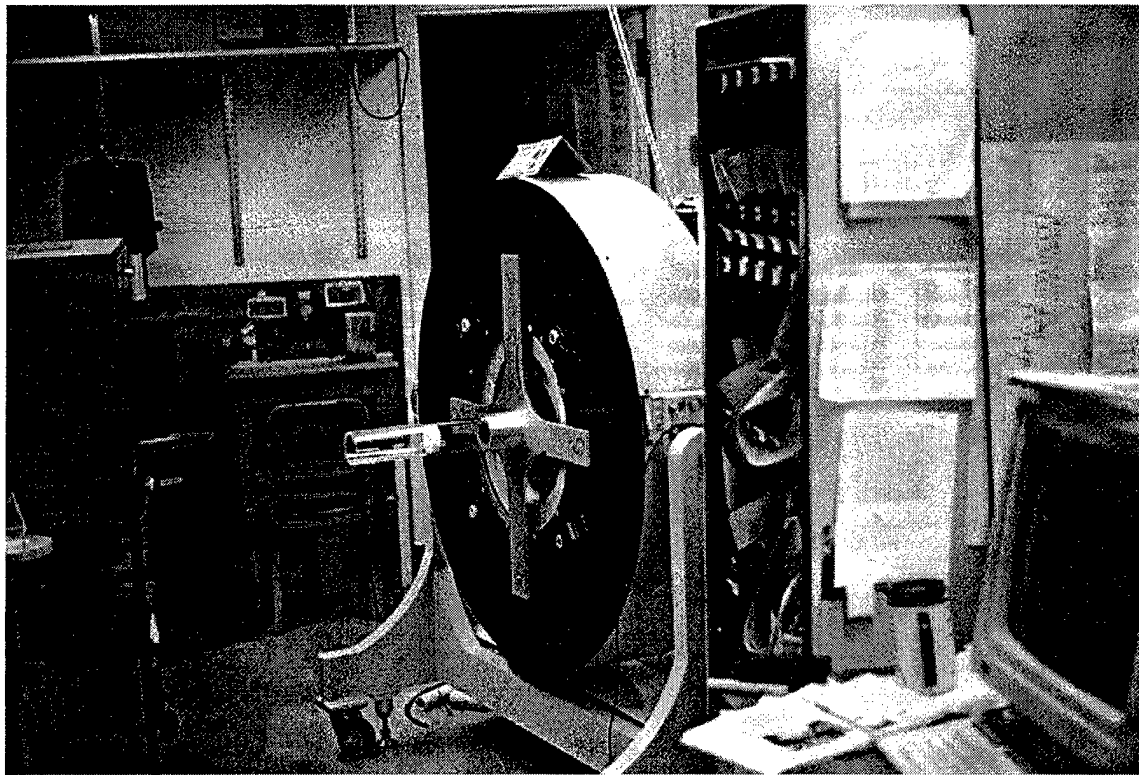


Figure 3.2. Picture and Exploded View of SPRINT-II Gantry, Slice Collimator and Slit Aperture. The cylinder at the center of SPRINT represents the approximate field-of-view.

Characteristics of SPRINT-II: A Second Generation Single Photon Ring Tomograph

The development of new single photon emitting radiotracers for brain imaging such as ^{123}I -HIPDM, ^{123}I -IMP, and ^{99}Tc -HMPAO, and for new tumor-specific therapy agents such as ^{131}I -MIBG and various iodine labeled monoclonal antibodies have generated the requirement for a dedicated single photon imaging system with better sensitivity and resolution than is available with general purpose imaging systems. Work by Rogers et. al. at the University of Michigan has focused on development of a stationary detector single photon ring tomograph (SPRINT-II) designed specifically for human brain imaging⁵. Revision of the collimator design and other characteristics of the original system has expanded its use for the imaging of small laboratory animals. The full ring design of SPRINT provides two specific advantages in SPECT. First, multiple projection data can be simultaneously sampled improving sensitivity and temporal resolution, while reducing temporal blurring in dynamic studies. Second, the fixed ring geometry maintains a rigid center of rotation and reduces electronic instability of the detectors, providing higher quality projection data.

Design and Construction

An exploded figure of the SPRINT-II gantry as configured for high-energy animal imaging is shown in figure 3.2. For animals, the illustrated system has an 8 cm (3.51") diameter field of view. This diameter is defined by the dimension of a rotating multi-slit aperture ring, currently configured with 6 slits at 60° intervals as depicted in figure 3.3. Projection data is acquired by stepping the aperture ring over a 60° arc which provides a full 360° projection set. The slit edges are made of depleted uranium (3.175 mm (0.125") on a side), embedded in lead for improved resolution at high energies. Slit spacing is cam-controlled and can be adjusted radially to change resolution. In order to enhance resolution for small animals and simultaneously utilize the available detector area, the slit

aperture placement is designed to increase magnification of object projections onto the detectors in inverse proportion to the size of the animal. The small animal aperture has a 6.5 cm slit radius and a 25.1 cm detector radius, providing an image-object magnification factor of three to one. The maximum field-of-view is defined by the projection of the object through adjacent slits, such that no overlap occurs of the rays in the detector plane. This is shown in figure 3.3. The salient characteristics of SPRINT are presented in table 3.1⁶.

Encircling the slit collimator is a slice collimator, a parallel or converging plate z-axis collimator which is fabricated from alternating layers of air equivalent closed cell foam and lead foil. Design, construction and performance of this collimator is covered in Chapter Five. The aperture and slice collimator work in tandem to determine the system extrinsic resolution. In-plane image resolution is determined by the slit aperture which provides collimation along the circumference (x-axis of the detector array) of the system. Axial image resolution will be limited by the slice collimator which provides collimation along the z-axis (central axis) of the system.

Surrounding the slice collimator are eleven two dimensional sodium iodide (NaI(Tl)) camera modules which use maximum likelihood position estimation logic⁷. They are arranged in a 50 cm diameter ring with a scintillator packing fraction of 96 percent. Each detector module is nominally composed of 44 NaI(Tl) bars 3 mm wide, 13 mm deep and 15 cm long. The bars lie parallel to the central axis of the gantry and the slit aperture. The 13 mm depth NaI(Tl) bars are comparable to the thickness of older conventional Anger cameras, designed optimally for the detection and resolution of 140 keV (Tc-99m) photons. Photoelectric detection efficiency for 511 keV photons in 13 mm of NaI(Tl) is estimated to be between only 7 percent, compared to 94% for 140 keV photons.

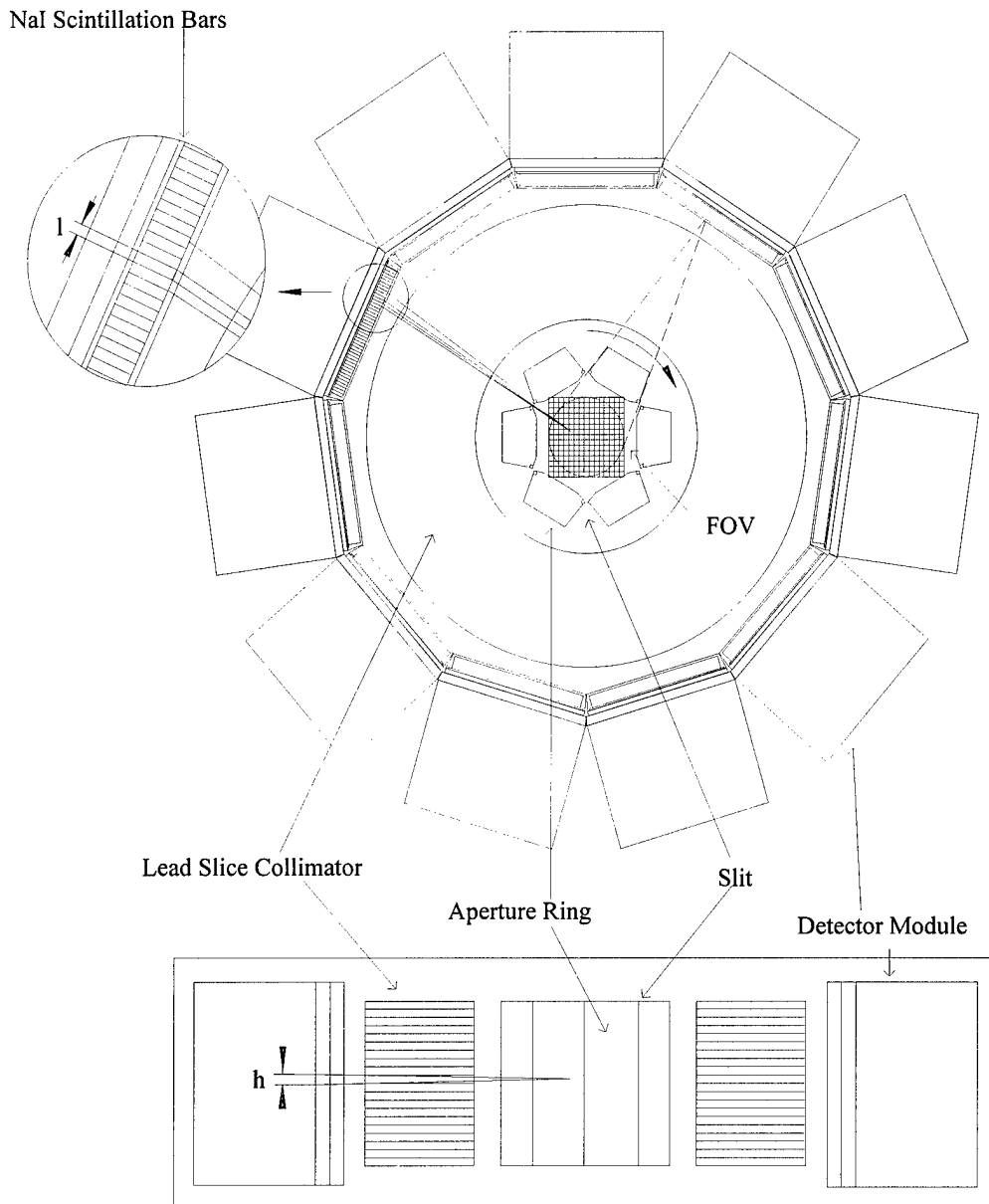


Figure 3.3. Cross Sectional View of SPRINT-II Showing Key Features

Table 3.1. SPRINT-II Salient Characteristics

No. Detector Modules	11
PMTs per Modules	20
Module Dimensions	14 cm x 15.2 cm
Detector Radius	25 cm
Slit Aperture Radius	6.5 cm
Magnification	3-to-1
Number Slits/Angular Separation	6/60°
Slit Width	0 - 4 mm
Slice Collimation	Low-Energy Parallel (140 keV) Medium Energy Converging (364 keV) High Energy Parallel (511 keV)
Axial FOV	9 cm
In-Plane FOV	9 cm

System resolution is dependent on the combined effects of inherent detector resolution, and the imaging geometry. The maximum resolution obtainable for SPRINT can be estimated with the help of Figure 3.4.

Given a point source emitting low energy photons at the center of the field of view, it will project an image onto the detector given by:

$$R_a = \frac{S_w (S_D + S_R)}{S_R}$$

For 511 keV imaging, a slit width of 3.175 mm (0.125") has been usedⁱ. This results in $R_a = 12.3$ mm. This geometric resolution must then be convolved with the intrinsic resolution provided by the detector module, which is approximately equal to the

ⁱ The choice of this slit width and discussion of penetration effects will be presented in Chapter VI.

detector bar width of 3 mm. Assuming spatial invariance and a Gaussian response function, the resolution at the detector is given by:

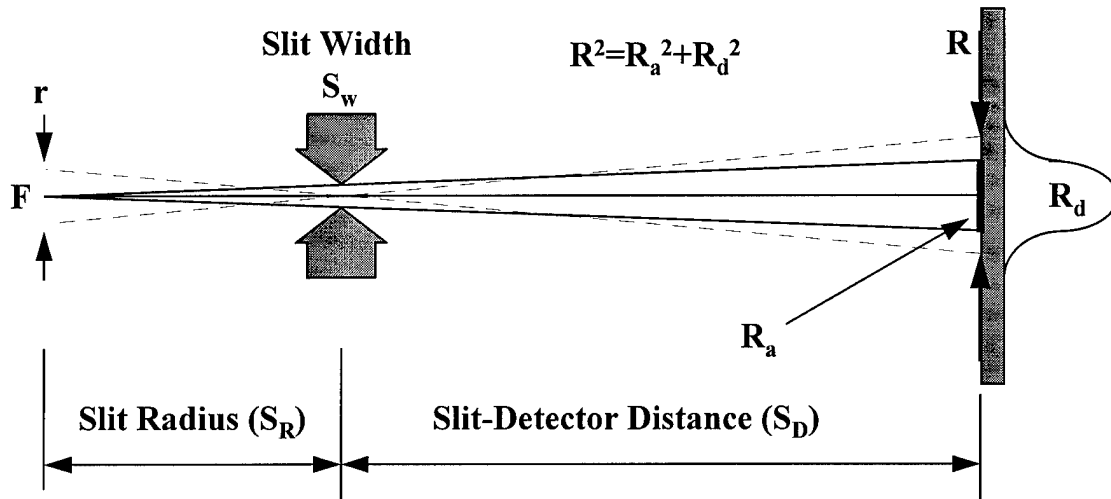


Figure 3.4. Calculation of Theoretical In-Plane System Resolution

$$R = \sqrt{R_a^2 + R_d^2} = 12.6\text{mm}$$

When this is projected back through the slit aperture onto the object space, the system resolution is determined as r , equal to:

$$r = \frac{S_R R}{S_D} = 4.4\text{mm}$$

Thus, assuming the object has a sufficient signal to noise ratio in the reconstructed image, the minimum size object which can be resolved is approximately 4.4 mm. A similar analysis can be used to determine the axial resolution of SPRINT. Since axial resolution is dependent on the slice collimator, the achievable axial resolution will be dependent on the collimator used. From figure 3.5, the collimator resolution is calculated as:

$$R_c = \frac{S_w (S_c + S_R)}{S_c}$$

which when convolved with the detector resolution of 4 mm, results in a predicted axial resolution of 2.3 mm for the medium energy converging collimator, 5.4 mm for the high

energy collimator and 9.3 mm for the low-energy collimator. Slice collimator performance will be reviewed in more detail in Chapter 5.

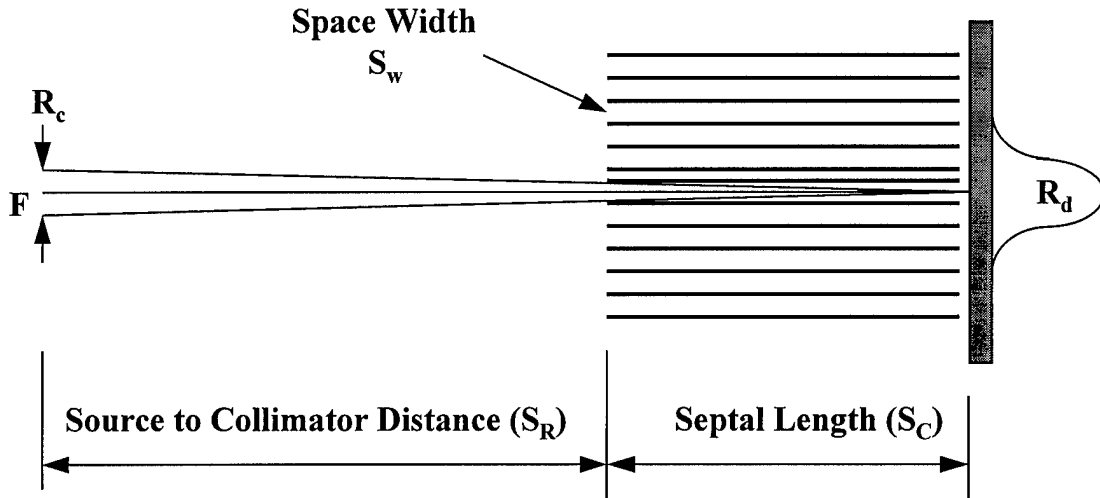


Figure 3.5. Determination of Geometric Axial Resolution

Based on a predicted system resolution of 5 mm for high energy imaging, it is informative to compare resolution with average organ dimensions in the typical laboratory rat to predict some of the limitations with SPRINT II assessment. Table 3.2 provides the typical dimensions and weights of organs in an adult rat with an adult weight of 200 to 250 grams. From the table, it is observed that quantification of activity in the adrenals, ovaries and pancreas would be very difficult due to either their small size or complex shape. Larger organs should have good potential for quantitative assessment, but measurement of heterogeneity of uptake within larger organs is still limited by system resolution.

Since rat organs are not isolated from activity in adjacent tissues, activity concentration in the central region of the organ is the best achievable measure available from animal SPRINT images. Total organ activity must then be assessed by measuring or estimating rat organ volume, and assuming that organ concentration is homogeneous. Several possible alternatives exist to make this determination including using average

organ weights or volumes from "standard" rat corrected to the weight of the animal used in the study, estimating organ volumes from high resolution MR images, and sacrificing the animal at the end of imaging and measuring the organ volume directly.

For organs which are well isolated from other activity in the body, e.g. the heart and brain for radiotracers which show preferential uptake in these organs and little uptake in the adjacent tissues, it is possible to use large regions of interest around the entire organ to estimate total organ activity. However, such estimates are sensitive to system resolution limits and partial volume effects.

Table 3.2. Anatomical Data for the Laboratory Rat⁸

Organ	Size (mm)	Weight (gm)	Comments
Adrenals	4-5.5 mm long, 3-4.5 mm wide, 2.5-3 mm thick	0.02 -0.022 gm	Right covered by caudate lobe of liver. Both near kidneys.
Brain (cerebrum)	8-10 mm high, 12-14 mm wide, 15-20 mm wide	1.5 - 2.2 gm	
Eye	4 mm diameter	0.12 gm (ea)	
Heart	20 mm long, 10-15 mm wide, 10 mm deep	0.9 - 1.0 gm	
Kidney	15-25 mm long, 10-15 mm wide, 10 mm deep	0.73 - 1.2 gm	
Liver	20-40 mm wide, 2-10 cm deep	8.3 gm for 200 gm rat	4 lobes, uneven structure
Lung	20 mm high 10 cm diameter	0.93 - 2.13 gm	uneven structure, surrounds heart
Ovaries	3-5 mm diameter	0.06 gm	
Pancreas		0.5 - 1 gm	very uneven structure, follows liver contour
Spleen	30-50 mm long, 10 mm diameter	0.75-1.3 gm	
Testes	Up to 20 mm long, Up to 14 mm diam.	2.0 - 3.5 gm	
Urinary Bladder	Empty: Pear Shaped, 10 mm long, 5 mm wide Full: Round, 15-25 mm diameter		

References to Chapter III

¹ Budinger TF, Derenzo SE, Huesman RH. *Role of tomography in providing radionuclide distribution and kinetic data*. Third International Radiopharmaceutical Dosimetry Symposium, Oak Ridge National Laboratory, HHS-Publ (FDA) 81-8166; 60-74, 1980.

² Kuhl DE, Edwards ED. Image separation isotope scanning. *Radiology* 1963;80:653-62.

³ Sorenson JA and Phelps ME, *Physics in Nuclear Medicine, 2nd Ed.* Philadelphia: W.B. Saunders Company; 1987;391-423.

⁴ Jaszczak RJ, Greer KL, Coleman RE. SPECT quantification of regional radionuclide distributions. *Fourth International Radiopharmaceutical Dosimetry Symposium*, Oak Ridge Associated Universities, CONF-851113-(DE86010102), 1985;82-96.

⁵ Rogers WL, Clinthorne NH, Shao L, Chiao P, Ding Y, Stamos JA, Koral KF. SPRINT II: A second generation single photon ring tomograph. *IEEE Trans Med Imag.* 1988;7:4:291-297.

⁶ Rogers WL. *ASP: A small animal tomograph for radiotracer evaluation*. University of Michigan, Proposal research summary. 1992.

⁷ Clinthorne NH, Rogers WL, Shao L, Koral KF. A hybrid maximum likelihood computer for scintillation cameras. *IEEE Tran. Nuc Sci* 1987;NS-34:97-101.

⁸ Hebel R, Stromberg MW, *Anatomy of the Laboratory Rat*, New York; Williams and Wilkins: 1976.

CHAPTER IV

TWO DIMENSIONAL IMAGE RECONSTRUCTION FOR SPRINT

Data acquisition in SPRINT is performed by incrementally rotating the slit aperture n times through a total arc of sixty degrees. The object is projected simultaneously through the six slits onto the detector ring for each position of the aperture, such that $6n$ projections are collected at $60/n$ degree increments. The resulting series of two dimensional scintigrams must be processed to reconstruct the transverse section of the original source distribution. The solution to calculating a density function from its projections was first presented by Radon in 1917 in the form of an integral equation.¹ Other approaches have since been presented including Fourier techniques and iterative solutions. This chapter will discuss the two general algorithms which have been implemented for image reconstruction with SPRINT: conventional filtered backprojection and statistical iterative reconstruction using the space alternating generalized expectation-maximization (SAGE) algorithm.

Filtered Backprojection Algorithms

Consider the simple case of a point source suspended in the center of an imaging system. Acquired projection images of the point map the location of the point in the direction parallel to the detector, however, the source could lie at any point along the line perpendicular to the profile. Since the depth of the activity is unknown, a first approximation of the source distribution is obtained by projecting the data from each projection back across an image field (figure 4.1). This simple operation is called backprojection. The resultant crude image of the point source is called a laminogram and

it demonstrates a build-up of intensity around the source creating a “star” effect. The star is caused by the complete projection of the point as a ray (figure 4.1(B)). If an infinite number of views were acquired of this point, the backprojected image would demonstrate a blurring proportional to $1/r$, where r is the distance from the point source. If the system is linear and spatially invariant, it can be shown that the backprojected image is equal to the true image convolved with a $1/r$ blur and to reconstruct the true image, this $1/r$ blurring must be removed. The most common method for removing this blur is by filtering the Fourier transform of the individual projections, and then backprojecting the filtered projections. To present why and how this is accomplished, the central section theorem is introduced².

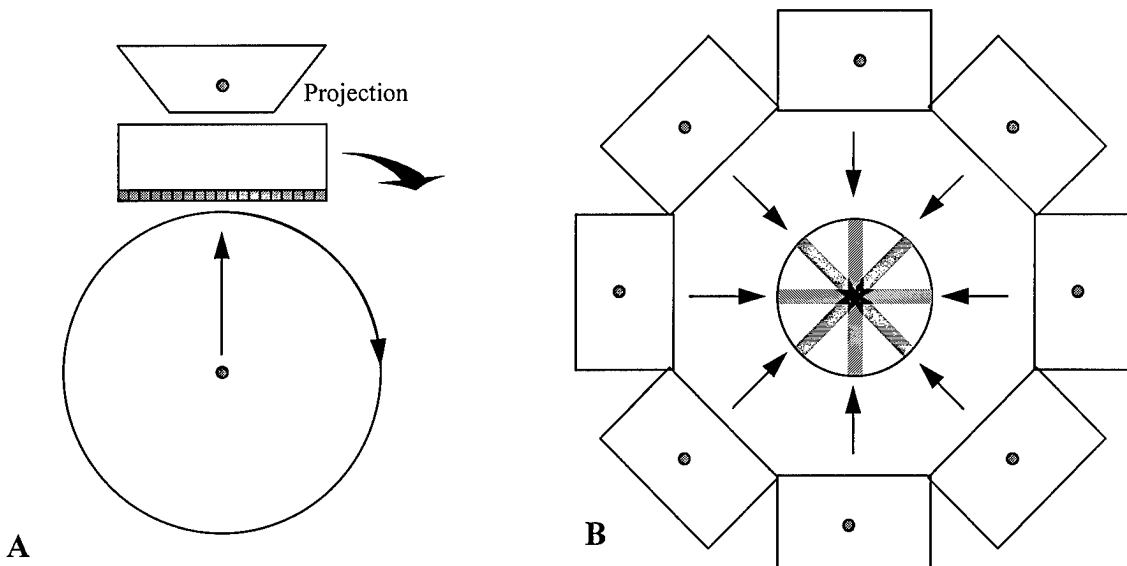


Figure 4.1. (A) Acquisition of Point Source Projection at First Detector Location. (B) Backprojected Distribution Of Source Into All Picture Elements Along Acquired Projection's Representative Angle. Cross section of source distribution is represented by the criss-cross of backprojected ray-sums.

The Central Section Theorem and Parallel-Beam Filtered Backprojection

Given a projection in the x direction of the source distribution $f(x,y)$, the resulting projection will be $g(y)$, such that:

$$g(y) = \int f(x,y)dx \quad (4.1)$$

This projection represents an array of line integrals in the x direction. According to the central section theorem, the Fourier transform of a parallel projection of a two-dimensional function $f(x,y)$ with respect to a radial distance R taken at angle θ gives a slice of a two-dimensional Fourier transform of the same function $F(u,v)$, subtending an angle θ with the u axis in the Fourier domain. This is depicted in figure 4.2. Since the transform of each projection forms a radial line in $F(u,v)$, we can fill $F(u,v)$ by acquiring many projections of the object and taking their transforms. Once filled, $F(u,v)$ can be inverse transformed to reconstruct the original distribution $f(x,y)$. The process can be illuminated further using figure 4.3. A source distribution $f(x,y)$ is observed by a camera, forming an array of line integrals, each being a distance R from the origin, with the camera rotated at angle θ . This forms a projection given by:

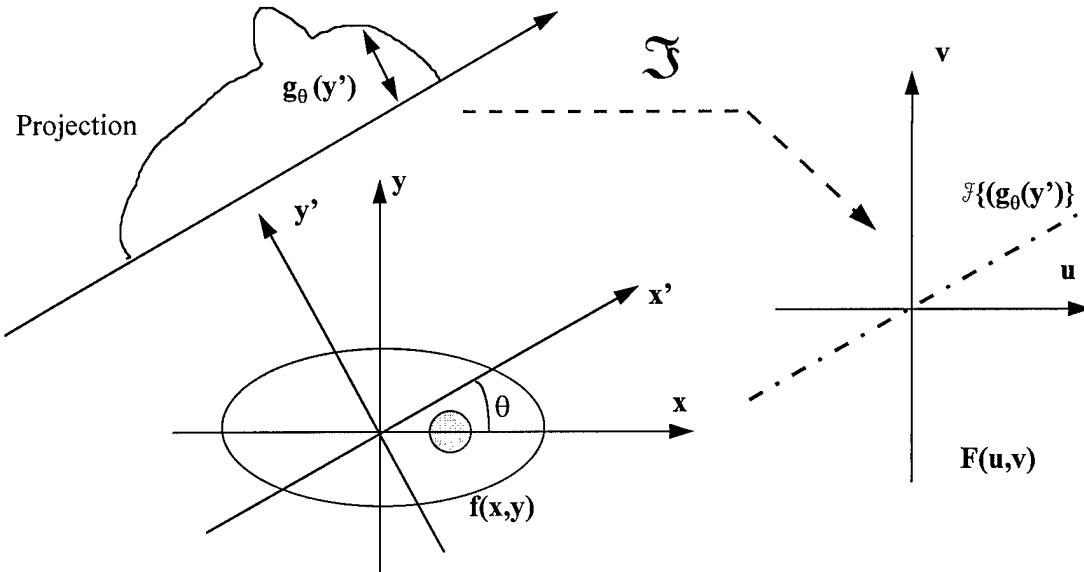


Figure 4.2. Illustration of the Central Section Theorem.

$$\begin{aligned}
 P_\theta(R) &= \iint f(x,y) \delta(x \cos \theta + y \sin \theta - R) dx dy \\
 &= \int_0^{2\pi} \int_0^\infty f(r, \phi) \delta[r \cos(\theta - \phi) - R] r dr d\phi
 \end{aligned} \tag{4.2}$$

where $P_\theta(R)$ is the projection information in the θ direction. The integration takes place along line $x \cos \theta + y \sin \theta = R$ or, in polar coordinates, $r, \phi, r \cos(\theta - \phi) = R$. The delta line in the integrand sifts out the desired line from $f(x,y)$, forming an effective line integral. We recognize $P_\theta(R)$ to be a series of one dimensional projection measurements taken as a function of R at different angle θ .

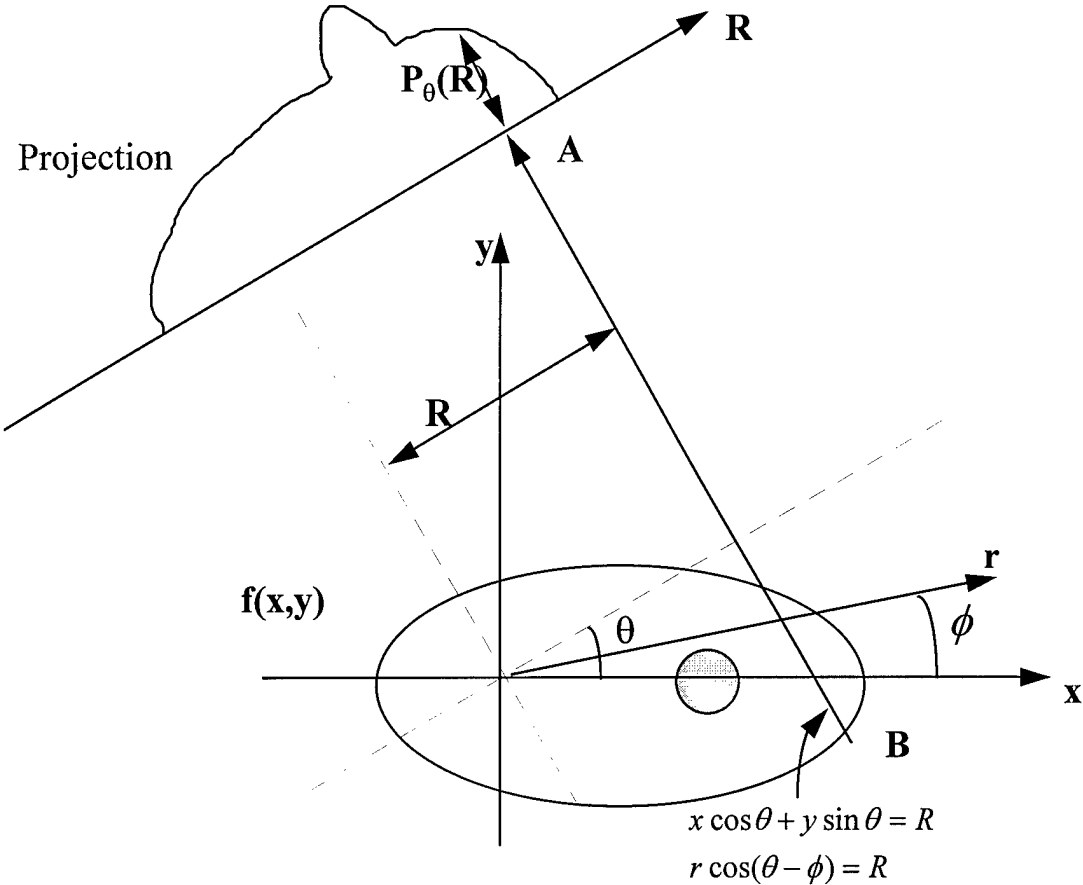


Figure 4.3. Projection of a Two-Dimensional Function

The derivation of the central section theorem is as follows. The two-dimensional Fourier transform of a source distribution is given as:

$$F(u, v) = \iint f(x, y) e^{-i2\pi(ux+vy)} dx dy \tag{4.3}$$

This can be expressed in polar coordinates $F(u, v) = F(\rho, \theta)$, where $u = \rho \cos \beta$ and $v = \rho \sin \beta$:

$$F(\rho, \beta) = \iint f(x, y) e^{-i2\pi\rho(x\cos\beta + y\sin\beta)} dx dy \quad (4.4)$$

Alternatively, if the Fourier transform of the original projection is taken with respect to R at a given angle θ :

$$\begin{aligned} F_\beta(\rho) &= \Im[P_\theta(R)] \\ &= \int_{-\infty}^{\infty} P_\theta(R) e^{-i2\pi\rho R} dR \\ &= \left[\iint f(x, y) \delta(x \cos \beta + y \sin \beta - R) dx dy \right] e^{-i2\pi\rho R} dR \\ &= \iint f(x, y) e^{-i2\pi\rho(x \cos \beta + y \sin \beta)} dx dy \end{aligned} \quad (4.5)$$

It is clear that equations 4.4 and 4.5 are equivalent, and therefore the central limit theorem can be stated as:

$$F(\rho, \beta)_{\beta=\theta} = \Im_1 \{ P_\theta(R) \} \quad (4.6)$$

Thus the Fourier transform of a projection at angle θ forms a line in the two-dimensional Fourier plane at the same angle, such that $\beta=\theta$.

The central section theorem indicates that after filling the entire $F(\rho, \theta)$ space with transforms of the projections at all angles, the reconstructed source distribution is provided by the two-dimensional inverse Fourier transform. In practice, a two-dimensional Fourier transform is computationally demanding and requires various interpolations and coordinate transformations. Further, since the Fourier domain is in polar coordinates, we observe that the information density is more sparse in the periphery of the Fourier image than at the center. This introduces larger interpolation errors in the high frequency aspects of the image, resulting in image degradation. To overcome these difficulties, and to resolve the original problem associated with the $1/r$ blur, filtered backprojection is used. The derivation of this algorithm begins from the previously derived result that the inverse Fourier transform of the Fourier image produces the desired source distribution:

$$\begin{aligned} f(x, y) &= \Im^{-1} [F(u, v)] \\ &= \iint F(u, v) \exp[i2\pi(ux + vy)] du dv \end{aligned} \quad (4.7)$$

Conversion from Cartesian coordinates into polar coordinates of the frequency domain, where $u=\rho \cos \theta$, $v=\rho \sin \theta$, and $dudv = \rho d\rho d\theta$, allows the following derivation:

$$\begin{aligned}
 f(x, y) &= \int_0^{2\pi} \int_0^{\infty} F(\rho, \theta) \exp[i2\pi\rho(x \cos \theta + y \sin \theta)] \rho d\rho d\theta \\
 &= \int_0^{\pi} \int_0^{\infty} F(\rho, \theta) \exp[i2\pi\rho(x \cos \theta + y \sin \theta)] \rho d\rho d\theta + \\
 &\quad \int_0^{\pi} \int_0^{\infty} F(\rho, \theta + \pi) \exp[i2\pi\rho(x \cos(\theta + \pi) + y \sin(\theta + \pi))] \rho d\rho d\theta \\
 &= \int_0^{\pi} \left[\int_{-\infty}^{\infty} F(\rho, \theta) |\rho| \exp[i2\pi\rho(x \cos \theta + y \sin \theta)] d\rho \right] d\theta \\
 f(x, y) &= \int_0^{\pi} \left\{ \int_{-\infty}^{\infty} \left[\int_{-\infty}^{\infty} F(\rho, \theta) |\rho| e^{i2\pi\rho R} d\rho \right] \delta(x \cos \theta + y \sin \theta - R) dR \right\} d\theta
 \end{aligned} \tag{4.8}$$

We observe that this solution composes three operations. The term in the inner bracket represents a filtering operation in the frequency domain which removes the $1/r$ blur. It was earlier presented that the backprojected image equaled the true image convolved with a $1/r$ blur. Based on the convolution theorem, the Fourier transform of the backprojected image equals the Fourier transform of the true image times the Fourier transform of $1/r$. It can be shown that the Fourier transform of $1/r$ is equal to $1/\rho$ in the frequency domain. Thus the Fourier transform of the true image can be obtained by multiplying the Fourier transform of the backprojected image by $|\rho|$:

$$\begin{aligned}
 \text{Backprojection} &= \text{True} * (1/r) \\
 \Im(\text{Backprojection}) &= \Im(\text{True}) \times \Im(1/r) \\
 \Im(\text{True}) &= \Im(\text{Backprojection}) \times |\rho|
 \end{aligned} \tag{4.9}$$

From the central section theorem, this $|\rho|$ filter can also be applied to each Fourier transformed projection to achieve the same filtering effect.

The next operation in (4.8) represents the backprojection operation of each filtered projection onto the x,y space along the line $x \cos\theta + y \sin\theta = R$.

$$\int_{-\infty}^{\infty} g(R) \delta(x \cos\theta + y \sin\theta - R) dR \quad (4.10)$$

The final integrand represents the backprojection operation for all angles θ over the range from 0 to π . Thus the three consecutive operations are filtering, backprojection, and moving to the next projection to repeat the process. These operations are carried out in the polar frequency domain, permitting a simple filtering operation and preservation of high frequency aspects of the image. These three operations can be better seen by rewriting equation 4.8 as:

$$f(x, y) = \int_0^{\pi} \left\{ \int_{-\infty}^{\infty} \left[\int_{-\infty}^{\infty} \mathfrak{J}_1 \{ P_{\theta}(R) \} |\rho| e^{i2\pi\rho R} d\rho \right] \delta(x \cos\theta + y \sin\theta - R) dR \right\} d\theta \\ \int_0^{\pi} \left\{ \int_{-\infty}^{\infty} \mathfrak{J}_1^{-1} [\mathfrak{J}_1 \{ P_{\theta}(R) \} |\rho|] \delta(x \cos\theta + y \sin\theta - R) dR \right\} d\theta \quad (4.11)$$

Here it is clearly observed that the function backprojected at all angles is a filtered version of the projection $P_{\theta}(R)$, where the filter provides $|\rho|$ weighting.

Convolution Backprojection

The back-projection function observed in (4.11) can be written as:

$$\mathfrak{J}_1^{-1} [\mathfrak{J}_1 \{ P_{\theta}(R) \} |\rho|] = P_{\theta}(R) * \mathfrak{J}_1^{-1} \{ |\rho| \} \quad (4.12)$$

again using the convolution theorem of Fourier transforms. This operation indicates that the multiplying by $|\rho|$ in the frequency domain is equivalent to convolving the inverse transform of $|\rho|$ in the space domain. This introduces the convolution back-projection algorithm, where each projection $P_{\theta}(R)$ is convolved with a function $c(R)$ and then immediately backprojected. The function $c(R)$ is chosen to correct the $1/r$ blur and provide any additional filtering which may be required. The convolution-backprojection algorithm thus becomes:

$$f(x, y) = \int_0^{\pi} \left\{ \int_{-\infty}^{\infty} [P_\theta(R) * c(R)] \delta(x \cos \theta + y \sin \theta - R) dR \right\} d\theta \quad (4.13)$$

Converging and Slit-Aperture Filtered Backprojection

The derivation just presented is suitable for cases where the line integrals are perpendicular to the surface of the detector, as when a parallel hole collimator is used with a gamma camera. In contrast, the SPRINT system makes use of a slit aperture which creates a two dimensional pinhole geometry with equally spaced rays and is similar to fan-beam type geometries. Figure 4.4 depicts the difference in detected rays experienced with parallel, fan-beam (converging) and pin-hole (slit) type collimators. In the fan-beam and pin-hole geometries we observe that while the field-of-view is diminished, the projection of the object onto the detector is magnified, assuming the object is sufficiently close to the collimator. This results in both increased sensitivity and resolution for the smaller objects being imaged. There are two specific categories of converging/pinhole systems for which simple filtered back-projection algorithms exist: one where the rays measured at the detector are equally spaced in angle, the other where they are equally spaced in distance on the detector. As an example of each, positron emission tomography systems normally have detectors equally spaced in angle. For conventional gamma cameras equipped with fan-beam collimators and for the case of SPRINT where a slit aperture is combined with a detector that is segmented into equally spaced bars, the rays are equidistant. This is observed in figure 4.5. The following derivation for fan-beam reconstruction follows that of Zeng and Gullberg³ modified for application to SPRINT. Additional information can be found in the work by Berthold and Horn⁴.

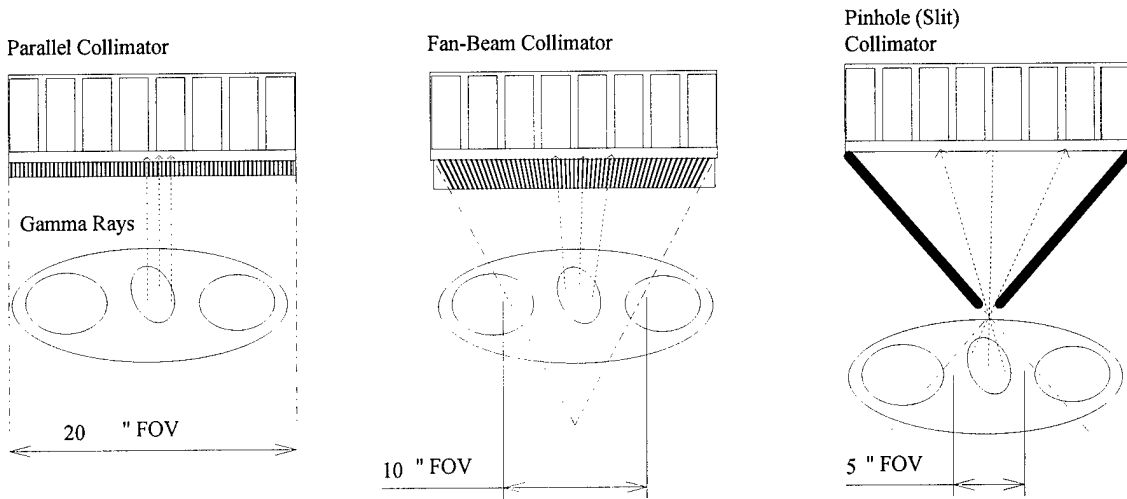


Figure 4.4. Comparison of Field-of-Views and Ray Paths for Three Collimators

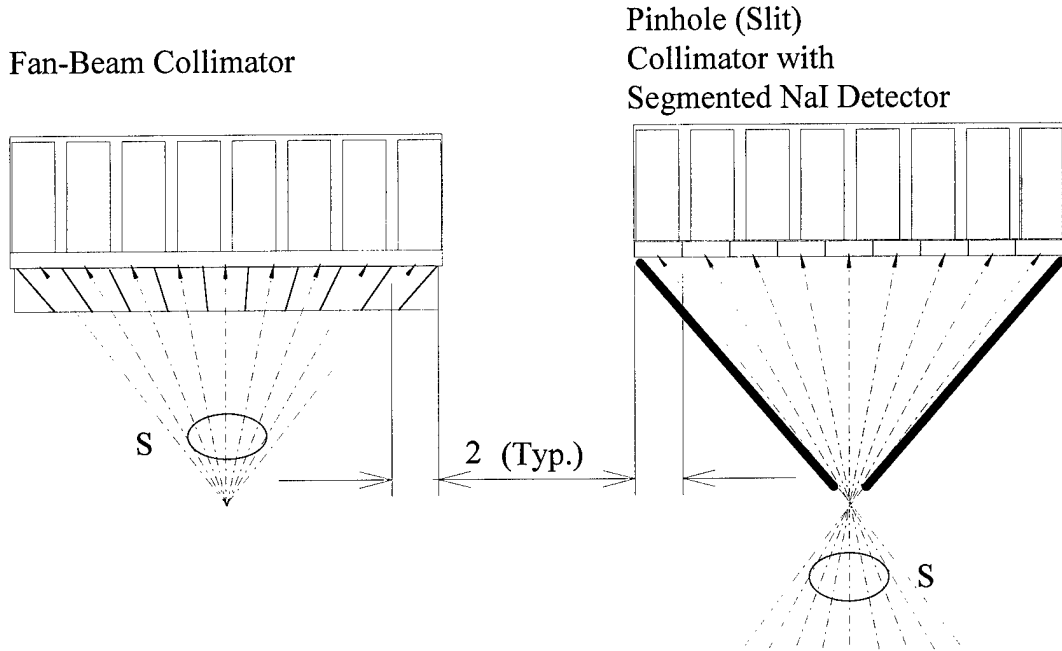


Figure 4.5. Comparison of Fan-Beam and Slit Aperture Showing Equidistant Rays (not to scale).

Consider the fan beam geometry presented in figure 4.6. Let the center of rotation be at distance D from the detector, and the focal length of the collimator is f . The fan beam is measured at equal intervals along the camera face, s , with the camera at angle β

resulting in projection $R_\beta(S)$. The rays of the fan beam are specified at angle α . In figure 4.6 B, we consider the projection being mapped to a parallel coordinate system along D1'-D2' which passes through the center of rotation. We note a projection $P_\gamma(t)$ in this new frame is equivalent to $R_\beta(S)$ in the original frame. From figure 4.6 B, the following relationships are noted and used in the derivation:

$$\begin{aligned}\lambda &= \alpha + \beta = \beta + \arctan\left(\frac{S}{D}\right) \\ t &= D \sin \alpha = S \cos \alpha = \frac{SD}{\sqrt{S^2 + D^2}} \\ dt d\lambda &= \frac{D^3}{\sqrt{(D^2 + S^2)^3}} dS d\beta\end{aligned}\tag{4.14}$$

From the parallel case of convolution-backprojection, let the source distribution be represented by the following:

$$f(x, y) = \int_0^{\pi} \left\{ \int_{-\infty}^{\infty} [R_\beta(S) * c(S)] \delta(x \cos \beta + y \sin \beta - S) dS \right\} d\beta\tag{4.15}$$

Substituting the relationship $P_\gamma(t)$ for $R_\beta(s)$ and expending the convolution:

$$\begin{aligned}f(x, y) &= \int_0^{\pi} \left\{ \int_{-\infty}^{\infty} [P_\gamma(\tau) c(t - \tau)] \delta(x \cos \gamma + y \sin \gamma - t) dt \right\} d\gamma \\ &= \int_0^{\pi} \left\{ \int_{-\infty}^{\infty} P_\gamma(\tau) c(x \cos \gamma + y \sin \gamma - \tau) d\tau \right\} d\gamma\end{aligned}\tag{4.16}$$

The conversion to polar coordinates can be made by substituting $x = r \cos \theta$ and $y = r \sin \theta$

$$f(r, \theta) = \int_0^{\pi} \left\{ \int_{-\infty}^{\infty} P_\gamma(\tau) c(r \cos(\gamma - \theta) - \tau) d\tau \right\} d\gamma\tag{4.17}$$

Consider reconstructing over an angular range from 0 to 2π for this geometry. Similarly, the radial range is limited from $-t_m$ to t_m . This converts 4.17 to:

$$f(r, \theta) = \frac{1}{2} \int_0^{2\pi} \left\{ \int_{-t_m}^{t_m} P_\gamma(\tau) c(r \cos(\theta - \gamma) - \tau) d\tau \right\} d\gamma\tag{4.18}$$

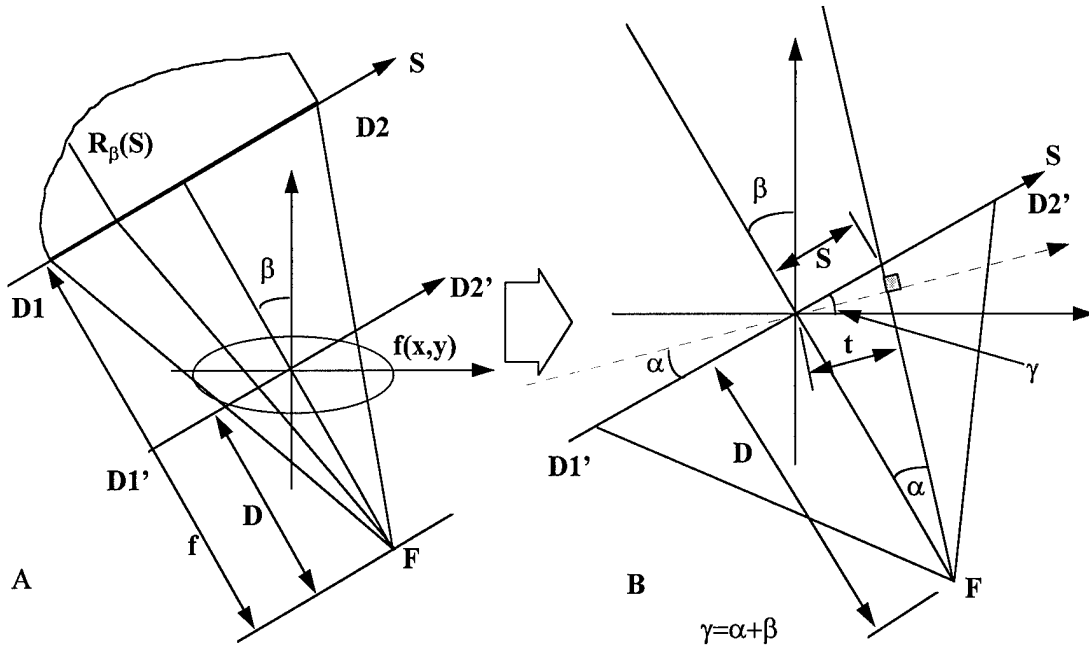


Figure 4.6. (A) Fan Beam Geometry With Imaginary Detector Plane at D1'-D2', (B) Nomenclature for Fan Beam Derivation

Let s_m correspond to t_m , and recognize that there are two periods in the range from 0 to 2π . Further, using the previously defined relationships in 4.14, the projection $R_\beta(S)$ is equal to:

$$R_\beta(S) = P_\gamma(t) = P_{\alpha+\beta} \left(\frac{DS}{\sqrt{D^2 + S^2}} \right) \quad (4.19)$$

Substituting 4.19 and 4.14 into 4.18:

$$f(r, \theta) = \frac{1}{2} \int_{-\arctan \frac{s_m}{D}}^{2\pi - \arctan \frac{s_m}{D}} \left\{ \int_{-s_m}^{s_m} P_{\alpha+\beta} \left(\frac{DS}{D^2 + S^2} \right) c(r \cos(\beta + \arctan \frac{S}{D} - \theta) \right. \\ \left. - \frac{DS}{\sqrt{(D^2 + S^2)}} \right) \frac{D^3}{\sqrt{(D^2 + S^2)^3}} dS \right\} d\beta$$

$$f(r, \theta) = \frac{1}{2} \int_0^{2\pi} \left\{ \int_{-s_m}^{s_m} R_\beta(S) c \left(r \cos(\beta - \theta + \arctan \frac{S}{D}) - \frac{DS}{\sqrt{(D^2 + S^2)}} \right) \right. \\ \left. \frac{D^3}{\sqrt{(D^2 + S^2)^3}} dS \right\} d\beta \quad (4.20)$$

In figure 4.7, consider the variables U and S' defined as:

$$\frac{S'}{FO} = \frac{\overline{EP}}{\overline{FP}} \\ S' = D \frac{r \cos(\beta - \theta)}{D + r \sin(\beta - \theta)} \quad (4.21) \\ U(r, \theta, \beta) = \frac{\overline{FO} + \overline{OP}}{D} = \frac{D + r \sin(\beta - \theta)}{D}$$

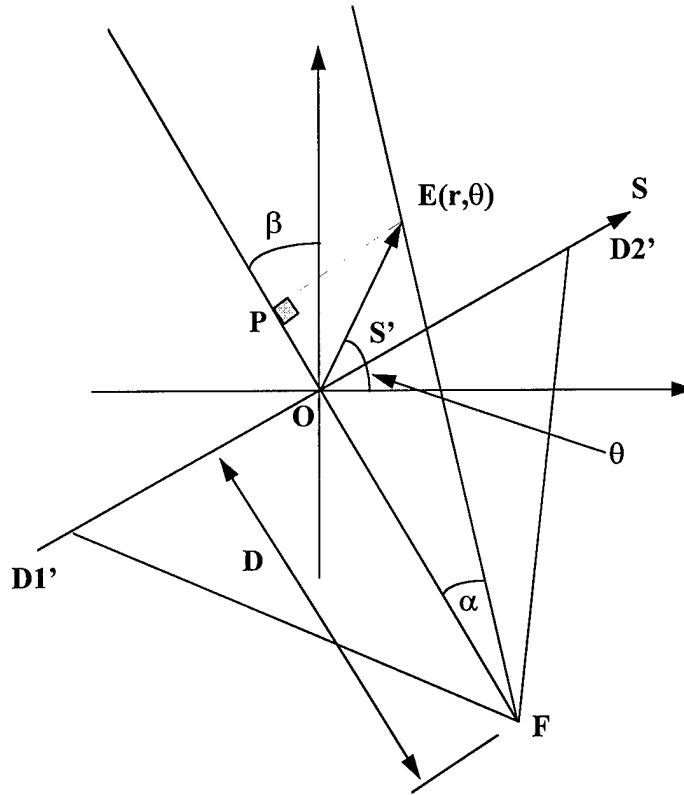


Figure 4.7. Given Pixel (r, θ) , Define a New Variable U and S'

The filter function $c()$ in 4.20 can be reduced to:

$$\begin{aligned}
r \cos(\beta - \theta + \arctan \frac{S}{D}) - \frac{DS}{\sqrt{(D^2 + S^2)}} &= r \cos(\beta - \theta) \frac{D}{\sqrt{D^2 + S^2}} - \\
&\quad (D + r \sin(\beta - \theta)) \frac{S}{\sqrt{D^2 + S^2}} \\
&= \frac{(S' - S)UD}{\sqrt{D^2 + S^2}}
\end{aligned} \tag{4.22}$$

Substituting these variables and the new filter function result back into 4.20:

$$f(r, \theta) = \frac{1}{2} \int_0^{2\pi} \left\{ \int_{-S_m}^{S_m} R_\beta(S) c\left((S - S') \frac{UD}{\sqrt{(D^2 + S^2)}}\right) \frac{D^3}{\sqrt{(D^2 + S^2)^3}} dS \right\} d\beta \tag{4.23}$$

Let:

$$\rho' = \frac{\rho UD}{\sqrt{D^2 + S^2}} \tag{4.24}$$

This reduces the filter function to:

$$\begin{aligned}
c\left((S - S') \frac{UD}{\sqrt{(D^2 + S^2)}}\right) &= \frac{D^2 + S^2}{U^2 D^2} \int_{-\infty}^{\infty} |\rho'| e^{i2\pi(S' - S)\rho'} d\rho' \\
&= \frac{D^2 + S^2}{U^2 D^2} c(S' - S)
\end{aligned} \tag{4.25}$$

The resulting fan-beam convolution-backprojection reconstruction algorithm resolves to:

$$f(r, \theta) = \frac{2\pi}{U^2} \int_0^{\infty} \frac{D}{\sqrt{(D^2 + S^2)}} R_\beta(S) \left[\frac{1}{2} c(S - S') \right] dS \tag{4.26}$$

Equivalently, the filtered backprojection form of the algorithm becomes:

$$f(x, y) = \frac{2\pi}{U^2} \int_0^{\infty} \int_{-\infty}^{\infty} \mathfrak{I}_1^{-1} \left[\mathfrak{I}_1 \left[\frac{D}{\sqrt{(D^2 + S^2)}} R_\beta(S) \right] \frac{1}{2} |\rho| \right] \delta(x \cos \theta + y \sin \theta - S) dS d\beta \tag{4.27}$$

Comparing the parallel beam filtered backprojection algorithm (4.11) with (4.27), we make the following observations. For fan-beam reconstruction, the original projection data is weighted by the factor $\cos \alpha$, equivalent to $D/\sqrt{D^2 + S^2}$. Also, the ramp filter is $1/2$

that used for parallel reconstruction. Finally, the backprojection is performed after weighting each filtered fan beam projection by $1/U^2$ where U is a function of r , β , and θ .

Slit (Pinhole) Reconstruction Factors for SPRINT

The slit aperture of SPRINT introduces a requirement to correct measured projection data for the effects of angular incidence onto the slit as well as the detector⁵. Consider figure 4.8A, which demonstrates the fluence of photons emitted from a point source which then impinge on a slit. As the angle of incidence increases, the effective width of the slit decreases by the factor $\cos \theta$. This causes a reduction in the measured flux which must be corrected by dividing the measured projection data by $\cos \theta$.

A similar effect is observed in figure 4.8B, which shows the obliquity factor introduced as a given flux impinges on the detector. As rays traverse from their source to the detector, there is an increase in the length of the ray path as the angle of incidence increases. In conventional pin-hole collimated systems this introduces an inverse square falloff with distance, and causes a $\cos^2 \theta$ dependence with incidence angle. In contrast, SPRINT maintains a 2-D geometry defined by the joint response of slit aperture and slice collimator. The subsequent decrease in projection intensity is proportional to $1/r$ introducing a $\cos \theta$ dependence. The rays upon arriving at the detector are again incident at a given angle to its surface. As this angle increases, there is an increased loss of intensity as the fluence spreads out to strike the detector surface. This effect introduces an additional $\cos \theta$ dependence. The net effect is a $\cos \psi \cos^2 \theta$ correction required for the measured projection data.

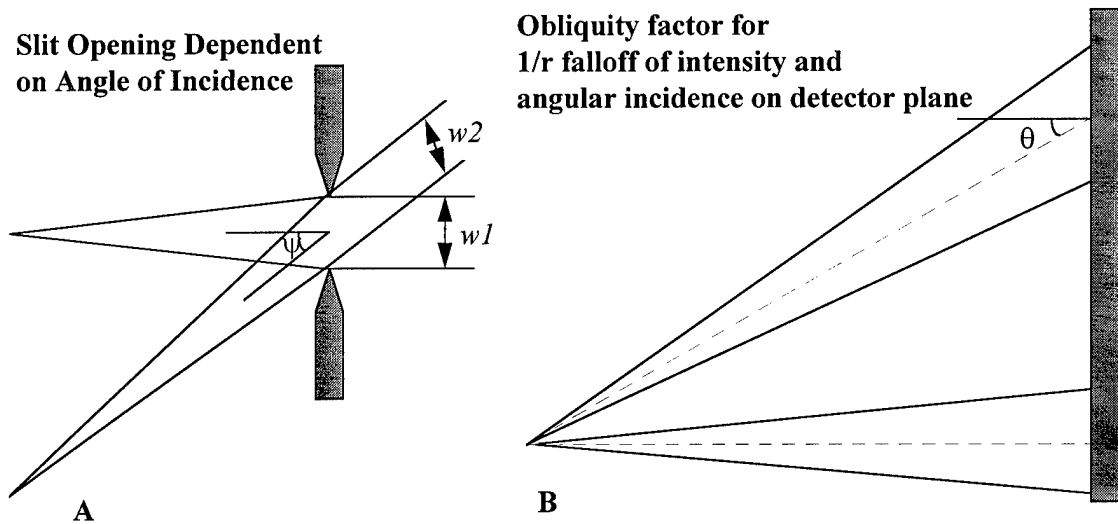


Figure 4.8. Obliquity Factors Effecting Measured Fluence Rates

The Filter in Filtered Backprojection

The ρ filter has a simple ramp shape in the frequency domain as shown in figure 4.9. Because of its shape it is frequently described as a ramp filter. It is not necessary nor desirable to have the filter continue on to very high frequencies since useful information from the image is only as high as the system geometric resolution and angular sampling permits. The cut-off frequency ν , applied to the ramp filter is determined from sampling theorem⁶ which states that to recover spatial frequencies in a signal up to a maximum frequency ν_{max} , the signal must be sampled with a minimum linear distance d :

$$d \leq \frac{1}{2\nu_{max}} \quad (4.28)$$

This means that the highest spatial frequency which can be recovered from the data must be sampled at a minimum of two points per cycle. Coarser sampling does not allow higher frequencies to be recovered accurately and the result is aliasing artifacts in the reconstructed image. Linear sampling in SPRINT is once per 3 mm in the image plane, which equates to 1 mm in the object plane due to system magnification. This limits the resolvable frequency to 0.5/mm, termed the Nyquist frequency of the system. The cut-off

frequency of the ramp filter ν , is chosen to be greater than the Nyquist frequency to insure the image maintains high frequency components. A cutoff frequency of 1/mm is therefore presently used for filtered backprojection reconstructions.

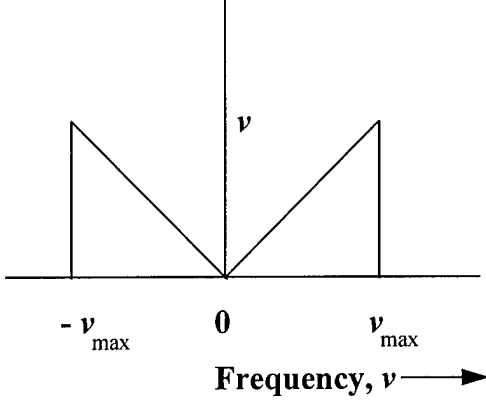


Figure 4.9. Ramp Filter to Correct for $1/r$ Blur in Frequency Domain

Since the ρ filter is a high-pass filter, high frequency noise in the image will be amplified by its application up to the cutoff frequency. To reduce this effect, low-pass filters are typically applied in conjunction with the ramp filter to reduce this high end noise. Typical examples of low pass filters include Hamming, Hanning, Butterworth and Shepp-Logan. Figure 4.10 demonstrates the effect of applying the Hamming and Hanning filters with the ramp filter. Here we observe the effect of the ramp filter is to exactly suppress the $1/r$ blur and very low frequency background components of the image. In contrast, the Hanning/Hamming filters suppress high frequency noise resulting from the statistical variation in counts experience between neighboring pixels. The filters are implemented through simple multiplication of their Fourier transform with the transformed projection data in the frequency domain.

Application of Low-pass Hanning and Hamming Filters with High-Pass
Ramp Filter

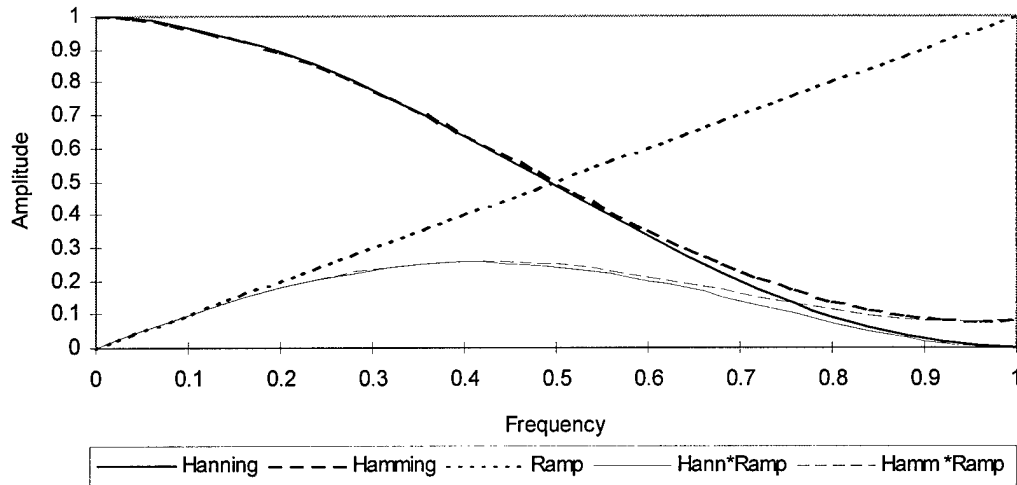


Figure 4.10. Combined High-Pass Ramp Filtering with Low-Pass Hamming or Hanning Filters

STATISTICAL RECONSTRUCTION ALGORITHMS

Filtered backprojection techniques are widely used for image reconstruction because of their relative simplicity to implement as well as the speed in which they can reconstruct a fairly good quality image. Despite these benefits, there are potentially significant advantages to using discrete estimation techniques for image reconstruction that are based on a statistically defined objective function. Iterative algorithms can readily include an accurate model of the imaging system which may include a spatially variant geometry, and the physical effects of scatter and attenuation. Through a geometrically and electronically accurate system model, it becomes possible to “deconvolve” geometric resolution to some degree. By incorporating biasing factors in the model (i.e. background radiation, etc.) the accuracy of the reconstruction can be improved. Further, these methods do not suffer from the uniform sampling requirements imposed by Fourier methods making them more capable of handling missing projection data. Because the reconstruction algorithm addresses the statistics of photon counting, reconstructed images can have more favorable noise characteristics than achieved with FBP. This is particularly important in SPECT, where projection data typically demonstrates high statistical variance from low counts due to the limited radioactivity used and the wide variance in statistical accuracy of different projection elements. The chief shortcoming of these algebraic techniques which impedes their widespread adoption is that they are iterative, causing them to be much slower and computationally more demanding than Fourier methods.

In matrix notation, the issue is to solve the inverse problem:

$$Y = A\lambda \quad (4.29)$$

where Y is the set of measured projection data, and λ is the source distribution to be determined. A is a matrix of weights, computed for a given imaging system geometry, the elements of which describe the mean contribution of each pixel to each ray-sum

measured by a particular detector element. These weights reflect the probability of detecting a photon emitted from a given source voxel by a given detector element. The weights matrix is readily adapted to include such factors as the solid angle of the detector, detector spatial resolution, attenuation and scatter within the object, cosmic background and the collimator response function.

Maximum Likelihood Estimation and the Expectation Maximization (EM) Algorithm

A specific approach to solving this inverse problem is based on the Poisson nature of the projection data, in which likelihood is the objective function to be maximized. The likelihood relationship is written:

$$L(\hat{\lambda}) = \log \text{likelihood}(Y|\lambda) \quad (4.30)$$

The most common class of algorithm used to resolve this problem are termed expectation-maximization (EM) algorithms; using iterative techniques to find the maximum likelihood estimate.

Lange and Carson⁷ present the original derivation of this algorithm. The observed data in an experiment can be represented as a random vector Y . Let Y have the density function (or likelihood) $L_y(Y, \lambda)$, where λ is some vector of parameters to be estimated. In general, it is difficult to maximize $L_y(Y, \lambda)$ with respect to λ . A possible solution to this problem is to conceive of a richer or larger sample space for Y where optimization problems are easier to resolve. Thus, the EM algorithm postulates a “complete data” random vector “ X ” such that Y is a function of $h(X)$. Furthermore, X is assumed to have a density function $L_x(X, \lambda)$ with respect to a measure $\mu(X)$. Using these assumptions, $L_x(Y, \lambda)$ can be recovered by integration:

$$L_y(Y, \lambda) = \int L_x(X, \lambda) d\mu(X) \quad (4.31)$$

All density functions under consideration are discrete. This reduces the above expression to:

$$L_y(Y, \lambda) = \sum L_x(X, \lambda) \quad (4.32)$$

Each iteration of the EM algorithm consists of two steps. In the expectation (E) step, one performs the conditional expectation:

$$E(\ln L_x(X, \lambda) | Y, \lambda^n) \quad (4.33)$$

where λ^n denotes the current vector of parameter estimates. In the maximization (M) step, this conditional expectation is maximized with respect to λ , λ^n being held constant, to give the new estimate of λ^{n+1} . The essence of the EM algorithm can be explained by considering the function:

$$\lambda \rightarrow H(\lambda | \lambda^n) = E(\ln L_x(X, \lambda) | Y, \lambda^n) - \ln L_y(Y, \lambda) \quad (4.34)$$

Regardless of the value of λ^n , $H(\lambda, \lambda^n)$ attains its maximum when $\lambda = \lambda^n$. The EM algorithm exploits this fact by choosing $\lambda = \lambda^{n+1}$ to maximize the relationship in 4.33. It follows that:

$$\ln L_y(Y, \lambda^{n+1}) \geq \ln L_y(Y, \lambda) \quad (4.35)$$

In other words, the EM algorithm is designed to increase the log likelihood at each iteration.

Properties of the Poisson Distribution

A non-negative, integer-valued random variable Z follows a Poisson distribution if:

$$P(Z = k) = e^{-\mu} \frac{\mu^k}{k!} \quad (4.36)$$

for some $\mu > 0$. The Poisson distribution has the following characteristics:

1. Z has the mean $E(Z) = \mu$.
2. If Z_1, Z_2, \dots, Z_m are independent Poisson variables, then $Z = \sum Z_i$ is also a Poisson variable.
3. Suppose that a random number of Z particles is created by a Poisson process with mean μ . Let each particle be independently distributed to one of m categories, the

kth of which occurs with probability p_k . If we let Z_k represent the number of particles which enter category k , Z_k follows a Poisson distribution with mean μp_k . Furthermore, the random variables, Z_1, \dots, Z_m are independent.

The relevance of these characteristics is directly applicable to SPECT imaging, where the number of photons recorded in a given element of the detector module are independent random variables and the number of photons recorded for the various projection measurements are independent and random. Because of this independence property, the likelihood over all projections reduces to the product of the separate projection likelihoods.

The EM Algorithm in Emission Computed Tomography

Consider the SPRINT II system depicted in figure 3.3. The field of view is divided into small pixels in a Cartesian grid. Let λ_j represent the source intensity in pixel j , and c_{ij} be the probability that a photon leaving pixel j reaches the i th projection detector. Assume the emission source is viewed by N detectors, and let N_{ij} denote the number of emissions from the j th pixel that are detected by the i th detector. From the Poisson nature of the source distribution, the mean number of detected photons originating from pixel j during the i th projection is:

$$\Delta t_i \lambda_j c_{ij} = A_{ij} \lambda_j \quad (4.37)$$

and

$$N_{ij} \sim \text{Poisson}\{A_{ij} \lambda_j\}$$

Here Δt_i is the time interval for collecting a projection, and A_{ij} are considered known constants. The intensities λ_j are to be estimated, which we will abbreviate as λ .

Define I_i as the set of pixels which contribute to projection i , and J_j as the set of projections to which pixel j contributes. Now let X_{ij} , $j \in I_i$, be the random number of photons that are emitted by pixel j and contribute to projection i . As mentioned above,

the mean of X_{ij} is $A_{ij}\lambda_j$. Also let Y_i be the total number of photons recorded for projection

i. From these assumptions:

$$Y_i = \sum_{j \in I_i} X_{ij} \sim \text{Poisson} \left\{ \sum_j A_{ij} \lambda_j \right\} \quad (4.38)$$

In view of the characteristics of the Poisson distribution, X_{ij} and Y_i have Poisson distributions. Y_i being the observed data for projection i, X_{ij} constitutes the unobserved but complete data set. This equation represents our system model.

To specify the E-step of the EM algorithm, we need the complete data log likelihood:

$$\ln L_x(X, \lambda) = \sum_i \sum_{j \in I_i} \left\{ -A_{ij} \lambda_j + X_{ij} \ln(A_{ij} \lambda_j) - \ln X_{ij}! \right\} \quad (4.39)$$

Taking the conditional expectation of X_{ij} with respect to Y_i and the *current* vector of parameter estimates λ^n yields:

$$E(\ln L_x(X, \lambda) | Y, \lambda^n) = \sum_i \sum_{j \in I_i} \left\{ -A_{ij} \lambda_j + N_{ij} \ln(A_{ij} \lambda_j) \right\} + R \quad (4.40)$$

where:

$$N_{ij} = E(X_{ij} | Y_i, \lambda^n) = \frac{A_{ij} \lambda_j^n Y_i}{\sum_{k \in I_i} A_{ik} \lambda_k^n}, \quad (4.41)$$

and R does not depend on the new λ .

The M-step is now trivial. Partial differentiation of equation 4.40 with respect to λ_j yields:

$$\frac{\partial}{\partial \lambda_j} E(\ln L_x(X, \lambda) | Y, \lambda^n) = -\sum_{i \in J_j} A_{ij} + \sum_{i \in J_j} N_{ij} \lambda_j^{-1}$$

which is set equal to zero, and solved:

$$\lambda_j^{n+1} = \frac{\sum_{i \in J_j} N_{ij}}{\sum_{i \in J_j} A_{ij}} = \frac{\lambda_j^n}{\sum_{i \in J_j} A_{ij}} \sum_{i \in J_j} \frac{A_{ij} Y_i}{\sum_{k \in I_i} A_{ik} \lambda_k^n} \quad (4.42)$$

for the jth component of the new parameter vector λ^{n+1} . This expression has a fairly simple intuitive explanation. N_{ij} is the best current estimate of the number of detected

photons that originate from pixel j during the i th projection. As above, the sum $\sum_{i \in J_j} N_{ij}$ is

the estimated number that originate from pixel j summed over all projection that pass through pixel j . This estimated number is set equal to the expected number $\sum_{i \in J_j} A_{ij} \lambda_j^0$ and

the resulting equation solved for λ_j .

Equation 4.42 has the following additional benefits. First, the non-negativity constraint, $\lambda_j^n \geq 0$ is automatically satisfied, assuming λ_j^0 is positive. Second, each iteration verifies that:

$$\sum_i \sum_{j \in I_i} A_{ij} \lambda_j^n = \sum_i Y_i$$

This indicates that the current expected number of photons stays fixed at the total observed number, thus preserving counts.

The Space-Alternating Generalized EM Algorithm for Penalized Maximum-Likelihood Image Reconstruction

EM algorithms have two important drawbacks which prevent their widespread use for routine image reconstruction. The first problem is that EM algorithms converge very slowly, particularly when random background events such as scatter, dark current, and background radiation are included in the algorithm. Second, because of the blurring effect of photon detection and position estimation the reconstruction process is ill-conditioned. Consequently, images that are reconstructed purely by using the maximum likelihood criterion are unacceptably noisy. To overcome this, a smoothness penalty or regularization parameter must be introduced into the objective function. Unfortunately, the M-step in the EM algorithm becomes intractable when one includes smoothness penalties, making its application difficult.

To overcome these issues, Fessler and Hero⁸ developed the space-alternating generalized EM (SAGE) algorithm which attempts to exploit the structure of the log-likelihood to hasten convergence and allow regularization. By comparison, the EM

algorithm simultaneously updates all pixels in the image at each iteration, whereas the SAGE algorithm implements a sequential pixel update. This method eliminates coupling between pixels at this step and enables use of local smoothness penalties. Further, the slow convergence of EM algorithms is tied to the massive size of their complete-data spaces⁹. The sequential update methodology of SAGE allows the use of small “hidden-data” spaces for image reconstruction, which leads to fast convergence. The actual details of the SAGE algorithm are complex, and beyond the scope of this work. The following briefly summarizes the salient features of SAGE as compared to the EM algorithm.

We begin with a more descriptive system model than presented in equation 4.38 for the EM case. Specifically:

$$Y_i = \sum_{j \in I_i} X_{ij} \sim \text{Poisson} \left\{ \sum_j A_{ij} \lambda_j + r_i \right\} \quad (4.43)$$

where r_i represents the cumulative random background rates stemming from dark current, background radiation, scatter, and aperture/collimator penetration. The conditional expectation of the log-likelihood is of the form:

$$E \left(\ln L_x(X^h, \lambda) | Y, \lambda^n \right) - \beta P(\lambda) = -A_{ij}(\lambda_j + z_j) + N_{ij} \ln(A_{ij}(\lambda_j + z_j)) - \beta P(\lambda) \\ z_j = \min_{i: A_{ij} \neq 0} \left\{ \frac{r_i}{A_{ij}} \right\} \quad (4.44)$$

where a penalty term is subtracted from the expectation, and z_j is introduced to incorporate the random background. When comparing to equation 4.40, the expectation step is conducted over a “hidden” but complete data space X^h which includes all ray-sums that pass through the pixel to intersect detector element i . This isolates (or decouples) the pixel being evaluated from the remainder of the estimated image permitting faster convergence and inclusion of a smoothness term. The expectation result is reduced by a quadratic smoothness penalty, $\beta P(\lambda)$, that weights the pixel currently being evaluated by the difference in values between it and the eight pixels which neighbor it. The larger this

difference is, the larger the penalty. The factor β can be varied to achieve different levels of smoothing in the reconstructed image. A factor z_i is added to the pixel estimate, λ_j , which provides inclusion of the random background. In contrast to conventional EM, there is no summation over j and i , as this expression is maximized and evaluated sequentially for each pixel. The M-step is performed by taking the partial derivative of the expectation with respect to λ_j , resulting in a quadratic expression from which λ_j^{n+1} is calculated. The projection estimate, N_{ij} , is then updated before proceeding to the next pixel, at which point the iteration loop is repeated. A more detailed presentation of the SAGE algorithm derivation can be found in the reference by Fessler.¹⁰

Generation of the SPRINT System Weights, A

The accuracy of the reconstructed image from any iterative algorithm, SAGE included, is directly dependent on the accuracy of the model used to determine the system weights matrix. Specifically, the geometry of the system must be well defined, and the detection efficiency, or relative detection efficiency of each detector element must be known. The system geometry of SPRINT is complex due to the combined geometry defined by the slit aperture and slice collimator, the obliquity factors of the aperture and detector, and the effect of rays which intersect partial voxels or partial detector elements. We will briefly examine each of these issues, and discuss their handling before concluding.

To simplify the determination of system weights, SPRINT is considered a two-dimensional geometry, with weights generated for a single image slice and then assumed applicable for all slices. This is a good approximation since the slice collimation defines a consistent geometry axially. The size of the weights matrix is determined by the number of projections, the number of detector elements, and the number of image pixels. The SPRINT gantry contains 488 three mm wide NaI(Tl) bars in its 11 modules, of which

459 are useable for high energy imaging¹. A single projection measurement consists of the recorded counts from approximately one-sixth of these bars, with six projections being acquired at each position of the slit aperture. The total number of projections required is derived from the sampling requirements necessary to obtain the desired image resolution. Bracewell¹¹ has shown that the number of angular samples per 360° required to give uniform resolution and freedom from angular aliasing is approximately:

$$N = \frac{2\pi D}{r_s} \quad (4.45)$$

where D is the diameter of the aperture ring equal to 13 cm, and r_s is the desired system resolution. If r_s is taken as 4 mm, which is somewhat less than the system resolution calculated in Chapter III, then approximately 200 projections would be required, necessitating 34 steps of the aperture (200/6). For simplicity, a forty-step acquisition protocol is thus used, which generates 240 projections. Since there are 459 measured elements in every set of six projections, there are 18,360 rows in the weights matrix which describe the probability that a photon emitted from a given voxel is recorded by a given element.

The nine centimeter wide field of view of SPRINT is segmented into a 100x100 pixel field, each pixel then being 0.88 mm on a side. The voxel depth (slice thickness) was chosen to be 3 mm, equal to the pixel size in the projection data. Each column of the weights matrix is associated with a given pixel, so the final weights matrix is large, 18,360 rows by 10,000 columns. The geometric detection probability expressed by each weight is to the solid angle subtended by a given detector pixel as seen by each image pixel. The probability is approximately equal to:

$$P = \frac{lh}{4\pi d^2} \quad (4.46)$$

¹ This will be elaborated upon in Chapter VII.

where l is the effective width and h the effective height of the detector pixel observed, taken as 3 mm (refer to figure 3.3). The distance d is that from the image pixel to the detector pixel. Weights are determined sequentially for a given detector element and all image pixels which can be “seen” by that element. Detector pixel centroids were determined from the detector response measured by rotating a highly collimated slit source around the detector ring. Primary image pixels include those intersected by a ray passing through the center of the detector pixel and the center of the slit. Secondary image pixels lie off-axis of the central ray and contribute (at least partially) to a given detector element response. Dependent on the image pixel location, the effective detector width, l , seen by the pixel will be greater than, equal to or less than the actual element width. The detector response is weighted accordingly to reflect the effective pixel width seen by an image pixel (figure 4.11).

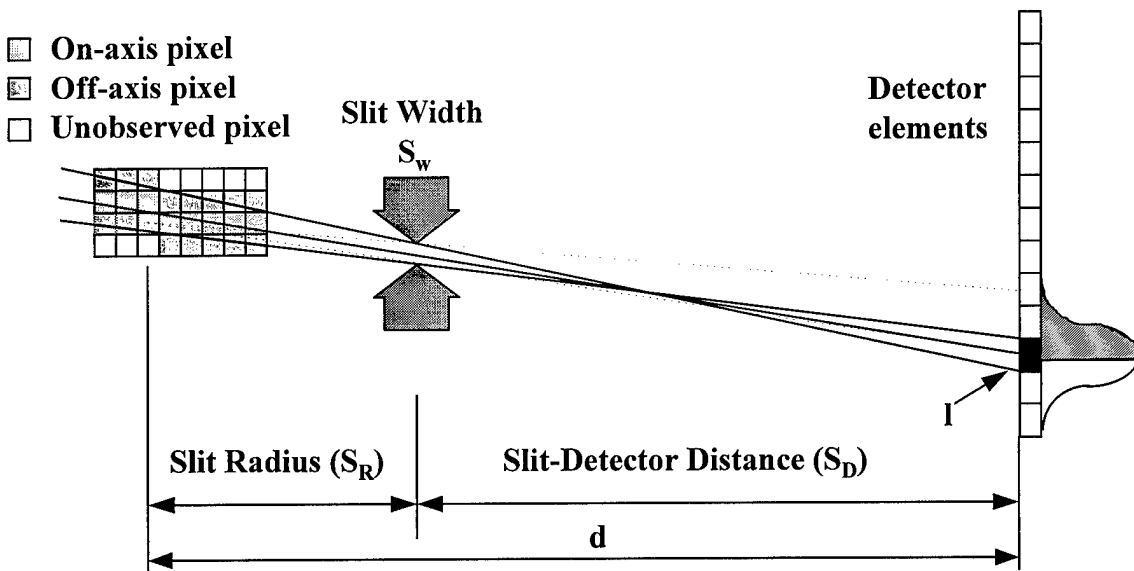


Figure 4.11. Weight Generation for Image Voxels Observed by a Detector Element (Solid Lines). Effective detector width, l , determined from part of detector element observed by image pixel (dotted line).

Weights are stored in the ASPIRE format to take advantage of the sparse data structure, and ASPIRE routines were used to perform vector operations^{5 12}.

References to Chapter IV

¹ Radon J. Über die Bestimmung von Funktionen durch ihre integralwerte langs gewisser Mannigfaltigkein, Ber. Saechs. Akad. Wiss. Leipzig. *Math-Phys.* 1917;KI.69:262.

² Macovski A. Medical Imaging Systems , Tomography, Chapter 7, pp 117-131, Prentice Hall, Neglewood Cliffs, New Jersey, 1983.

³ Zeng GL, Gullberg GT. A cone-beam tomography algorithm for orthogonal circle and line orbity. *Phys Med Biol.* 1992;37(3):563-577.

⁴ Berthold KP, Horn. Fan-beam reconstruction methods. Proceedings of the IEEE, 1979;67(12).

⁵ Zhang Y, Improved SPECT radioactivity quantification using MRI side information. PhD Dissertation, Dept of Bioengineering, University of Michigan, 1996.

⁶ Oppenheim AV, Wilsky AS: Signal and Systems. Prentice Hall, Inc, Englewood Cliffs, New Jersey, Chapter 8, 1983.

⁷ Lange K, Carson R. EM reconstruction algorithms for emission and transmission tomography. *J Comp Assis Tomo.* 1984;8(2):306-316.

⁸ Fessler JA, Hero AO. Space-alternating generalized EM algorithms for penalized maximum-liklihood image reconstruction. Technical Report 286, Communications and Signal Processing Library. Dept of Elec Eng and Comp Sci. Univ of Mich. Feb 1994.

⁹ Dempster AP, Laird NM, Rubin DB. Maximum-likelihood from incomplete data via the EM algorithm. *Journal of the Royal Statistical Society Series B*, 1977;39(1):1-38.

¹⁰ Fessler JA, Hero AO. Space-alternating generalized expectation-maximization algorithm. *IEEE Transactions on Signal Processing* 1994;42(10):2664-2677.

¹¹ Bracewell RN, Riddle AC. Inversion of fan-beam scans in radioastronomy, *Astrophys J*, 1967;150:427.

¹² Fessler JA. ASPIRE 3.0 User's Guide: Sparse iterative reconstruction library. Technical Report #293. Communications and Signal Processing Library. Dept of Elec Eng and Comp Sci. Univ of Mich. 1995.

CHAPTER V

DESIGN, CONSTRUCTION AND PERFORMANCE OF ONE-DIMENSIONAL LEAD FOIL PARALLEL PLATE AND FAN-BEAM COLLIMATORS FOR SPRINT

SPRINT imaging requires construction of precision slice collimators which are specific to the gamma-ray energy being imaged and the desired object (organ) size to be examined. The first requirement then for SPRINT imaging of 511 keV photons is establishing a system axial resolution which is significantly less than rat organ sizes of interest. This chapter describes the design criteria and methods developed for constructing parallel and converging ring collimation for SPRINT and ASP^{1,2}. The measured performance of the constructed collimators is also presented.

Design criteria and Early Construction Methods

As described previously, collimation of SPRINT detector modules is provided by a rotating multi-slit ring aperture which collimates radiation azimuthally combined with a stationary slice collimator which provides axial collimation. Slice collimators are composed of alternating annuli lead foil and air equivalent foam, and can have either parallel or converging designs. SPRINT was designed for human brain, primate brain and small canine brain imaging of ^{99m}Tc labeled compounds at 8 mm resolution and tumor imaging of ¹³¹I labeled compounds in small animals at 3.5 mm resolution. This work considers biodistribution assessment of positron labeled radiotracers in the rats, requiring a 5 mm resolution. Each application requires a unique collimator to achieve the specified resolution. To image 140 keV ^{99m}Tc gamma rays and 511 keV annihilation

radiation, two parallel plate collimators were constructed, respectively. A converging collimator with 2:1 magnification was constructed to achieve the very small resolution desired for imaging ^{131}I . Designs were developed for $^{99\text{m}}\text{Tc}$ and ^{131}I collimators using ray-tracing techniques. Monte Carlo simulations were used to design the 511 keV collimator and confirm the design for the ^{131}I converging collimator³.

Figure 5.1 shows the comparative performance of several collimator designs simulated for 511 keV imaging. The designs are specified by the thickness of lead and air equivalent spacer in thousandths of an inch. The three sets of bars show the relative sensitivity between designs obtained by summing over the response function FWHM and FWTM, as well as the peak amplitude of the response. A tradeoff is observed up to the 60x80 or 30x60 designs when either increasing lead foil thickness or decreasing the spacer thickness leads to an increase in resolution but decrease in sensitivity. Other considerations in design selection included spatial variance of the response function and the availability of spacer material in desired widths.

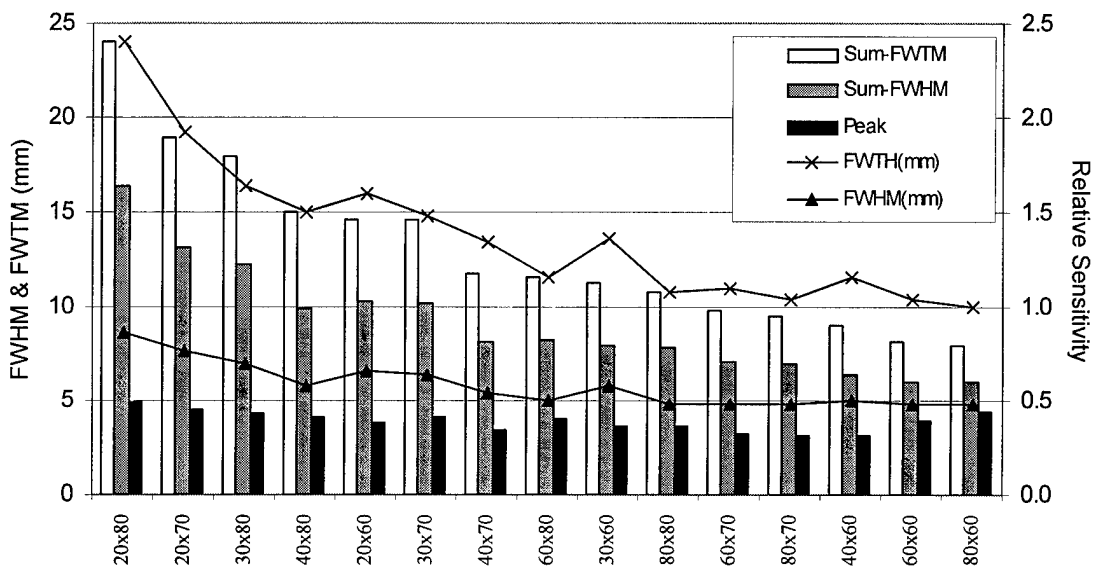


Figure 5.1. Design comparison of collimator performance from Monte Carlo simulations. Each design simulated in the x-axis shows the lead foil thickness (mils) by the air gap thickness (mils).

The final designs chosen were a compromise between resolution, sensitivity and spatial variance. The low energy collimator used 0.23 mm lead foil and 2.0 mm spacers with a septal length of 6.8 cm. The medium energy converging collimator required tapered slices, with 0.50 mm lead foil and 0.9 mm spacers at the collimator face with an 11.6 cm length. Finally, the high energy collimator used 0.76 mm lead foil and 1.5 mm spacers, again with a length of 11.6 cm. Schematic cross-sections of the low-energy collimator and ^{131}I converging collimators are shown in figure 5.2. The high energy collimator is similar in design to the low energy collimator, but with exterior dimensions and septal length equal to the converging collimator. The figure emphasizes the major difference in construction patterns and lead foil spacing for the two collimator types. The 47.4 cm focal length of the converging collimator restricts the field of view to half that of the parallel plate collimators, but provides a 2-to-1 axial magnification factor.

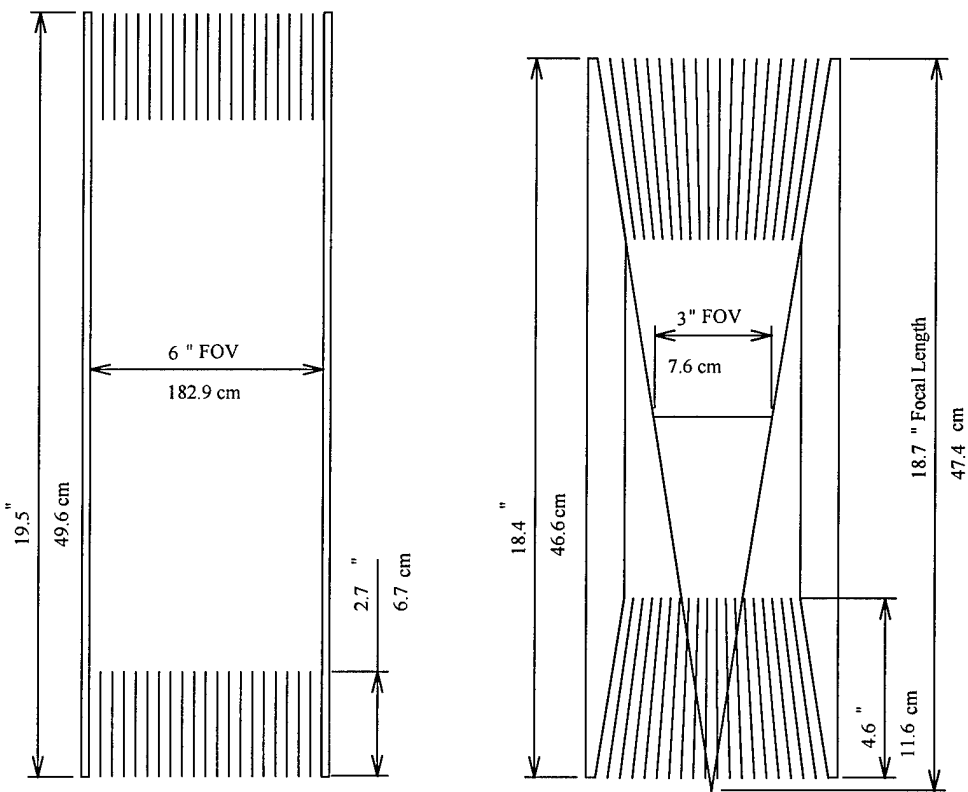


Figure 5.2. Cross-Sectional Views of Low Energy Parallel and ^{131}I Converging Collimators. Parallel designs provide a 15 cm axial field of view (FOV).

Construction of these collimators proved to be very challenging. Tolerances could not exceed 50 microns between individual slices to obtain adequate azimuthal and axial uniformity. Early efforts at construction used Styrofoam sheet bonded to pure lead foil using epoxy compounds. Styrofoam is not readily machinable nor can Styrofoam sheet be accurately molded, so that is was virtually impossible to produce accurate spacers of the desired thickness. Although expanded Styrofoam beads can be molded with high precision, the process is difficult and was not attempted. Attempts were made to mold expanding urethane foam to the desired width and taper. Severe difficulties were encountered in releasing the material from the mold and maintaining dimensional tolerance and uniform density.

Other complications were encountered using pure lead and liquid adhesives. Pure lead foil is highly malleable and too easily wrinkled or dented during the fabrication process. The bond strength of epoxy resins for both Styrofoam and lead foil was very poor, and it was impossible to maintain high tolerances on epoxy thickness.

These problems were overcome through the careful selection of materials and design of a precisely controlled construction process. The method could repeatedly produce either flat and tapered collimator slices with a 50 micron tolerance over a wide range of foam and lead thicknesses.

Collimator Materials

The foam product chosen was a rigid polymethacrylimide foam, trade name Rohacell, which had a number of highly desirable mechanical characteristics including high dimensional stability and strength, and excellent bonding and radiation transmission characteristics⁴. The foam can be ordered in sheets over a wide range of thickness' appropriate for collimator construction, and is readily cut and machined to tolerances of 50 microns. Thicknesses of foam sheets obtained from the supplier had a tolerance of 0.1

mm. The foam density was 0.052 g/cm^3 with linear attenuation coefficients of 0.0076 cm^{-1} , 0.0055 cm^{-1} , and 0.0048 cm^{-1} for 140 keV , 364 keV and 511 keV gamma rays, respectively. This results in an approximate 5% scatter and attenuation probability for all three collimators.

The high malleability of pure foil was reduced by purchasing a lead alloy with 2% antimony and 0.5% tin by weight. This foil was stiff enough that sheets could be handled and cut to size without any significant deformation of the surface or edges. The lead remained sufficiently malleable that any surface contours were readily flattened during the bonding process. Foil could be ordered at the desired width and precise thickness (<25 micron tolerance) required for a given collimator design.

DOW DAF 899 thin film adhesive was used to bond the lead foil and foam⁵. This dry, tack-free adhesive is a hot-melt film which formed a strong bond to both lead and foam at a melting temperature of 100° C . The product has a nominal thickness of 0.1 mm with a tolerance of ± 0.025 mm. After bonding, joint thickness was approximately 0.05 mm.

Collimator Construction Methods

Parallel Collimators

Foam sheets were vacuumed to provide a clean surface for bonding. The sheets were precut using a square template slightly larger than the diameter of the finished collimator. Thin film adhesive squares were precut 2 mm smaller than the foam to prevent the adhesive from bonding to a heated press.

Lead foil was dispensed from a roller assembly onto a smooth PVC cutting surface with extreme care taken to avoid deforming the lead. The lead foil was cut to the size of the foam sheets using a hand-held rotary fabric cutter with tungsten blades (figure

5.3). The precut thin film adhesive and polymethacrylimide foam were carefully stacked and aligned on top of the lead and the stack was sandwiched between a pair of thin aluminum sheets for transportation and uniform compression. The assembly was moved directly to a heated press which was preheated to 100° C and compressed for thirty to forty five seconds depending on the thickness of lead used. The press with an assembly ready for compression is shown in figure 5.4.

The bonded assembly was moved to a milling machine mounted vacuum chuck shown in figure 5.5 for final cutting. Accurate cutting of the inner and outer diameters of each slice was a critical step in this construction process. The method required circular patterns to be cut in each slice with 100 micron tolerance, without damaging or feathering the foil edges for a range of foil thickness from 0.23 to 0.76 mm. The vacuum chuck featured a surface that was flat to within 50 microns, and had a series of surface perforations through which a vacuum could be drawn. PVC rings were embedded in the surface at the specified inner and outer diameters of the collimator to provide a cutting surface.

The lead-foam slice was placed on the vacuum chuck, lead-side down, and a vacuum applied to hold the piece firmly in place. Slice radii were cut using tungsten blades from a rotary fabric cutter. The cutter assembly was mounted in the milling machine spindle as shown in figure 5.6. The cutter was lowered onto the PVC cutting surface using the spindle height adjustment, locked into place, and rotated by hand to make the cut.

Finished slices were stacked on a surface table with two right angle fixtures used to assure precise slice alignment. Between each pair of slices a piece of thin film adhesive was added which was precut to the slice dimensions. The stack in progress for the low energy collimator is shown in figure 5.7. When the desired stack height was reached, aluminum endplates and compression plates were added and the entire assembly compressed using large C-clamps (Figure 5.8). The required width of the finished

collimator was 15 cm. Each adhesive layer thickness decreased 50 microns during bonding, and this needed to be accounted for in order to obtain the proper finished dimensions. The resulting Tc-99m collimator had 59 slices, while the 511 keV collimator had 63 slices. Final bonding of the assembly was accomplished by placing the collimator in a large glass drying oven at a temperature of 100°C for several hours to allow uniform heating. To protect the exposed lead edges during handling, several thin coats of epoxy resin were applied to the exterior of the collimator. It was important that the epoxy used did not contain solvents that would attack the foam.

Fan-Beam Collimators

The design of a converging geometry slice collimator introduced additional complexity into the construction process because of the requirement to mill a radial taper in the foam surface of each slice. Each annulus required a 0.2331° taper to obtain 2 to 1 axial object magnification from the finished collimator. Each slice was also a conical form in the stack. Consequently, each symmetric pair of slices had a unique inner and outer diameter, and required a precise azimuthal wedge to be removed from the annulus so that the slices would stack tightly together without stretching the lead-foam ring.

Bonded lead-foam slices were placed lead side down on a radially tapered vacuum chuck which was mounted on a rotary table on the milling machine. The angle of taper, 0.2331°, was gradual enough so that bonded slices were held in place firmly by an applied vacuum. On one side of the rotary mill table, a tooling fixture was mounted to the milling table which would cut the inner and outer diameter of the slice, again using rotary cutters. Adjustments were available on this fixture for the angle of cut, the depth of cut, as well as the radius of the cuts. On the opposing side of the rotary table a fixture was mounted which allowed a slotted plate to be pivoted onto the slice surface. The slot provides a template to produce radial cuts in the slice so that a precise angle wedge could

be cut from the annulus. A fly-cutter was used to taper the foam and a hood assembly was used to collect the foam dust generated.

The taper was defined by the radial taper of the vacuum chuck so that the fly cutter need not be tilted. The slice was rotated azimuthally under the fly-cutter a full 360° degrees using the rotary mill table, with a fast spindle speed and slow rotation of the table critical to obtaining a smooth uniform surface in the tapered foam. The fly cutting operation is shown in figure 5.9. The side-mounted rotary cutters were next used to cut the slice radii (figure 5.10). Finally, the wedge cut was made using a hand-held rotary cutter and the slit fixture discussed above (figure 5.11).

The final dimensions of our fan-beam collimator required 78 total slices. Slices were constructed in symmetric pairs, each with unique radii and removed wedge angle, and stacked separately on two endplates machined with a 9.125° angle to match the top and bottom slice angles. The cut seam was sealed with a narrow strip of thin aluminum tape and then tack soldered to prevent the seam from splitting during compression and heating. Between each prepared slice a layer of thin film adhesive was placed which was also pattern cut to the same conical shape as the slice. For the center twenty slices of the collimator, the required radius change was less than a millimeter and the required wedge angle was less than 0.3° so that no wedge cut was required and the radii were held constant. When all slices were constructed, one stack of slices was inverted onto the other stack with right angle fixtures used to assure flush alignment of the slice stack. Finally, the top endplate and compression plates were added, and the entire stack compressed and bonded as described for the parallel collimators. The three completed collimators are shown in figure 5.12, with the fan-beam collimator shown inserted into the SPRINT-II gantry.

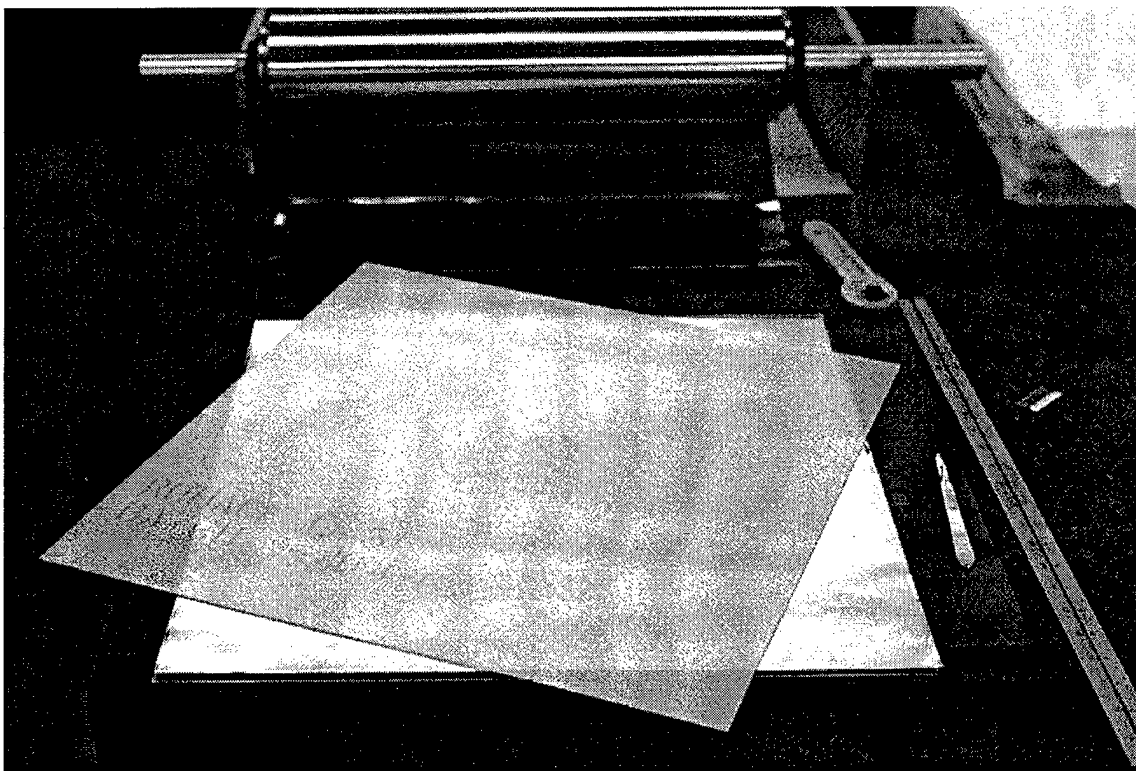


Figure 5.3. Stock Materials for Collimator Construction

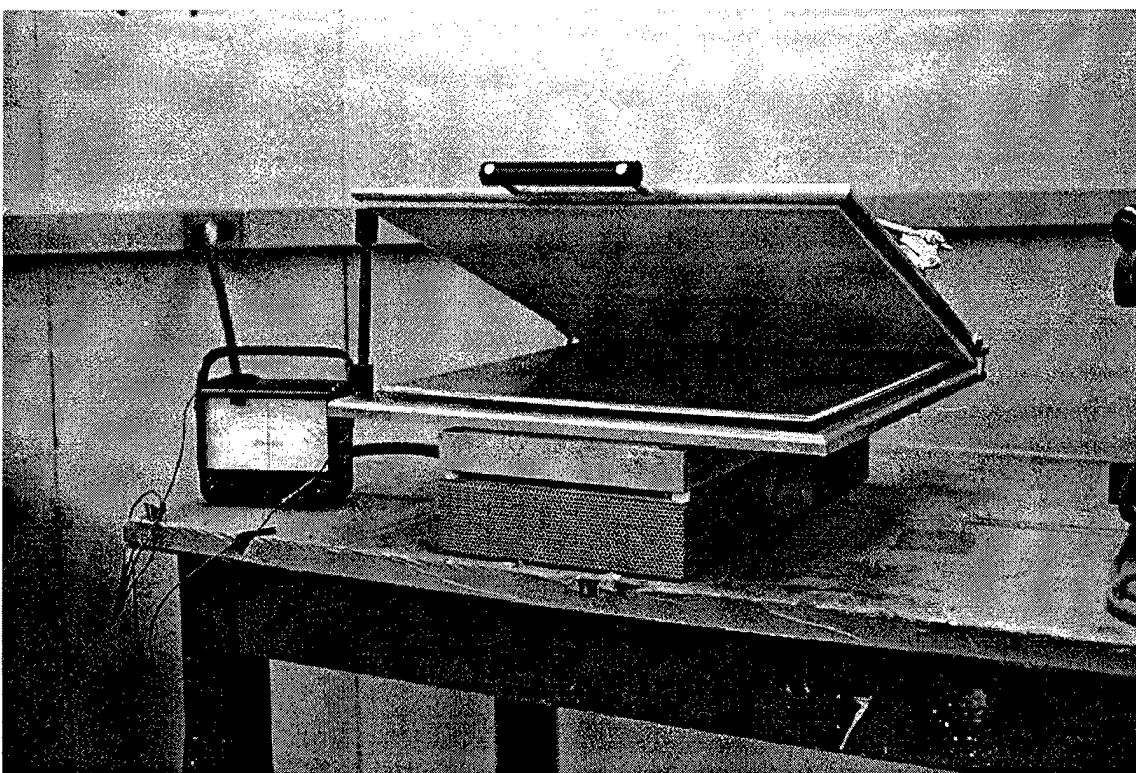


Figure 5.4. Heated Press for Slice Bonding

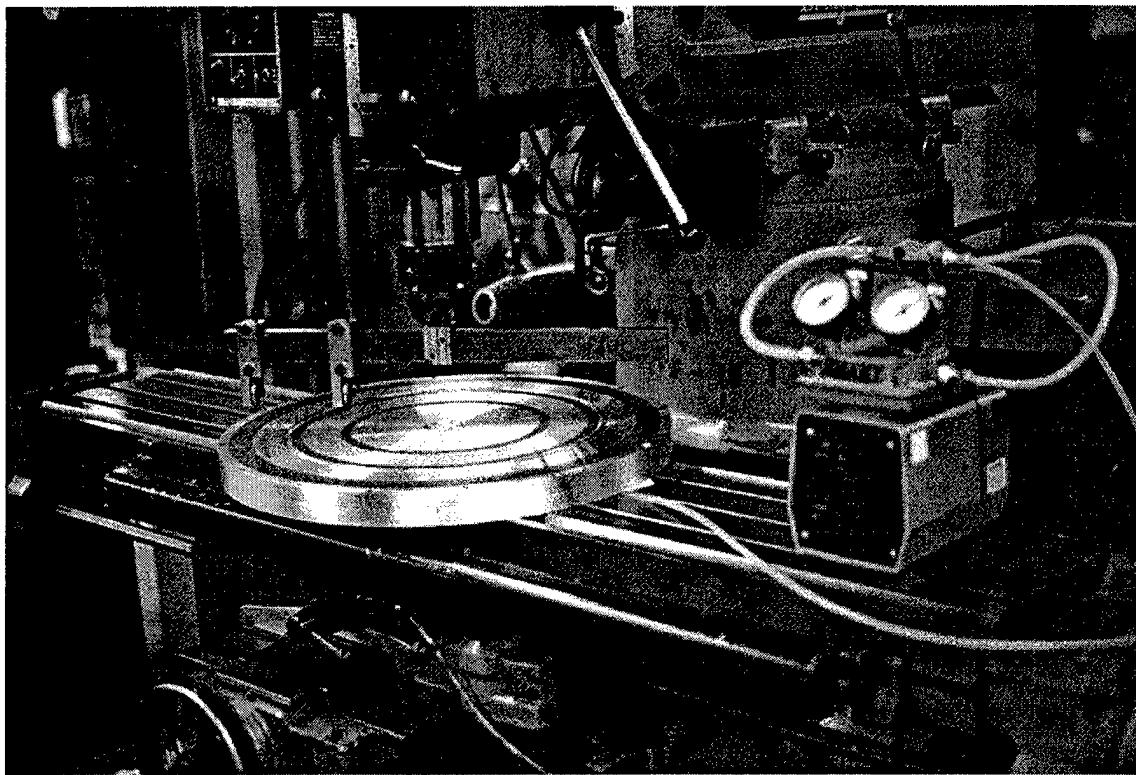


Figure 5.5. Vacuum Chuck for Slice Milling

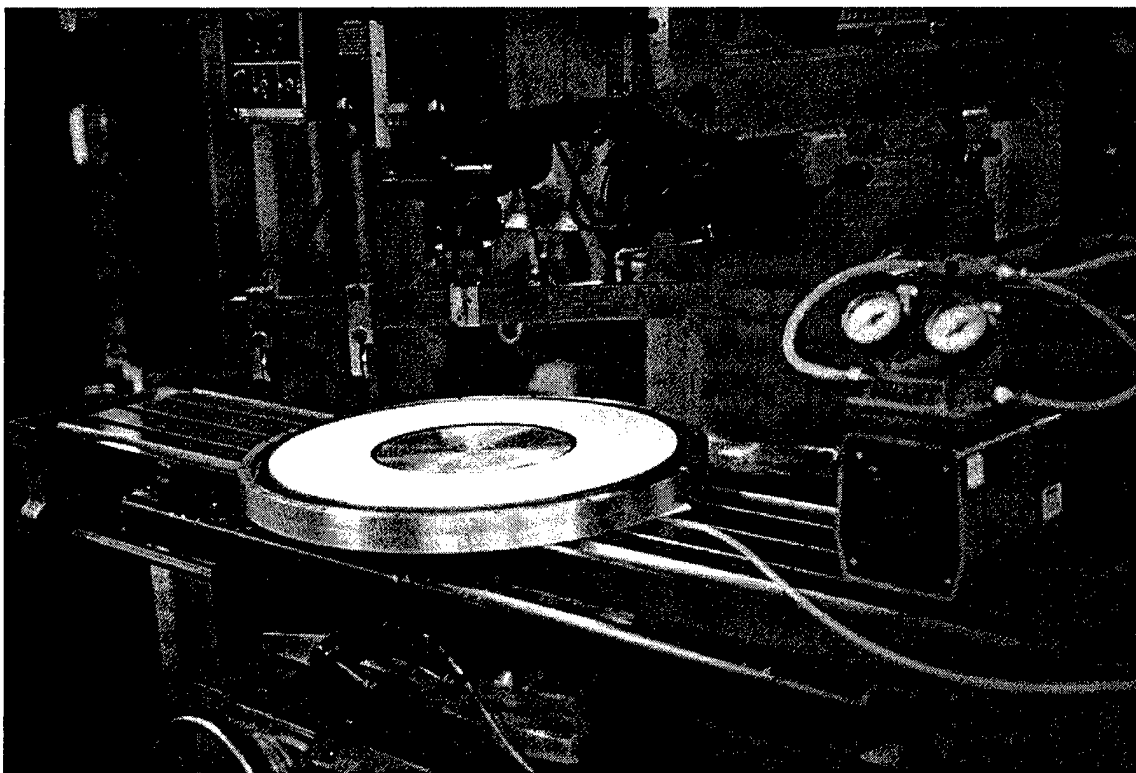


Figure 5.6. Mounted Rotary Cutters Shown with Completed Collimator Slice

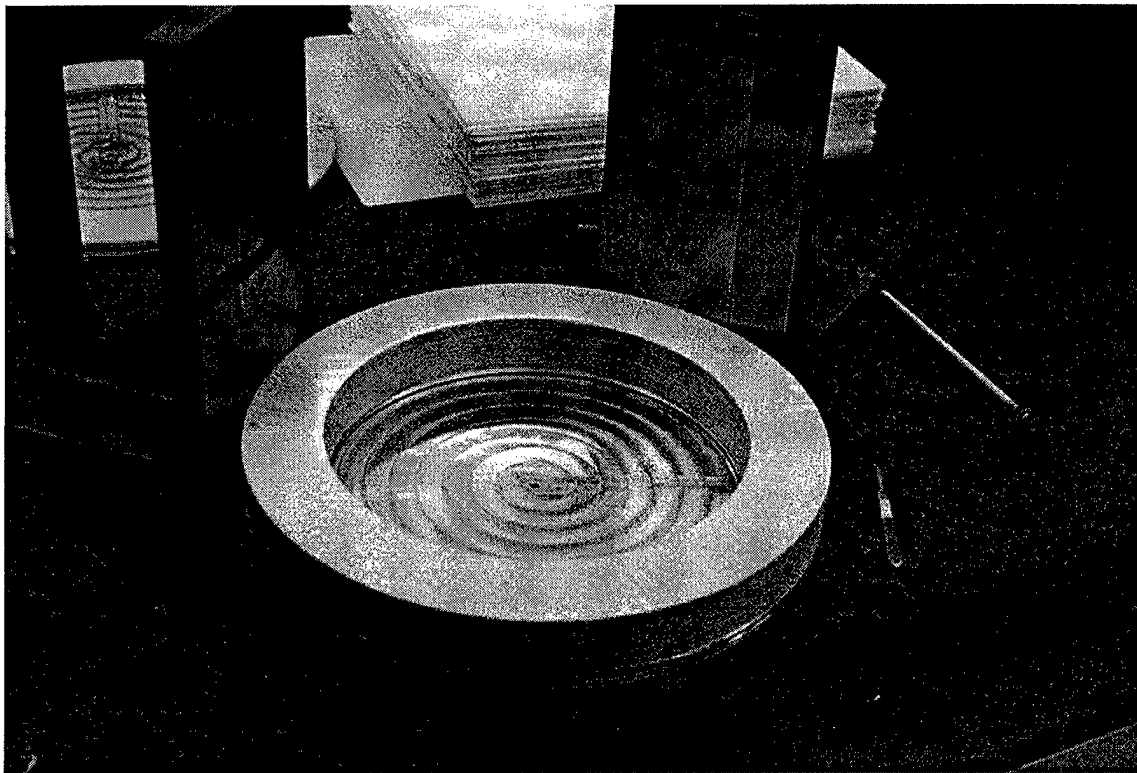


Figure 5.7. Low Energy Collimator Stack in Progress

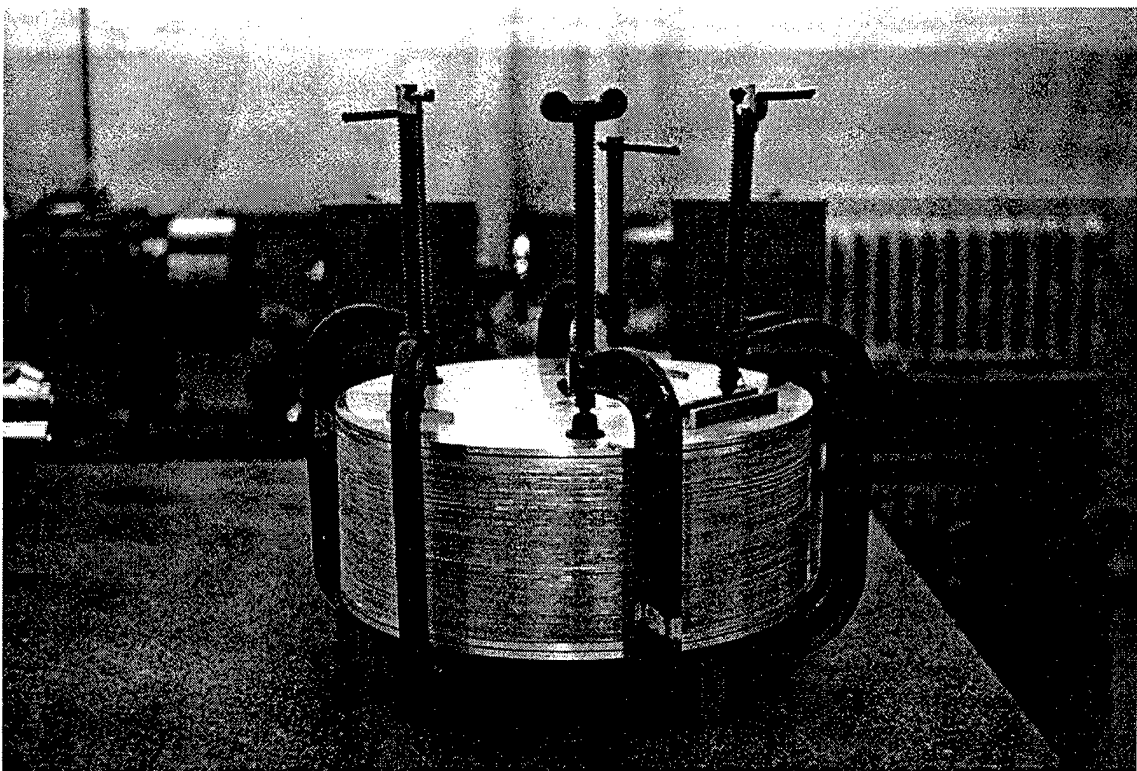


Figure 5.8. Completed Collimator Stack Under Compression, Prepared For Heating

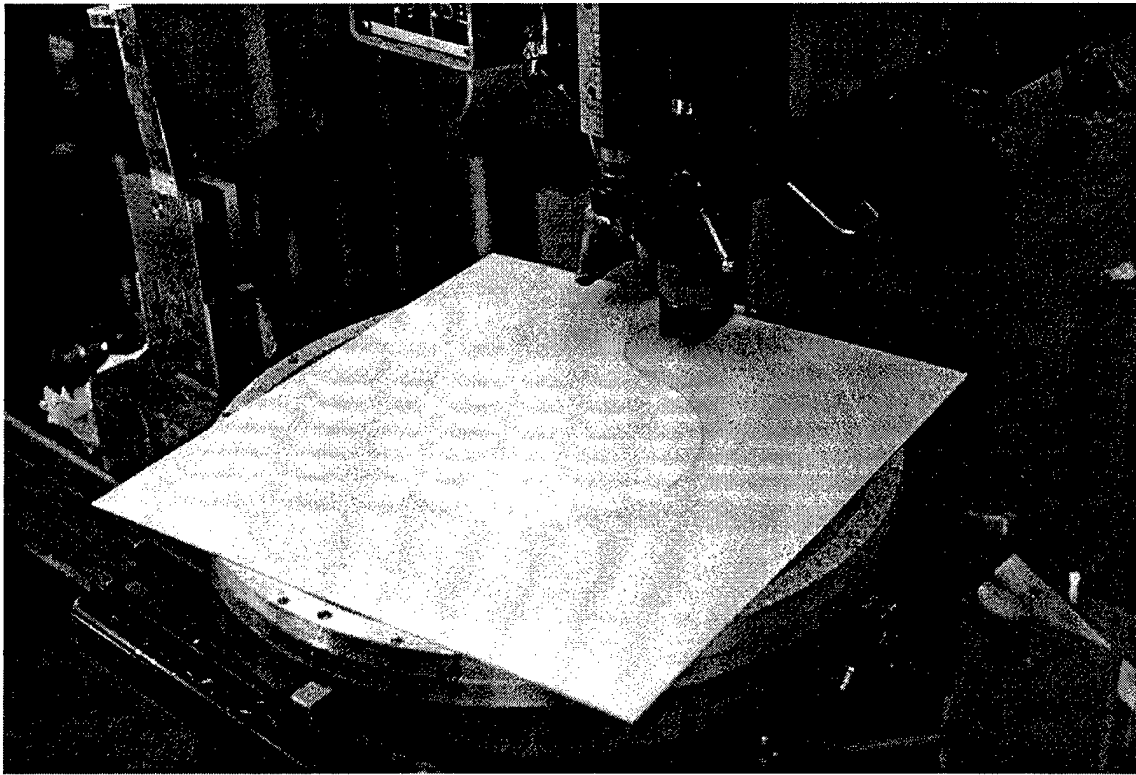


Figure 5.9. Spindle Mounted Fly-Cutter Producing Radial Taper

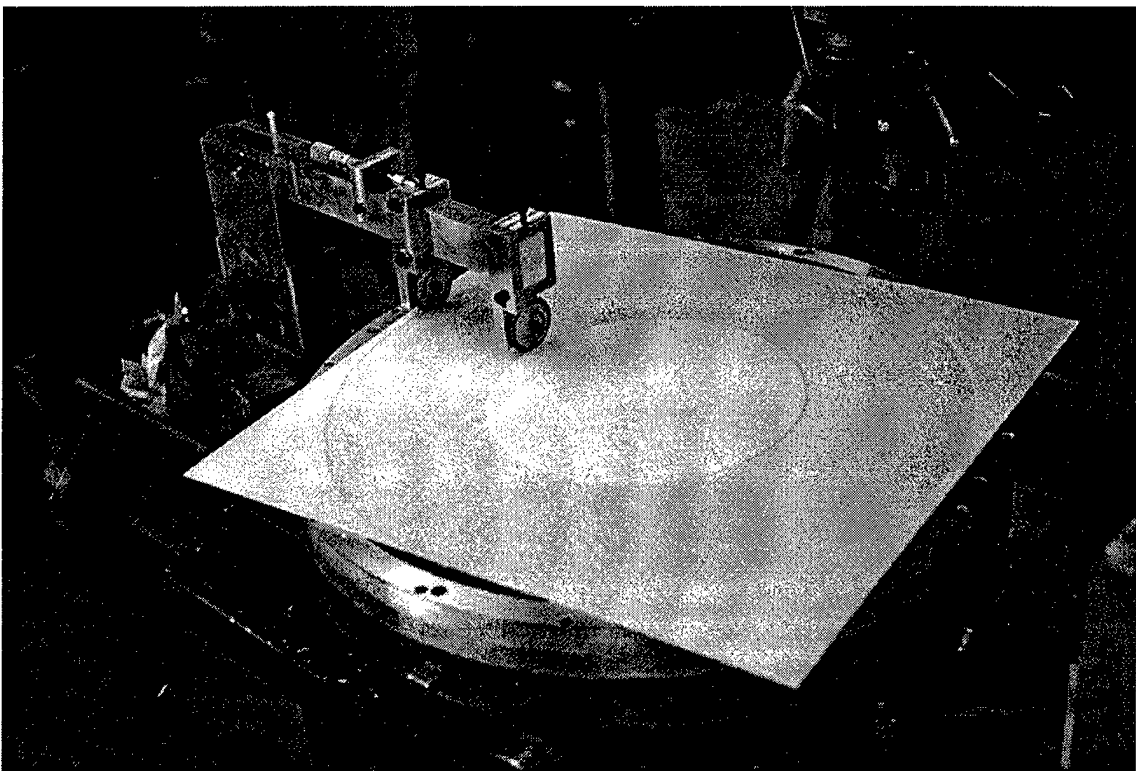


Figure 5.10. Side Mounted Rotary Cutters Making Inner and Outer Radii Cuts

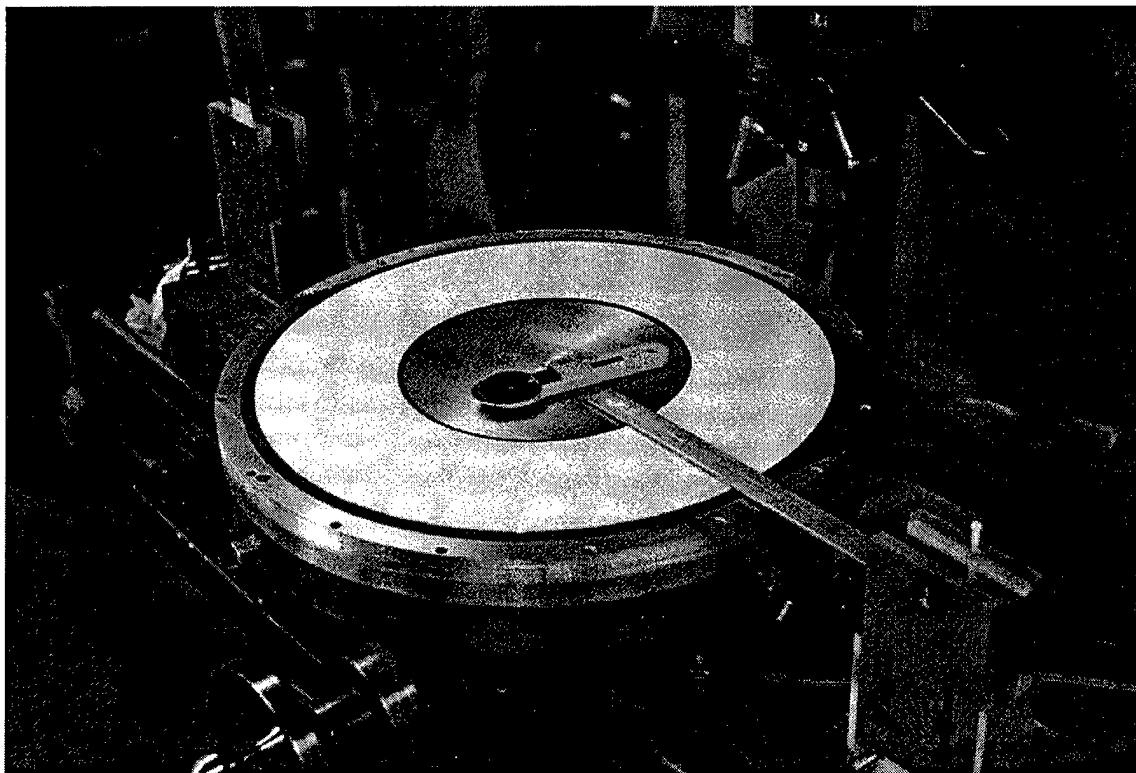


Figure 5.11. Slice Prepared for Radial Cut Using Side Mounted Template

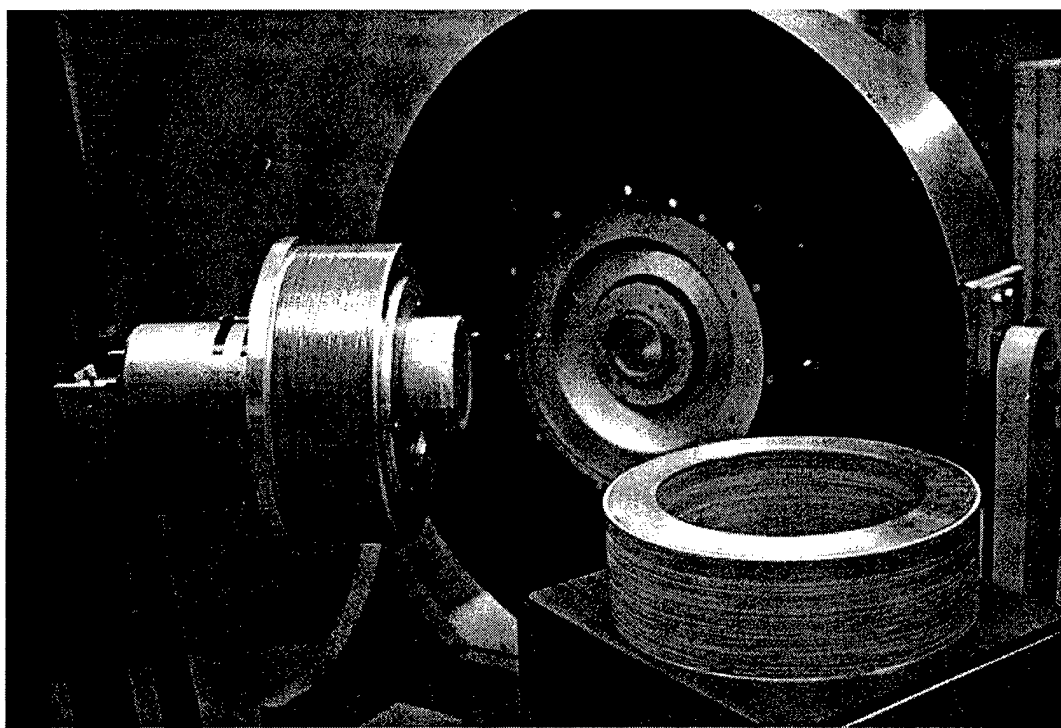


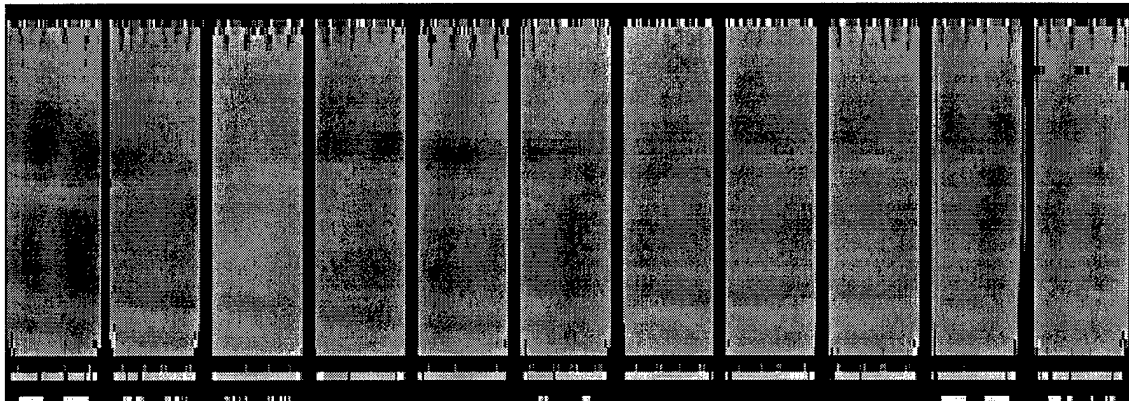
Figure 5.12. Completed Collimators: High Energy, Converging and Low Energy from Left to Right, with Converging Collimator Mounted in SPRINT.

Performance Results

Intrinsic Collimator Uniformity

Evaluation of collimator uniformity is performed by collecting a detector uniformity correction map for each of the 11 detector modules with no collimator. Next, images of a uniform line source are acquired with each slice collimator. These are corrected using the detector correction map to obtain intrinsic collimator non-uniformity. Figure 5.8 shows the resulting contrast-enhanced flood image for the ^{131}I converging collimator and 511 keV collimator acquired with 140 keV gamma rays to intensify collimator artifacts. The images are composed of 11 sub-images, one for each module around the circumference of the SPRINT gantry. Summary measures of uniformity for all three collimators are provided in Table 5.1. Standard deviation in uniformity was calculated from the variance in pixel counts within a region of each module which excluded detector artifacts.

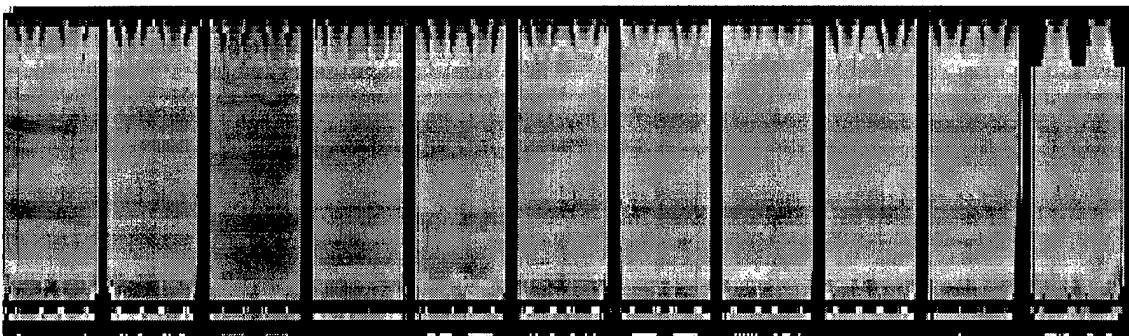
The $^{99\text{m}}\text{Tc}$ collimator demonstrated the best uniformity, with no gross artifacts visible in the image. The ^{131}I collimator had the greatest variance, with visual artifacts including several striations and a large region of slightly increased transmission. Close observance of this image also indicates point areas of increased penetration associated with the seam connection of each slice. The 511 keV collimator had good measured uniformity, but shows obvious striations across its width when contrast is enhanced. The fractional non-uniformity corresponds directly to variation in lead foil spacing so that the maximum non-uniformity of 14% for the ^{131}I collimator indicates a 0.13 mm (inner surface) to 0.20 mm (outer surface) variation in spacing. The non-uniformity in the parallel collimators is in good agreement with the variation in bond thickness and the manufacturer's specified 0.1 mm tolerance in foam thickness.



A. Uniformity of Tc-99m collimator



B. Uniformity of I-131 converging collimator



C. Uniformity of F-18 parallel collimator

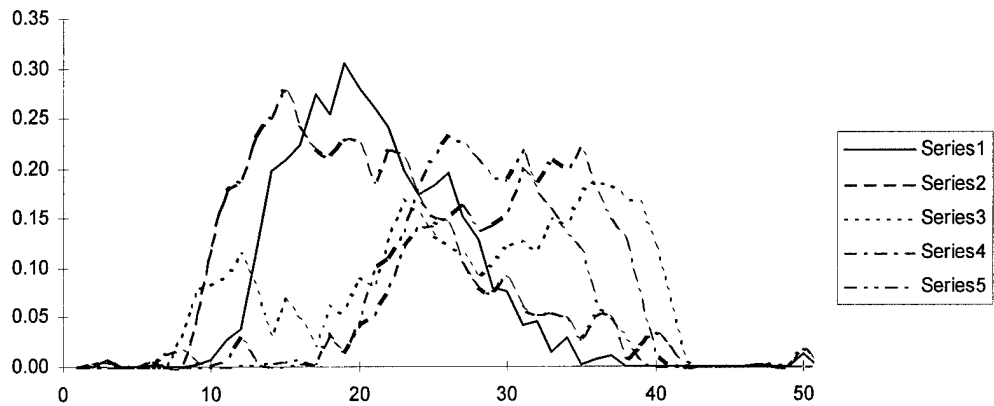
Figure 5.13. Uniformity of Collimators: Images are Shown for Each of the 11 Detectors Comprising the SPRINT Detector Ring. Contrast is enhanced to 40% of full intensity range. Structure at detector ends lies outside the useful axial field-of-view

Table 5.1. Uniformity of Collimators at Different Energies

	<i>Uniformity of collimators, standard deviation of flood images</i>		
Collimator	^{99m}Tc	^{131}I	^{18}F
^{99m}Tc Parallel	5%		
^{131}I Converging	14%	10%	7%
511 keV Parallel	10%	8%	6%

Intrinsic Resolution

Intrinsic resolution is determined from an iterative unfolding of the detector point response function from the joint system point response (collimator and detector)⁶. Detector response is measured using a highly collimated slit source translated along the detector surface. The system response is measured using a point source translated along the central axis of the gantry. Sample intrinsic collimator response functions acquired for the three collimators at adjacent 0.5 mm increments are shown in figure 5.14-5.16. The five responses shown cover an interval corresponding to the separation of two adjacent lead foil rings. Specifically, slice separation was 2.5 mm for the ^{99m}Tc collimator, 1.9 mm for the ^{131}I converging collimator (outer edge), and 2.4 mm for the 511 keV collimator. The measured intrinsic collimator resolution (FWHM) compared to the geometric resolution of each collimator is shown in Table 5.2. Range values provided in the table represent the mean resolution achieved for measurements taken between septa compared to those taken under septa. Full-width at tenth maximum (FWTM) data are also provided in the table. System axial resolution is one to two millimeters wider than the intrinsic collimator resolution.



**Figure 5.14. Low Energy Parallel Collimator Intrinsic Response Functions
Measured at 0.5 mm Intervals Along Center of SPRINT Field-of-View**

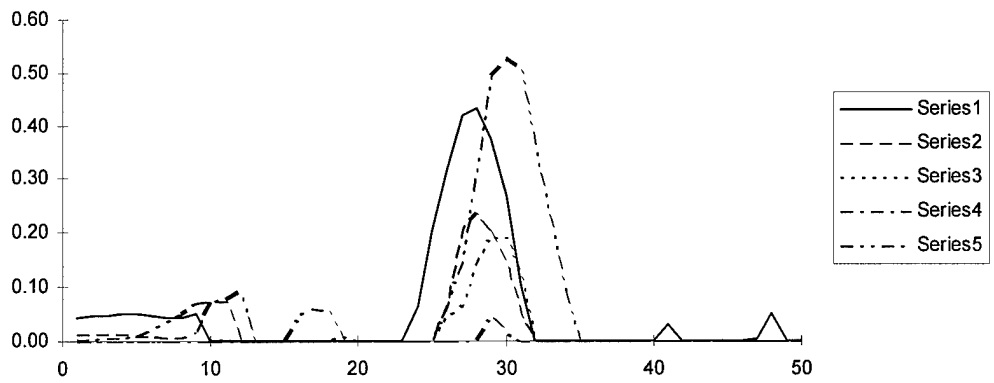


**Figure 5.15. Medium Energy Converging Collimator Intrinsic Response Function
Measured at 0.5 mm Intervals Along the Center of SPRINT Field-of-View**

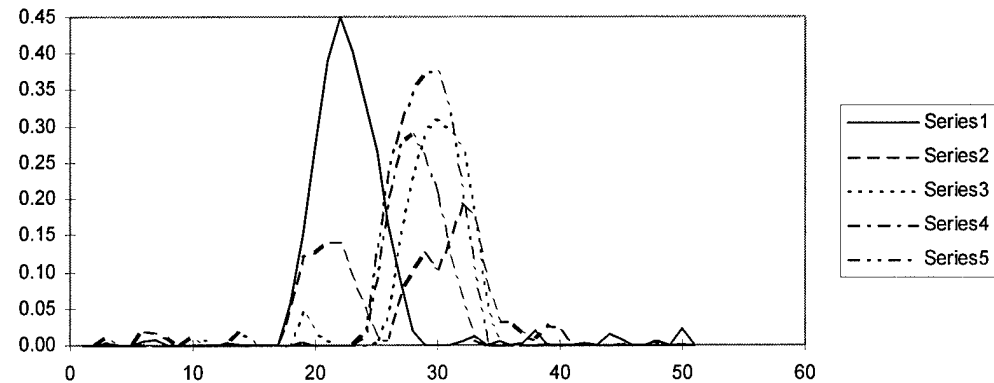


**Figure 5.16. High Energy Parallel Collimator Intrinsic Response Functions
Measured at 0.5 mm Intervals Along the Center of SPRINT Field-of-View**

Geometric collimator resolution generally agreed well with that measured, with the ^{131}I collimator and 511 keV collimator having slightly better performance than expected. The plotted response functions demonstrate the spatially variant response of these collimators, with a minimum response occurring at locations directly behind lead septa. This effect is most pronounced for the ^{131}I collimator which had an almost complete loss of response when a septa was aligned directly over the source. In comparison, the 511 keV collimator had a reduced spatial dependence because of poorer intrinsic resolution as well as septal penetration.

Table 5.2. Intrinsic Collimator Resolution. Range Values Indicate Average Values Between Septa and Average Values Under Septa.

Collimator	Geometric Resolution	Axial Resolution		
		$^{99\text{m}}\text{Tc}$	^{131}I	^{18}F
$^{99\text{m}}\text{Tc}$ Parallel	8.3 mm	8.5 ± 2.9 mm FWHM (range 8.0 - 14.8 mm)*		
		13.6 \pm 2.0 mm FWTM		
^{131}I Converging	2.0 mm	1.1 \pm .19 mm FWHM	1.9 \pm .45 mm FWHM	2.4 \pm .38 mm FWHM
		1.8 \pm 2.7 mm FWTM	3.1 \pm .56 mm FWTM	4.2 \pm 1.2 mm FWTM
511 keV Parallel	3.5 mm	2.5 \pm 0.91 mm FWHM (range 2.2 to 5.0 mm)	2.9 \pm 1.3 mm FWHM (range 2.4 to 7.0 mm)	3.3 \pm 1.7 mm FWHM (range 2.5 to 7.3 mm)
		4.5 \pm 1.6 mm FWTM	4.7 \pm 1.8 mm FWTM	5.6 \pm 2.1 mm FWTM

System Sensitivity

Sensitivity is measured for all three collimators using a point source at locations showing a moderate, high and low response based on uniformity maps. A 20% energy window is used centered on the photopeak. Results are shown in Table 5.3. The $^{99\text{m}}\text{Tc}$ collimator when used with a slit aperture set for 2.9 mm FWHM in-plane resolution provided a system sensitivity that is comparable to current two-head SPECT systems,

using low-energy all-purpose collimators⁷. ^{99m}Tc when used with either the ^{131}I converging or 511 keV parallel collimator demonstrated a factor of four reduction in sensitivity due to increased collimator length, thicker septa and smaller slice spacing. An additional factor of three reduction is experienced when ^{131}I is used with the high energy collimators due to a reduced photoelectric cross-section (16% detection probability), and slightly smaller abundance of the detected gamma ray. The 12 mm thick sodium-iodide detectors demonstrate only a 7% photoelectric interaction probability for 511 keV photons. However, some sensitivity is gained for positron emitters due to the 200 percent abundance of annihilation radiation. Although the two gamma-rays are correlated, the poor detection sensitivity makes it unlikely that both gamma rays will be detected. Overall there is an approximate factor of 10 reduction in system sensitivity between the ^{99m}Tc collimator and the two high energy collimators.

Table 5.3. Sensitivity of Collimators as Measured With a Point Source Centered in the SPRINT-II Gantry. Values in parentheses represent system sensitivities obtained with a 2 mm wide slit aperture.

	Sensitivity in cpm/ $\mu\text{Ci}/\text{deg}$ and cpm/ μCi for 2 mm slit (2 mm slit results in 2.9 mm in-plane resolution for ^{99m}Tc)		
Collimator	^{99m}Tc	^{131}I	^{18}F
^{99m}Tc Parallel	$61 \pm 5.2\%$ cpm/ $\mu\text{Ci}/\text{deg}$ ($670 \pm 5.2\%$ cpm/ μCi)		
^{131}I Converging	$17 \pm 13\%$ cpm/ $\mu\text{Ci}/\text{deg}$ ($180 \pm 13\%$ cpm/ μCi)	$6.2 \pm 10\%$ cpm/ $\mu\text{Ci}/\text{deg}$ ($67 \pm 10\%$ cpm/ μCi)	$7.7 \pm 7.8\%$ cpm/ $\mu\text{Ci}/\text{deg}$ ($83 \pm 7.8\%$ cpm/ μCi)
511 keV Parallel	$17 \pm 12\%$ cpm/ $\mu\text{Ci}/\text{deg}$ ($180 \pm 12\%$ cpm/ μCi)	$5.5 \pm 5.7\%$ cpm/ $\mu\text{Ci}/\text{deg}$ ($59 \pm 5.7\%$ cpm/ μCi)	$7.3 \pm 4.8\%$ cpm/ $\mu\text{Ci}/\text{deg}$ ($79 \pm 4.8\%$ cpm/ μCi)

Summary

Novel construction techniques and materials were used to build precision slice collimators for SPRINT-II. These methods proved successful over a range of material dimensions, and for the production of both parallel and converging geometries. Observed collimator performance generally met design objectives. The ^{99m}Tc collimator showed excellent uniformity and sensitivity, with moderate spatial variance and adequate resolution. The ^{131}I and 511 keV collimators demonstrated excellent resolution, but suffered from larger variance in uniformity, increased spatial variance and greatly reduced sensitivity when compared to the ^{99m}Tc collimator. Measured resolution and sensitivity are as expected for the design specifications of each collimator. Variance in uniformity is directly dependent on measured variance in foam and bond thickness between slices which can be reduced for the parallel collimators by machining the foam rather than accepting the manufacture's tolerances. Although the methods developed are for a specific imaging system, they should find general application in the construction of foil collimators for other purposes .

References to Chapter V

¹ Rogers WL, Clinthorne NH, Shao L, Chiao P, Ding Y, Stamos JA, and Koral KF, SPRINT II: A second generation single photon ring tomograph. *IEEE Trans. Med. Imag.* MI-7:4(1988)291-297.

² Rogers WL, Slosar J, Hua L, Chiao P, Zhang Y, Clinthorne NH. A high resolution slit aperture for imaging small animals with SPECT. *J. Nucl Med* 1993;34(5):9P.

³ Wilderman SJ. Vectorized Algorithms for Monte Carlo simulation of kilovolt electron and photon transport, PhD Thesis, School of Engineering, University of Michigan, 1990.

⁴ Rohm Tech Inc, Rohacel Polymethacrylimide Rigid Foam Product Reference, 195 Canal St, Malden MA 02148, USA.

⁵ Dow Chemical Company, DAF 899 DOW Adhesive Film Data Sheet, Form No. 500-1200-590X SMG, Midland MI 48674.

⁶ Clinthorne NH, Wrobel MC, et al. Conference Proceedings of 1995 IEEE Nuclear Science Symposium and Medical Imaging Conference, 1995.

⁷ Siemens Medical Systems, Collimators for MULTISPECT Gamma Camera Systems, Data sheet, 2501 N. Barrington Road, Hoffman Estates, IL, USA, 1994.

CHAPTER VI

CORRECTING FOR APERTURE PENETRATION BY HIGH ENERGY GAMMA-RAYS

SPRINT's in-plane resolution is determined by a rotating slit aperture, as discussed in Chapter III. It is desirable to establish an image resolution which is at least equal to or less than that achieved axially. By using a slit opening of 3.125 mm, the predicted geometric resolution is approximately 4.4 mm FWHM, comparable to the system resolution measured axially (Chapter V). Unfortunately a problem specific to 511 keV photon imaging is penetration of these gamma rays through the aperture edges which results in a subsequent loss of resolution. This chapter will focus on an innovative method developed to compensate for aperture penetration in high energy slit aperture or pin-hole SPECT.

Background

In reconstructing of images acquired with pin-hole and slit aperture geometries one usually assumes the measured projection data is exclusively from gamma rays that pass through the slit. As gamma ray energy increases, the aperture edges are less effective attenuators, resulting in projection data being contaminated by photons that pass through the aperture edges as well as through the collimator body. As a result, the system point response function is significantly broadened with a subsequent loss in image resolution and contrast. Ideally, this problem would be overcome by simply using more effective attenuators in the construction of the aperture. Unfortunately, at the photon energies of iodine-131 (364 keV, 637 keV) and positron emitters (511 keV), edge

penetration is significant even for depleted uranium (DU) or gold. These materials are the best attenuating materials that are obtainable. For SPRINT imaging 511 keV photons, approximately half the measured projection data stems from photons that penetrate the hybrid lead-DU small animal aperture. The effect is graphically depicted in figure 6.1 which shows a comparison of the aperture penetration predicted by ray-tracing to that measured for an ^{18}F line source centered in the SPRINT gantry. For comparison, the normalized profile of a measured $^{99\text{m}}\text{Tc}$ line source is also shown.

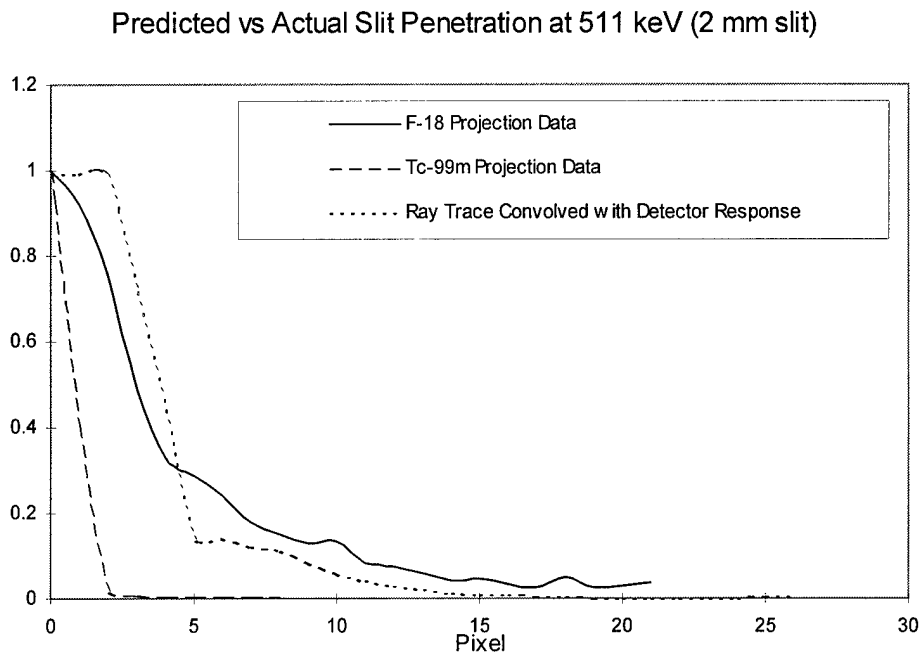


Figure 6.1. Demonstrated Aperture Penetration Measured for 511 keV Annihilation Radiation

Due to this effect, high energy planar and SPECT imaging are conventionally performed using parallel, converging or fan-beam collimators that are designed with thick septa and long lengths to provide effective collimation. For example, the Siemens 511 keV parallel hole collimator is designed with 0.25 cm septa, 0.34 cm holes, and has a length of 7.5 cm¹. Such collimators are heavy, suffer from poor intrinsic sensitivity and resolution, have severe spatial variance in their response, and parallel collimators do not magnify the object as do pin-hole apertures. Thus pin-hole or slit aperture SPECT is an

attractive option for high resolution animal imaging if aperture penetration can be corrected.

Methods

Initial Attempts to Correct for Penetration

Projection data acquired from ^{18}F line sources indicates that the penetration component of the projection appears as a smooth background added to true signal. This was observed to be similar in effect to scatter radiation originating from within the measured object in low-energy SPECT and PET. Hence, methods successfully used for scatter correction were explored as to their efficacy in correcting aperture penetration. A direct compensation technique that could be applied to existing projection data is the convolution-subtraction technique² originally applied to SPECT and later to PET image reconstruction³. Application of this method begins with the premise that projection data is composed of the true signal, $P_{\text{Sig}}(x)$, and penetration $P_{\text{Pen}}(x)$:

$$P_{\text{measured}} = P_{\text{Signal}} + P_{\text{Penetration}} \quad (6.1)$$

The projected penetration distribution is then assumed to be of the following analytical form:

$$\hat{P}_{\text{Pen}} = \int_{-D}^D P_{\text{measured}} * h(x - t, t) dt \quad (6.2)$$

Where $h(x, t)$ is the convolution kernel describing the penetration as a function of x (image plane) and t (detector plane). If an accurate kernel can be determined, the true projection signal is estimated by:

$$\hat{P}_{\text{Signal}} = P_{\text{measured}} - \int_{-D}^D P_{\text{measured}} * h(x - t, t) dt \quad (6.3)$$

The projection data from line sources translated across the field-of view were measured to empirically determine the blurring (convolution) function (figure 6.2). It is

observed that the tails of these distributions are highly spatially variant, presenting an immediate obstacle to implementing this simple correction method. The tails are found to be a function of both source location within the field of view, as well as projection angle. The resulting three-dimensional kernel is complicated further by being discontinuous in x where rays pass directly through the slit opening and the kernel becomes zero. Because of these factors, implementation of this technique was not pursued.

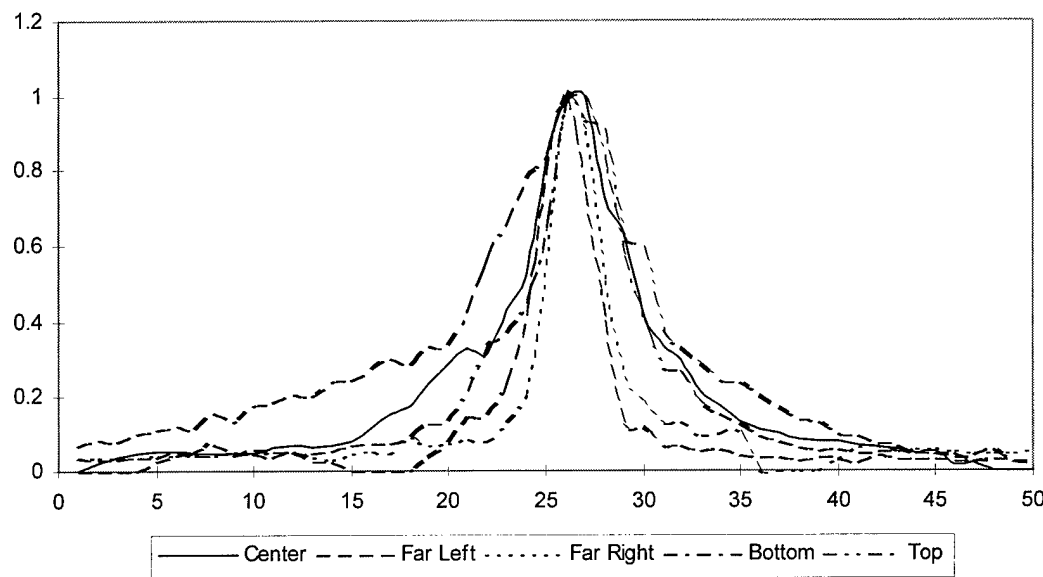


Figure 6.2. Spatially Variant Penetration Tails Observed for Line Sources Moved Throughout the Field-of View

These same issues prohibit an iterative solution to this problem, where aperture penetration is modeled and incorporated into the system response matrix. The first complication is that for each source location and for each aperture position the probability of a photon penetrating the aperture and interacting in a given detector element must be determined. This would require an extensive Monte Carlo assessment of the SPRINT imaging geometry that is both difficult and time consuming. Second, a non-sparse system matrix results from the penetration tails extending across the projection space (figure 6.2). This infers a finite probability of aperture penetration for all detector pixels from all

source pixels thus causing the system matrix to be “full” or complete. For SPRINT, this would require a 390 MByte weight matrix, which is too large for RAM storage on most computer platforms and substantially lengthens image reconstruction.

A Proposed Solution: Correction Through Blocking

The developed method attempts to measure the aperture penetration by “blocking” the slit aperture. We observe that the measured projection data is composed of both true signal and aperture penetration (Equ. 6.1). If the “penetration” aspect of the projection data can somehow be measured directly or estimated from measurements, then the true projection signal is estimated as:

$$\begin{aligned}\hat{P}_{Signal} &= P_{measured} - \hat{P}_{Penetration} \\ \hat{P}_{Signal} &= (P_{Signal} + P_{Penetration}) - \hat{P}_{Penetration}\end{aligned}\quad (6.4)$$

In this case, blocking the aperture provides projection data which serves as an estimate of the penetration background. This can then be subtracted from the open slit projection to obtain a true net signal. Experiments were conducted on the effect of blocking the aperture slit with a depleted uranium bar (3.125 mm x 6.25 mm) and measuring the resulting projection for an on-axis line source. The results are shown in figure 6.3. The blocked slit data has the expected form of the penetration signal, except that it does not drop to zero at the center of the projection. This is because the block is not completely opaque to 511 keV gamma rays. The figure also shows the net projection data resulting when the blocked slit projection data is subtracted from the open slit data. The normalized projection profile of a ^{99m}Tc source is presented for reference. The net projection data is observed to have a resolution that approaches that for the ^{99m}Tc data, with the penetration tails significantly reduced. The method’s efficacy was assessed for extended objects by making a series of off-axis source measurements (figures 6.4 and 6.5). Again, the method demonstrates good improvement in resolution and tail-reduction

for the net responses obtained by subtracting the matched open and blocked slit measurements.

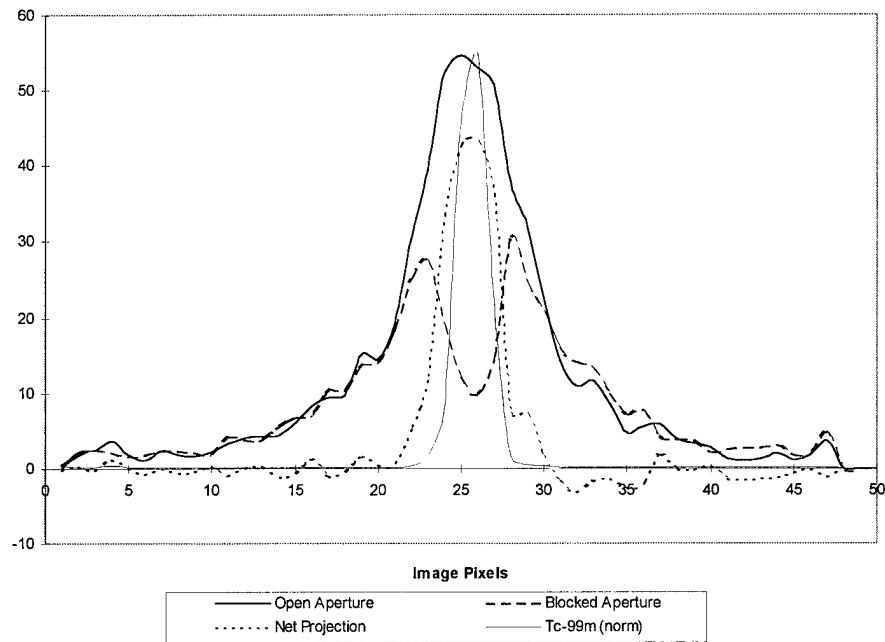


Figure 6.3. Projection Profiles for Open Slit and Blocked Slit Apertures

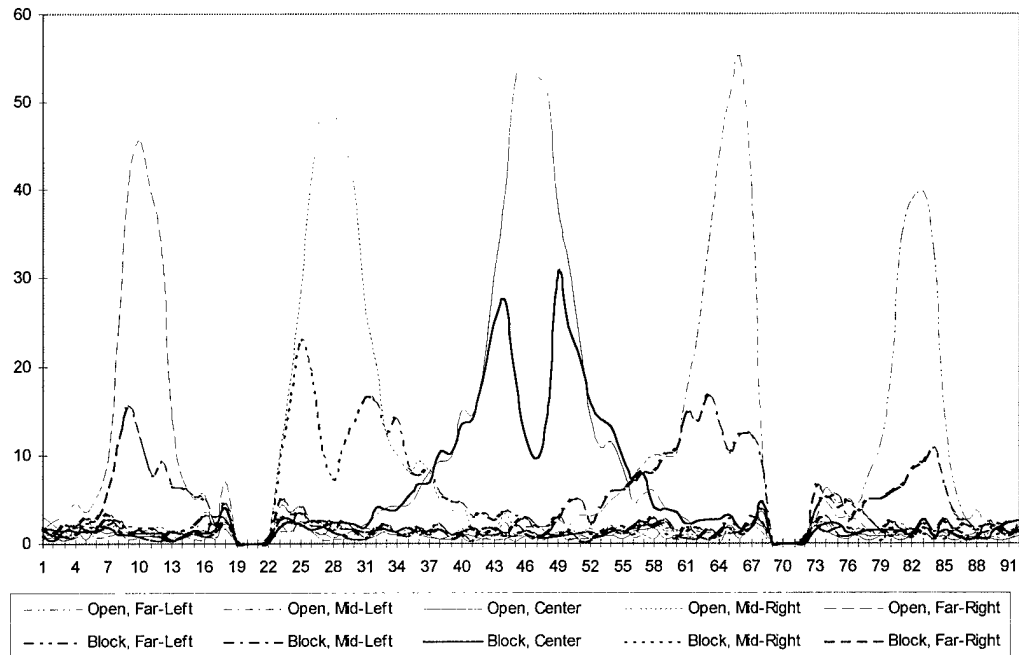


Figure 6.4. Comparison of Open and Blocked Slit Profiles for Various Location Across the Field of View

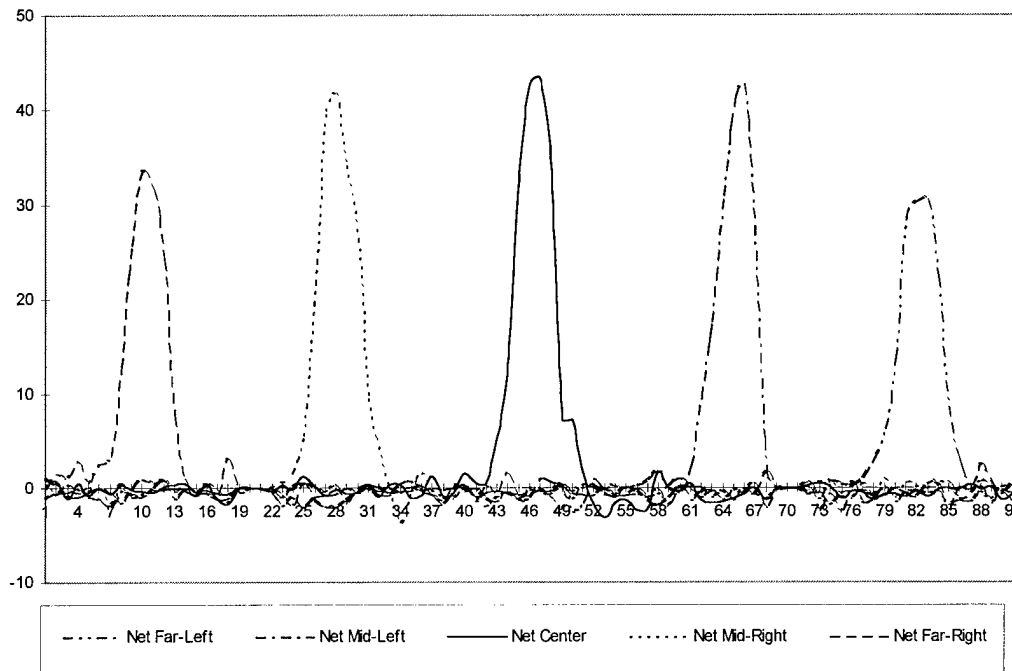


Figure 6.5. Net Line Source Projections Obtained from Difference Between Open and Blocked Slit Data

Correcting for the Non-Ideal Block Response

The devised algorithm was applied to imaging a cylinder filled with a uniform distribution of activity. Reconstructed images however demonstrated a significant depression in counts in the central region of the object. Two factors contribute to this effect: the finite attenuating properties of the depleted uranium block and the finite thickness of the block. First, 6.2 mm of DU permits approximately 10% of incident 511 keV photons to be transmitted (based on total interaction cross-sections⁴). These photons contribute to the measured blocked projection causing an overestimate of the aperture penetration where, by definition, penetration should be zero. The second factor causes a “penumbral” effect between the aperture edge and block, where photons incident on the aperture edge can also be incident on the DU bar. The result in an underestimation of the penetration data since the block introduces additional attenuation of the aperture edges.

The spatial dependence of these two effects are better observed in Figures 6.6 and 6.7, where the ray traced profiles through the DU block are presented for four point sources in the field of view. For points along the central axis, the block acts as a rect (Π) function, attenuating the incident radiation with little penumbral effect. In contrast, far off-axis locations approach a Λ function. An asymmetric Λ function is reached at a 26.5° angle from normal, associated with an off-axis point of 33 mm. The figure also demonstrates the severity of the penumbral effect, depicted as the overlap region between solid (DU block) and dashed (aperture edge) lines. The effect changes as the source location moves towards the edge of the field-of view.

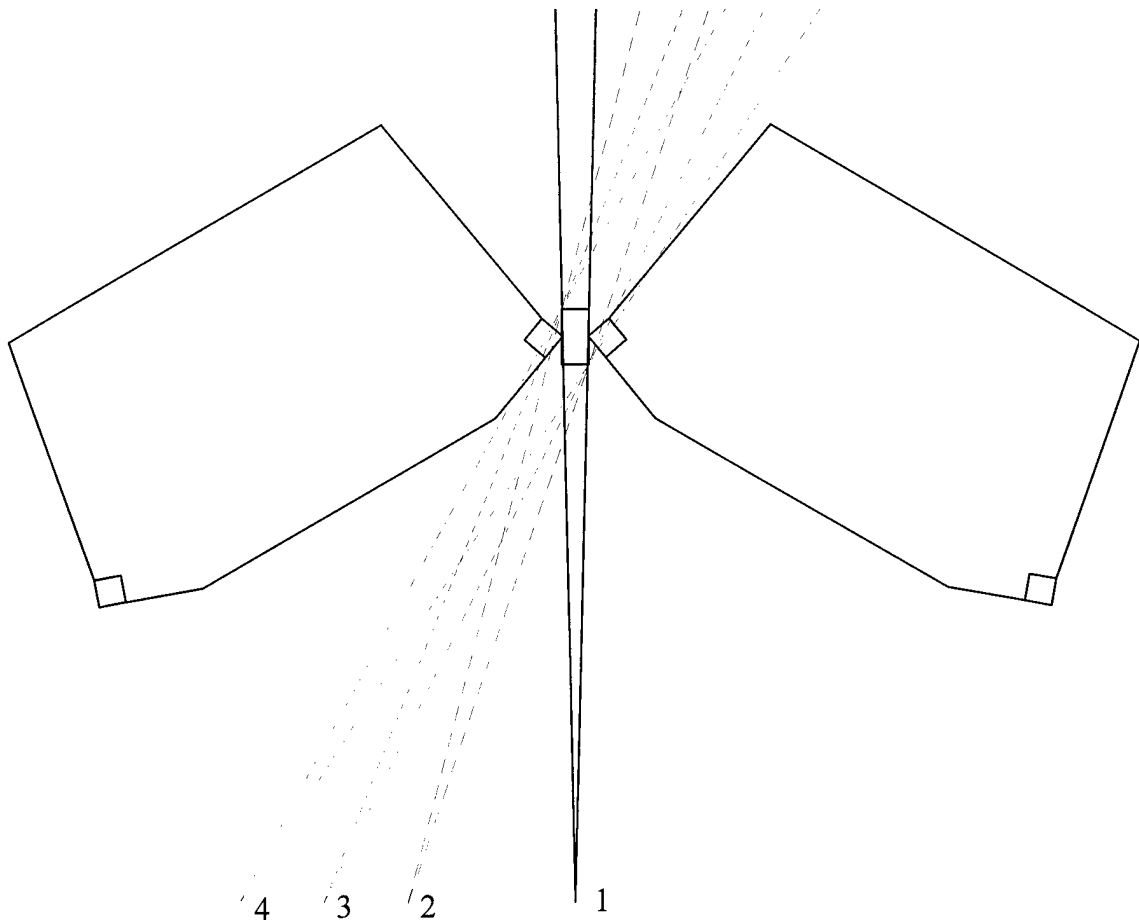


Figure 6.6. Ray-Tracing from Point Source Locations in Field of View Through DU Block and Aperture Edges

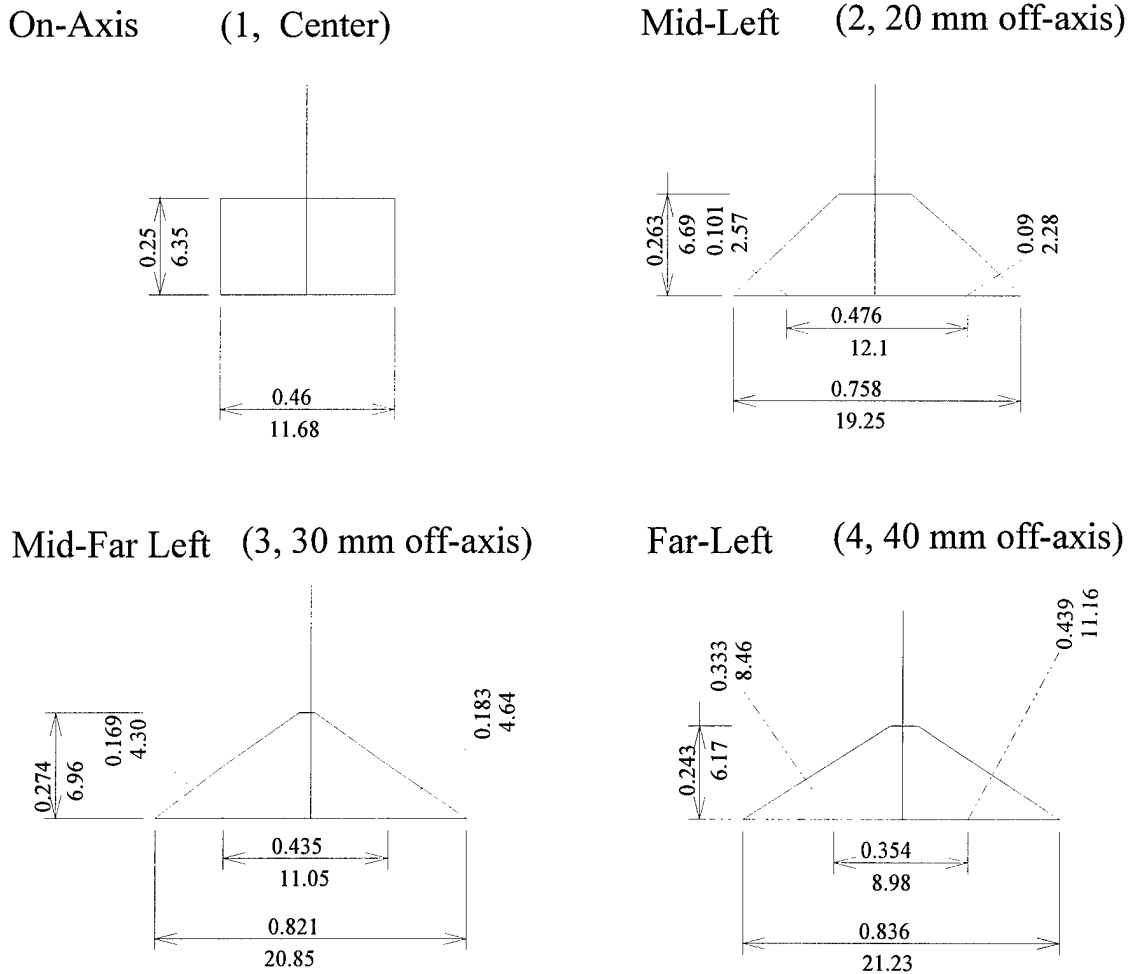


Figure 6.7. Demonstration of Spatially Variant Penetration and Penumbral Effects Observed with Actual Block (Dimensions are in/mm)

To correct for these effects, an inverted Blackman window was applied as a spatial weight to the measured penetration projection data, such that:

$$\text{Blackman Weight}(i) = 1 - k * \left(0.42 - 0.5 \cdot \cos\left(\frac{2\pi(i-1)}{(N-1)}\right) + 0.08 \cdot \cos\left(\frac{4\pi(i-1)}{(N-1)}\right) \right) \quad (6.5)$$

where i is a projection element, N is the number of elements in a projection (91 or 92), and k is an empirically derived constant equal to 0.18. The constant was derived to achieve a uniform profile across a uniform object. The resulting function required a minimum weighting of 0.82 in the center of the projection, up to 1.0 at the projection edges. Results are shown in figure 6.8. Reconstruction of the uniform object using the

uncorrected penetration data shows a central depression (figure 6.8A). Filtered back-projection reconstruction with the weighted penetration data (figure 6.8B) demonstrates recovery of the central area to produce a uniform field. For comparison, the image without penetration correction is shown in figure 6.8C, which has approximately twice the counts of the corrected image. This is in good agreement with measured projection data indicating penetration accounts for approximately 50% of the measured count rate.

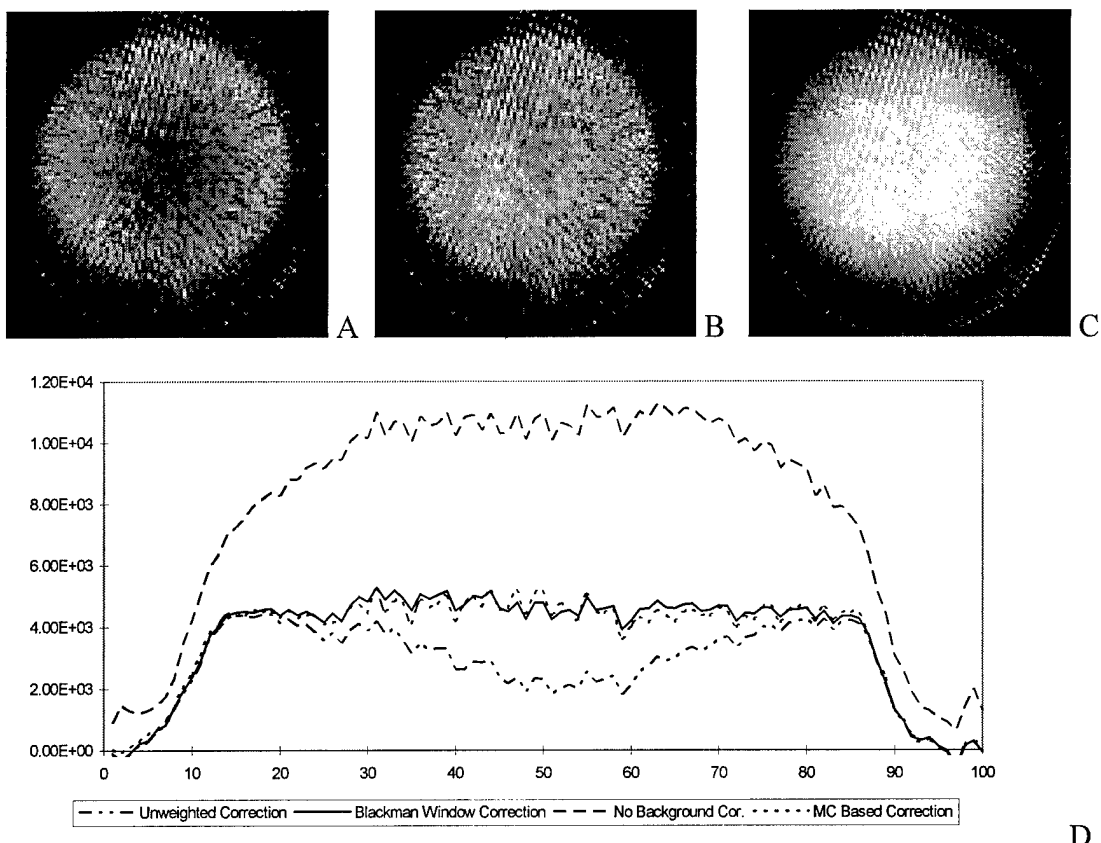


Figure 6.8. Effect of Imperfect Aperture Blocking. Figure A and Bottom Profile Indicate Effect of Directly Subtracting Measured Penetration from Open Slit Data.

Data Acquisition and Image Reconstruction

To measure aperture penetration as part of a normal tomographic acquisition, the slit aperture was modified so that every other slit was blocked by a depleted uranium bar. Available material dictated the bar size of 3.125 mm by 6.25 mm, and 150 mm long.

This bar size then determined the minimum open slit width of 3.125 millimeters. A tomographic acquisition sequence was then implemented which rotated the aperture 80 steps, 1.5 degree per step, sweeping the aperture in a 120° arc. This doubled the number of projections acquired compared to conventional low-energy imaging, providing an open slit and blocked slit projection for each aperture position. Post-processing of the acquired raw projection data was conducted to form two complete data sets of open and blocked slit data. The blocked slit data were then weighted to correct for the effect of penetration and penumbra. The modification of the aperture design and the implemented sampling protocol are shown in figure 6.9.

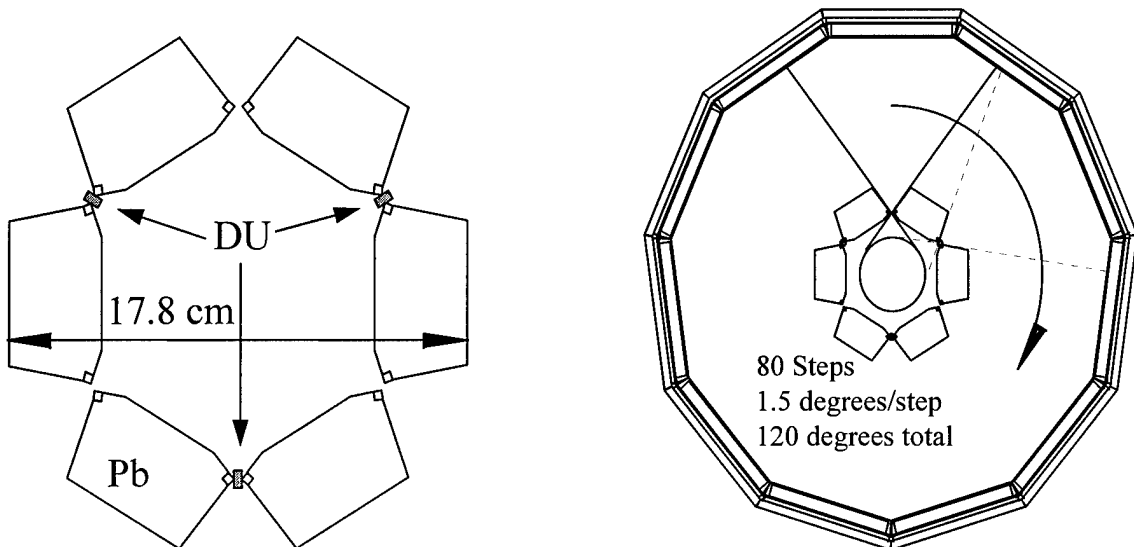


Figure 6.9. Slit Aperture Arrangement and Sampling Protocol for High Energy Imaging. Edges of Slit are Edged with DU. Aperture Ring Rotates While Detector Ring is Stationary.

Reconstruction of images was conducted using both filtered back-projection and the SAGE iterative algorithm⁵. In applying FBP, the open-slit projection data was preprocessed by subtracting the weighted blocked-slit projection data and then applying suitable uniformity correction P_e .

$$Y_p = P_e^{-1} \cdot \{ Y_{Open} - w Y_{Blocked} \} \quad (6.6)$$

Where "w" represents the Blackman window. High frequency noise in the reconstructed image was smoothed slightly using a Butterworth filter with a 0.9 cm^{-1} frequency cutoff.

For iterative reconstruction, the SAGE algorithm was applied, with the weighted blocked slit projection data used as the random background term:

$$Y_{Open} \sim Poisson\{P_e(A_{Tc}\lambda + wY_{Blocked})\} \quad (6.7)$$

The system model employed weights generated using the geometric slit opening, noted as A_{Tc} , that excluded any aperture penetration effects. Regularization was performed to optimize image quality, typically in the range of $\beta=2^{-23}$ for low count images to 2^{-28} for high count images (reference Equ. 4.44).

Results

Penetration correction was assessed using ^{18}F line sources arrayed across the field-of-view. Reconstruction performed using FBP without penetration correction is shown in figure 6.10A, with the associated horizontal profile shown in figure 6.10B. Qualitatively, the image suffers from poor resolution with long tails introduced on each line as well as a tangential and radial dependence in resolution. The same lines reconstructed with penetration correction are seen in figure 6.10C, with a matched profile in 6.10D. This image shows a significant improvement in resolution across the field of view, and resolution is now more isotropic. There is also a notable reduction in the tails of each source. Quantitatively, the non-penetration corrected image had a central resolution of 8.8 mm FWHM and 18 mm FWTM due to large penetration tails. Images reconstructed with penetration subtraction resulted in a 5.7 mm FWHM and a 10.8 FWTM resolution. If the blocked slit projection data are not spatially weighted and used directly for correction, a slightly better resolution of 5.0 mm FWHM and 8.6 mm FWTM is achieved due to over-correction. Images of lines reconstructed using SAGE ($\beta=2^{-28}$) demonstrate significant additional improvements in image quality. Qualitatively, backprojection

artifacts are removed and resolution approaches the calculated theoretical limit of 4.4 mm, with a FWTM of 8.0 mm.

Sensitivity assessed after correction for these line sources was only 66 ± 5.5 cpm/ μ Ci ^{18}F , compared to 127 ± 6.0 cpm/ μ Ci assessed for the high energy collimator with a slit width of 3.175 mm (Chapter 5). The approximate halving of sensitivity is again attributed to the dual measurement correction method.

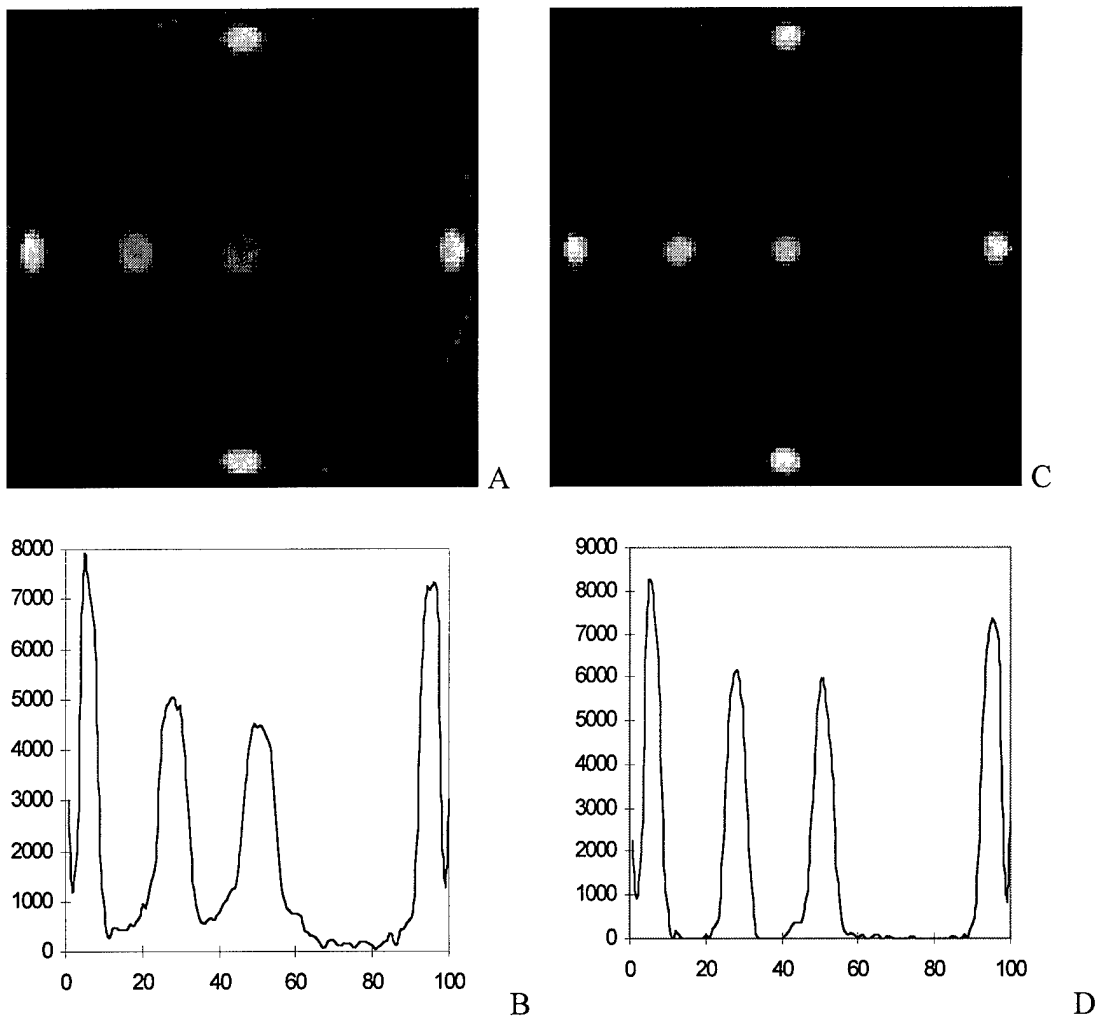


Figure 6.10. Six Line Source Array Reconstructed Using FBP, Without and With Penetration Correction.

An ^{18}F filled micro-Jaszczak phantom consisting of holes ranging from 1.5 to 4.0 mm in diameter was also imaged. Figure 6.11A shows a ramp filtered FBP reconstruction without penetration correction. The image was created with 87.6 million counts, but resolution and contrast are poor. Figure 6.11B illustrates the same image

reconstructed with penetration correction from 40.1 million net counts. Figure 6.11C demonstrates the effect of reconstructing using penetration correction and the SAGE algorithm ($\beta=2^{-26}$). In uncorrected images, the 4 mm line set was barely discernible and a uniform background level was present. Images produced with correction resulted in clear observation of the 3 mm holes and negligible background, with the SAGE reconstruction demonstrating reduced noise and ray artifacts.

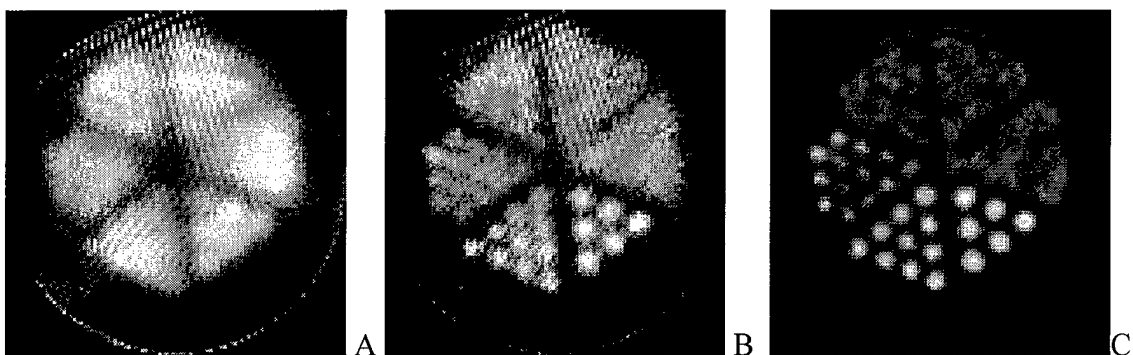


Figure 6.11. Images of μ Jaszczak Phantom, Hot Lines from 4.0 mm to 1.5 mm.

Finally, two ^{18}F line sources (2 mm wide) formed into a “U” and “M” were imaged without and with penetration correction, respectively. The resulting FBP images are shown in figure 6.12, with the “U” demonstrating poorer resolution and a diffuse background as compared with the reconstructed “M”.

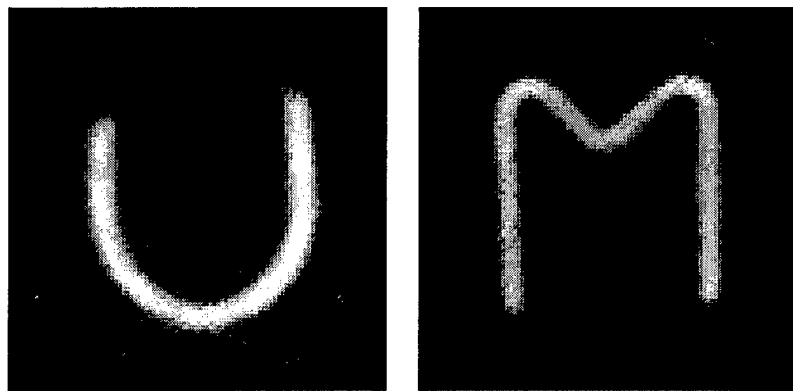


Figure 6.12. U of M, Without and With Penetration Correction.

Discussion

To evaluate in greater detail why a Blackman window was effective in correcting the observed depression in central object counts, we conducted a series of Monte Carlo simulations for 511 keV gamma-rays imaged with SPRINT⁶. Simulations were performed by Dr. Wilderman of the University of Michigan's Department of Nuclear Engineering. An accurate representation of the SPRINT aperture was simulated using three designs: with a 3.125 mm open slit, with the slit blocked by the depleted uranium bar, and with the slit blocked by an infinitely thin perfect absorber. Point sources were then simulated for each of these geometries both on-axis and at four off-axis locations. To simplify implementation, the simulations did not include the detector response. Figure 6.13 shows the difference in detected photons falling within a $\pm 10\%$ energy window and incident at the detector surface between the DU blocked aperture and perfectly blocked aperture for the on-axis and two off-axis points. In these profiles we note the two separate effects attributable to the finite size and finite attenuating properties of the DU bar. For both the on-axis and off-axis cases, there is notable penetration through the bar, compared to zero flux for the perfectly blocked slit. The effect is somewhat mitigated in the off-axis cases as the bar is traversed at an angle from normal, increasing the effective thickness of the block. As discussed previously, this effect causes an overestimation of the measured penetration background that is most pronounced in the central region of the projection. The penumbral effect is only demonstrated for the off-axis points. This result is evidenced by the diminished intensity in the side lobes of the response profile. For the ideally blocked slit, there are highly peaked responses on either side of the block, associated with rays passing through region where the aperture knife edge meets the block. These responses are greatly diminished as rays incident in this area impinge on both the aperture edge and finite size DU bar.

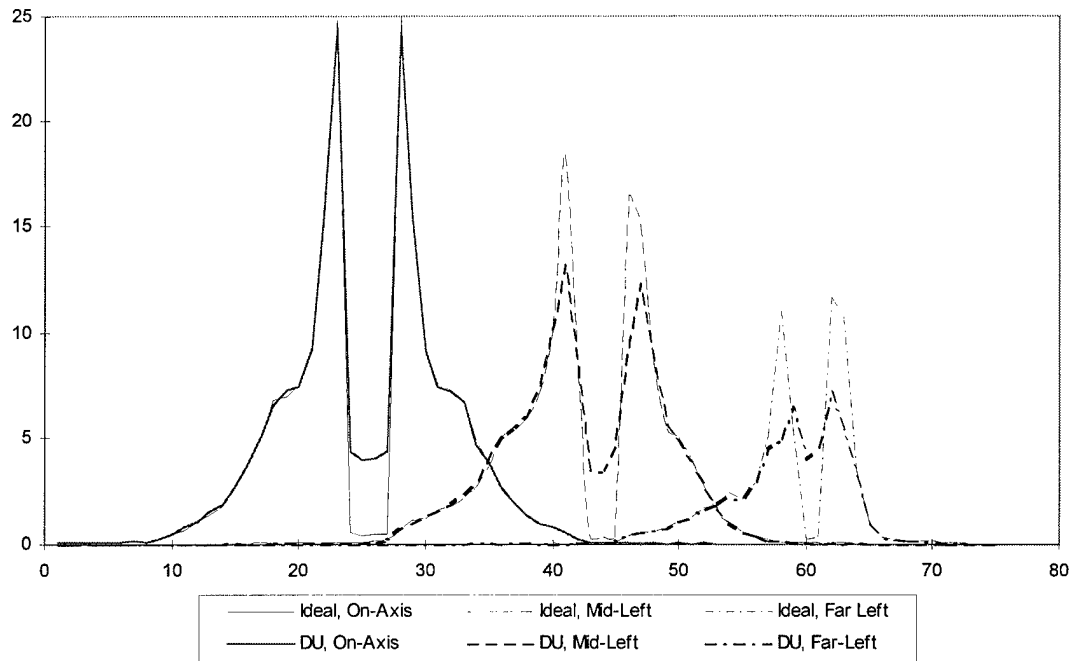


Figure 6.13. Comparative Point Source Profiles of Aperture Blocked with DU Bar and a Perfect Attenuator.

The combined effects of block penetration and penumbra are better observed in figure 6.14 which shows the net difference between the DU blocked and perfectly blocked aperture. The net responses are presented for the on-axis source, followed by source positions to the far left of the field of view. Values greater than zero are attributed to penetration through the aperture block, causing an overestimation in the measured penetration data. Negative values correspond to penumbral effects between the aperture edge and aperture block and result in an underestimation of the measured penetration.

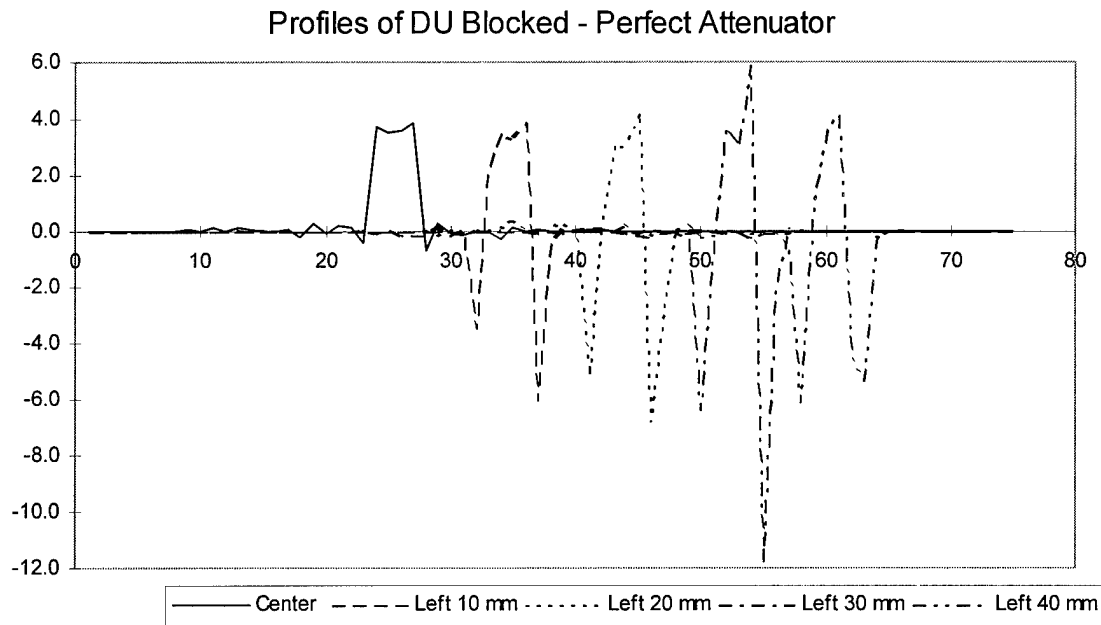


Figure 6.14. Simulated Assessment of Penumbral Effects and Aperture Block Penetration.

The empirically derived Blackman window is explained by examining the ratio of integrals of the DU blocked slit data and the perfectly blocked slit data. By plotting these normalized ratios as a function of projection centroid, the points in figure 6.15 result. For the on-axis case, the ratio is approximately 1.1, in good agreement with the expected 10% transmission through the block. As source position is moved to the far left of the field of view, the ratio approaches 0.91, indicating the joint effects of penumbra and penetration result in off-axis positions being underestimated by 9%. The Monte Carlo data were fit to a three-parameter Blackman-Gaussian function which provided a 99.7% R^2 correlation with the data. This expression is presented below and as the dashed line in the figure.

$$\text{Monte Carlo Weight}(i) = 1 - \left(\frac{k_1}{\sqrt{2\pi k_2^2}} \exp\left(-\frac{(i - N/2)^2}{2 * k_2^2}\right) + k_3 \cdot \left(0.42 - 0.5 \cdot \cos\left(\frac{2\pi(i-1)}{(N-1)}\right) + 0.08 \cdot \cos\left(\frac{4\pi(i-1)}{(N-1)}\right) \right) \right)$$

Where N are the number of projection elements, and $k_1=0.533$, $k_2= 4.54$, and $k_3=0.139$.

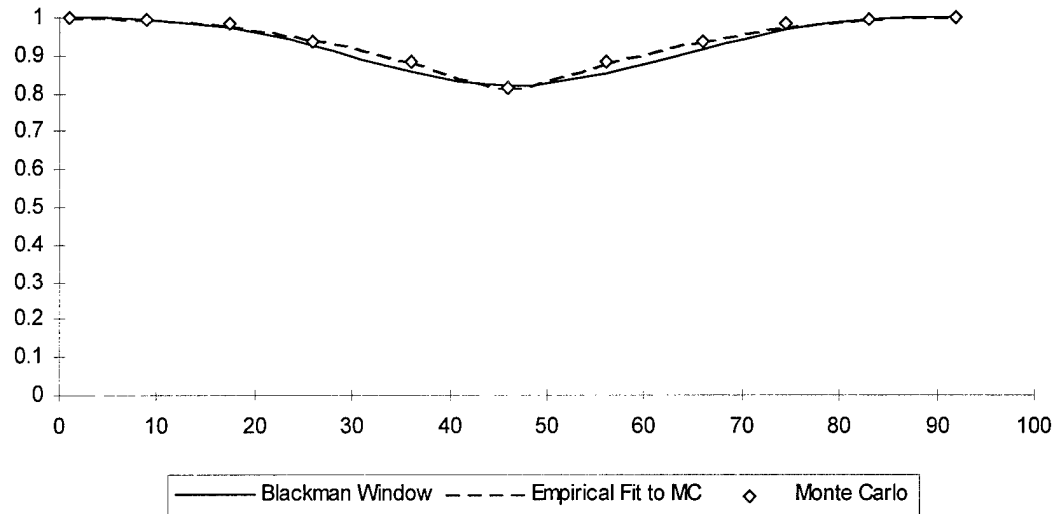


Figure 6.15. Comparison of Monte Carlo Based Weight to Empirically Derived Blackman Window

Comparing the Monte Carlo results with the plotted Blackman window demonstrates a maximum difference of 3.5%. The simulation based function was refined by convolving a Gaussian detector response (2 pixel σ) to account for the detector blurring introduced into the simulation results. This had the effect of further improving the agreement between the Blackman to approximately 2.5%. A profile of the uniform object reconstructed with the Monte Carlo based response is shown in figure 6.8D. It is noted there is only slight difference between the Blackman and simulation based corrections. Notably, the simulation based correction is slightly higher peaked centrally than the Blackman reconstruction, in agreement with the form of the correction. Differences between the two weighting schemes are partially attributed to the limited accuracy in reproducing the SPRINT imaging geometry in the simulations, particularly magnification effects and blurring introduced by interactions within the scintillator.

An Iterative Technique for Improving the Proposed Aperture Penetration Correction Method

The first order correction applied to the penetration data provides acceptable qualitative improvements in image quality, but does not actually correct for the non-ideal behavior of the block. If the blocked projection data was biased only from penetration through the block (i.e. no penumbral effects), further improvements in image quality could be achieved through a semi-iterative correction technique. The proposed system model for such a solution is:

$$\begin{aligned} Y_P &\sim \text{Poisson}\{P_e(A_{Tc}\lambda + b)\} & (a) \\ Y_B &\sim \text{Poisson}\{P_e(\alpha A_{DU}\lambda + b)\} & (b) \end{aligned} \quad (6.8)$$

Where Y_P is the measured projection data with the open aperture, A_{Tc} are system weights derived for the geometric slit opening, and b is the background component composed of aperture penetration, scatter and environmental background. The blocked slit projection data, Y_B , is modeled as the sum of aperture penetration plus penetration through the block taken as $\alpha A_{DU}\lambda$, where A_{DU} are system weights generated from Monte Carlo simulations of the block penetration, and α is a scale factor.

The penetration background projection b can be estimated from the following expression, which uses the spatially weighted blocked projection data to provide a first estimate of the object, $\hat{\lambda}_{FBP}$.

$$\hat{b} = P_e^{-1}[Y_B] - \alpha A_{DU} \hat{\lambda}_{(FBP-SAGE)} \quad (6.9)$$

This estimate of b can then be used in equation 6.8(a) to solve for the object distribution using a discrete estimation algorithm such as SAGE. Iteration between equations 6.8(a) and 6.9 provide improved estimates of the object distribution, $\hat{\lambda}$.

The potential for implementing this method was investigated through a series of Monte Carlo simulations of the SPRINT aperture blocked by a cylindrical DU bar. Projection data were obtained for the five point source locations used in the previous

simulations. Figure 6.16 shows the comparison between the cylinder blocked aperture and the perfectly blocked aperture. A comparison of these data with the profiles in figure 6.13 shows that the cylinder is clearly a less effective attenuator, allowing more primary photons to be transmitted.

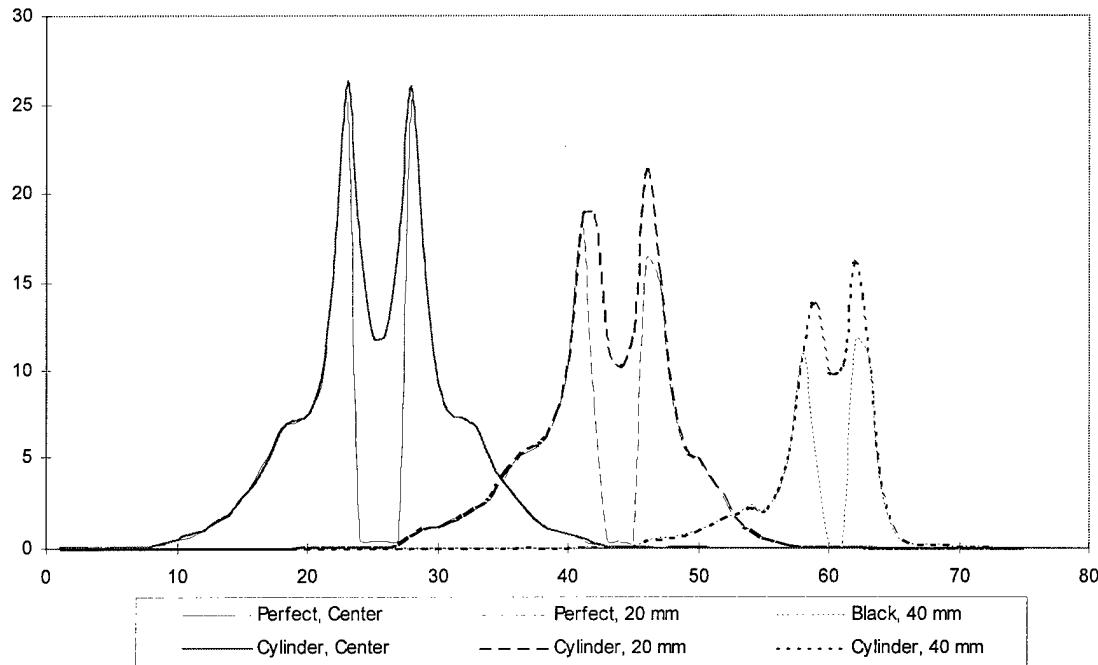


Figure 6.16. Comparative Point Source Profiles of Aperture Blocked with Cylindrical DU Bar and a Perfect Attenuator. The cylinder is a less effective attenuator than the rectangular DU bar (ref fig 6.13).

The advantage of using a cylindrical block becomes apparent when the net penetration through the cylinder is determined from the perfectly blocked aperture. This is shown in figure 6.17 as the heavy lined profiles for each of the five source locations. If these profiles are compared to those shown in figure 6.14, it is noted that the underestimation of the penetration data is eliminated. The resulting overestimation of the penetration data has a form which can be readily incorporated into a sparse systems weights matrix, A_{DU} . As an example, point sources at the same positions used in the simulations were forward projected using a SPRINT weights matrix generated with a 3 mm slit. The resulting projections were normalized and overlaid onto the net cylindrical

penetration profiles, shown as the lighter profiles in figure 6.17. The good agreement between the two sets of data suggests that even the use of a geometric weights matrix, A_{Tc} , may provide good reconstructions using this iterative block penetration technique. Optimizing weights matrix generation to match the Monte Carlo based results should provide very good reconstructions with improved resolution and sensitivity over the demonstrated technique.

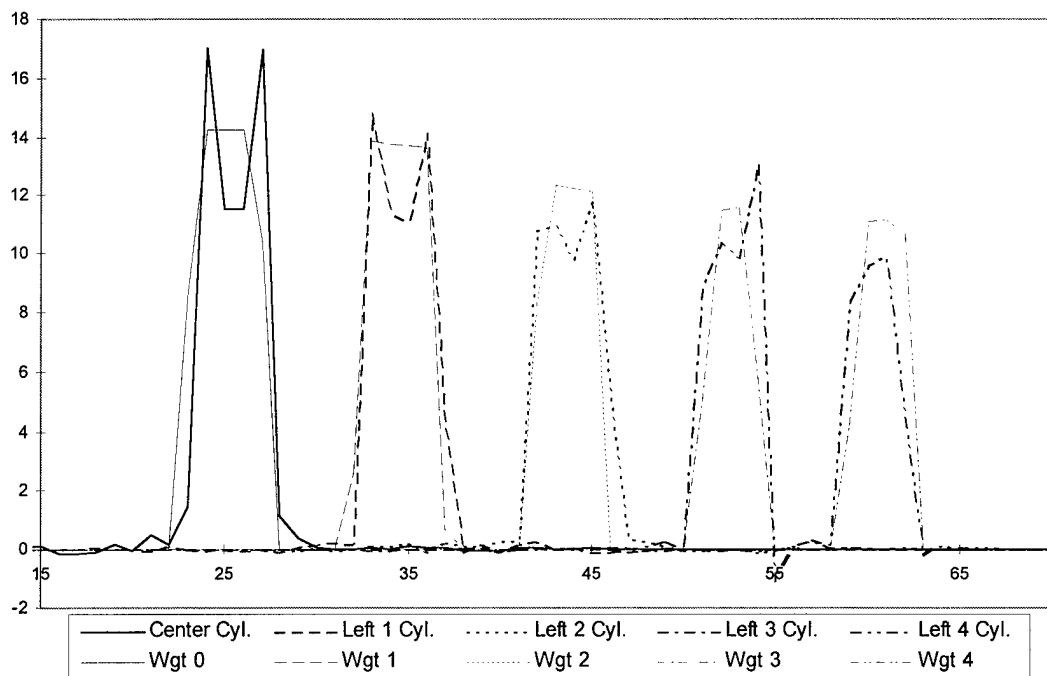


Figure 6.17. Comparison of the Net Penetration Through a DU Cylinder Compared to Forward Projected Point Sources Using SPRINT System Weights. Note that there is no penumbra with the net responses, and relatively good agreement with geometric weights.

Summary

Clear improvement in SPECT imaging of high energy gamma-rays can be obtained through the proposed penetration correction method. The method allows recovery of resolution to within one mm of the system geometric resolution, and significantly improves contrast by removing the long penetration tails of the system point response function. Implementation of this method, combined with use of a high energy

slice collimator, allows SPRINT to achieve an axial and in-plane resolution of approximately 5 mm for 511 keV photons. This should allow good accuracy in quantifying organ radioactivity concentrations for large rat organs such as the heart, brain and liver,

There are two important disadvantages imposed by this proposed correction method however. First, the protocol requires measuring two complete data sets to arrive at an estimate of the true signal. System sensitivity is thus effectively halved. Second, the variance in the estimated signal is twice the variance of the penetration background since this background is measured twice (reference Eqn. 6.4). If the penetration background were modeled and included in the reconstruction process, there would be a substantial increase in sensitivity and decrease in signal variance. Unfortunately, this is also a complicated approach. The full system matrix produced poses large memory requirements and dramatically slows the reconstruction process. Moreover, the limited accuracy of modeled penetration will introduce bias in the reconstructed image.

Further improvements in the “blocked” aperture technique are predicted using iterative reconstruction methods that accurately model the imperfect attenuation of the depleted uranium block. Such methods should provide an improvement in both sensitivity and resolution.

Although the effects are not as dramatic, pin-hole imaging of ^{131}I labeled radiotracers is also significantly degraded by aperture penetration. Application of this method is expected be even more effective for iodine imaging due to better attenuation characteristics of the block for 364 keV photons, and the capacity to correct for high energy iodine emissions. The devised method should be germane to both planar and SPECT imaging and be well suited to clinical application on two-head and four-head commercial gamma cameras.

References to Chapter VI

¹ Siemens Medical Systems, Product Data Sheet, Ultra-high energy collimators for 511 keV photon imaging, 1995.

² Axelsson B, Msaki P, Israelsson A. Subtraction of Compton scattered photons in single-photon emission computerized tomography. *J Nucl Med* 1984;25:490-494.

³ Bergstrom M, Eriksson, Bohm C, Blomqvist G, Litton J. Correction for scattered radiation in a ring detector positron camera by integral transformation of the projections. *J Comput Assist Tomog* 1983;7(1):42-50.

⁴ National Nuclear Data Center, Brookhaven National Laboratory, Upton NY 11973.

⁵ Fessler JA, Hero AO. Space-alternating generalized expectation-maximization algorithm. *IEEE Transactions on Signal Processing* 1994;42(10):2664-2677.

⁶ Wilderman SJ, Vectorized algorithms for Monte Carlo simulation of kilovolt electron and photon transport. University of Michigan, School of Engineering, Department of Nuclear Engineering, *Dissertation Thesis*, 1990.

CHAPTER VII

QUANTITATIVE HIGH ENERGY SPECT IMAGING USING SPRINT

This chapter will address the calibration methods adopted for high energy imaging and factors examined to perform accurate image quantification using SPRINT. Methods and results are presented for qualitative and quantitative imaging of two-dimensional and three-dimensional phantoms and live rats. Finally, a comparison is made between SPECT images acquired using SPRINT, and those acquired under similar conditions using positron emission tomography.

SPRINT Calibration and Factors Addressed for Image Quantification

System Set-Up and Calibration

SPRINT was originally designed for low to medium energy imaging up to 364 keV. Calibration of SPRINT for high energy imaging required adjusting system gain so that the photopeak from 511 keV photons was at an energy (voltage) approximately equal to 140 keV photons. This was required because of the limited dynamic range of the position calculation circuits. To accomplish this, the photomultiplier tube high voltage was lowered to reduce the tube gain of all detector modules. Module specific energy gain factors and lower level discriminators were then adjusted to fine tune photopeak and spectrum agreement between energies. This relatively simple set of adjustments greatly simplified the overall calibration process and permitted use of existing system calibration software. For 511 keV imaging, a phototube voltage of 855 volts gave an output pulse height equal to the 140 keV photopeak acquired with a phototube voltage of 1000 volts.

Calibration of SPRINT after these adjustments followed procedures identical to low-energy imaging. This included adjusting each phototube gain within a module to a module specific target gain, generating energy correction maps for a module¹, and establishing energy windows that trigger event detection and position estimation. A detailed description of calibration procedures is available elsewhere¹. Energy spectra observed for 511 keV photons were found to have photopeak centroids in good agreement with ^{99m}Tc, and energy resolution of 13% FWHM compared to 12% for 140 keV photons.

Event Position Estimation and Edge Effects at High Energy

Gantry modules use maximum likelihood position estimation to establish the XY position coordinates of photons interacting within the scintillator. Weights used for position estimation are derived using a highly collimated source of 140 keV photons that is translated parallel to the module surface. Photomultiplier tube responses are recorded for each source position, forming a matrix of response versus position. Maximum likelihood position weights are computed as a function of this response. These weights are used for all photon energies imaged by SPRINT. Application of low-energy position weights to high energy imaging is expected to introduce errors in position estimation due to the differences in energy deposition within the scintillator.

To determine the extent of position estimation error and assess the detector response for high energies, Monte Carlo simulations were used to compute the spatial energy distribution and centroid position as a function of incident photon energy, scintillator thickness, and scintillator block dimensions². Table 7.1 summarizes the salient results of these simulations for a highly collimated beam of photons incident on a 5 cm block of NaI(Tl). Figure 7.1 shows the vertical energy deposition for events which

¹ Energy correction maps are generated for each module to correct for small gain differences among phototubes, and differences in light collection at different locations within the detector.

result in a total energy deposition greater than 460 keV (10% energy window) for 12.7 mm and 25.4 mm thick crystals. We observe from the figure that energy deposition for 364 and 511 keV photons is roughly uniform throughout the crystal. The vertical centroid is in fact greater than half the scintillator thickness for both energies. Since photons can be incident on the detector modules at angles up to 22 degrees, a uniform energy deposition in the detector can introduce a maximum 3 mm blur parallel to the detector plane.

Table 7.1. Simulation Results of Highly Collimated Photons Incident on a 5x5 cm NaI Slab Sampled at 0.5 mm Intervals with a Lower Energy Window of 460 keV.

Incident Energy (keV)	Slab Thickness (mm)	Total Fraction of Energy Deposited	Fraction On-Axis of Ray	Fraction Off-Axis of Ray	Vertical Centroid (mm)	Horizontal Centroid (mm)	Error * \pm (mm)
141	12.7	0.93	0.85	0.15	3.71	0.31	± 0.0029
364	12.7	0.28	0.53	0.47	6.06	1.75	± 0.0213
511	12.7	0.17	0.42	0.58	6.27	2.29	± 0.0292
141	25.4	0.98	0.84	0.16	4.34	0.35	± 0.0035
364	25.4	0.51	0.46	0.54	11.26	2.50	± 0.0188
511	25.4	0.35	0.33	0.67	11.81	3.08	± 0.0296

* The standard deviation of the average radial centroid position.

Additional blur results from scatter reactions that displace the centroid of incident photons radially from the line of incidence. Table 7.1 indicates that for 511 keV photons, approximately 60% of the energy is deposited in pixels off-axis of the incident beam, as compared to 15% at 140 keV. Simulation data indicates that the energy is deposited in an exponential profile around the central pixel (figure 7.2). The detector response observed in this figure has an approximate resolution of 3.5 mm off-axis for the 12.7 mm scintillator and 4.3 mm FWHM for the 25.4 mm scintillator. These tails cause additional

resolution loss as compared to 140 keV photons, which have much smaller centroids and resolution.

Errors introduced in position estimation at high energy are indicated by figure 7.3 which shows a comparison of SPRINT flood image profiles acquired using ^{99m}Tc and ^{18}F with a 20% energy window ($\pm 10\%$). The normalized fluorine data demonstrates a jagged pattern across a given module caused by an enhanced response at locations between tube locations. Position estimation is worst at the module edges where the light response function is distorted. Figure 7.3 shows a depressed response for 511 keV photons at the edge of most modules. This is better observed in figure 7.4 which shows the contrast enhanced difference image between a ^{99m}Tc flood and a normalized ^{18}F flood. White areas in the image represent areas of diminished response for 511 keV photons. The left side of module ten demonstrates a region of gross signal deficit thought to be partly due to decoupling of the photomultiplier tubes from the scintillator.

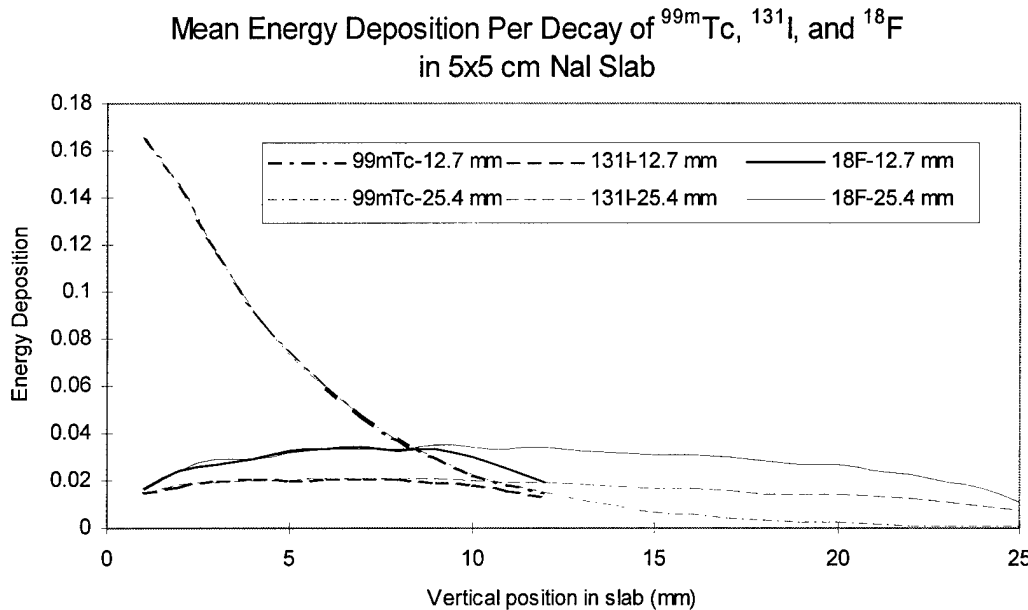


Figure 7.1. Vertical Energy Deposition as a Function of Incident Energy.

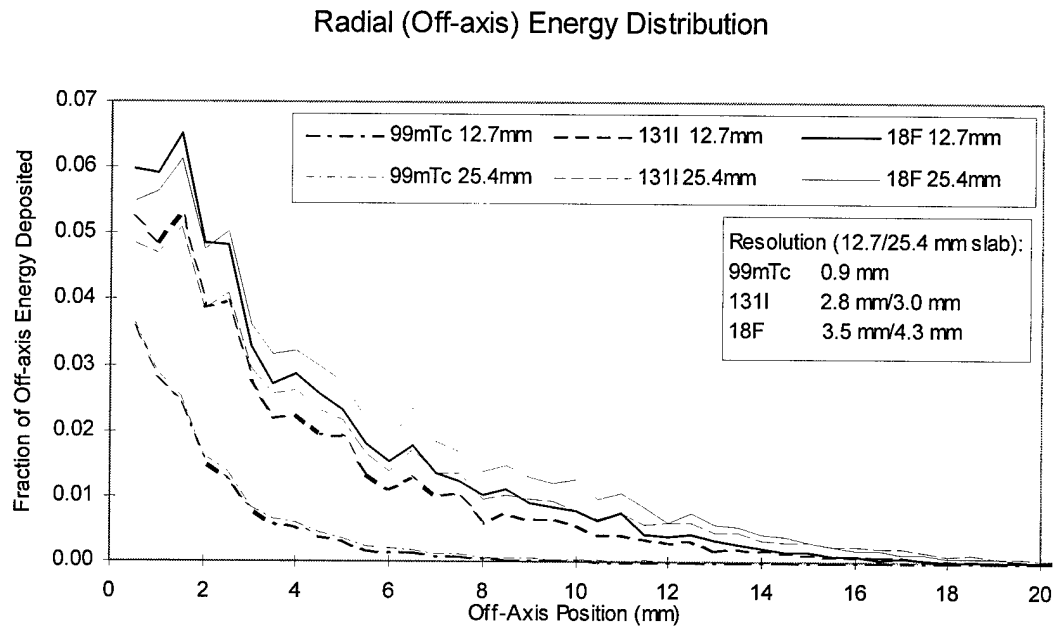


Figure 7.2. Horizontal Fractional Energy Deposition as a Function of Incident Energy. Approximate Resolution of Response is Presented, Relative to a Maximum Fraction of Off-Axis Energy Deposited of 0.06.

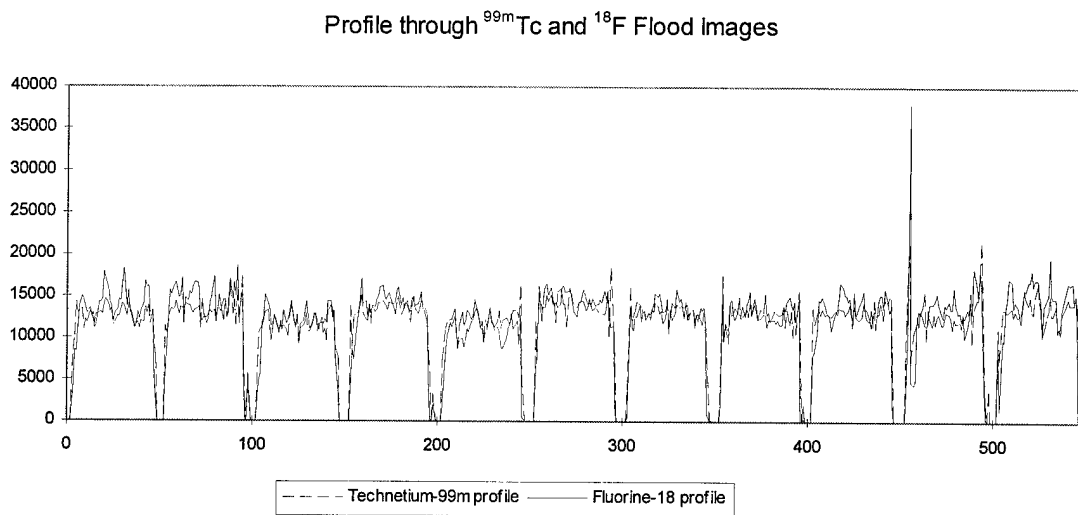


Figure 7.3. Comparison of ^{99m}Tc and ^{18}F Flood Profiles. Note the Regular Pattern in the 511 keV Profile and the More Severe Variation at the Module Edges Prior to Diminishing to Zero.

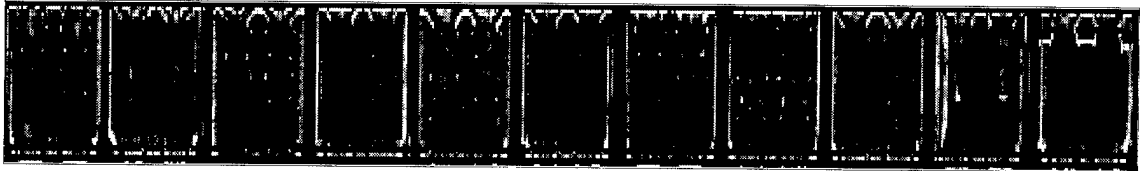


Figure 7.4. Difference Flood Image for ^{99m}Tc and ^{18}F . Bright Bands at Module Edges Indicate Low Count Areas For ^{18}F

There are limited options available to overcome the blurring and distortion effects of high energy imaging. Ideally, detector position weights would be generated and applied for each imaged energy. However, position weight generation is time consuming, requires a highly collimated source and is performed for each module in a calibration set-up prior to installation in SPRINT. The difficulty in creating a highly collimated point source of annihilation radiation, limited flexibility in existing SPRINT software, and the complexity of the calibration process mitigates against a separate determination of position weights. Instead ^{99m}Tc derived weights are applied, with some degradation in image quality. Edge affects on the other hand were found to have a severe effect on image quality since back-projection of erroneous low count data greatly increases structural noise. To minimize this effect, projection data was modified to exclude low count detector bars. While ^{99m}Tc imaging makes use of all 488 available bars, ^{18}F imaging uses only 459 bars, reducing the geometric sensitivity by 6%. To partially compensate for the uniform energy deposition through the scintillator depth, the system weights matrix used in SAGE reconstruction incorporates a 6 mm mean interaction depth.

Decay and Deadtime Correction

Positron emitters have a relatively short physical half-life, on the order of 2 minutes for ^{15}O to 110 minutes for ^{18}F . Further, the high photon energy of annihilation radiation results in poor photopeak sensitivity for conventional SPECT systems. These factors, together with the relatively low sensitivity of collimated systems, dictate that large amounts of activity be used with long imaging times to obtain images of acceptable

signal to noise. The use of long count times for SPRINT requires application of decay correction to the projection data, since significant decay of the radiotracer can occur during imaging. The use of high activities introduces the requirement for deadtime correction, since large activities result in large module count rates.

The effect of deadtime in SPRINT is observed in figure 7.5, which presents the number of X-Y position board starts as a function of ^{99m}Tc source activity. The count rate reflects scintillator events above the lower level discriminator that triggers position estimation. The graph indicates module three has a significantly worse deadtime than other modules, and module six has a somewhat smaller deadtime than other modules.

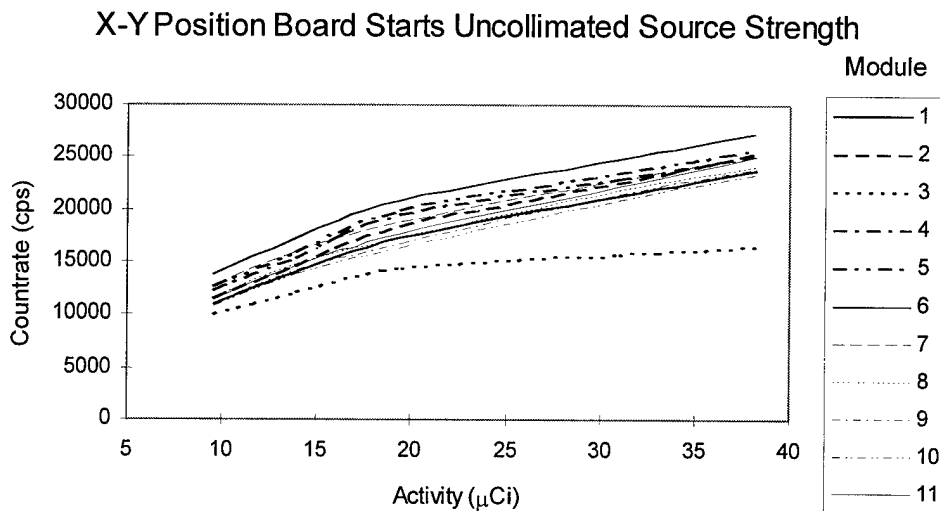


Figure 7.5. Observed Module Count Rate as a Function of Source Activity.

Deadtime in the modules is principally nonparalyzable and assessed using the two-source method as discussed by Knoll³. Two sources of approximately equal strength were measured for equal times in the uncollimated SPRINT gantry. Sources were measured together and separately, and a background measurement was acquired. Acquired images were analyzed for total counts occurring in each module, and then divided by the acquisition time to provide a count rate. Deadtime was then calculated from the rate data.

Deadtimes are presented in Table 7.2, calculated from X-Y position starts and total image counts. The difference between image based deadtime and start pulse based deadtime is unexplained and being investigated. Deadtime correction is incorporated into the projection shuffling algorithm by scaling the projection data by:

$$\text{Dead Time Correction Factor} = \frac{1}{1+n\tau}$$

where n is the total measured count rate in the image, including additional window images if acquired, and τ is the module deadtime. For extended sources such as the micro-Jaszczak phantom where 40 mCi of activity were imaged, deadtime corrections were found to be as high as a factor of 1.9. Low activity line sources had deadtime corrections equivalent to one. The effect of deadtime correction on an image is demonstrated in figure 7.6 showing a uniform cylinder phantom reconstructed without and with deadtime correction. The associated profiles, though noisy, demonstrate a much more uniform image with correction.

Table 7.2. Deadtimes for SPRINT Modules.

Modul e	Deadtime (s)		
	X-Y Start	Image (^{99m}Tc)	Image (^{18}F)
1	2.42E-05	4.07E-05	6.02E-05
2	2.41E-05	4.05E-05	5.45E-05
3	4.34E-05	7.67E-05	0.000104
4	2.42E-05	4.26E-05	6.58E-05
5	2.45E-05	4.43E-05	7.95E-05
6	2.42E-05	4.16E-05	6.92E-05
7	2.34E-05	4.41E-05	7.81E-05
8	2.33E-05	4.78E-05	7.6E-05
9	2.38E-05	4.25E-05	6.57E-05
10	2.35E-05	4.63E-05	6.11E-05
11	2.37E-05	4.47E-05	5.93E-05

The significance of decay correction is clearly dependent on the half-life of the nuclide and the count time. For 80 step acquisitions performed over a 55 minute period

(40 seconds per step), there is a 1.4 correction factor for the last projection compared to the first for ^{18}F , and a 6.7 correction factor for ^{11}C . Since one hour long acquisition times are typically employed with SPRINT, such large corrections make imaging of carbon-11 radiotracers prohibitive. Decay correction is applied during the projection shuffling operation described in Chapter VI, directly after deadtime correction. A given projection is corrected to the start of the acquisition using the elapsed time between the start of the tomographic acquisition and the time of the projection measurement. The effect of decay during a given projection measurement is trivial for ^{18}F and longer lived radionuclides.

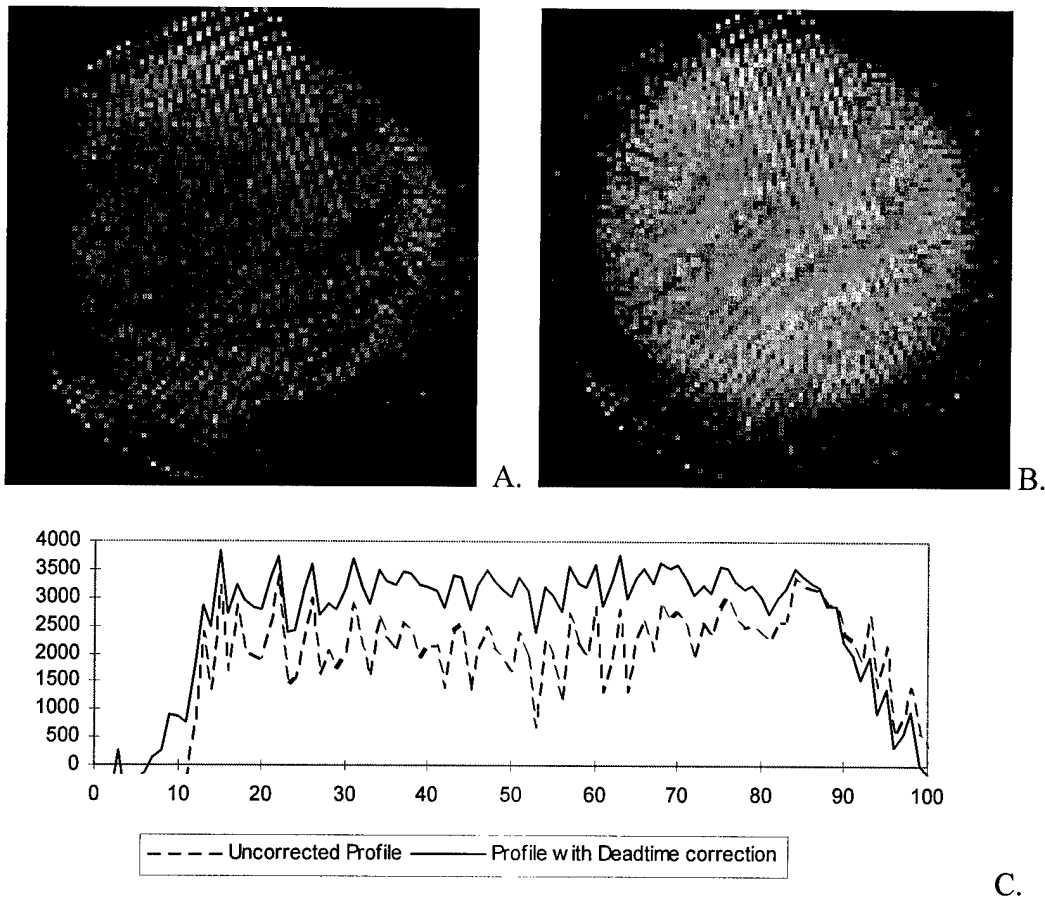
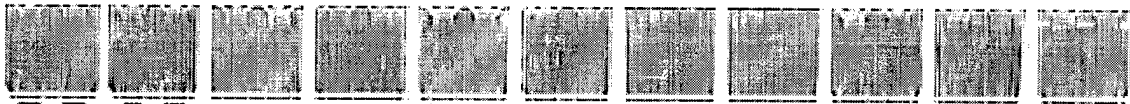


Figure 7.6. Comparison Of Uniform Cylinder Imaged Without (A) and With (B) Deadtime Correction. Profile Through Center of Object (C) Shows Reduced Noise and More Uniform Appearance.

Flood Correction

To correct for non-uniformity in the slice collimator and the non-uniform response of the actual SPRINT detector modules, extrinsic flood correction maps are generated. The maps provide pixel-by-pixel relative sensitivity correction factors for each module, as well as normalization for the variation in sensitivity between modules. They are determined from long acquisitions of a uniform line source with the slice collimator installed in the SPRINT gantry. Because of the slice collimator, this required use of a moderate to high activity line source of 500 μ Ci (18.5 MBq) for 99m Tc and 700 μ Ci (30 MBq) for 18 F imaged for 50 minutes. Resulting flood images for each of the eleven modules are shown in figure 7.7.



A. 99m Tc Flood Image acquired with Low-Energy Collimator



B. 18 F Flood Image Acquired with High Energy Collimator

Figure 7.7. Extrinsic Flood Images of 99m Tc and 18 F. Images are Generally Similar In Appearance.

The flood images demonstrate good uniformity for both nuclides. Characteristic artifacts corrected by the maps include the visible tube pattern in several of the modules as well more subtle azimuthal bands. In the 18 F flood, point defects can be observed at inter-tube locations associated with point errors in the module energy correction maps. Gross defects in modules 10 and 11 can also be observed. Module 10 is thought to have a defect in the scintillator or has experienced decoupling of the phototube from the light

pipe. Module 11 has an electronic defect in the X-position electronics. These artifacts are partially handled for ^{99m}Tc , but are too severe for correction with ^{18}F .

The long flood images are converted to flood correction maps by determining the module deadtime correction factor and then averaging the central 400 pixels of each detector. Average values are divided by all deadtime corrected pixels to derive a correction factor up to a user specified maximum value. Generated maps are then applied to the raw projection data during reconstruction.

Attenuation and Scatter Correction

Attenuation correction and scatter correction must be considered for accurate quantification of organ concentrations⁴. For SPRINT imaging 511 keV photons, the significance of attenuation and scatter within an extended object is shown in Table 7.3. For animal bodies and phantoms, the maximum diameter object imaged is limited by the field-of-view to be ~ 8 cm. For photons emitted at the center of a tissue equivalent cylinder of this diameter, there is an interaction probability of 25% to 32% based on a total attenuation cross-section. Since attenuation and scatter directly affect the measured line integral through the object, a correction for each is desirable in the reconstruction algorithm to provide images that accurately reflect activity concentration.

Attenuation correction is conventionally performed in filtered backprojection using a first order or second order Chang correction⁵. An attenuation coefficient for this method is derived from a theoretical value for the attenuating medium and the energy of the gamma ray. If scatter correction is first applied, the total attenuation coefficient of 0.095 cm^{-1} for 511 keV photons in water is used⁶. Effectively, a first order Chang correction method derives a pixel by pixel correction factor for attenuation at point (x_o, y_o) equal to:

$$c(x_0, y_0) = \frac{1}{\frac{1}{M} \sum_{i=1}^M \exp(-\mu l_{\theta_i})}$$

where M is the total number of projections taken in a 360° scan measurement and l_{θ_i} is the distance along the ray between point (x_0, y_0) and the boundary point of the object at projection angle θ_i . Alternatively, iterative reconstruction allows direct integration of object attenuation into the system weights matrix. In this case, element-by-element multiplication is performed using a two-dimensional attenuation map of the object (which can be other than uniform) and the system weights matrix⁷.

Table 7.3. Effective Transmission and Interaction Probabilities for Annihilation Radiation in Various Tissue Thickness.⁸

Thickness (cm)	Non-interacting Transmission	Interacting Probability	Scatter/Primary Ratio (SF) ⁱ
1	91%	9%	0.6%
2	82%	17%	1.4%
3	75%	25%	2.1%
4	68%	32%	3.2%
5	62%	38%	3.9%
6	56%	44%	4.4%
7	51%	49%	4.9%
8	46%	54%	5.6%

ⁱThe ratio of 511 photons emerging from the phantom which have been scattered to those which escape without interaction.

Scatter is by comparison a more complicated process to correct. Originally, we had planned to use the dual energy window method, originally proposed by Jaszczak^{9 10}. In essence, the scatter corrected projection data is given by:

$$P_{corr} = P_{pp} - kP_{scat}$$

where P_{corr} is the corrected projection, P_{pp} is the photopeak measured projection and P_{scat} is a projection measured from a lower energy window in the Compton scatter region of

the spectrum. The factor k is empirically derived using the method described by Koral et al.¹¹, where k is assumed to be independent of position in the object. Unfortunately this method could not be adapted to high energy imaging. Spectra acquired of an ^{18}F line source in air and within a 7.3 cm phantom filled with water are shown in figure 7.8. There is a observed a very high Compton background both with and without the presence of a scattering medium. By comparison, the baseline scatter level is 83% of that when the phantom is used. Much of this high Compton background is attributed to Compton interactions within the scintillator followed by an escape of the scattered photon. Approximately 83% of the interactions in the scintillator with 511 keV photons are from incoherent and coherent scatterⁱⁱ. Scatter is also contributed from interactions with the slice collimator and slit aperture.

Comparison of Energy Spectra for Line Sources in Air and in Center of Water Filled Phantom

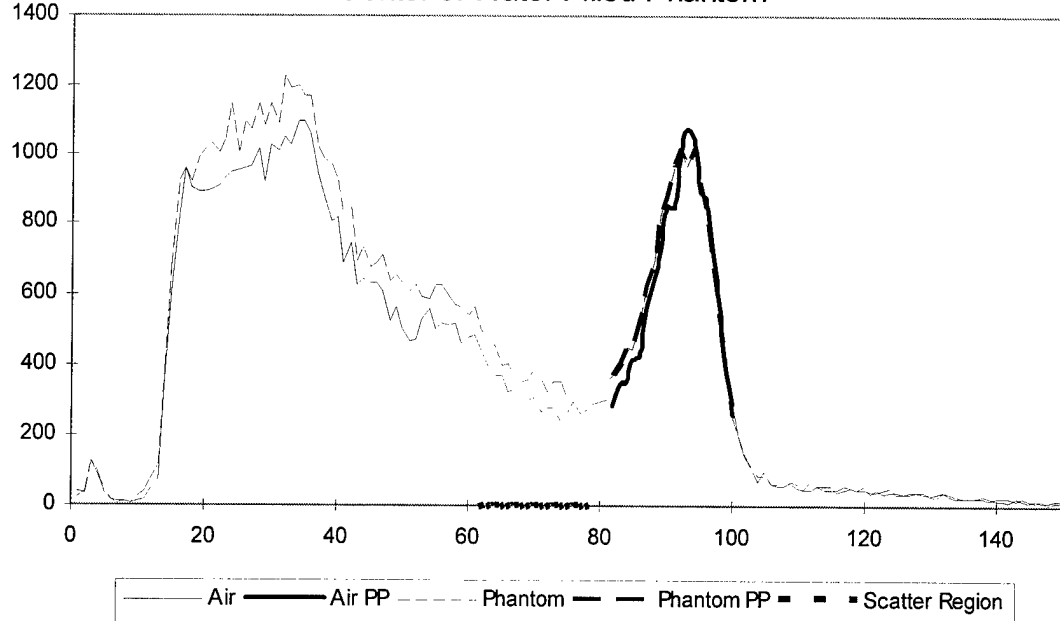


Figure 7.8. Comparison of Energy Spectra from Normalized Line Sources in Air and in Water Filled Phantom. Note Comparable Spectra and High Compton Regions for Both Cases.

ⁱⁱ Based on NNDC cross-section values for NaI(Tl) and a 12.5 mm scintillator thickness.

Consequently, use of a secondary energy window does not accurately reflect Compton interactions within the object. As an alternative, a first-order attenuation correction was investigated to correct for both attenuation and scatter using an effective attenuation coefficient that is less than the theoretical value ^{12 13}. A value of 0.06 cm^{-1} was empirically derived from projection data of a line source in the center of a water filled phantom. When this value was applied to FBP reconstructions of the line source in the phantom, total counts from the line image were found to agree well with that for an uncorrected line source in air. Comparative profiles of the two reconstructed images are shown in figure 7.9. Regions of interest constructed around the lines indicate that the line in air was detected with an average sensitivity of $110 \pm 2.5 \text{ cpm}/\mu\text{Ci}$, whereas the attenuation corrected line source within the phantom was detected with a sensitivity of $108 \pm 2.39 \text{ cpm}/\mu\text{Ci}$.

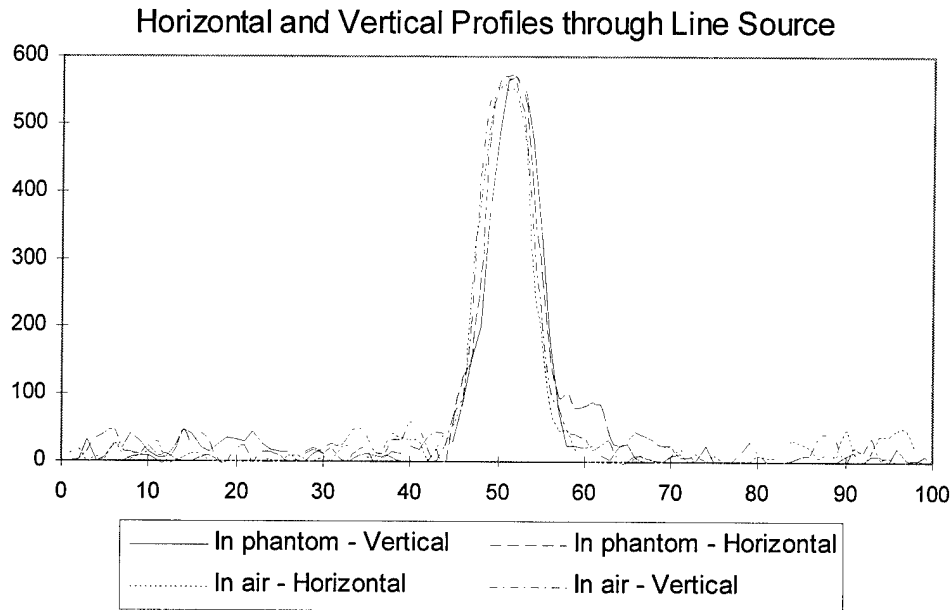


Figure 7.9. Line Source Profiles, in Air and Attenuation Corrected Within Phantom. Profiles Have Been Normalized by Only Decay Correction.

The use of an effective attenuation coefficient does not truly correct for scatter. To determine the errors in quantification which could be expected from scattered radiation, Monte Carlo simulations were performed. The geometry assessed was a cylindrical tissue equivalent phantom filled with uniformly distributed activity. Results using the SIMIND code¹⁴ are presented in Table 7.3. Note that approximately 5% of photons emanating from a 7 to 8 cm cylinder have undergone a scattering reaction. Since laboratory rats imaged with SPRINT have a diameter usually smaller than 8 cm, it is reasonable to expect that scatter will introduce small errors in image quantification.

Correction for Background Radiation

Background radiation adds counts to acquired projection data and can affect contrast in the reconstructed image if background count rates within the photopeak window are significant. Background in SPRINT stems from environmental background and that from the depleted uranium bars mounted in the slit aperture. Flood images acquired without any external sources in the gantry indicated that background introduces a uniform exposure of the modules with no significant spatial pattern observed. Figure 7.10 shows the measured energy spectra from environmental background with and without the aperture present. During SPECT imaging, typical activities used generate photopeak count rates ranging from several hundred to well over ten thousand counts per second. It is apparent from the background count rates shown in the figure that background radiation is typically less than 1% of the measured projection data, and is consequently ignored.

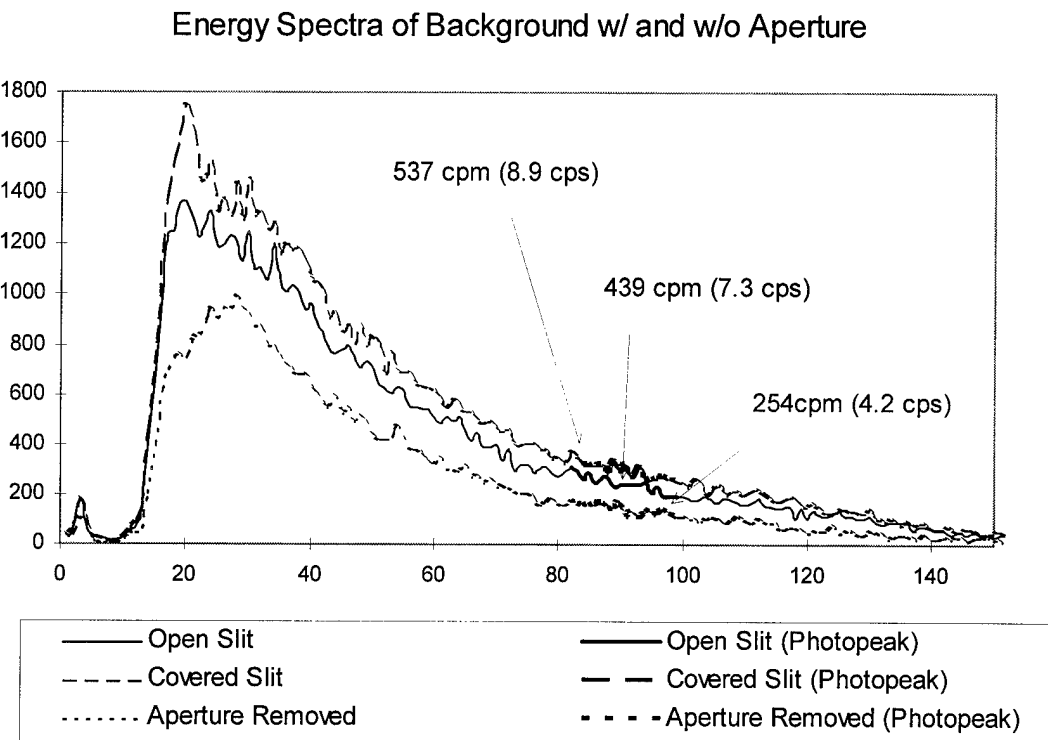


Figure 7.10. Energy Spectra of Background Radiation.

Summary

Raw projection data are manipulated through the application of numerous corrections to enhance both image quality and quantitative accuracy. These factors are summarized in Table 7.4. The most substantial correction was that devised for aperture penetration from high energy gamma rays. This was found to have a dramatic impact on both image contrast and resolution. Other significant corrections included the exclusion of low-count module bars, deadtime correction and decay correction. These corrections improved the noise characteristics of the reconstructed image as well as accuracy. Similarly, flood and energy correction maps serve to provide modest improvements in image quality and uniformity. Attempts to correct for the biasing effects of scatter, attenuation and background were also examined. Because of the difficulties encountered

in applying a dual window scatter correction technique, a simple Chang attenuation correction was applied using an effective attenuation coefficient for FBP reconstructed images. This effective attenuation coefficient was also integrated into the system weights matrix (assuming a uniform object) for SAGE iterative reconstructions. Since scatter effects were predicted to be small, this correction was thought adequate for the purposes of this study.

Table 7.4: Corrections Applied to SPRINT Projection Data and Incorporated into Image Reconstruction.

Correction Factor	Primary Issue and General Effect and Limitations
Aperture Penetration	Corrects for high energy photons penetrating the aperture. Results in improved resolution and contrast.
Module Edge Exclusion	Removes low count detector data to improve image contrast and remove structured noise.
Deadtime	Corrects for loss of counts due to finite pulse processing time. Particularly important at high count rates. Improves image uniformity and quantitative accuracy.
Decay	Corrects for loss of counts as radionuclide decays during imaging. Improves quantification accuracy.
Energy Mapping	Corrects for small gain differences among phototubes, and differences in light collection at different locations within the detector. Improves system uniformity and energy resolution
Flood Mapping	Corrects for pixel to pixel and module to module variation in detector and electronic sensitivity. Improves system uniformity.
Attenuation/Scatter	Corrects for attenuation and scatter of primary photons emitted within the object. Uses an effective attenuation coefficient for uniform object. The method is simple and not does not really "correct" for scatter. Improves quantification accuracy.

Quantitative Imaging of 2-D and 3-D Phantoms

SPRINT quantitative performance was assessed initially using a two-dimensional and a three-dimensional phantom. This provided known object activities that could be directly compared to results obtained by region-of-interest analysis of the reconstructed SPECT images.

The two-dimensional phantom and three-dimensional phantom used are shown in figures 7.11 and 7.12, respectively. The phantom body consists of a 6.8 cm inner diameter, 5.7 long cylindrical vessel (left) with a screw-on o-ring sealed lid (right). The empty phantom has a volume of 236 ml. On the surface of the phantom holder are two sets of ten cylindrical holes each with a 10 μ l volume. One set of holes forms a straight line along the phantom body at 6 mm intervals. The second series follows a helical pattern around the body, with hole positions in the same axial plane as the straight line set. Holes were filled with a Gd-DTPA solution during MR imaging, and an ^{18}F solution during SPECT imaging to serve as fiducial markers for image comparison. The base and lid of the phantom holder are fitted with injection ports to allow for controlled introduction of radioactive material and complete filling of the phantom.

The two-dimensional phantom insert is seen in the center of figure 7.11. It consists of a base fitted with two holes to accept the hub of two 10 ml plastic syringes trimmed to a filled volume of 6 ml. It is attached to the phantom body with nylon screws. Ten milliliter syringe bodies were chosen because of their ease of filling with a precise volume, and because their inner diameter (14 mm) was greater than two times the system resolution (~5 mm). This was required for accurate quantification. The phantom design allowed for one rod to be filled with a “hot” concentration of radioactivity approximately five times the concentration of the “warm” background solution in the body of the phantom. The other rod does not contain activity and is used to assess scatter.

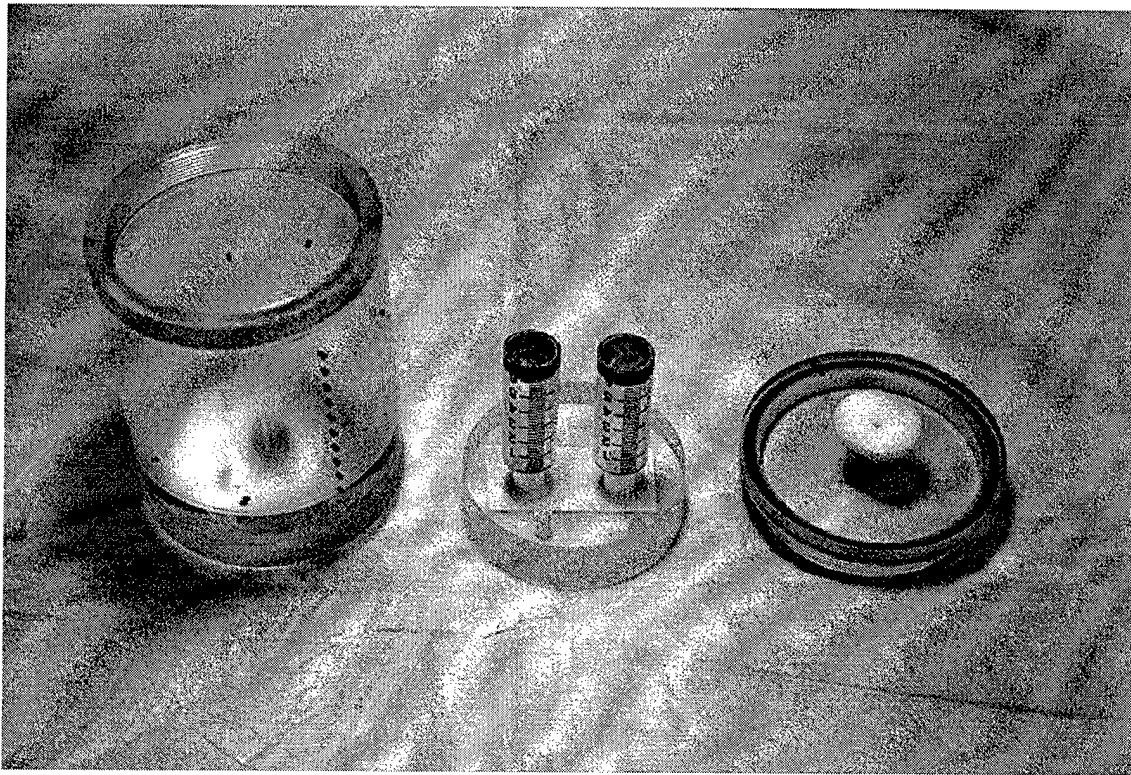


Figure 7.11. Two-Dimensional Syringe Phantom, with Holder (Note Fiduciary Markers) and Lid (Note Injection Port).

The three-dimensional phantom insert is observed in the center of figure 7.12. A base was constructed to accept two plungers from of a 5 ml syringe. These served as support posts for two hollow plastic “eggs” each with a 3 ml volume, and linear dimensions of 15 mm by 24 mm. These objects were again chosen because of their relatively precise volume, ease of filling, and acceptable linear dimensions. Eggs were sealed after filling and affixed to the support stems with small dabs of hot melt glue. As with the 2-D phantom, one egg is filled with a concentration five times the background activity concentration, and one egg is “cold”.

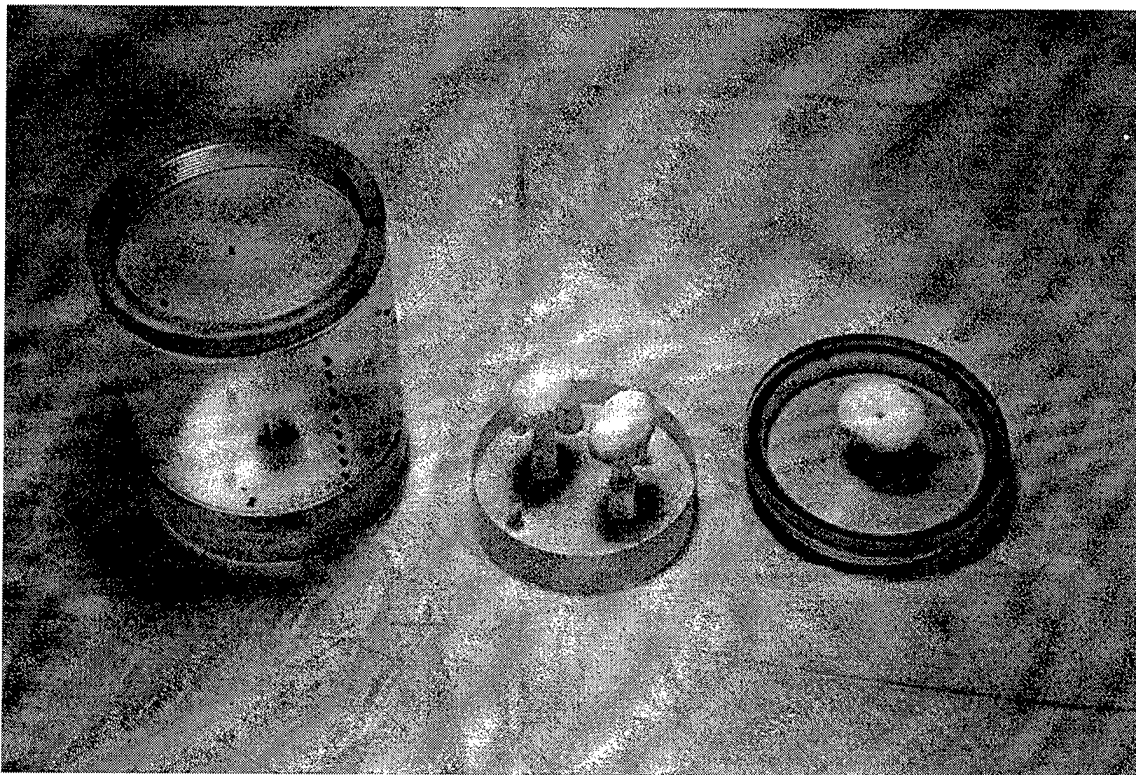


Figure 7.12. Three-Dimensional Phantom Consisting of Two 3 ml Egg Shaped Objects. One was Filled with Five Times the Surrounding Activity Concentration, One was Cold.

SPECT Imaging Procedures

Fluorine-18 in water with a minimum activity of 40 mCi and a minimum concentration of 6 mCi/ml was acquired from the University of Michigan PET Facility. Phantom objects were filled and sealed such that the “hot” object had an activity concentration five times that of the surrounding background activity. Object activities were assessed using a Capintec CRC-4R dose calibrator. The other object in each phantom was “cold” and was filled with either epoxy resin (rod) or distilled water (egg). Fiducial markers were filled with residual ^{18}F solution to provide an activity of 50 to 100 μCi per marker. Fiducial marker holes were covered with electrical tape to prevent leaking. After assembling the phantom, the body was filled with distilled water and activity was added using the injection ports. The sealed phantom was then shaken, not

stirred. Total initial activity within the egg phantom was 30 mCi (1110 MBq) ^{18}F as compared to 25 mCi (925 MBq) for the rod phantom.

Phantoms were imaged in SPRINT directly after the phantom was assembled. SPRINT acquisition parameters for the 2-D phantom (one acquisition) and the 3-D phantom (8 acquisitions) are presented in Table 7.5. The phantoms were centered radially and axially within the gantry, and planar imaging was performed to verify position. Two energy windows were set prior to acquiring projection data: a photopeak window set to $\pm 10\%$ the peak channel; and a scatter window set three channels below the photopeak window and equal to the photopeak window width. The phantoms were then imaged using SPRINT tomographic acquisition software. For the rod phantom a single 55 minute (27 minute effective count time) acquisition was performed. The egg phantom was imaged sequentially over a 10 hour period using two acquisition times, 55 minutes and 10 minutes (4 minute effective count time). These were the maximum and minimum acquisition times permitted by existing software when using aperture penetration correction. The decay of the phantom permitted observation of image degradation as total image counts decreased by a factor of 18 over this time. The short acquisition times gave additional data with a factor of 10 reduction in image counts.

It was found that SPRINT phototubes drift substantially over time. To partly correct for this effect, energy correction maps were generated within 12 hours of imaging, and photopeak windows were set just prior to imaging. Flood correction maps were then generated from flood images acquired immediately following (or just prior to) phantom imaging using a uniform line source with the slice collimator in-place.

Image reconstruction was performed using filtered backprojection and the SAGE iterative algorithm. Raw acquisition data was first reorganized to create open and weighted blocked slit projection data sets. Decay correction and deadtime correction were applied at this time. This data was processed to form flood corrected slice projection sets (sprintograms) which had low count bins rejected. Finally reconstruction

was performed using the two algorithms. In filtered backprojection, penetration correction was performed, followed by filtering, backprojection and attenuation correction. In SAGE, attenuation was addressed within the system weights. A regularization constant (β) was selected to provide a desired level of smoothing, and the system model directly incorporated the weighted penetration data as the random background.

Accurate quantification of the resulting images required calibration of SPRINT with a known activity source. Two different calibration factors were used: one based on the known concentration in the 3-D phantom's uniform background; the other based on total activity in a capillary tube filled with a known lineal activity. Image reconstruction was performed again using FBP and SAGE, with attenuation for the phantom, and without attenuation correction for the line. Acquisition and reconstruction details are provided in Table 7.5. Reconstructed line source images were analyzed by scribing large regions of interest (ROIs) around the line to measure the total counts in the line image. The counts were divided by the total acquisition live time to arrive at a count rate. The calibration factor was then calculated using the decay corrected lineal activity of the source and the slice thickness of the reconstructed image:

$$\text{Calibration Factor (cpm/uCi)} = \frac{\text{ROI Countrate (cpm)}}{\text{Lineal Activity } (\mu\text{Ci}/\text{mm}) \cdot \text{Slice Thickness (mm)}}$$

Images of the 3-D phantom were analyzed by scribing large regions of interest within the uniform background region of several 6 mm thick slices. This provided the average number of counts per voxel, and from the total acquire time, the average count rate per voxel. Activity concentration of the phantom was determined from the known injected activity and the phantom volume. The calibration factor was then determined as:

$$\text{Calibration Factor (cpm/pixel/uCi/ml)} = \frac{\text{ROI Countrate(cpm/pixel)}}{\text{Activity Concentration(uCi/ml)}}$$

Table 7.5. Acquisition Parameters for Rod (2-D) and Egg (3-D) SPRINT Imaging.

	ROD Imaging	Egg Imaging	Line Source
No. Steps	80	80	80
Time/Step	40 s	40 or 6 s	30 s
Total Time	55 m	55 or 10 m	48 m
Live Time	26.67 m	26.67 or 4 m	20 m
Reconstruction:	SAGE/FBP	SAGE/FBP	SAGE/FBP
FOV	86x86 mm	86x86 mm	86x86 mm
Image Size	100x100	100x100	100x100
Slice Thick:	6 mm	3 mm	6 mm
No. Slices	1	10	12
Filters (FBP)	Ramp/Butterworth 0.9 cm ⁻¹ cutoff	Ramp/Butterworth 0.9 cm ⁻¹ cutoff	Ramp/Butterworth 0.9 cm ⁻¹ cutoff
Beta/Convergence	2 ⁻²⁷ /0.01	2 ⁻²⁵ /0.01	2 ⁻²⁸ /0.01
Lvl (to halt iterations)			

Image analysis of the phantoms was conducted by scribing small regions of interest well within the boundaries of the phantom objects. This was necessary to avoid the affects of finite spatial resolution in the reconstructed images. Typical ROIs for the rods and eggs contained less than 20 pixels. For the hot object in each phantom, the maximum single pixel counts was also recorded. An average pixel count rate (cpm/pixel) was calculated from the average counts per pixel within a region and the total acquisition time. The activity concentration of a given region was then calculated using both of the following equations with the appropriate calibration factor:

$$\text{Radioactivity Concentration}(\text{uCi} / \text{ml}) = \frac{\text{ROI Specific Countrate}(\text{cpm} / \text{pixel})}{\text{Cal Factor}(\text{cpm} / \text{uCi}) \cdot \text{Voxel Size}(\text{ml} / \text{pixel})}$$

$$\text{Radioactivity Concentration}(\text{uCi} / \text{ml}) = \frac{\text{ROI Specific Countrate}(\text{cpm} / \text{pixel})}{\text{Cal Factor}(\text{cpm} / \text{pixel} / \text{uCi} / \text{ml})}.$$

The error as a percent difference from each single measurement was determined from the above calculated concentration and the known concentration of the phantom regions.

To provide a relative indication of noise in the uniform regions of an image, the standard deviation in the average pixel counts was calculated. It must be emphasized that this standard deviation, and the resulting deviation in that region's concentration, should not be confused with the actual standard deviation for this region resulting from the measurement process. The mathematical operations of backprojection, ramp filtering and other filtering (smoothing) operations introduce correlation between the pixels of a reconstructed image. The nature of statistical iterative reconstruction introduces similar covariance between pixels, dependent on the degree of regularization. Consequently, it is not possible to differentiate the bias nor variance in the measurement process from a single measure. The measured standard deviation in a given single region is used as only an estimate of "noise" in the region, and the percent difference calculated for a region is taken as an approximate "error" in the assessed concentration.

Actual bias and standard deviation were estimated from the serial acquisitions of the 3-D phantom. Since there is considerable decay occurring between each acquisition, it was not possible to treat the estimated concentrations from each acquisition as identical independently distributed random processes. However, without knowing the distribution of estimates from each acquisition, it is possible to derive weighted least square estimators for the mean and the variance of these observations¹:

$$\hat{\mu}_{q_0} = \frac{\sum_{i=1}^N DF_i \cdot \hat{q}_{oi}}{\sum_{i=1}^N DF_i} \quad \text{and} \quad \hat{\sigma}_{q_0}^2 = \frac{1}{N-1} \sum_{i=1}^N \frac{DF_i}{DF_1} \cdot (\hat{q}_{oi} - \hat{\mu}_{q_0})^2$$

Where DF_i is the decay correction factor for acquisition i , \hat{q}_o is the estimated activity concentration at $t=0$ for measurement i , and N is the number of observations. The decay corrected activity concentration for acquisition i is given by:

$$\hat{q}_{oi} = \frac{\text{ROI Countrate}_i}{\text{CalFactor} \cdot DF_i} \quad \text{where } DF_i = \exp\left(\frac{-\ln(2)\Delta T_i}{T_{1/2}}\right)$$

Substituting the expression for q_o into the equations for the estimated population mean and variance results in:

$$\hat{\mu}_{qo} = \frac{\sum_{i=1}^N \frac{\text{ROI Countrate}_i}{\text{CalFactor}}}{\sum_{i=1}^N DF_i} \quad \text{and}$$

$$\hat{\sigma}_{qo}^2 = \frac{1}{N-1} \sum_{i=1}^N \frac{DF_i}{DF_1} \cdot \left(\frac{\text{ROI Countrate}_i}{\text{CalFactor} \cdot DF_i} - \frac{\sum_{i=1}^N \frac{\text{ROI Countrate}_i}{\text{CalFactor}}}{\sum_{i=1}^N DF_i} \right)^2$$

The subsequent bias and STD are estimated as:

$$\hat{bias} \approx \hat{\mu}_{qo} - q_{known}$$

$$\hat{STD} \approx \sqrt{\hat{\sigma}_{qo}^2}$$

It is recognized that due to deadtime corrections, the process is not truly Poisson, and hence the above expressions are only approximate.

MRI Imaging Procedure

To assist in image analysis, phantoms were imaged using nuclear magnetic resonance to provide a high resolution physical template of the phantom cross-section. The instrument used was an Omega CSI 2T Animal Imaging System manufactured by General Electric. Phantom imaging in this system required construction of a small bore receiver probe to improve the object signal-to-noise ratio. This probe was designed with an 8.25 cm inner diameter, which is 5 mm larger than the outer diameter of the phantom. This provides an improvement in signal by a factor of 3.5 as compared to using the system's large probe.

Image acquisition using the CSI 2T for the egg phantom and rod phantom was performed a minimum of 24 hours after SPECT imaging to allow complete decay of the

original ^{18}F . Fiducial markers were emptied and replaced with a 0.1 mM solution of Gd-DTPA which provides a bright signal during MR imagingⁱⁱⁱ.

The prepared phantom was placed in the small bore receiver probe, which was then installed in the CSI 2T core. The phantom was oriented so that the linear markers were superior. The probe was tuned to establish the proper excitation frequency, and a single coronal image was acquired through the fiducial markers to determine slice locations. System parameters were then adjusted to acquire eight 3 mm thick slices of the object, with each slice centered on a pair of fiducial markers (Table 7.6). To minimize acquisition time, a T1 weighted spin-echo imaging sequence was employed, which featured a relatively short repetition time (TR). Acquired images were 256x128, corresponding to 256 frequency encoding steps and 128 phase encodings. MR images were interpolated to create a 256x256 image and then scaled to provide a pixel size equivalent to SPECT images.

Table 7.6. Parameters Used for MR Phantom Imaging on CSI 2T System.

MRI Parameters	Rod Phantom	Egg Phantom
FOV	150 mm	100 mm
Slice Thickness	3 mm	3 mm
Slice Separation	6 mm	3 mm
Image Size	256x128	256x128
Pixel Size	0.585 mm	0.391 mm
Image Type	T1-spin-echo	T1-spin-echo
TR	600 ms	1000 ms
TE	20 ms	18 ms
Elapsed Time	2:33 min	6:24 min

ⁱⁱⁱ Gadolinium (Gd) is a paramagnetic MR contrast agent which induces a large decrease in the spin-lattice relaxation time of surrounding tissue (or water). In T1-weighted spin echo imaging, the result is a very bright signal in areas where Gd is present.

Results

Reconstructed SPECT and MR images of the rod phantom are presented in figure 7.13. The images are shown without contrast enhancement. In figure 7.13A we observe a single MR image of the phantom with the fiducial markers clearly visible. The epoxy in the “cold” rod emits no MR signal but still provides a scattering medium for the SPECT measurements. The first SPECT image represents the rod reconstructed with filtered backprojection. It is observed that considerable noise exists in the image despite being reconstructed with over 50×10^6 counts in the slice. Backprojection artifacts occur from the hot and cold rods, appearing as a spreading of activity in horizontal bands. Images 7.13C and 7.13D show the same projection data reconstructed using the SAGE iterative algorithm. The difference between these images is the weighting applied to the penetration projection data. The data for the left image data are weighted by the Blackman window, and the right image data are weighted using the Monte Carlo based window. Both images are qualitatively superior to the FBP reconstruction but the Blackman windowed reconstruction has several dark line artifacts running through the object which are of indeterminate origin. Because these artifacts are effectively eliminated when using the Monte Carlo based weights, this window was used preferentially in the reconstruction of the three dimensional phantom as well as for animal imaging.

The profile plots presented at the bottom of figure 7.13 represent two horizontal slices through figure 7.13D, centered on the hot rod and cold rod. The profiles demonstrate the relatively low noise provided by SAGE reconstruction. The finite resolution of SPRINT is also observed by the sloped edges of the hot and cold objects. The counts for the cold rod approaches zero within the object, supporting the simulation-based observation that scatter is a small effect. The “hot” rod has an absolute magnitude four to five times that of the surrounding activity, as expected.

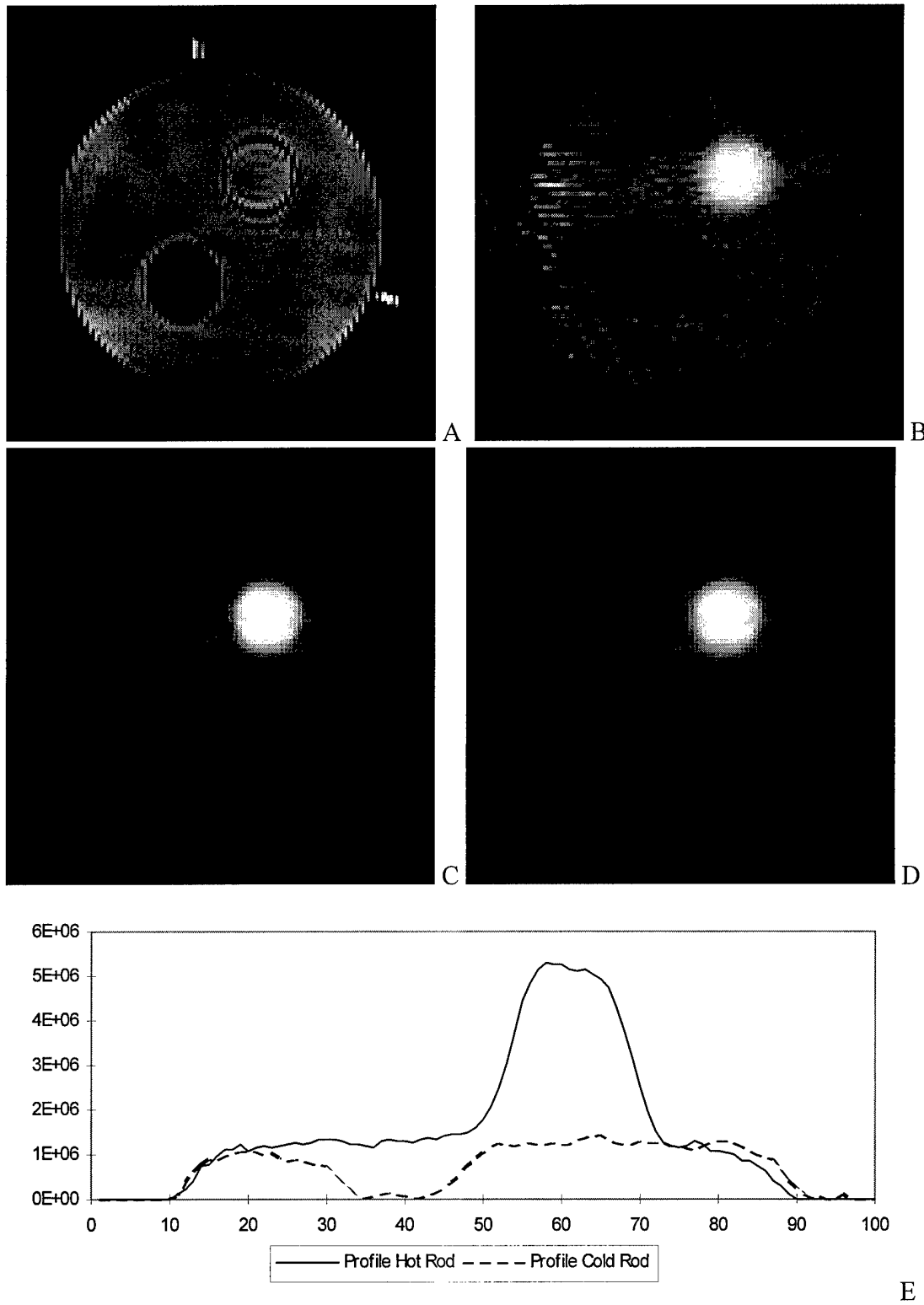


Figure 7.13. MR and SPECT Images of Rod Source (A) MR Image, (B) FBP SPECT Image (C) SAGE w/ Blackman Weighting (D) SAGE w/ MC Weighting, and (E) Horizontal Profiles Through D.

Quantitative results for these images are presented in Table 7.7, with the applied calibration factor presented at the bottom. For the hot object, two assessments were made, one for the pixel of maximum counts and the other for a small region of interest (<20 pixels). The region-based assessment results in a small increase in error compared to the single pixel. The activity of the hot region is underestimated from the ROI analysis by 16% to 26%, and the background concentration is underestimated by 12%. The positive error of the cold rod is about five percent of the background concentration. The results are generally consistent when using either FBP or SAGE for image reconstruction, although SAGE provides slightly improved precision and accuracy.

Table 7.7. Quantitative Analysis for 2-D Phantom, FBP and SAGE Reconstruction.

FBP Reconstruction			True Conc.	Error (%) [*]
	cpm/pixel [‡]	$\mu\text{Ci/cc} \pm \mu\text{Ci/cc}$	$\mu\text{Ci/cc}$	
Hot (pixel) [†]	327	588	703	-16.2%
(ROI)	304 ± 15.63	548 ± 90.2		-22.1%
Background	72.6 ± 21.8	129 ± 36.5	136	-4.9%
Cold Rod	5.48 ± 7.28	9.9 ± 13.2	0	7.6%
SAGE Reconstruction			True Conc.	Error (%) [*]
	cpm/pixel	$\mu\text{Ci/cc} \pm \mu\text{Ci/cc}$	$\mu\text{Ci/cc}$	
Hot (pixel) [†]	43770	543	703	-22.73%
(ROI)	41590 ± 1422	516 ± 83.1		-26.58%
Background	9631 ± 1397	119 ± 25.5	136	-12.03%
Cold Rod	449 ± 466	5.57 ± 5.85	0	4.66%

Calibration Factors (cpm/pixel/ $\mu\text{Ci/ml}$)	FBP:	0.555 ± 0.087
	SAGE:	80.6 ± 12.6

^{*} Value presented for cold rod is fraction of background activity measured.

[†] No standard deviation reported because a single (maximum) pixel is used.

[‡] Standard deviation equal to the variance in average pixel counts within single ROI.

The single measurement standard deviation in the assessed background concentration is high. Although this effect can be reduced by increased filtering of the image, this will result in increased error. The cold rod has a standard deviation in excess of 100% for both reconstruction methods attributable to low count statistics in this region. This is reasonable, considering that if there were no biasing due to scatter, the variance in the cold region would be infinite.

The imaging conditions for the two-dimensional phantom are considered ideal in that high activity was used in objects large compared to the resolution of the system, and the object did not vary axially. This removes the effects of a finite axial resolution. A more realistic assessment of SPRINT image performance is obtained by imaging the 3-D phantom over a range of object activities. Image quality for the highest activity acquisition is shown in figure 7.14 with matched MR images for reference. Slices are contiguous with a 3 mm thickness. MR and SPECT axial alignment is approximate, as evidenced by only partial agreement of the fiducial markers between the matched images. The fifth image of the sequence (slice E) is taken as the center of the object for purposes of quantification.

Each of these SPECT images was reconstructed from approximately 8 million open slit projection counts and 4 million blocked slit counts using the SAGE algorithm and regularization of $\beta=2^{-25}$, chosen as the best compromise between image resolution and noise for this acquisition. Despite high image counts, considerable noise is observed in the images. The figure also shows the effect of the limited axial resolution provided by the slice collimator. Activity from the “hot” egg and “cold” egg is seen to blur slightly into slices above and below the actual object.

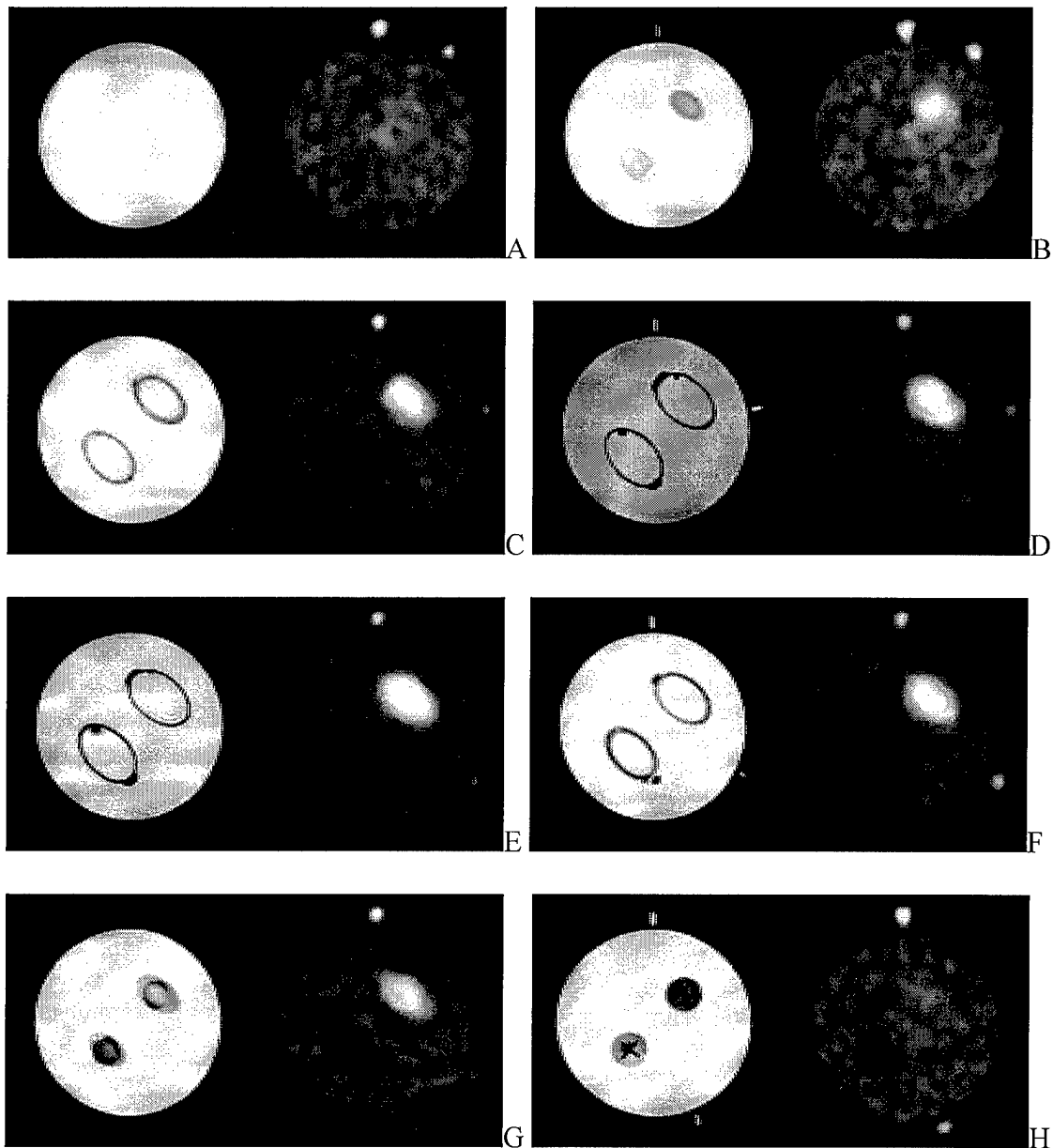


Figure 7.14. MR and SPECT Images of 3-D Egg Phantom. Images are Contiguous 3 mm Thick Slices. Slice E is Approximately in the Center of the Phantom.

The effect on image quality of reducing total image counts is shown in figures 7.15 and 7.16. The first figure shows FBP reconstructions of the center slice of the phantom, and the second figure shows SAGE reconstructions of the same slice. All images were reconstructed using the parameters shown in Table 7.5. The top row in each figure shows the effect of a 2 hour decay period between 55 minute acquisitions. This

results in neighboring images having total image counts reduced by a factor of 2.6. The lower sets of images were acquired approximately one hour after the start of the overlying image, and using a 10 minute acquisition time. This reduced the image counts between top and bottom images by an approximate factor of 10. We observe that at the end of the imaging sequence, the hot and cold objects are just discernible against the high background noise of the image.

A requisite for accurate quantification of phantom objects and animal organs is that the system be linear over a wide range of object activities. To assess the linearity of SPRINT, total projection counts and total image counts for the center phantom slice were plotted as a function of total phantom activity times the image acquisition time. This latter function is directly proportional to the total flux emitted from the phantom during a given image acquisition. The results are shown in figure 7.17. The figure shows that for the first three acquisitions (as labeled), the number of image counts and projection counts are consistently less than expected based on a linear fit of the last four acquisitions when the phantom activity is lowest. The bias is better observed in table 7.8 which shows percent difference in measured counts compared to a linear fit of the data. The effect is believed to originate from paralyzable deadtime effects in module signal processing which are not addressed by the simple non-paralyzable model described previously.

Results of the region of interest analysis are shown in Table 7.9. The table shows the average count rate per pixel for the various phantom regions reconstructed using the SAGE algorithm. Results using FBP were found to be of poorer accuracy and precision than those obtained using SAGE, and are not presented. The hot egg concentration was determined from both a small region of interest (<40 pixels) as well as the pixel of maximum counts within the object. Background concentrations were assessed using large regions (several hundred pixels) averaged over the center slice and slices above and below the hot and cold objects. The cold region was assessed from a small region drawn within the cold egg boundaries.

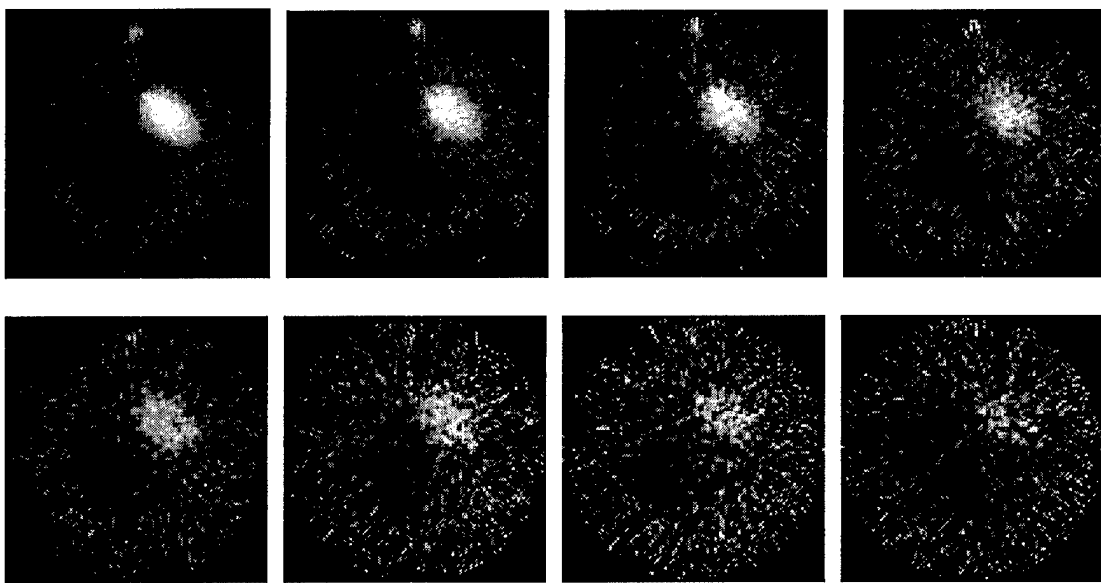


Figure 7.15. Serial Acquisitions of Center Slice of Egg Phantom Reconstructed with FBP and Butterworth Filtering (0.9 cm^{-1}). Adjacent Images are Decreased in Counts by 2.6, and Bottom Images are Factor of 10 Less in Counts Than Overlying Images. Hot egg Concentrations vary from $853 \mu\text{Ci}/\text{ml}$ to $28.4 \mu\text{Ci}/\text{ml}$.

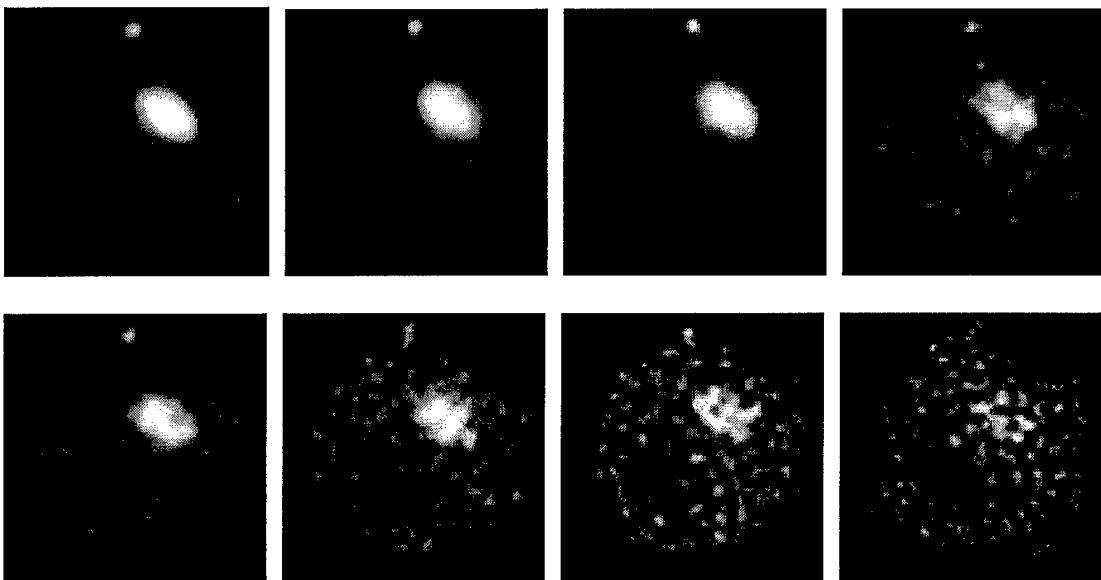


Figure 7.16. Serial Acquisitions of Center Slice of Egg Phantom Reconstructed with SAGE and $\beta=2^{-25}$. Phantom Activity and Concentrations are in Tables 7.8 and 7.9.

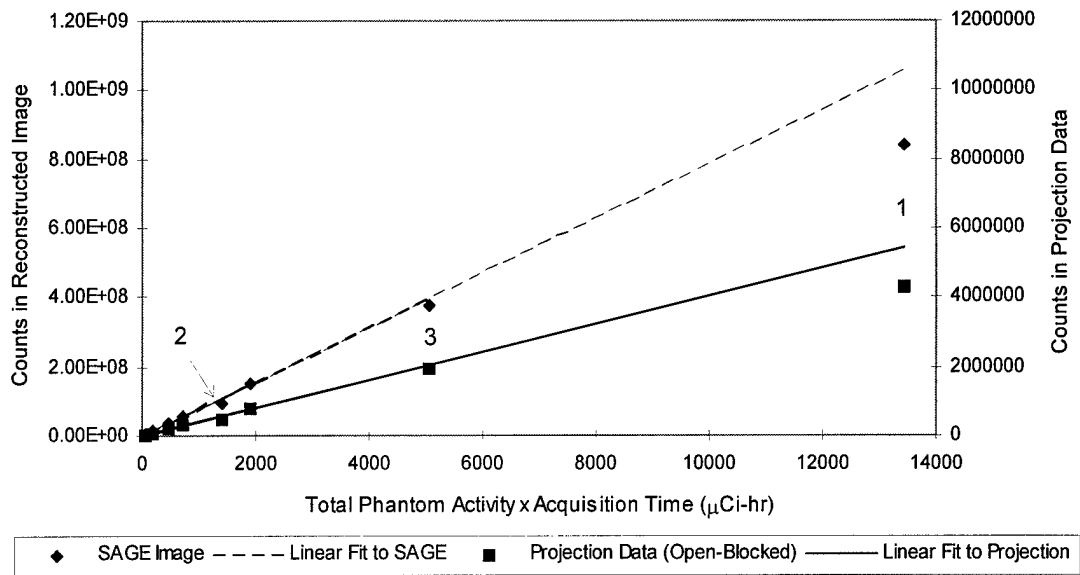


Figure 7.17. Total Image Counts as a Function of Total Flux Emitted by the Phantom. The Product of Total Phantom Activity and Time the Phantom was Imaged ($\mu\text{Ci}/\text{hr}$) is Proportional to Total Flux. Note the Bias for the First Three Acquisitions.

Table 7.8. Bias Introduced by Uncompensated System Deadtime.

	Total Phantom (mCi)	Acquire Live Time (min)	Net Projection Counts ($\text{Counts} \times 10^3$)	Bias from Linear	SAGE Image (Counts $\times 10^6$)	Bias from Linear
1	30.26	27	5430	-21.6%	1060	-20.7%
2	21.26	4	572	-16.7%	111	-15.7%
3	11.39	27	2040	-5.16%	398	-5.49%
4	7.10	4	191	-2.06%	37.2	-1.74%
5	4.29	27	769	-0.14%	150	0.06%
6	2.81	4	75.7	0.87%	14.7	2.82%
7	1.62	27	290	0.60%	56.4	-2.61%
8	1.01	4	27.1	-4.35%	5.27	0.08%

The activity concentration was assessed in these regions using the background derived calibration factor. This factor was based on images acquired with phantom activities less than 7 mCi to avoid the paralyzable deadtime effects discussed previously. Results were compared to the known object activity concentration at each acquisition time, providing the error in the single measurement as a percent difference. The error in the cold egg concentration was determined as a fraction of the background concentration.

The most notable observation made from these data is the change in bias of the hot egg and background regions as the activity within the phantom decays. When the phantom is at its highest activity, there is a -28% error in the assessed hot egg concentration. When total phantom activity diminishes to less than 7 mCi (260 MBq), the average error approaches 3% for the hot egg. This same trend is noted for the ROI analysis of this region, but activity concentration is consistently underestimated, even for low phantom activities. Similarly, the background error is initially -20%, which then increases to a residual positive error of -3%. There is generally good agreement between the initial acquisition results for the 3-D phantom, and the single acquisition result for 2-D phantom. The measured activity concentration within the cold egg shows a fairly uniform activity concentration that is 3% to 20% of the background.

As with the two-dimensional phantom, it must be recognized that the standard deviation presented for each measurement is not the actual variance of the measurement. This is again because the reconstruction process and effects of filtering or regularization correlate the image pixels. No standard deviation for the count rate of the hot egg is reported since only a single pixel value was used. The measure is observed to increase as source concentration diminishes and acquisition time is reduced (reference Table 7.8 for true acquire times), as expected. The standard deviation in the cold region is again extreme, approaching several hundred percent in some instances due to low counts.

Table 7.9. Quantitative Analysis for 3-D Egg Phantom, SAGE Reconstruction.

Hot Egg Region	Region count rate	Measured Concent.	True Conc	Error (%)*
Acquisition	cpm/pixel \pm cpm/pixel [†]	$\mu\text{Ci}/\text{ml} \pm \mu\text{Ci}/\text{ml}$	$\mu\text{Ci}/\text{ml}$	
1 (max pixel)	24600 [†]	611	853	-28.3%
(ROI)	24000 \pm 530	595 \pm 94.2	853	-30.2%
2 (max pixel)	19400	482	599	-19.6%
(ROI)	17600 \pm 799	437 \pm 71.2	599	-27.2%
3 (max pixel)	10984	273	321	-15.14%
(ROI)	10500 \pm 218	261 \pm 40.2	321	-18.64%
4 (max pixel)	7660	190	200	-5.01%
(ROI)	7070 \pm 477	176 \pm 30.0	200	-12.32%
5 (max pixel)	4520	112	121	-7.21%
(ROI)	4330 \pm 110	107 \pm 17	121	-11.20%
6 (max pixel)	3580	88.7	79.3	11.93%
(ROI)	3000 \pm 357	74.6 \pm 14.6	79.3	-5.88%
7 (max pixel)	1690	41.8	45.5	-8.11%
(ROI)	1540 \pm 96	38.3 \pm 6.44	45.5	-15.97%
8 (max pixel)	1450	36.0	28.4	26.74%
(ROI)	1000 \pm 338	24.9 \pm 9.26	28.4	-12.43%
Background Region				
1	5383 \pm 676	134 \pm 27.0	167	-20.0%
2	4114 \pm 1286	102 \pm 35.4	117	-12.9%
3	2297 \pm 327	57 \pm 12.1	63	-9.30%
4	1525 \pm 702	38 \pm 18.4	39	-3.43%
5	950 \pm 193	24 \pm 6.05	24	-0.41%
6	621 \pm 432	15.4 \pm 11.0	15.5	-0.70%
7	361 \pm 121	8.9 \pm 3.31	8.9	0.41%
8	204 \pm 220	5.1 \pm 5.52	5.6	-8.86%
Cold Egg Region				
1	680 \pm 425	16.9 \pm 10.9	0	11.7%
2	371 \pm 562	9.21 \pm 14.0	0	8.9%
3	492 \pm 190	12.2 \pm 5.12	0	19.6%
4	49.0 \pm 130	1.22 \pm 3.23	0	2.96%
5	173 \pm 108	4.29 \pm 2.75	0	17.4%
6	73.3 \pm 136	1.82 \pm 3.38	0	10.3%
7	59.8 \pm 59	1.48 \pm 1.48	0	18.3%
8	14.1 \pm 40	0.35 \pm 0.99	0	5.83%
Calib. Factor:	40.3 \pm 6.30	cpm/pixel/ $\mu\text{Ci}/\text{ml}$		

* Value presented for cold rod is fraction of background activity measured.

[†] No standard deviation reported because a single (maximum) pixel is used.

[‡] Standard deviation equal to the variance in average pixel counts within single ROI.

Estimations of the bias and standard deviation (STD) for the regions of the three dimensional phantom are presented in Table 7.10. To avoid the effects of unrecovered deadtime, only the last five acquisitions were used in the determination. Both weighted least squares, as discussed earlier, and unweighted least square estimates are presented.

Table 7.10. Bias and Standard Deviation Assessed for Hot Egg and Uniform Background of Three Dimensional Phantom. Weighted and Unweighted Least Square Estimates are Presented (n=5).

	$\hat{\mu}_{q_0}$ ($\mu\text{Ci}/\text{ml}$)	q_{known} ($\mu\text{Ci}/\text{ml}$)	% Bias	STD ($\mu\text{Ci}/\text{ml}$)	%STD
Hot Egg					
Weighted*	843	853	-1.14%	132	$\pm 15.7\%$
Unweighted	884		3.67%	130	$\pm 14.7\%$
Weighted [†]	756	853	-11.3%	143	$\pm 18.8\%$
Unweighted	754		-11.6%	148	$\pm 19.7\%$
Background					
Region					
Weighted	158	167	-5.04%	9.72	$\pm 6.13\%$
Unweighted	161		-3.72%	6.65	$\pm 4.14\%$
Cold Egg					
Weighted	16.5	0	12.3% [‡]	31.3	$\pm 190\%$
Unweighted	18.7		18.3%	23.5	$\pm 126\%$

* Based on maximum pixel

[†] Based on region of interest

[‡] Reported as percent of uniform background

Discussion

Results obtained from phantom imaging show the limitations of high energy pin-hole or slit aperture SPECT. Filtered backprojection reconstructions show very high noise and artifact characteristics. This is due to the low intrinsic detector sensitivity (11%) and the use of high resolution collimators, the large penetration component of the projection data and the projection subtraction technique employed to correct it. Additional noise is introduced in the FBP reconstructions from the arithmetic operations of back-projection¹⁵ and the use of almost a pure ramp filter that enhances high frequency noise. Because projection data are not weighted by their statistical significance (as is done in SAGE) noisy projection introduce streak artifacts in FBP images. Image reconstruction performed using the regularized SAGE algorithm provides significant improvements in image quality over FBP, but limitations posed by system sensitivity still require use of extremely high activities to provide high quality images. Although phantom images are noisy, they also demonstrate very good resolution for this energy. This is achieved through high resolution collimation, and a magnifying imaging geometry combined with the application of aperture penetration correction.

Table 7.9 indicates that for uniform background regions, a limiting activity concentration which could be imaged for 26.7 minutes and provide images with less than a 10% standard deviation in pixel counts exceeds 160 $\mu\text{Ci}/\text{ml}$ (5.6 MBq/ml). By comparison, all 4 minute acquisitions provided images with background standard deviations greater than 30%. Clearly, obtaining these activity concentrations routinely in small animals for all target organs of interest would require prohibitive levels of radioactivity to be used.

Examining the error in each of these measurements indicates that for high phantom activities, the activity concentration is underestimated on the order of 20% to 30%. Therefore, the best qualitative images are acquired at the cost of using very high

activities and result in a negative bias in quantified hot objects originating from deadtime effects not corrected by a non-paralyzable model. As total phantom activity decays to less than 7 mCi, the residual error becomes small but noise in the image becomes large.

The bias and standard deviation observed in Table 7.10 indicates that it is possible to measure the activity concentration in large organs (relative to system resolution) with fair precision and good accuracy. It is recognized that this particular assessment does not have high statistical power, but experimental conditions limited the number of samples that could be acquired.

The measured activity concentration was found to be dependent on numerous factors. Use of a line source based calibration factor was found to result in an overestimate of measured activity concentrations by up to 14%. The effect is attributed to errors in the assumed pixel volume, which is required when assessing concentrations using the line source based calibration factor. Further, it was found that if background measurements are made in the central slice of the phantom, the background is overestimated by about 10%. This is thought due blurring and scatter of the hot region activity into the neighboring background region.

In assessing the hot egg concentration, the use of other than the maximum count pixel in the region causes in an underestimation of the concentration by 10%. The egg object had linear dimension of 14 mm by 24 mm in-plane and 14 mm axially (as positioned in the phantom). In-plane resolution of SPRINT, assessed using SAGE reconstruction, was 4.4 mm FWTM and 8.0 mm FWTM. Axial resolution was approximately 5 mm FWHM and 8 mm FWTM, but with considerable variance. We note that for these dimensions, even small (4 to 6 mm diameter) regions of interest will be affected by the limited axial and in-plane resolution. The negative bias observed for this object thus originates from the blurring of activity out of the finite sized ROI. It is also likely that scatter out of the region contributes to the observed negative bias, since the method adopted for attenuation and scatter correction was not ideal. The hottest central

pixel of the region serves as the best estimator of region concentration (minimum bias) because it is located at approximately the systems FWTM from the object boundary and thus experiences the least impact from the systems limited resolution.

Results for the cold object in each phantom show the effects of scatter as well as the limited axial resolution provided by the high energy slice collimator. For the rod phantom where the object is uniform axially, contribution from scatter causes a measured concentration approximately 5% of the surrounding background. This is in good agreement with Monte Carlo simulation results presented earlier. For the 3-D phantom, limited axial resolution contributes additional activity to this region. The resulting error of 10% is thus reasonable. In theory, a better estimate of cold region activity would be achieved by only measuring the single central pixel of the object. However, the significant noise demonstrated in this region made such a measure unreliable. For all cold region measurements, the high noise is again attributable to the low count characteristics of this area.

Quantitative Rat Organ Imaging

To establish the accuracy and precision of SPRINT as applied to high energy animal imaging, two studies were conducted using Sprague-Dawley rats injected with [¹⁸F]fluorodeoxyglucose (¹⁸FDG). Images were acquired of the head and thoracic regions of each animal, and quantification was attempted for the heart, brain and lungs. Results were compared to invitro biodistribution measurements obtained after imaging

Methods

Two female Sprague-Dawley rats with weights of 250 to 275 gm were sedated with 40 mg/kg pentobarbital under ether anesthesia. After a 10 minute waiting period, the animal was loaded into a specially designed animal holder compatible with SPRINT and MR imaging. The holder was fitted with Teflon nose and tail rings to hold the animal securely during imaging. Fiducial markers along the holder walls (10 μ l volume, 8 mm axial separation) were filled with 2 mM Gd-DTPA. A picture of the sedated animal prepared for MR imaging is presented in figure 7.18.

The animal was then imaged using the CSI 2T MR scanner described previously. Image acquisition parameters are presented in Table 7.11. As with the phantom, a special MR probe was constructed to precisely match the outer diameter of the animal holder in an effort to maximize the detected RF signal. The animal was positioned in the receiver probe with the linear array of fiducial markers facing upward, with the first fiducial marker located just within the sensitive field of the probe. The animal and probe were then inserted into the MR coil. A coronal image was acquired to assess slice location, and then a T1-weighted multi-slice spin-echo imaging sequence was performed. Figure 7.19 depicts the animal within the CSI 2T, and supported by the receiver probe.

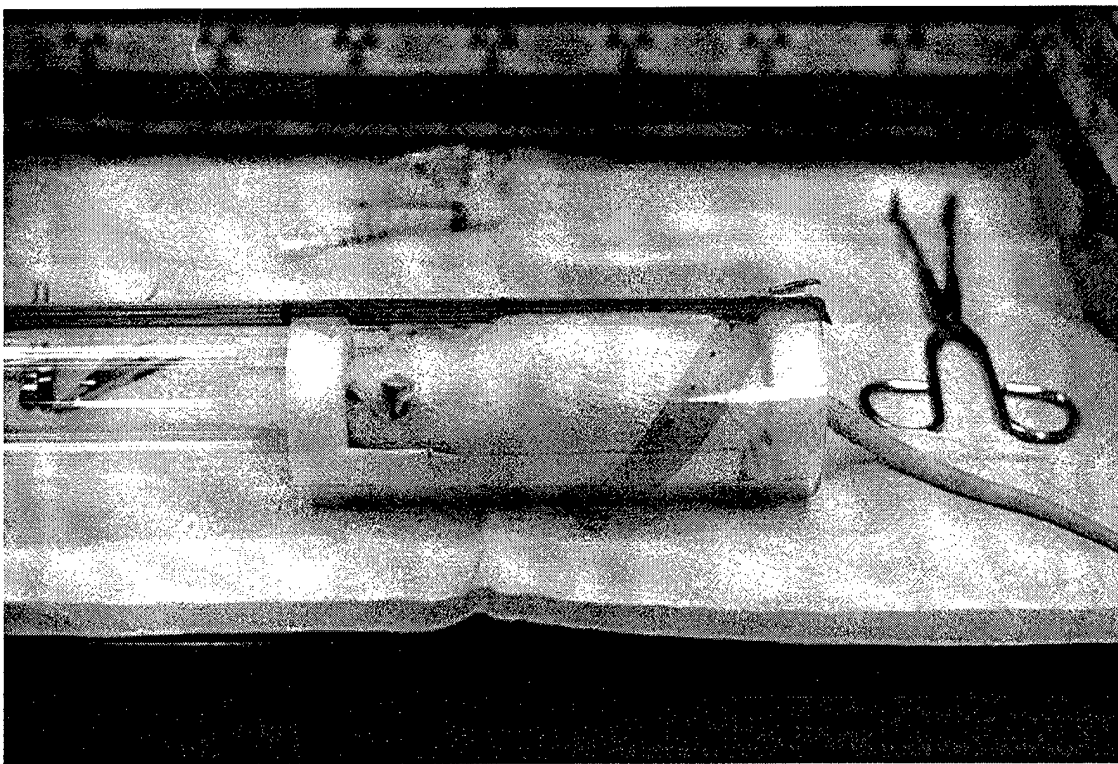


Figure 7.18. Animal Prepared for MR and SPECT Imaging.

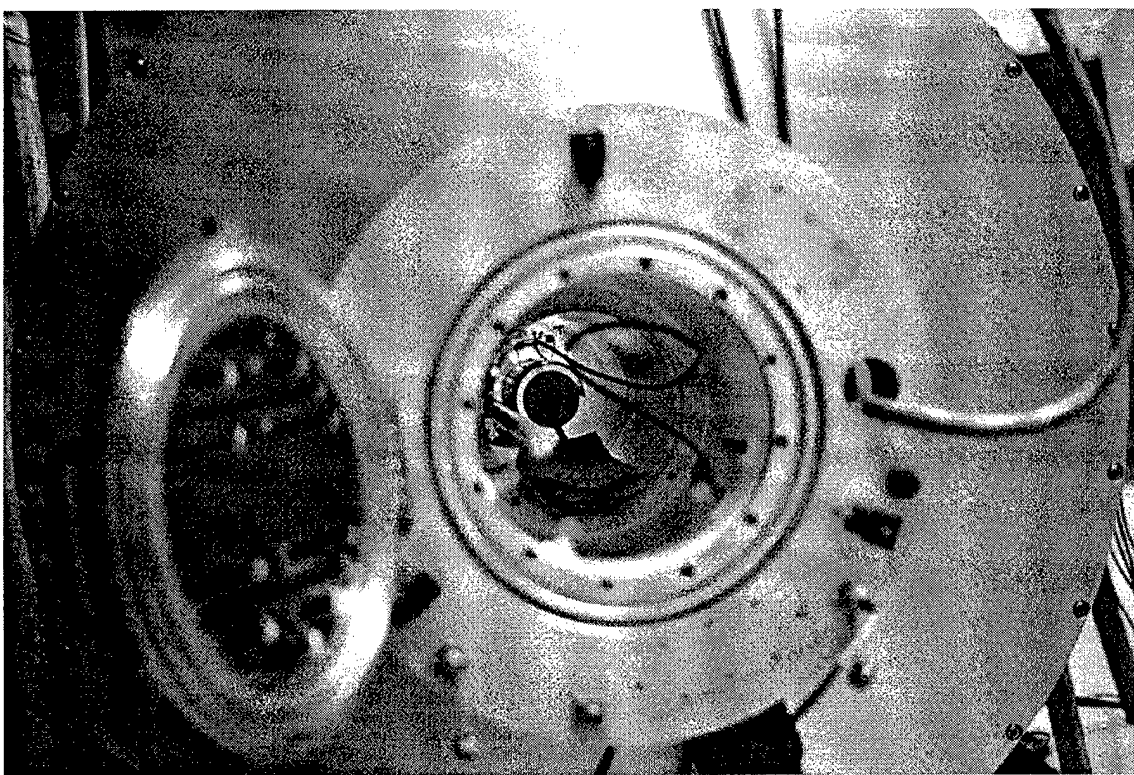


Figure 7.19. Animal During MR Imaging: The Receiver Probe Supports the Rat.

After MR imaging, [¹⁸F]fluorodeoxyglucose was obtained from the University of Michigan PET Facility. The available specific concentration dictated the maximum radioactivity that could be injected in the animal. One ml of solution was prepared for each animal, allowing injection 13 mCi for the first animal, and 3.84 mCi for the second. Injected doses and residual syringe activity were assessed using the Capintec dose calibrator. After animal injection, fiducial markers were emptied of the Gd-DTPA solution and filled with residual ¹⁸FDG, resulting in 66 µCi per marker for the first animal, and 100 µCi per marker for the second. A thirty minute waiting period was permitted between injection and the start of SPRINT acquisitions to allow metabolism of the ¹⁸FDG. The animal was then placed within SPRINT using a holder that precisely centered the animal within the gantry. The mounting system can be observed in figure 3.2. Imaging was then performed in a manner analogous to the phantom studies using the parameters shown in Table 7.11. Two images were acquired of each animal, using a 55 minute and 10 minute acquisition time. An animal (tail) during an acquisition is observed in figure 7.20.

At two hours post injection, the animal was sacrificed and biodistributions measured for the brain, heart, lung, liver and blood. Total organ weights were recorded for the heart and brain. Organ activities were measured using a Packard Tricarb 578 autogamma system with a 3"x3" NaI(Tl) detector. Results were reported as %dose per gram for all organs, and %dose per organ for the heart and brain. From the known injected activity, the time of imaging, and assuming the biodistribution was constant between imaging and sacrifice, the total organ activity and activity concentration at the time of imaging were estimated:

$$Total\ Activity(\mu Ci) = \frac{\%Dose}{Organ} \cdot \frac{Inj.\ Activity(\mu Ci)}{100} \cdot e^{\frac{-\ln(2)*DecayTime(min)}{110}}$$

$$Activity\ Concentration(\mu Ci / ml) = \frac{\%Dose}{gm} \cdot \frac{Inj.\ Activity(\mu Ci)}{100} \cdot e^{\frac{-\ln(2)*DecayTime(min)}{110}}$$

Table 7.11. Acquisition Parameters for Rat MR and SPRINT Imaging.

MRI Parameters		SPRINT Parameters	
Image Type	T1-spin-echo	No. Steps	80
TR	600 ms	Time/Step	40 s (1,3) 6 s (2,4)
TE	20 ms	Total Time	55 m(1,3) 10 m(2,4)
NEX	2	Live Time	26.67 m and 4 m
Phase Encoding	128	Reconstruction:	SAGE/FBP
Frequency Encoding	256	Image Size	100x100
FOV (mm)	80x80	FOV (mm)	86x86
Pixel Size	0.3125 mm	Slice Thick:	3 mm
Acquire Time	2.33 m	Sum Interval	2
Slice Thickness	3 mm	No. Slices	14
Slice Separation	8 mm	Beta/Convergence	2^{-27} and $2^{-25}/0.01$

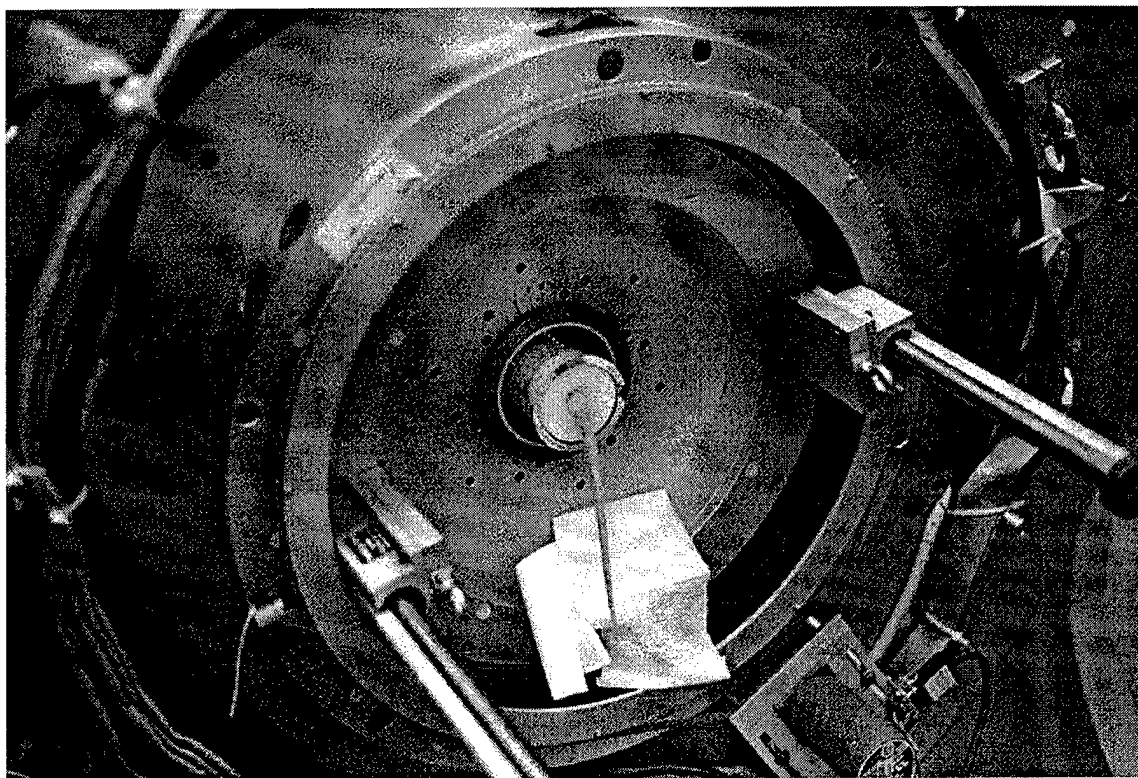
**Figure 7.20. Animal (Tail) in SPRINT During SPECT Acquisition.**

Image reconstruction was performed using filtered backprojection and the SAGE iterative algorithm. Image analysis was conducted by drawing regions of interest around and within the brain and heart, and within the approximate regions for the lungs. Three measures were obtained for the brain and heart: the total counts in a large region surrounding the organ, counts per pixel for small regions within the organ, and the total counts of the maximum pixel. This allowed assessment of total organ activity and organ activity concentration using the calibration factors derived from the 3-D phantom and line source, and the following expressions:

$$\text{Radioactivity Concentration}(\text{uCi} / \text{ml}) = \frac{\text{ROI Specific Countrate}(\text{cpm} / \text{pixel})}{\text{Cal Factor}(\text{cpm} / \text{pixel} / \text{uCi} / \text{ml})}$$

$$\text{Total Activity}(\text{uCi}) = \frac{\text{ROI Countrate}(\text{cpm})}{\text{Cal Factor}(\text{cpm} / \text{uCi})}.$$

For the heart and brain, measurements were made in the two or three contiguous 6 mm slices where activity from these organs could be observed. For the brain and lung, the standard deviation in average pixel counts was measured from the region of interest. This again provided a relative indication of noise in these regions. From the activity concentration and total activity of these organs determined by invitro measurements, the error (as %difference) in the SPECT measurement was calculated.

Results

SAGE reconstructed images are presented in figure 7.21 for the animal injected with 13 mCi and imaged for 55 minutes, with matched MR images to the left. The rodent had an approximate total body activity of 10 mCi at the time of imaging. Images are presented without contrast enhancement. Because of slice separation, there are three MR images presented for every four SPECT images. MR images were only acquired for the head and upper thoracic region. SPECT images were acquired using a larger field of view to include the cardiac region, as observed in figure 7.22.

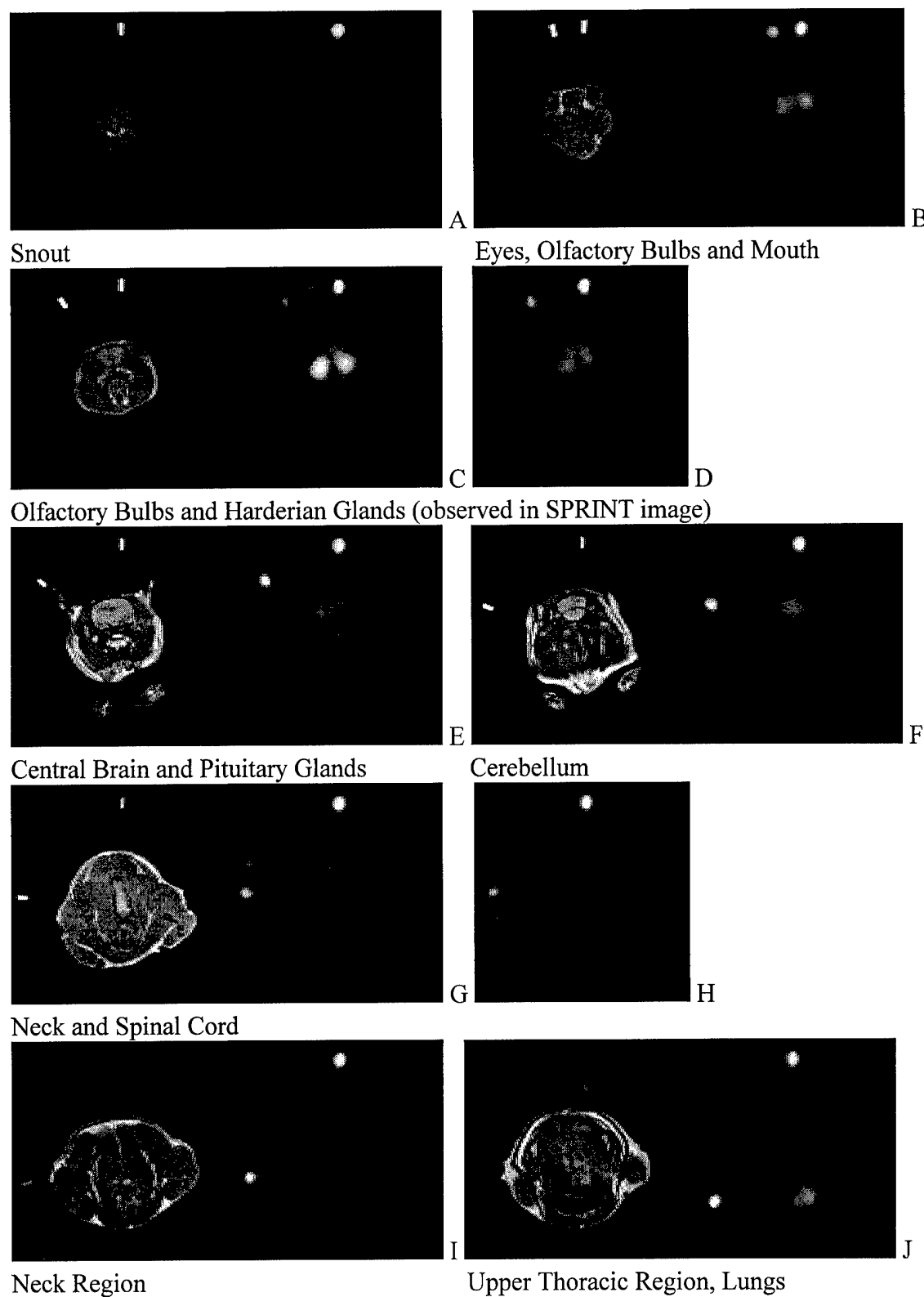


Figure 7.21. MR and SPECT Images of Rat Head and Upper Chest. MR Images are 3 mm Thick at 8 mm Intervals, SPECT Image are Contiguous and 6 mm Thick.

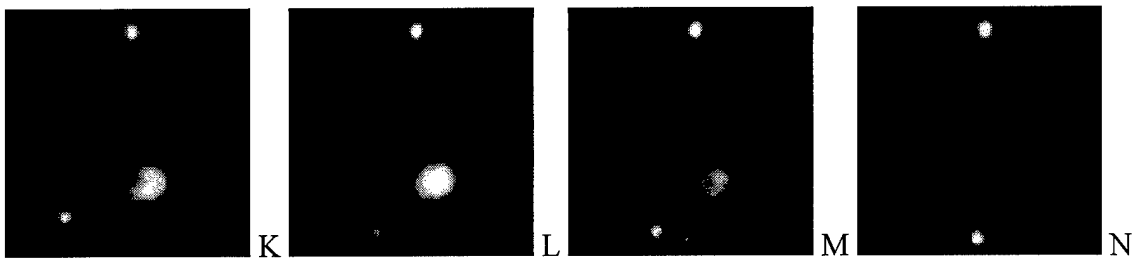
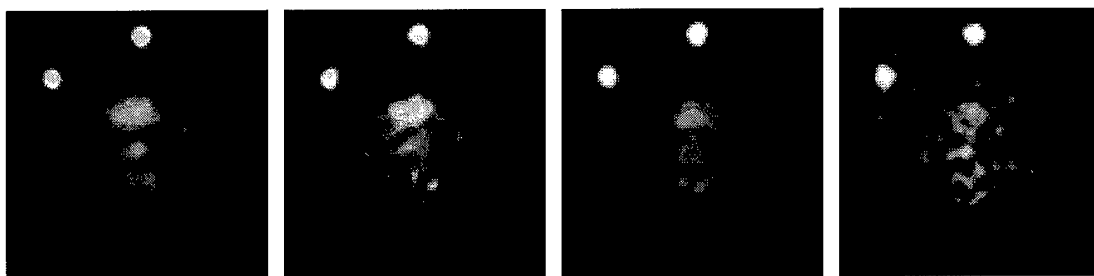


Figure 7.22. SPECT Images of Rat Cardiac Region, 6 mm Thick Slices Continued from Figure 7.21.

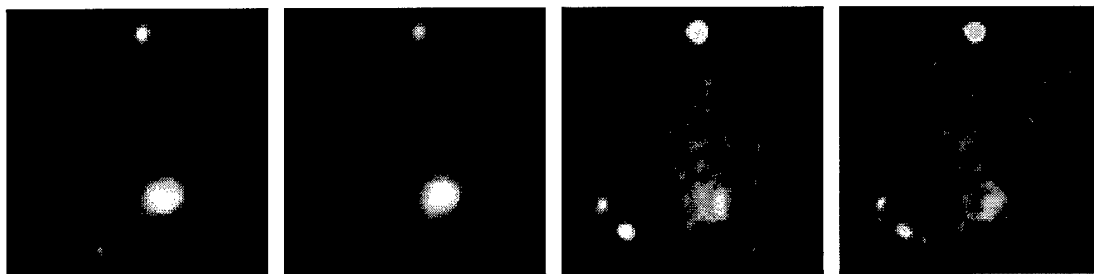
Each image shows well visualized fiducial markers, one superior to the animal, and the other rotating in a counter-clockwise fashion around the animal holder. The central regions of the rat brain are observed in SPECT slices D, E and F of figure 7.21, assessed principally on the anatomical information provided by the matched MR images. Determination of brain location exclusively from SPECT images leads to the erroneous conclusion that the brain is principally in slice C. This high activity region will be discussed in greater detail in the following section. Since MR image information was not available for the thoracic cavity, cardiac regions of interest were based purely on SPECT image contrast.

Contrast and resolution of the MR brain images allows differentiation of the cortical structure, corpus callosum, and left and right caudate putamen (slice E). In slice C, the left and right olfactory bulbs are seen and in slice F the cerebellum is found with its pyramids and parafloccular bulbs. Matched SPECT images show relatively uniform uptake in the these regions. In contrast, cardiac uptake was quite high in both animals studied, while the assessed lung uptake was very low. This results in the appearance of a well defined cardiac region in slices K and L of figure 7.22. These images are continued spatially from the last SPECT image of figure 7.21. Limited axial resolution and partial volume effects permit cardiac activity to be visible in slice J of figure 7.21 and M of figure 7.22. Cardiac motion prevents any anatomical structure (e.g., left ventricle) from being observed in these images.

The central SPECT slice for the brain and heart for all four animal acquisitions is presented in figure 7.23. Each SAGE image has been contrast enhanced to overcome the suppression in detail caused by the hot fiducial markers. The first two images of each row are for the animal injected with 13 mCi ^{18}FDG , and imaged for 55 minutes and 10 minutes, respectively. The second two images are for the second animal injected with 3.84 mCi and imaged for the same periods. Table 7.12 shows, for each of these images, the invitro assessed organ activity and activity concentration decay corrected to the acquisition time, and live acquire time used for each acquisition. Comparing the images to the tabulated data, the effects on image quality of decreased acquisition time and organ content are observed.



A. Brain Images, Acquisitions 1 - 4



B. Cardiac Images, Acquisitions 1-4

Figure 7.23. Contrast Enhanced SPECT Images of Rat Brain (Top Row) and Cardiac Regions (Bottom Row). First Two Images: Rat Injected with 13 mCi ^{18}FDG , Second Two Images: Rat Injected with 3.8 mCi ^{18}FDG .

Table 7.12. Measured Invitro Biodistribution and Estimated Organ Activity Concentrations for the Rat Heart and Brain. Each Column Shows the Decay Corrected Organ Concentration and Total Activity of ^{18}FDG at Start of an Image Acquisition, Based on the Invitro Measured Value.

Animal 1, imaged 30 and 90 minutes post injection with 13 mCi ^{18}FDG			Animal 2, imaged 30 and 90 minutes post injection with 3.84 mCi ^{18}FDG			
Injected:	13:20			14:18		
Acquired:	11:04	12:06		14:46	15:42	
Acqu. Time	55 min	10 min		55 min	10 min	
Invitro Biodistribution %dose/g [*]	Decay Corrected [†] Organ Concentration μCi/g		Invitro Biodistrib. %dose/g [*]	Decay Corrected [†] Organ Concentration μCi/g		
Brain	0.840	88.1	59.6	1.20	38.5	27.1
Heart	6.14	644	436	3.65	117.4	82.5
Invitro Biodistribution %dose/org [*]	Decay Corrected [†] Organ Activity μCi		Invitro Biodistrib. %dose/org [*]	Decay Corrected [†] Organ Activity μCi		
Brain	1.68	176	119	2.31	74.2	52.2
Heart	5.60	588	398	2.92	94.0	66.1

* No precision is reported for biodistribution measurements since only one animal was used in each assessment.

† Invitro biodistribution data is decay corrected to the start of image acquisition.

Results of the quantitative assessment of these images is presented in Table 7.13.

For each organ, activity concentration (μCi/ml) and total activity (μCi) is presented.

Results are compared to the invitro measured organ activity and concentration to provide a percent difference measure of error. The total activity assessed in the brain and heart had modest errors. Similarly, the activity concentration for the brain varied from -3% to +7%. The concentration in the heart was assessed from the pixel of maximum counts.

This value still resulted in the estimated organ concentration to be approximately 50% less than the invitro measured organ concentration. For the assessed lung concentration, results were inconsistent and had errors ranging from ±20% between animals. A standard deviation in assessed organ concentration is presented only for the lung and brain, where the variance in measured pixel counts for relatively large regions is reported.

Table 7.13. Quantitative Image Analysis of Rat Heart, Brain and Lung.

Activity Concentration Assessment	Small region count rate (brain & lung) and single hot pixel (heart)*	Calculated Concentration (ROI cpm/pixel/CF)	Estimated [†] Concentration	Error (%)
Brain	cpm/pixel \pm cpm/pixel	μ Ci/cc \pm μ Ci/cc	μ Ci/cc	
Acquis. 1	7480 \pm 1030	93 \pm 15.4	88.1	5.40%
Acquis. 2	5380 \pm 685	66.8 \pm 10.4	59.6	12.1%
Acquis. 3	2880 \pm 244	35.7 \pm 4.43	38.5	-7.41%
Acquis. 4	2110 \pm 177	26.2 \pm 3.23	27.1	-3.36%
Heart	cpm/pixel	μ Ci/cc	μ Ci/cc	
Acquis. 1	29300	364	644	-43.5%
Acquis. 2	23200	287	436	-34.0%
Acquis. 3	4170	55.2	117	-53.0%
Acquis. 4	3880	53.6	82.5	-35.0%
Lung	cpm/pixel \pm cpm/pixel	μ Ci/cc \pm μ Ci/cc	μ Ci/cc	
Acquis. 1	2780 \pm 556	34.5 \pm 7.58	28.9	19.6%
Acquis. 2	1760 \pm 439	21.9 \pm 6.79	19.5	11.9%
Acquis. 3	1230 \pm 215	15.2 \pm 3.00	18.8	-19.1%
Acquis. 4	837 \pm 260	10.4 \pm 3.36	13.2	-21.4%
Calibration Factor (CF): 80.6 \pm 12.6 cpm/pixel/ μ Ci/ml				

Total Activity Assessment	Large region count rate [†]	Calculated Activity (ROI cpm/CF)	Estimated [§] Organ Activity	Error (%)
Brain	ROI cpm	μ Ci	μ Ci	
Acquis. 1	3040000	189	176	7.28%
Acquis. 2	1930000	120	119	0.73%
Acquis. 3	1160000	72.2	74.2	-2.73%
Acquis. 4	857000	53.6	52.2	2.65%
Heart	ROI cpm	μ Ci	μ Ci	
Acquis. 1	9660000	600	588	1.99%
Acquis. 2	7390000	400	398	0.57%
Acquis. 3	1430000	89.5	94	-4.81%
Acquis. 4	1140000	71.2	66	7.73%
Calibration Factor (CF): 16100 \pm 600 cpm/ μ Ci				

* ROI analysis based on small to moderate size regions within the organ boundaries to provide an estimate of organ concentration.

[†] ROI analysis based on large regions which completely encompass the observed organ.

[‡] Estimated organ activity concentration based on invitro measured organ concentration at time of sacrifice, decay corrected to start time of imaging.

[§] Estimated organ activity based on invitro measured organ activity (%dose/organ) decay corrected to the start time of image acquisition

Discussion

For the limited number of acquisitions made, there was generally good agreement between the invitro biodistribution measurements of the brain and heart, and those measured from SPECT images. An obvious exception is the assessed concentration of activity in the rat heart, where the invivo result is half that expected. This is attributed to heart motion and limited SPRINT resolution which combine to decrease the estimate of myocardial concentration. Specifically, the myocardial wall thickness of 1 to 3 mm is blurred by motion of the heart wall. This blurred concentration is further distributed in the reconstructed image by the four to five mm resolution of SPRINT. The consequence is a significant underestimate of the myocardial concentration compared to invitro measurements. The inconsistent results for the lungs are attributed to the lack of anatomical information available when drawing regions of interest. Since lung regions were estimated purely from cardiac SPECT position, it is likely that region counts were affected by activity in the mediastinum or even by including areas outside of the animal.

One of the purposes of this work was to determine total organ activity invivo to determine organ time-activity profiles more accurately. The error observed in organ concentration measurements are compounded if an inaccurate determination of organ mass or volume is made. Since it appears possible to accurately assess the organ activity concentration for organs having a substantial uptake, invivo measurements can be used to determine the time-activity biodistribution pattern of a given compound. The total organ volume can then be assessed ex-vivo following the imaging sequence. By measuring the biodistribution of the organ or tissue at the end of imaging, an organ specific calibration factor be also be derived using image data from the last acquisition.

For both the brain and heart, significant local uptake of ^{18}FDG was experienced compared to surrounding tissue. Brain uptake may have in fact been mitigated by the use of CNS depressant to anesthetize the animal. In these cases, large regions of interest that completely encompass the organ provide an estimate of total activity that appears to be close agreement to invitro measurements. Success was dependent on summing activity in all slices where the organ was present, and included three contiguous slices for the brain and two slices for the heart. Unfortunately, with the possible exception of the rodent testes, the brain and the heart are the only organs which could be assessed in this manner due to their location and high glucose metabolism. Determining the biodistribution of organs which have significant activity surrounding them (e.g. organs in the abdominal region), must be assessed from small regions within the organ to estimate activity concentration.

As was the case for phantom studies, significant noise and limited resolution compromise the ability to quantify organ concentration. For the organs measured, ROI based standard deviations were reasonable, considering the relatively high activities present. However, it is evident that assessing all significant animal organs for uptake of a given compound is not possible. Limited resolution and poor sensitivity effectively limit accurate and precise assessment to animal organs that are large compared to system resolution and demonstrate substantial uptake of the compound.

It is again emphasized that the reported errors and standard deviations in Table 7.13 are only approximate indicators of the accuracy and precision of this measurement process due to correlation between image pixels. Although improved estimates of the bias and variance could have been obtained for the organs examined by imaging a sequence of animals, this was considered beyond the scope of the dissertation.

Acute ^{18}FDG Uptake by the Harderian Gland

A casual observation of figure 7.21C, without anatomical reference provided by the MR images, would lead to the conclusion that fluorodeoxyglucose uptake in the brain was significant and well differentiated between hemispheres. The two bright foci could easily be interpreted as local uptake in the parietal cortex or caudate putamen. It is only after the fiducial marked MR images are overlaid with the SPECT images that these foci appear to be lateral and superior to the animal brain. It is noted that SPECT slice C lies between adjacent MR slices B and C. Figure 7.24 presents the effect of splitting slice C into two adjacent 3 mm slices, and overlaying the peak activity regions onto the adjacent MR slices (figure 7.24 E and F). We observe in MR slice A, the right eye and a white region that is medial and inferior to both eyes. Because the MR data was acquired with T1 weighting, this region is recognized as probably having a high fat content. The MR/SPECT overlaid image indicates that activity is concentrated in this area, and that it extends posterior to this region. Gross dissection of a rodent head suggests that this high regional uptake may be attributed to the Harderian gland. This gland is horseshoe shaped and encircles the optic nerve, extending medially from the eye to the dorso-lateral region of the orbit¹⁶. The gland is found in most mammals, and is particularly well developed in swimming mammals, responsible for an oily secretion to lubricate and protect the eye¹⁷. This is in good agreement with both MR position and composition information.

To verify that the Harderian gland has preferential uptake of ^{18}FDG or a fluorine labeled metabolite, a biodistribution study was performed on three Sprague-Dawley rats. Animals were prepared in a fashion identical to the imaging studies and injected with approximately 80 μCi ^{18}FDG each. At two hours post injection the rat brain, pituitary gland, olfactory bulbs, eye, temporalis muscle and Harderian gland were dissected and measured for radioactivity content as described previously.

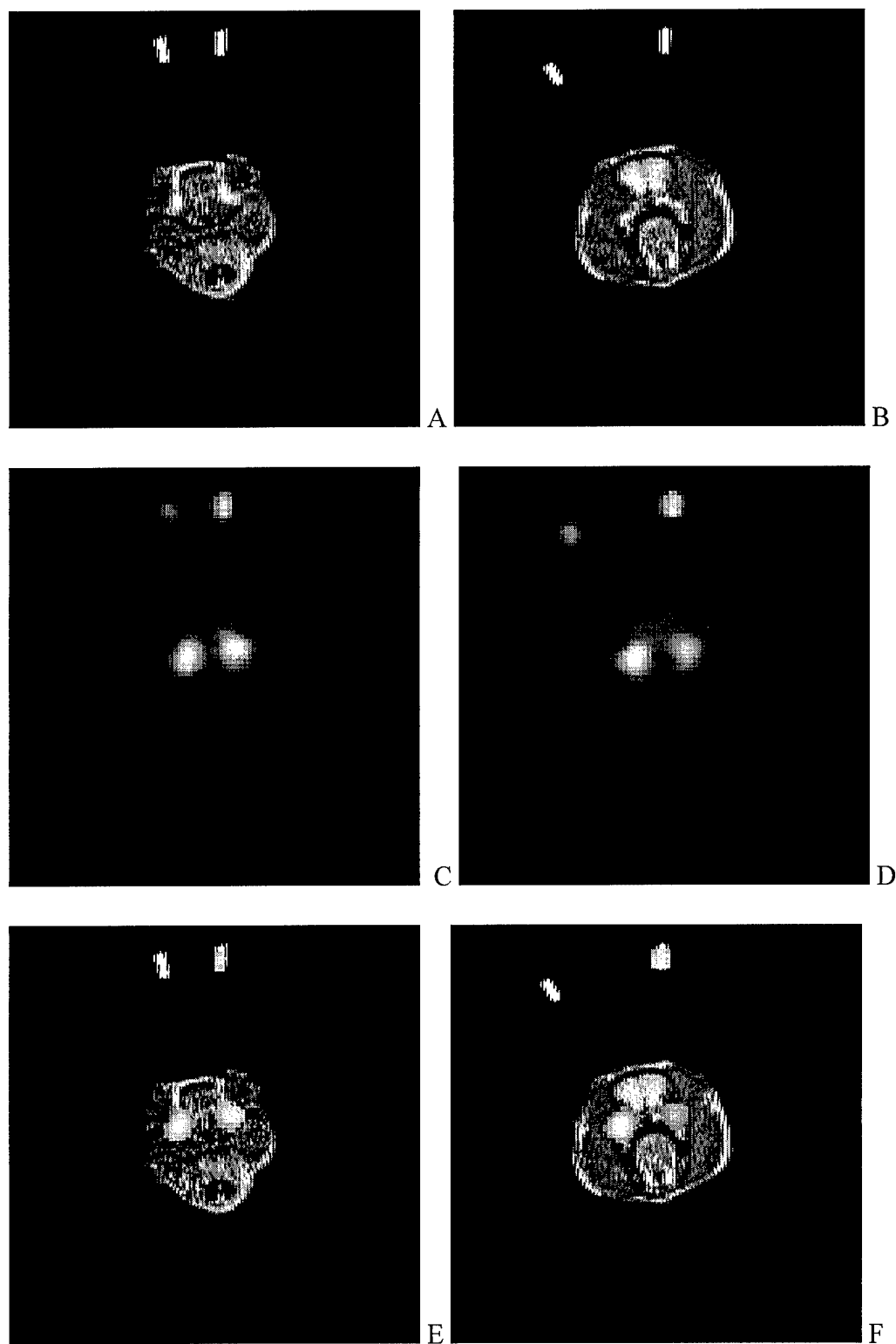


Figure 7.24. Assessment of Focal ^{18}FDG Uptake Medial, Inferior and Posterior to Rodent Eye. Figure A and B: Adjacent 3 mm Thick MR Images with 8 mm Separation; Figure C and D: Contiguous 3 mm SPECT Images Between MR Images. Figure E and F: Overlay of SPECT Peak Information onto MR Images.

Results of the study indicated that the Harderian gland had a biodistribution of 5.39 ± 0.19 %dose/gm (1.29 ± 0.09 %dose/organ), compared to 1.13 ± 0.14 %dose/gm (2.14 ± 0.22 %dose/organ) for the brain. The small organ mass of this gland (0.12 gm/gland) results in the bright foci observed in the SPECT images. ROI assessed gland activity for the two imaged animals results in fair agreement with these biodistribution measurements, with an error of $\pm 14\%$. Specific activity determined from ROIs was a factor of two lower than the invitro results. The differences can be attributed to many factors including: differences in biodistribution for the imaged animals and those assessed invitro; and finite resolution of SPRINT compared to the size of the gland.

The acute uptake expressed by the Harderian gland emphasizes the significant physiological and anatomical differences between research animals and humans. Side anatomical information is required during the invivo assessment of organ activity, not only to assist in region of interest analysis, but to differentiate and reveal physiological data that may confound measurements and affect their application to humans.

Comparison of Image Performance with Positron Emission Tomography

It is useful to provide a baseline by which the qualitative and quantitative results obtained with SPRINT can be compared. This was accomplished by imaging a simple uniform phantom and a single rat injected with ^{18}FDG using a conventional two-dimensional positron emission tomography (PET) system. The PET scanner used was a model PCT4600 produced by the Cyclotron Corporation, which is available for animal imaging. Images were acquired of a line source and a cylinder of uniformly distributed activity to determine system sensitivity and image noise. Images were then acquired of a Sprague-Dawley rat injected with $[^{18}\text{F}]\text{fluorodeoxyglucose}$.

Methods

The PET scanner featured three rings of bismuth germinate (BGO) detectors, forming three slices axially. Individual rings and adjacent rings are in coincidence, allowing five slices to be reconstructed with a 10 mm slice thickness and an 11.5 mm slice separation. Sensitivity and resolution were determined by imaging an ^{18}F line source with a lineal activity of 0.84 $\mu\text{Ci}/\text{mm}$ for 15 minutes. Sensitivity was verified and image uniformity was evaluated using a cylinder phantom filled with a uniform activity concentration (1.85 $\mu\text{Ci}/\text{ml}$) and again imaged for 15 minutes. Projection data was reconstructed using filtered backprojection with a pure ramp filter with a 1.8 cm^{-1} cutoff, equal to the Nyquist frequency of the system. Corrections for non-uniformity, deadtime, decay, attenuation, and wobble^{iv} were applied during reconstruction.

Phantom imaging was followed by imaging the brain and thoracic region of a 275 gm female Sprague-Dawley rat. The animal was anesthetized with 40 mg/kg pentobarbital and then placed in the animal holder described previously. Fiducial

^{iv} The detector ring is wobbled during acquisition to increase the spatial sampling of the system.

markers were filled with 4 mM Gd-DTPA. T1-weighted spin-echo MR images were acquired of the animal using the CTI 2T system. Acquisition parameters are shown in Table 7.14. The rat was then injected with 1170 μ Ci of ^{18}FDG , and distribution was permitted for 30 minutes during which time the fiducial markers were replaced with ^{18}FDG ($\sim 1 \mu\text{Ci}/\text{marker}$). The animal was imaged for three 15 minutes scans on the PCT4600, as observed in figure 7.25, using the parameters in Table 7.14. The rat was sacrificed at two hours post injection, with brain, heart, lungs, liver and blood being harvested and activity measured using the Packard-Tricarb well counting system.

Table 7.14. Acquisition Parameters for Rat MR and PET Imaging.

MRI Parameters		PET Parameters	
FOV	80 mm	FOV	160 mm
Slice Thickness	3 mm	Slice Thickness	9-11.5 mm
Slice Separation	8 mm	Slice Separation	11.5 mm
Size	256x128	Size	128x128
Pixel Size	0.312 mm	Pixel Size	1.25 mm
Image Type	T1 weighted	Reconstruction	FBP
TR	600 ms	Filters	Ramp Only
TE	20 ms	Cutoff	1.8 cm^{-1}
Elapsed Time	2:33 min	Elapsed Time	15 min
F1	85.495 MHz		

Calibration of the PCT 4600 was performed using appropriate ring sources and blanks for normalization and attenuation correction, and using the cylindrical phantom and line source to obtain system calibration factors. A concentration based calibration factor was determined from a region of interest analysis of the uniformly distributed cylindrical phantom. Activity concentration was assessed using a 0.5 ml aliquot of the phantom measured in a NaI(Tl) well counting system. Activity concentration was

verified against the known injected activity and phantom volume. Calibration factors were calculated in a manner identical to those for SPRINT.

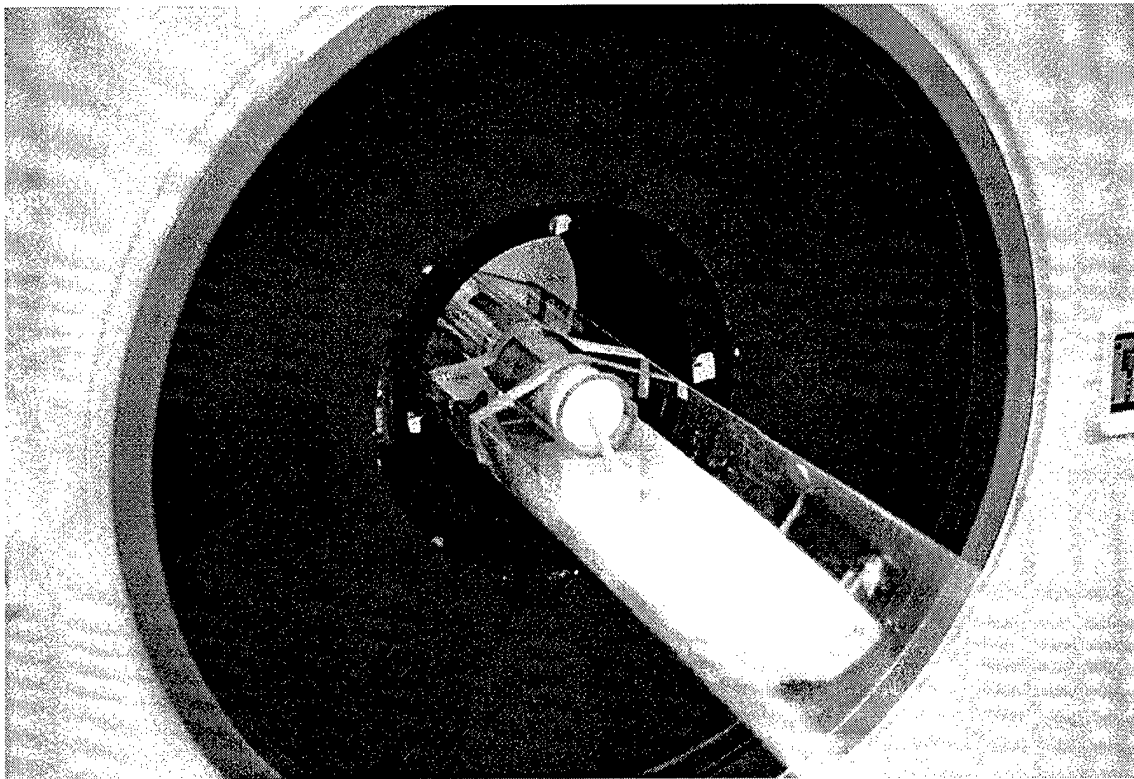


Figure 7.25. Rat in Animal Holder During PET Imaging.

Animal image analysis was performed by drawing regions of interest around and within organ boundaries of the reconstructed images. A pixel count rate (cpm/pixel) was calculated from the average pixel counts found within a region and the total acquire time. The activity concentration was then assessed by dividing by the concentration based calibration factor. Alternatively, total organ activity was assessed using the line source calibration factor and total region count rates for ROIs that encompassed the organ, as was done for SPECT image analysis.

Results and Discussion

The central slice of the line source is shown in figure 7.26A, with associated horizontal and vertical profiles in figure 7.26B. The reconstructed image of the cylindrical phantom is shown in figure 7.26C, with its profiles in 7.26D. Analysis of the line source indicated a system resolution of 7.6 mm FWHM and 14.79 mm FWTM. This is two to three mm wider than that achieved by SPRINT using a 3.175 mm slit aperture and aperture penetration correction. The lineal activity concentration in the line source was used to obtain an absolute system sensitivity from the total counts obtained in a given slice during a 15 minute acquisition. Sensitivity was measured at 10600 ± 270 cpm/ μ Ci (4750 ± 120 cps/MBq), approximately 160 times that achieved with SPRINT equipped with the high energy parallel collimator, a 3.125 mm slit, and use of aperture penetration correction. It should be noted that PET sensitivity is not a function of resolution, as it is in SPECT based systems.

A direct comparison of the noise characteristics in reconstructed images between PET and SPRINT is difficult because of the strong dependence on the reconstruction algorithm and filters used. However, the dramatic difference in sensitivity between these systems indicates that for equal activities and imaging times, PET images will have significantly better noise characteristics than SPRINT images. Conversely, the sensitivity difference indicates that PET imaging requires 160 times less activity than SPRINT to obtain an equivalent quality image when using the same reconstruction method. As an example, the standard deviation in the PET image of a uniform cylinder was approximately 3.8%, reconstructed with an average of 2600 count per pixel (5.8×10^6 total counts), FBP and a pure ramp filter. The image was composed of 1.56 mm^2 pixels and the activity concentration in the phantom was $1.85 \mu\text{Ci/ml}$. A SPRINT image of the uniform 2-D phantom region had a standard deviation of 24%, and was reconstructed with an average of 1800 counts per pixel (8×10^6 total image counts), using SAGE with

$\beta=2^{-26}$. The image was composed of 0.77 mm^2 pixels and the background activity concentration was $135 \mu\text{Ci}/\text{ml}$. We observe that despite using a more noise tolerant algorithm (SAGE versus FBP) there is considerably more noise in the SPRINT image. This is partially due to the poorer count statistics (fewer counts in smaller pixels), and variance added by the penetration correction method employed for SPRINT.

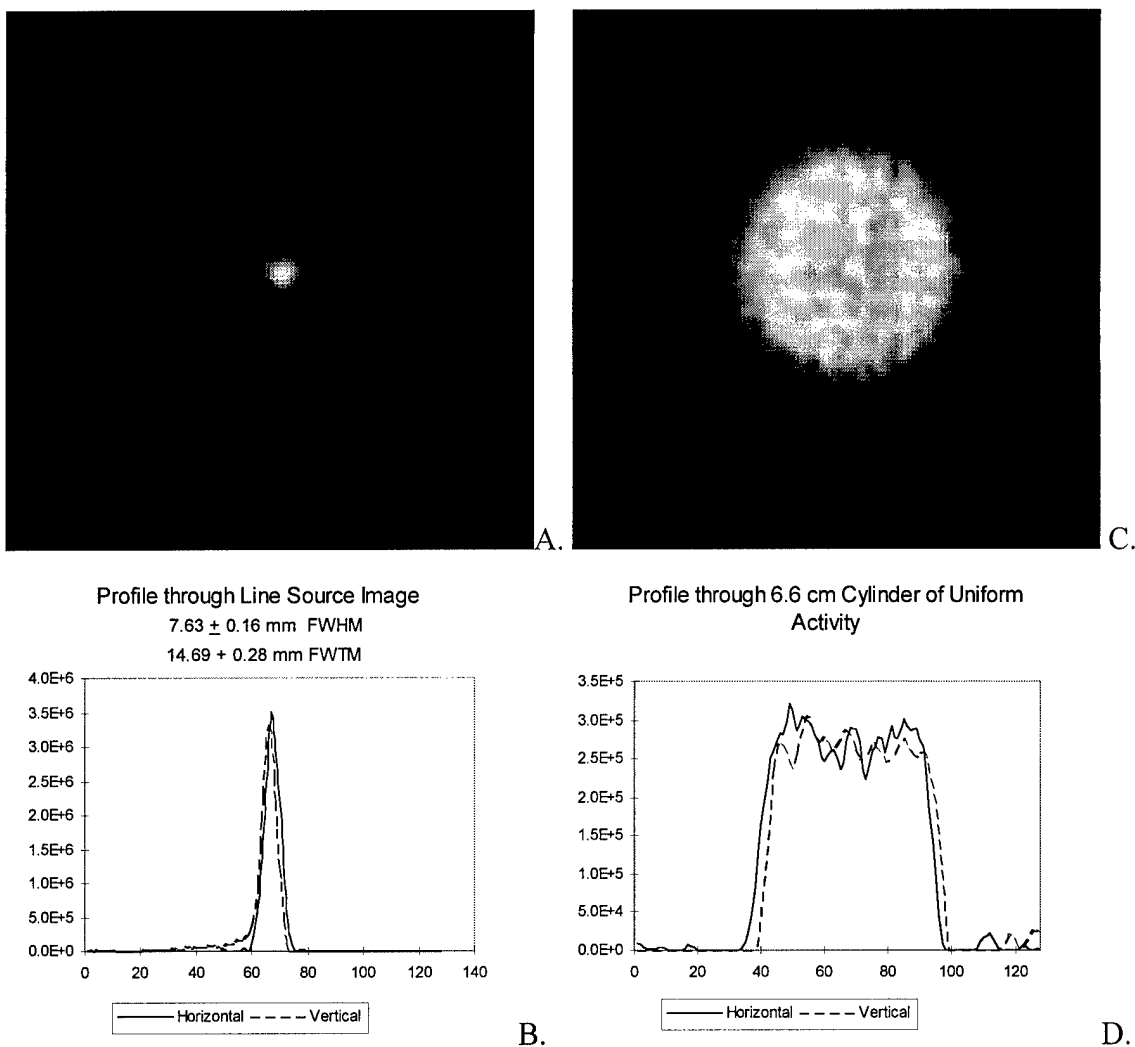


Figure 7.26. Image and Profiles for Uniform Cylinder Source and Line Sources Imaged by Positron Emission Tomography.

The reconstructed animal images are shown in figure 7.27, covering the region from the top of the animals head to the upper thoracic region. Matched MR images are

shown above the PET image for anatomical reference. The first PET image shows Harderian gland uptake and regional brain uptake. The second slice shows only brain uptake. The fourth image covers at least a portion of the cardiac region. Comparing these images to those in figure 7.21, the PET images have considerably worse resolution, both axially and transaxially. However, the FBP images are of generally low noise, with the area of the Harderian gland, brain and heart well defined and of high contrast compared to surrounding tissue.

Table 7.15 shows the relatively poor results obtained when attempts were made to quantify image data. Regions of interest were scribed within and around the total brain (image B) and cardiac region (image D). Biodistributions at two hours post injection were 2.16 %dose/organ for the brain and 4.87 %dose/organ for the heart, in reasonable agreement with the animals used for SPECT imaging. These levels correspond to brain and heart activities at the time of imaging of 17 and 48 μ Ci, respectively. For both these organs, there is a considerable underestimate of both tissues concentration and total organ activity. For the brain, concentrations were a factor of two less than that measured invitro, and total activity was a factor of four less. For the heart, there is a consistent factor of four difference for both concentration and total activity between the invitro and invivo measurements. Since the calibration process was accomplished using two different methods, it is unlikely that errors in calibration account for these differences. Examination of the corresponding MR images indicates that for both brain and heart, there may be serious inaccuracies in quantification because of poor axial resolution, and limited field of view of this system. For the brain, the large slice thickness may cause scribed regions to include areas of low uptake outside the brain. This effect, compounded by the larger pixel size and poorer in-plane resolution as compared to SPRINT cause ROIs to measure an activity concentration considerably lower than what is actually present. Similarly, the determination of total activity requires summing the total count rate for all region in which the brain is observed. An underestimate of brain activity is

likely due to excluding the first slice, which had considerably activity contributed by the Harderian glands. If this slice is included, the brain activity is overestimated by several hundred percent. For the heart, a significant portion of the heart may have been outside the sensitive region of the system, resulting in the negative biases observed for concentration and total activity. This argument is supported by examining the MR and PET images of figure 7.27. The last available PET image appears to be above the primary cardiac region as noted by the MR images.

Table 7.15. Quantitative Results Obtained from PET Image Analysis.

Activity Concentration Assessment	Small region count rate (brain and heart)*	Calculated Concentration (ROI cpm/pixel/CF)	Estimated‡ Concentration	Error (%)
Brain	cpm/pixel \pm cpm/pixel	μ Ci/cc \pm μ Ci/cc	μ Ci/cc	
Acquis. 1	65560 \pm 5540	6.86 \pm 0.60	8.74	-21.5%
Acquis. 2	57693 \pm 4718	6.04 \pm 0.51	7.90	-23.6%
Heart	cpm/pixel \pm cpm/pixel	μ Ci/cc \pm μ Ci/cc	μ Ci/cc	
Acquis. 1	97933 \pm 10467	10.25 \pm 0.17	46.5	-77.9%
Acquis. 2	94667 \pm 12867	9.91 \pm 0.19	42.0	-76.4%
Calibration Factor: 1160000 \pm 41200 cpm/ μ Ci				

Total Activity Assessment	Large region count rate [†]	Calculated Activity (ROI cpm.CF)	Estimated‡ Activity	Error (%)
Brain	cpm	μ Ci	μ Ci	
Acquis. 1	5383333	4.65	18.0	-74.1%
Acquis. 2	4392000	3.80	16.3	-76.6%
Heart	cpm	μ Ci	μ Ci	
Acquis. 1	10200000	8.82	40.5	-78.3%
Acquis. 2	10486667	9.07	36.7	-75.3%
Calibration Factor (CF): 9550 \pm 212 cpm/pixel/ μ Ci/ml				

* ROI analysis based on small to moderate size regions within the organ boundaries to provide an estimate of organ concentration.

† ROI analysis based on large regions which completely encompass the observed organ.

‡ Estimated organ activity concentration or total activity based on invitro measured organ concentration at time of sacrifice, decay corrected to start time of imaging.

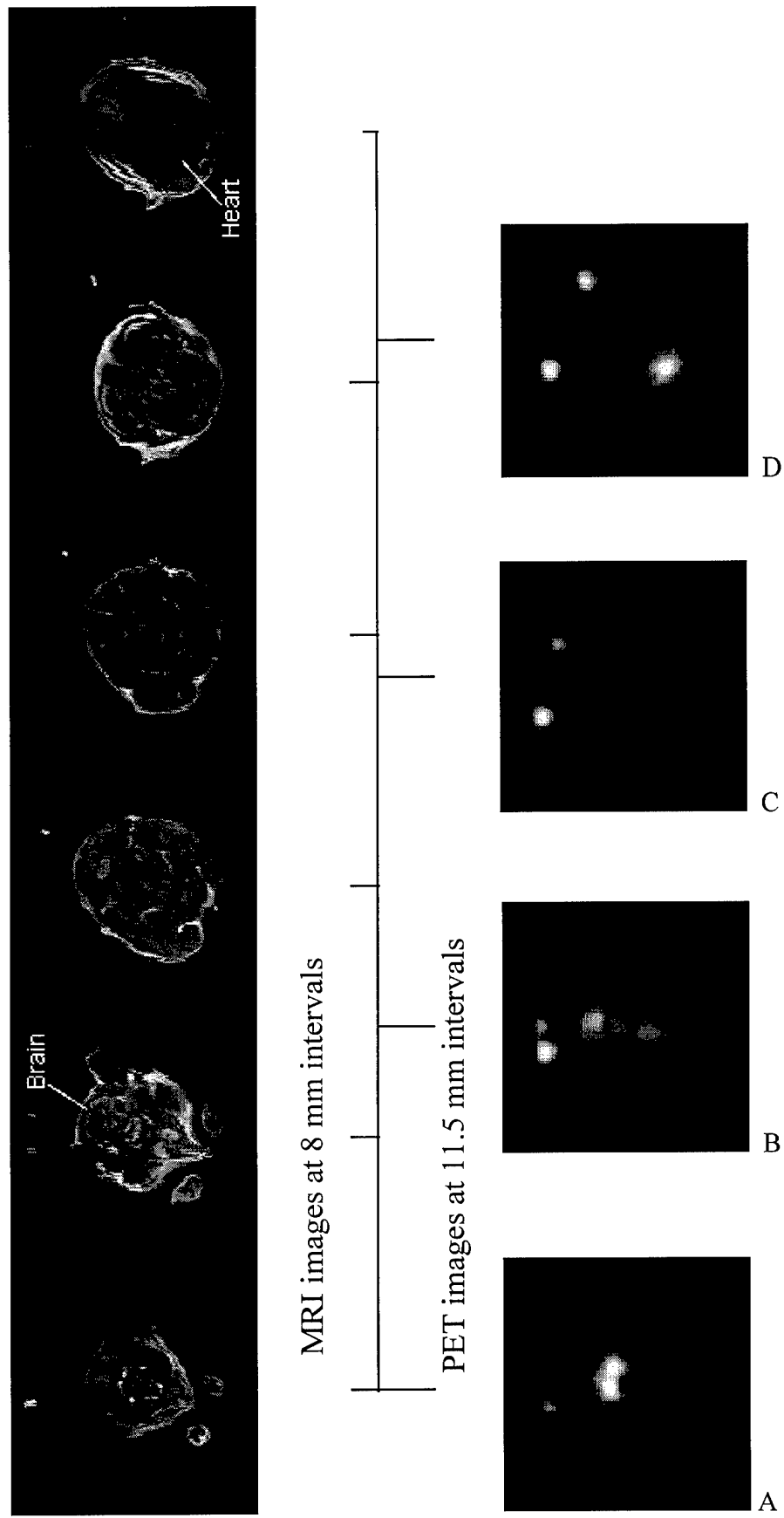


Figure 7.27: Comparative MRI and FDG PET images of a 275 gm SD rat, The brain is observed in the first through third MRI images, while the heart is in the fifth image.

Although there is poor accuracy in these PET images, the PET images show much lower noise when using FBP with a pure ramp filter, than similar SPRINT images reconstructed with SAGE ($\beta=2^{-27}$), which devalues noisy data. For PET, the animal was injected with three to ten times less activity than used in SPRINT imaging, and image acquisition times were almost half (15 minutes for PET compared to 27 minutes for SPRINT). The lower noise is again due principally to the much higher sensitivity of PET.

Summary

Qualitative and quantitative analysis of SPRINT images indicated that good accuracy and fair precision could be obtained of large objects in simple phantoms and of large animal organs that have significant radiotracer uptakes. Accuracy was dependent on numerous corrections to the raw projection data, as well as the methods employed for image reconstruction, image analysis and system calibration.

The very poor sensitivity of SPRINT for 511 keV photons, and variance introduced by aperture penetration correction caused all SPECT images to be noisy. Minimum standard deviations of 20% or greater were observed in the uniform background regions of very high count phantom studies, increasing up to several hundred percent for low activity cold regions. Reconstruction using SAGE provided considerable improvement in reducing noise when compared to filtered backprojection reconstruction where minimum filtering was used. A result of the iterative algorithm weighting the projection data by its statistical significance. Low noise SPRINT images were only acquired by using very high activities (30 to 40 mCi of ^{18}F) and imaging for long periods, particularly in comparison to PET. Unfortunately, high activities also introduced bias in quantified results due to uncorrected deadtime effects.

An important disadvantage posed by using long acquisition times (in addition to the requirement for decay correction) is loss in temporal resolution of animal

biodistributions. Since imaging times are long compared to the short uptake and biodistribution of most PET agents, is impossible to observe specific biodistribution patterns. The poor sensitivity of SPRINT thus precludes the assessment of ^{11}C labeled compounds, since images could not be collected fast enough (<5 min) and still provide images of high signal to noise.

Despite SPRINT's poor sensitivity, the ability to achieve high resolution images that can provide good quantitative results has been demonstrated. This resolution is achieved through a magnifying slit aperture geometry, high resolution collimation and correcting acquired projection data for aperture penetration by 511 keV photons. The resulting in-plane resolution was as low as 4.4 mm for SAGE reconstructed images, 2 to 3 mm less than that obtained with a commercial 2-D SPECT system. SPRINT also demonstrated good axial resolution provided by the specially designed high energy slice collimator. These developments indicate that quantitative high energy animal imaging can be performed, but only if the object to be assessed has sufficient volume and uptake, and poor sensitivity can be tolerated.

References to Chapter VII

¹ Zhang Y, Improved SPECT Radioactivity Quantification Using MRI Side Information, Ph D Thesis, School of Engineering, University of Michigan, 1996.

² Wilderman SJ, Vectorized Algorithms for Monte Carlo simulation of kilovolt electron and photon transport, Ph D Thesis, School of Engineering, University of Michigan, 1990

³ Knoll GF. Radiation Detection and Measurement. New York. John Wiley and Sons, 1979:97-102.

⁴ Jaszcak RJ, Floyd CE, and Coleman RE. Scatter Compensation Techniques for SPECT. *IEEE Tran Nuc Sci*, 1985;32:1:786-793.

⁵ Chang LT. A method for attenuation correction in radionuclide computed tomography. *IEEE Transactions on Nuclear Science*, 1978;NS-25(1):638-643.

⁶ National Nuclear Data Center, INEL, 1992.

⁷ Fessler JA. ASPIRE 3.0 User's Guide: Sparse iterative reconstruction library. Technical Report #293. Communications and Signal Processing Library. Dept of Elec Eng and Comp Sci. Univ of Mich. 1995.

⁸ Hubbel JH. Photon Mass Attenuation and Energy Absorption Coefficients from 1 keV to 20 MeV. *Int J Rad Isot*. 1982;33:1269-1290.

⁹ Jaszcak RJ, Coleman RE, Greer KL. The subtraction of scattered events from SPECT photopeak events. *J Nucl Med* 1983;24:P82.

¹⁰ Jaszcak RJ, Greer KL, Floyd CE, et al. Improved SPECT quantification using compensation for scattered photons. *J Nucl Med* 1984;25:893-900.

¹¹ Koral KF, Swailem FM, Buchbinder S, Clinthorne NH, Rogers, WL and Tsui BMW. SPECT dual-energy window Compton correction: scatter multiplier required for quantification. *J Nucl Med* 1990;31:90-98.

¹² Oppenheim BE. Scatter correction for SPECT. *J Nucl Med* 1984;25:928-929.

¹³ Wu RK and Siegal JA, Absolute quantitation of radioactivity using a build-up factor. *Med Phys* 1984;11:189-192.

¹⁴ Ljungberg M, Hademenos. A user's manual for SIMIND, version 1.4. Dept of Radiation Physics, University of Lund, Switzerland LUNFD6/(NFRA-3093). 1995

¹⁵ Sorenson JA, Phelps ME. Physics in Nuclear Medicine. Philadelphia. WB Saunders Company, 1987:419-423.

¹⁶ Greene EC. Anatomy of the Rat. New York. Hafner Publishing Company, 1963:86:95.

¹⁷ Leydig F. Sur Anatomie der mannlichen Geschlechtsorgane und Analdrusen der Säugetiere. *Ztschr f wiss Zool Bd. 2*, 1850,1-57.

CHAPTER VIII

SUMMARY AND CONCLUSIONS

This study has examined two methods of biodistribution assessment in rats for ligands labeled with positron emitting radionuclides. The first objective of this work was to explore ways to simplify conventional invitro methods of biodistribution assessment. For the case of ^{11}C labeled tracers, evidence has been presented that indicates examining the biodistribution within the first 15 minutes post injection is sufficient to characterize the overall biodistribution for solid organs. A reduced sacrifice protocol based on two measurements during this period provides estimates of cumulated activity that are either equivalent or conservative compared to those obtained using multiple sacrifice intervals. For the gallbladder and urinary bladder, a correction is required to the assessed cumulated activity to compensate for delayed organ uptake. For the ten radiotracers examined, the maximum activity which could be injected and not exceed a five rad absorbed dose limit to a given organ was found to range from 410 MBq (11 mCi) for $[^{11}\text{C}]$ FNZPAM to 3441 MBq (93 mCi) for $[^{11}\text{C}]$ MTBZ.

The use of 3D PET imaging systems provides greater relevance to this proposed method. These new systems have sensitivities that are six to ten times that achievable with 2D systems, allowing preliminary studies of new radiotracers to be conducted with significantly lower dosages. Thus, even the more conservative measures of absorbed dose assessed with this method result in allowable injected doses which can readily be used for clinical evaluation of new compounds.

The second objective of this work was to examine the capabilities and limitations of using SPRINT to assess biodistributions invivo of positron emitting radiotracers. It

has been demonstrated that there are severe limitations in the use of SPRINT for imaging 511 keV photons, especially when using high resolution collimation. Specifically, system sensitivity at high energies is simply inadequate to acquire projection data with the necessary time resolution to trace organ specific time-activity profiles of short half-life emitters.

Although sensitivity is low for positron imaging, it has been established that SPRINT can provide high quality images if activity concentrations on the order of 100 μ Ci per ml can be attained and long acquisition times are employed. The system can produce images of 4 to 5 mm resolution axially and in-plane, with modest noise in uniform regions (<20% standard deviation). Rodent imaging with injected dosages of 3 to 10 mCi [18 F]fluorodeoxyglucose provided images with good contrast and resolution of the brain and heart. The capacity to image 511 keV photons at high resolution is attributed to the magnifying slit-aperture geometry of SPRINT, the development of a simple method to overcome aperture penetration by high energy photons, and a precision high energy slice collimator. The compromise made in achieving high system resolution was a loss in system sensitivity. For the slice collimator, an effective open area of 66% resulted in a point source sensitivity of only 127 cpm/ μ Ci, when a 3.125 mm slit opening was used. This already low sensitivity is reduced by more than half when implementing the blocked slit method for correcting aperture penetration.

Very low system sensitivity in turn affects the ability to successfully estimate organ concentration from image data. Low noise images were only observed in very high count images which were negatively biased due to uncompensated deadtime. Alternatively, low count images were very noisy (>50% SD in uniform regions), providing quantitative estimates with low precision. Despite these issues, “hot” phantom objects, and the rodent brain and heart were assessed with errors ranging from +12% to -8%.

Comparison of the sensitivity of SPRINT (configured with a 3.175 mm slit and implementation of penetration correction) with that of the PCT 4600 PET system demonstrated a 160 fold reduction in sensitivity, chiefly due to the use of electronic collimation and the high intrinsic efficiency of the BGO detector elements. This difference approaches a factor of 1600 with septaless 3D PET systems. The resolution of clinical PET systems is generally worse than that achieved with SPRINT, on the order of 6 to 8 mm FWHM. (Note that if SPRINT were designed for 8x8 mm resolution, sensitivity would be improved by a factor of 2.5). However, new research in the area of PET imaging has reported the development of high resolution, small field-of-view PET systems designed specifically for small animals^{1 2 3 4 5 6}. These systems report in-plane resolutions ranging from 1.8 mm to 4.6 mm FWHM (3.1 mm to 5.4 mm axially) and sensitivities ranging from 3300 cps/ μ Ci/ml (198,000 cpm/ μ Ci/ml) to 20700 kcps/ μ Ci/ml (1.24×10^6 cpm/ μ Ci/ml), which are comparable to 2D clinical systems. Further, these instruments have already been applied to the measurement of glucose metabolism and ¹¹C biodistribution assessment in the rat^{7 8 9}. The greater sensitivity and higher resolution afforded by these small animal PET systems make these instruments superior for *invivo* biodistribution assessments of positron emitters compared to SPRINT and other SPECT based imaging systems.

Recommendations for Future Work

It is evident that increasing system sensitivity is highly desirable if further qualitative (and quantitative) improvements are to be achieved with SPRINT imaging at high energies. Thicker scintillators with higher stopping power than NaI(Tl) are an effective solution if resolution losses can be minimized. Current research suggests that lutetium oxyorthosilicate (LSO) may provide considerable improvements in detection efficiency, while still providing a very fast decay time and good light output¹⁰. Characteristics of this scintillator in comparison to NaI are provided in Table 8.1. The use of a 25 mm thick LSO scintillator can provide a 50% photoelectric detection efficiency at 511 keV, as compared to 7% for 13 mm of NaI(Tl). Disadvantages of this material is that it is presently very expensive and it is mildly radioactive due to a naturally occurring contaminant. Resolution losses in thick scintillators can potentially be limited by use of digital light pipes¹¹, energy specific position weights, and implementation of surface altering technologies which would shape the light distribution within the scintillator¹².

Table 8.1. Characteristics of LSO as a High Efficiency Scintillator.

	Photoelect. Density (g/cm ³)	Photoelect. Attenuat. Coefficient (cm ⁻¹)	Photoelect. Interaction Probability (25 mm)	Relative Scintillation Efficiency %	Decay Time (ns)	Radioactive? Yes/No	Hygro.?
NaI	3.67	0.0585	14%	100	230	No	Yes
LSO	7.4	0.27	50%	75	40	Yes	No

If SPRINT detectors were made 100% efficient for 511 keV photons, overall system sensitivity would increase by an approximate factor of 10ⁱ. This is still considerably less than PET systems because of the different sensitivities provided by

ⁱ This is based on the current 12.7 mm NaI SPRINT modules having an 11% detection probability assessed from Monte Carlo simulations (7% photoelectric effect detection probability).

electronic versus mechanical collimation. To improve SPECT sensitivity further, either the means of mechanical collimation must be optimized, or a method for electronic SPECT collimation must be employed. The latter serves as the basic operating premise for the Compton aperture camera which uses electronic coincidence between a primary scattering detector and a secondary scintillation detector (e.g. SPRINT) for position estimation^{13 14}. Theoretical performance of these systems suggests high spatial resolution and good sensitivity can be achieved for high energy photons. Currently, these systems are being aggressively investigated for their application in high energy medical and industrial imaging.

Reengineering the mechanical collimation of SPRINT through use of a six pin-hole aperture (instead of slits) and removing the slice collimator could also improve sensitivity. Installing a pin-hole aperture would provide three-to-one axial magnification increasing sensitivity for a reduced axial field of view. Other researchers have investigated the use of pin-hole SPECT systems and cone-beam FBP algorithms to conduct high resolution low-energy animal imaging of ^{99m}Tc labeled compounds^{15 16 17 18 19 20}. Typical performance for two of these systems as compared to SPRINT are listed in Table 8.2. In general, resolutions and sensitivities between systems are similar. SPRINT's higher sensitivity originates from its full ring design and six apertures, offset by the reduced sensitivity of a longer source to aperture distanceⁱⁱ and its present fan-beam geometry.

Aperture penetration in such geometries still requires correction if penetration blurring of the PSRF is to be minimized. This could be accomplished by blocking alternate pinholes and correcting the projection data for block penetration and penumbra using a two-dimensional weighting function. Investigating an optimal block design to

ⁱⁱ Pinhole collimator efficiency decreases inversely with the square of the aperture to source distance.

minimize penumbral effects and developing an iterative solution for the penetration corrected image may provide additional qualitative improvements when using this “block” technique.

The optimal solution to aperture penetration is to accurately model the penetration effect and incorporate it into the system response matrix. A statistical iterative reconstruction technique, such as SAGE, can then be used to provide images that should have the best achievable sensitivity and resolution. The usefulness of this method is dependent on the accuracy by which penetration can be modeled for the entire system, and the availability of computer platforms capable of handling the resultant non-sparse weights matrix.

Successful development of an aperture penetration correction algorithm suitable for pin-hole geometries would allow high resolution small field-of-view pin-hole SPECT to be performed using clinical imaging systems. Since low energy pin-hole SPECT has already been investigated using a clinical four head gamma camera^{21 22}, application of the developed correction method to clinical multi-head systems should be relatively straightforward.

Table 8.2. Comparison of Pinhole Collimator Resolution and Sensitivities for ^{99m}Tc for Several Imaging Systems.

Weber et al. ^{(17)*}			Jaszczak ^{(18)*}			SPRINT [†]		
(Source to Aper. 4.0 cm)			(Source to Aper. 4.0 cm)			(Source to Aper. 6.5 cm)		
(FOV - 3.0 cm)			(FOV=6.0 cm)			(FOV=9 cm)		
d [‡] (mm)	Resolution (mm)	Sensitivity (cps/ μCi)	d (mm)	Resolution (mm)	Sensitivity (cps/ μCi)	d (mm)	Resolution (mm)	Sensitivity (cps/ μCi)
				0.6	1.5	0.9		
1.0		1.1	1.2	1.9	2.6			
2.0	2.8	4.0	2.0	2.8	5.7	2.0	2.9	11
3.3		10.9				3.1	4.4	17

* Single head gamma cameras

† Full ring tomograph

‡ Aperture opening

Improvements in SPRINT sensitivity would allow its application to other high energy imaging applications, including qualitative and quantitative tumor imaging. Tumor metabolism could be assessed using [¹⁸F]fluorodeoxyglucose, and the diagnostic and therapeutic efficacies of iodine labeled compounds such as [¹³¹I]MIBG and ¹³¹I labeled monoclonal antibodies could be examined. The importance of *invivo* assessment of tumor radioactivity originates from the unique nature of xenografted tumors in laboratory animals. In contrast to the typically small variance in biodistributions seen between organs in normal animals (reference Chapter II), the biodistribution in tumors are extremely variant due to the unique physiology and anatomy of a given tumor. Consequently, there is a clear advantage in determining the time activity profile of a radiopharmaceutical or radiotracer within the same animal. Further, *invivo* assessment provides long term tracking of tumor progression and can allow comparison of the pharmacological affect of different compounds in the same subject.

Since SPRINT acquisition software now allows multi-window image acquisitions, the potential does exist to monitor within the same animal the biodistributions of ¹⁸FDG and an iodine labeled radiotracer simultaneously. Figure 8.1 demonstrates the difference in spectra resulting from ¹³¹I and ¹⁸F imaged separately and jointly with the high energy parallel collimator in place. Both peaks have a resolution of approximately 13 percent when imaged separately, with the iodine peak showing some degradation in resolution when imaged with ¹⁸F. For equal source activities, the annihilation peak area is approximately 1.3 times the iodine peak (this is explained in Chapter V). Most notably when both sources are imaged, approximately 37% of the iodine peak is attributable to scattered annihilation radiation, whereas 7% of the annihilation peak is attributable to scattered high energy iodine energies. Dual energy imaging would therefore require integrating methods to correct for photopeak contamination from opposing nuclides. Methods include spectrum stripping and the use of injected activities of iodine and fluorine which balance the level of contamination in the adjacent photopeaks.

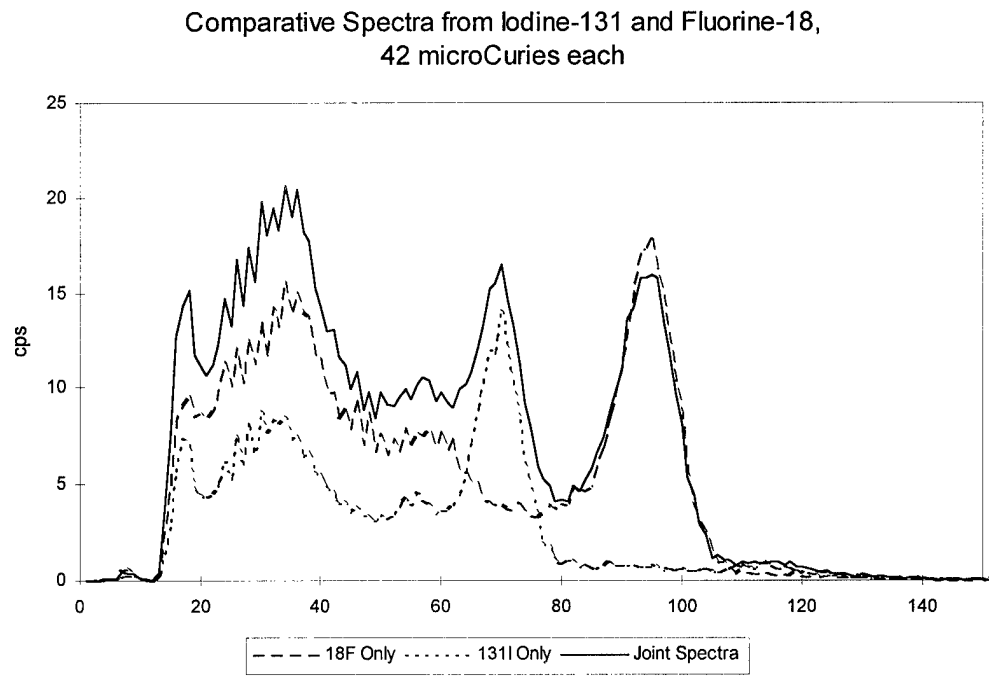


Figure 8.1. Module Spectra of Simultaneously Acquired ^{131}I and ^{18}F Sources.

Conclusions

The major focus of this work has investigated the application of SPRINT to quantitative animal imaging for rats injected with positron emitting radioligands. It has been shown that measuring the biodistribution of very short half-life compounds is not possible due to the limited sensitivity of SPRINT and the constraints made on injected activity in the animal. Further, it has been shown that the general application of SPECT to 511 keV imaging is extremely unfavorable compared to the use of coincidence imaging. However, good qualitative and quantitative results have been observed when using high activities and long acquisition times for SPECT imaging of ^{18}F . Implementing technologies to improve system sensitivity will allow more rapid imaging and provide improved image quality. A more thorough evaluation of such factors as deadtime and scatter should allow higher quantitative accuracy in image assessment and allow SPRINT be a more effective tool in assessing animal biodistributions of high-energy emitting radiotracers.

References to Chapter VIII

¹ Cutler PD, Cherry SR, Hoffman EJ, Digby WM, Phelps ME. Design features and performance of a PET system for animal research. *J Nucl Med* 1992;33(4):595-604.

² Tavernier S, Bruyndonckx P, Shuping Z. A fully 3D small PET scanner. *Phys Med Biol* 1992;37(3):635-43.

³ Lammertsma AA, Hume SP, Myers R, Ashworth S, Bloomfield PM, Rajeswaran S, Spinks T, Jones T. PET scanners for small animals *J Nucl Med* 1995;36(12):2391-2.

⁴ Marriott CJ, Caderette JE, Lecomte R, V. Scasnar V, Rousseau J, and vanLier JE. High-resolution PET imaging and quantitation of pharmaceutical biodistributions in a small animal using avalanche photodiode detectors. *J Nucl Med* 1994;35:1390-1397.

⁵ Watanabe M, Uchida H, Okada H, Shimizu K, Satoh N, Yoshikawa E., Ohmura T Yamashita T, Tanaka E. A high resolution PET for animal studies. *IEEE Trans Med Imag* 1992;11:577-580.

⁶ Rajeswaran S, Bailey DL, Hume SP, et al. 2D and 3D imaging of small animals and the human radial artery with a high resolution detector for PET. *IEEE Trans Med Imag* 1992;11:386-391.

⁷ Magata Y, Saji H, Choi SR, Tajima K, Takaki T, Sasayama S, Yonekura Y, Kitano H, Watanabe M, Okada et al. Noninvasive measurement of cerebral blood flow and glucose metabolic rate in the rat with high-resolution animal positron emission tomography (PET): a novel in vivo approach for assessing drug action in the brains of small animals. *Biol Pharm Bull* 1995;18(5):753-6.

⁸ Hume SP, Myers R, Bloomfield PM, Packa-Juffry J, Cremer JE, Ahier RG, Luthra SK, Brooks DJ, Lammertsma AA. Quantitation of carbon-11-labeled raclopride in rat striatum using positron emission tomography. *Synapse* 1992;12(1):47-53.

⁹ Rajeswaran S, Hume SP Cremer JE Joung J Bailey DL Ashburner J Luthra SK Jones AK Jones T. Dynamic monitoring of [¹¹C]diprenorphine in rat brain using a prototype positron imaging device. *J Neurosci Methods* 1991;40(2-3):223-32.

¹⁰ Melcher CL, Schweitzer JS. A promising new scintillator: cerium-doped lutetium oxyorthosilicate. *Nuc Instr Med A* 1992;212-214.

¹¹ Siemens Medical Systems, 1996 Society of Nuclear Medicine Meeting, Denver CO, *Personal Communication*, Jun 1996.

¹² Roger WL, Proposed methods to increase scintillator resolution through surface patterning. Dept of Nuclear Medicine Research, University of Michigan, Ann Arbor MI, *Personal Communication*, Jun 1996.

¹³ Singh M. An electronically collimated gamma camera for SPECT, Part I, Theoretical considerations and design criteria. *Med Phys* 1983;10(4):421-427.

¹⁴ Singh M. An electronically collimated gamma camera for SPECT, Part II, Image reconstruction and preliminary experimental measurements. *Med Phys* 1983;10(4):428-435.

¹⁵ Palmer J, Wollmer P. Pinhole emission computed tomography: method and experimental evaluation. *Phys Med Biol* 1990;35:339-350.

¹⁶ Moore RH, Ohtani H, Khaw BA and Strauss HW. High resolution pin-hole sequence imaging of small laboratory animals. *J Nucl Biol* 1991;(32):987.

¹⁷ Weber DA, Ivanovic M, Franceschi D, Strand SE, Erlandsson K, Franceschi M, Atkins HL, Coderre JA Susskinf H Button T et al. Pinhole SPECT: an approach to invivo high resolution SPECT imaging in small animals. *J Nucl Med* 1994;35(2):342-8.

¹⁸ Jaszczak RJ, Li J, Wang H, Zalutsky MR, and Coleman RE. Pinhole collimation for ultra-high resolution small field-of-view SPECT studies. *Phys Med Biol* 1994(39):425-437.

¹⁹ Li J, Jaszczak RJ, Greer KL, Coleman RE. A filtered backprojection algorithm for pinhole SPECT with a displaced center or rotation. *Phys Med Biol* 1994;39:165-176.

²⁰ Strand SE, Ivanovic M, Erlandsson K, Franceschi D, Button T, Sjogren K, Weber DA. Small animal imaging with pinhole single-photon emission computed tomography. *Cancer* 1994;73(3 suppl):981-4.

²¹ Ishuza K, Mukai T, Yonekura Y, Pagani M, Fujita T, Magata Y, Nishizawa S, Tamaki N, Shibasaki H Konishi J. Ultra-high resolution SPECT system using four pinhole collimators for small animal studies. *J Nucl Med* 1995; 36(12):2282-7.

²² Weber D. Pinhole SPECT: ultra-high resolution imaging for small animal studies, editorial. *J Nucl Med* 1995; 36(12):2287-9.